

**AN EMBEDDED BOUNDARY APPROACH FOR SIMULATION OF REACTING  
FLOW PROBLEMS IN COMPLEX GEOMETRIES WITH MOVING AND  
STATIONARY BOUNDARIES**

A Dissertation  
Presented to  
The Academic Faculty

By

Balaji Muralidharan

In Partial Fulfillment  
of the Requirements for the Degree  
Doctor of Philosophy in the  
School of Aerospace engineering

Georgia Institute of Technology

August 2017

Copyright © Balaji Muralidharan 2017

**AN EMBEDDED BOUNDARY APPROACH FOR SIMULATION OF REACTING  
FLOW PROBLEMS IN COMPLEX GEOMETRIES WITH MOVING AND  
STATIONARY BOUNDARIES**

Approved by:

Dr. Suresh Menon, Advisor  
School of Aerospace Engineering  
*Georgia Institute of Technology*

Dr. Stephen M. Ruffin  
School of Aerospace Engineering  
*Georgia Institute of Technology*

Dr. Lakshmi N. Sankar  
School of Aerospace Engineering  
*Georgia Institute of Technology*

Dr. Julian J. Rimoli  
School of Aerospace Engineering  
*Georgia Institute of Technology*

Dr. Alexander Alexeev  
School of Mechanical Engineering  
*Georgia Institute of Technology*

Date Approved: April 28, 2017

Big things have small beginnings

*Lawrence of Arabia*

This thesis is dedicated to my family.



## ACKNOWLEDGEMENTS

This thesis would not have been possible without the support of many others. I thank and appreciate each of them for being part of my thesis journey. First and foremost, I would like to thank my thesis advisor Professor Suresh Menon for his guidance throughout my Ph.D. I am grateful to him for providing me the opportunity to work on some of the most interesting research problems in the field of computational combustion. His attitude to challenge everything and high standards he demanded has helped me become a better researcher. I would like to thank Prof. Rimoli, Prof. Ruffin, Prof. Sankar from the aerospace department and Prof. Alexeev from the mechanical department for accepting to be on my thesis committee. Their valuable comments and suggestions were very helpful in improving the quality of this thesis.

I would like to express my thanks to the U.S. Air Force Research Laboratory (AFRL), Eglin Air Force Base (Program managers: Dr. Douglas V. Nance and Pedro Lopezfernandez) for financially supporting this work. In addition, computational support provided by the DoD HPC Centers at the Air Force Research Laboratory (Wright Patterson AFB, Ohio) and the Engineer Research and Development Center (Vicksburg, Mississippi) are gratefully acknowledged.

I was fortunate to work with some of the best researchers in the field of numerical combustion at Computational Combustion Lab (CCL). I am thankful to the senior students Dr. Joseph Schulz, Dr. Matthieu Masquelet, Dr. Andrew Smith and Timothy Gallagher for their help in making me understand the concepts, pitfalls, and nuances of our in-house code. The research engineers at CCL, Dr. Srikant Srinivasan, Dr. Jung Choi, Dr. Reetesh Ranjan and Dr. Michel Akkiki had always been very helpful, and I highly value the interactions I had with them. I express my thanks to the past CCL members (in no particular order): Kaushik, Kalyan, Karthik, Aditya, Chaitanya, Sayop, Umesh, Amrita, Alex, Joel, Leandro, Yogin, Jason, Sai, Veera and the present CCL members: Principio, Achyut, Soumyo, Petro, Marc,

Kyle and others for the help and support they had provided me at various times during my stay at CCL.

Finally, I would like to express my gratitude to my family for their unflinching support, understanding and unwavering affection. My wife Jayashree Kalyanaraman has been a pillar of support throughout the ups and downs of my Ph.D. journey. She has taken up multiple roles as my friend, guide and harshest critic and gracefully endured the lengthy period my Ph.D. required. She gave me her complete support in spite of her academic commitments as a Ph.D. student at Georgia Tech. and personal commitments as a mother. The newest addition to our family, my two-year-old son Rohan Balaji has been an everlasting source of inspiration. Thoughts of his infectious smile have many times lifted my spirits when I felt desperate from lack of progress in my research. Special thanks to my parents for coming to the United States and staying with us for six long months multiple times to help us take care of our little one. I am forever indebted to my father for the constant encouragement he gave me over the years to pursue my dreams and for instilling confidence during difficult phases in my graduate life.

## TABLE OF CONTENTS

<b>Acknowledgments</b> . . . . .	v
<b>List of Tables</b> . . . . .	xiii
<b>List of Figures</b> . . . . .	xv
<b>Summary</b> . . . . .	xxvi
<b>Chapter 1: Introduction and background</b> . . . . .	1
1.1 Mathematical modeling of moving boundary problems . . . . .	2
1.2 Adaptive Mesh Refinement . . . . .	5
1.2.1 Cell based AMR . . . . .	5
1.2.2 Block structured patch based AMR . . . . .	6
1.3 Existing numerical approaches for stationary and moving solid boundaries .	7
1.3.1 Ghost fluid finite difference IB method . . . . .	10
1.3.2 Cartesian grid based Cut-cell finite volume method . . . . .	13
1.4 Summary of the existing numerical capabilities . . . . .	17
1.5 Thesis objectives . . . . .	20
1.5.1 Development of numerical approach for simulation of moving bound- ary reacting flow problems . . . . .	21

1.5.2	Development of sub-grid closures for turbulent reacting flow in the presence of local refinement and embedded boundaries . . . . .	24
1.5.3	Application studies involving high speed turbulent reacting flow problems with complex/moving geometries . . . . .	24
1.6	Thesis organization . . . . .	26
<b>Chapter 2: Governing equations and mathematical formulation . . . . .</b>		<b>27</b>
2.1	Governing equations . . . . .	27
2.1.1	Unfiltered Navier-Stokes equation . . . . .	27
2.1.2	Filtered Navier-Stokes equation for LES . . . . .	32
2.2	Mathematical formulation . . . . .	37
2.2.1	Finite volume approach for moving boundary problems . . . . .	37
2.2.2	Inviscid flux evaluation . . . . .	40
2.2.3	Viscous flux evaluation . . . . .	40
<b>Chapter 3: Block structured Adaptive Mesh Refinement . . . . .</b>		<b>42</b>
3.1	Basic concepts of block structured AMR . . . . .	42
3.2	AMR data operations . . . . .	46
3.3	Implementation of AMR into a multi-block CFD solver . . . . .	49
3.4	Refinement criteria . . . . .	52
3.5	Validation of AMR for non-reacting/reacting problems . . . . .	53
3.5.1	1D shock tube studies . . . . .	53
3.5.2	2D Riemann problem . . . . .	54
3.5.3	Sedov blast studies . . . . .	57
3.5.4	2D detonation propagation . . . . .	60

3.5.5	3D blast studies . . . . .	62
3.6	Performance of block structured AMR implementation . . . . .	64
<b>Chapter 4: Cartesian based cut-cell embedded boundary method . . . . .</b>		<b>67</b>
4.1	Formulation and implementation of cut-cell method . . . . .	67
4.1.1	Higher order $k$ -exact least squares reconstruction . . . . .	69
4.1.2	Boundary conditions at embedded surfaces . . . . .	72
4.1.3	Flux computation near embedded surfaces . . . . .	73
4.1.4	Cell clustering algorithm for small cell treatment . . . . .	75
4.1.5	Corrections near moving boundaries using cell clustering method . .	81
4.1.6	Time integration for moving boundary problems . . . . .	86
4.1.7	Hybridization of flux computation in regions of flow discontinuity .	89
4.2	Validation of high-order cut-cell for stationary boundaries . . . . .	90
4.2.1	Order of accuracy analysis for scalar and its gradient reconstruction	91
4.2.2	Order of accuracy analysis for a 2D elliptic problem . . . . .	93
4.2.3	Laminar flow over a single cylinder . . . . .	97
4.2.4	$Re_d=100$ flow over two side-by-side cylinders in cross-flow . . . . .	103
4.2.5	Low Reynolds number flow over a corrugated airfoil . . . . .	107
4.2.6	Three dimensional flow over single and multiple spheres in cross-flow	111
4.3	Validation of second order cut-cell method for moving boundaries . . . . .	117
4.3.1	Smoothly expanding piston . . . . .	118
4.3.2	Non-reacting piston with prescribed supersonic motion . . . . .	119
4.3.3	Oscillating membrane . . . . .	120

4.3.4	Moving cylinder in a viscous flow under subsonic conditions . . . .	124
4.3.5	Moving cylinder in a viscous flow under supersonic conditions . . .	128
4.3.6	Cylinder driven by shock impact . . . . .	130
<b>Chapter 5: Multi-level subgrid kinetic energy based closure . . . . .</b>		<b>135</b>
5.1	Multi-level nomenclature . . . . .	135
5.2	Subgrid closure modeling for multi-level LES . . . . .	138
5.3	Assessment of multi-level AMRLES . . . . .	143
5.3.1	LES of homogeneous turbulence convecting across coarse/fine AMR interface . . . . .	144
5.3.2	LES of $Re_d=3900$ flow past a cylinder . . . . .	151
5.3.3	LES of $Re_d=3700$ flow past a sphere . . . . .	156
<b>Chapter 6: Multi-level reaction rate closure for chemistry . . . . .</b>		<b>162</b>
6.1	Formulation and implementation of a multi-level closure for filtered reaction rate . . . . .	162
6.2	LES and DNS of a freely propagating premixed flame interacting with a decaying isotropic turbulence . . . . .	169
<b>Chapter 7: Application 1: LES of shock turbulence interaction . . . . .</b>		<b>176</b>
7.1	Introduction . . . . .	176
7.2	Results and discussion . . . . .	177
7.2.1	Planar shock in isotropic turbulence . . . . .	177
7.2.2	Blast turbulence interaction . . . . .	186
7.3	Conclusions . . . . .	191

<b>Chapter 8: Application 2: LES of non-reacting/reacting jet in cross flow . . . . .</b>	<b>193</b>
8.1 Introduction . . . . .	193
8.2 Problem description . . . . .	194
8.3 Results and discussion . . . . .	195
8.3.1 Non-reacting JICF . . . . .	197
8.3.2 Reacting JICF . . . . .	202
8.4 Conclusions . . . . .	213
<b>Chapter 9: Application 3: Detonation initiation and stabilization by moving projectiles in a reactive mixture . . . . .</b>	<b>214</b>
9.1 Introduction . . . . .	214
9.2 Results and discussion . . . . .	215
9.2.1 Piston initiated detonation. . . . .	215
9.2.2 Detonation initiation due to an impulsive cylinder motion . . . . .	220
9.2.3 Detonation initiation and stabilization over spherical projectiles . . . . .	222
9.3 Conclusions . . . . .	229
<b>Chapter 10:Conclusions, contributions and future research directions . . . . .</b>	<b>231</b>
10.1 Conclusions . . . . .	231
10.2 Thesis contributions . . . . .	236
10.3 Future recommendations . . . . .	237
<b>Appendix A: Conservation analysis for moving boundaries in a uniform cross flow</b>	<b>241</b>
<b>Appendix B: Computational performance . . . . .</b>	<b>244</b>

<b>References</b> . . . . .	261
<b>Vita</b> . . . . .	262



## LIST OF TABLES

1.1	Comparison of various numerical techniques with respect to grid related aspects	18
1.2	Comparison of embedded boundary methods . . . . .	19
3.1	Summary of AMR test cases and their motivation. . . . .	53
4.1	Summary of test cases and their motivation. . . . .	91
4.2	Error in reconstruction of a scalar $\psi$ and order of accuracy at the embedded boundary using a quadratic reconstruction( $k=2$ ). . . . .	92
4.3	Error in reconstruction of gradient of a scalar, $ \nabla\psi $ and order of accuracy at the embedded boundary using a quadratic reconstruction( $k=2$ ). . . . .	92
4.4	Error in reconstruction of a scalar $\psi$ and order of accuracy at the embedded boundary using a cubic reconstruction( $k=3$ ). . . . .	92
4.5	Error in reconstruction of gradient of a scalar, $ \nabla\psi $ and order of accuracy at the embedded boundary using a cubic reconstruction( $k=3$ ). . . . .	93
4.6	Error norms for solution to Laplace equation for different orders of $k$ -exact reconstruction. . . . .	96
4.7	Various grid resolutions used for viscous flow over cylinder case. . . . .	97
4.8	Grid convergence of $C_d$ for $Re_d = 40$ . . . . .	102
4.9	Grid convergence of $\bar{C}_d, St$ for $Re_d = 100$ . . . . .	102
4.10	Comparison with past studies: Left - $C_d$ for $Re_d = 40$ , Right - $\bar{C}_d$ and $St$ for $Re_d = 100$ . . . . .	102
4.11	Drag coefficients for flow over sphere at different $Re_d$ . . . . .	114

4.12	Drag, lift coefficients and Strouhal number for flow over sphere at $Re_d = 300$ .	114
4.13	Summary of test cases and their motivation. . . . .	118
4.14	Various grid resolutions used for the moving cylinder at $Re=40$ case. . . . .	125
4.15	Grid convergence of $C_d$ for $Re_d = 40$ . . . . .	127
5.1	LES of advection of homogeneous turbulence across a AMR grid discontinuity	146
6.1	Initial turbulent premixed flame parameters for cases considered in this study.	172
7.1	Summary of STI cases . . . . .	178
7.2	Closure models for various terms in transport equation of $k^{sgs}$ . . . . .	185
8.1	Jet conditions different JICF cases . . . . .	195
9.1	Flow conditions of the mixture. . . . .	216
9.2	C-J characteristics of the mixture for various grid resolution for the moving piston problem. . . . .	219
9.3	Case conditions for the detonation initiation study by supersonic spherical projectiles. . . . .	224
B.1	Fraction of time spent by various routines for a time integration step. . . . .	245

## LIST OF FIGURES

1.1	Schematic of the different application problems of interest a) direct ignition IC engines b) explosively formed projectile[3] c) super detonative ram accelerator d) Propellant grains in a gun barrel configuration . . . . .	2
1.2	Comparison of (a) a uniform grid (b) an adaptively refined grid for capturing a sinusoidal front. . . . .	6
1.3	Block diagram summarizing different approaches to solve moving body problems involving complex geometries . . . . .	19
1.4	Workflow between the different components of the proposed numerical framework . . . . .	22
2.1	Schematic of a (a) 2D normal cell and (b) 2D cut-cell. . . . .	39
3.1	Schematic of block based refinement for a front (a) flattened view (b) hierarchical view. . . . .	43
3.2	Schematic for AMR nomenclature and different data operations. . . . .	43
3.3	Process flow describing implementation of AMR using BoxLib into a multi-block CFD solver . . . . .	50
3.4	Creation of the mapping between the multi-block data structure and BoxLib hierarchical AMR data structure . . . . .	51
3.5	Profiles for shock testube configuration 1. . . . .	55
3.6	Profiles for shock testube configuration 2. . . . .	55
3.7	Comparison of density contours between (a) AMR and (b) uniform mesh at $t = 0.25$ . . . . .	56

3.8	Snapshot of the block structure refinement at $t = 0.25$ . Red - coarsest level, green - finer level, blue - finest level. . . . .	57
3.9	Pressure contours at various time instants for the 2D sedov test case . . . .	58
3.10	Comparison of the blast characteristics (a) blast radius and (b) radially averaged pressure profile between AMR and uniform mesh for 2D Sedov problem.	59
3.11	Comparison of the blast radius evolution between AMR and uniform mesh for 3D Sedov problem. . . . .	59
3.12	Instantaneous snapshot of the detonation front at various stages of the triple point motion along the leading shock front. . . . .	60
3.13	Comparison of the triple point structure with theory. . . . .	61
3.14	Regular oscillation of the detonation velocity, $D$ tracked using temporal history of triple point. . . . .	61
3.15	Instantaneous snapshots of $\log(\rho)$ at the x-y plane for 3D NitroMethane blast.	63
3.16	Comparison of (a) blast overpressure for TNT and NitroMethane charges and (b) blast radius evolution for a NitroMethane charge with past studies. . . .	64
3.17	Snapshot of the AMR levels for the free blast of Nitro Methane. . . . .	65
3.18	Comparison of (a) computational cost and (b) storage space required for the 3D Sedov problem. . . . .	66
3.19	Time taken by various solver steps for the 3D Sedov problem for the $256^3$ case.	66
4.1	Schematic of a three dimensional cut-cell: (a) creation from levelset description $\phi$ with cut-surface described by $\phi(x, y, z) = 0$ . (b) Various geometric variables for defining a cut-cell to represent an embedded boundary. . . . .	68
4.2	Illustration of the $k$ -exact reconstruction stencil used for (a) $k=2$ and (b) $k=3$ . Stencil highlighted by the gray shaded region. Subscript $i$ denotes the cell for which $k$ -exact reconstruction is done and $j$ is one of the neighbor cells. .	71
4.3	Numerical oscillations in the pressure coefficient and the skin friction coefficient on a cylinder surface placed in a $Re_d = 40$ cross flow. Cell-mixing algorithm [100] was used for the small cell treatment and the grid resolution used was based on a previous study using cut-cells [94] (Solid black dots indicate data from a previous study [17] with body-fitted grid). . . . .	76

4.4	Cell cluster groups colored based on cluster number for the case of viscous flow 2D cylinder. Clusters are shown for various values of limiting volume fraction $\alpha_{lim}$ . . . . .	80
4.5	Plot of (a) co-efficient of pressure ( $C_p$ ) and (b) skin friction co-efficient ( $C_f$ ) for different values of limiting volume fraction $\alpha_{lim}$ with the proposed cell clustering method: $-\cdot-\alpha_{lim} = 0.25$ ; $-\cdot-\alpha_{lim} = 0.50$ ; $—\alpha_{lim} = 0.75$ demonstrating that the smoothness of solution is not affected by changing $\alpha_{lim}$ (Solid black dots indicate data from a previous study [17] with body-fitted grid). . . . .	82
4.6	Plot of (a) co-efficient of pressure ( $C_p$ ) and (b) skin friction co-efficient ( $C_f$ ) for different values of limiting volume fraction $\alpha_{lim}$ with the proposed cell clustering method: $-\cdot-\alpha_{lim} = 0.25$ ; $-\cdot-\alpha_{lim} = 0.50$ ; $—\alpha_{lim} = 0.75$ for a coarser grid using 20 cells for resolving the cylinder (Solid black dots indicate data from a previous study [17] with body-fitted grid). . . . .	82
4.7	Schematic depicting (a) a fluid cell vanishing and (b) a new fluid cell emerging because of boundary motion. The thick arrow indicates the direction of transfer of mass, momentum and energy between a cell and its neighbor. . .	84
4.8	Schematic of a 2D cut-cell undergoing a volume change due to boundary motion. . . . .	87
4.9	Error norms in reconstruction of a scalar $\psi$ and its gradient $\nabla\psi$ on a immersed boundary. Solid black lines indicate the design order of accuracy . .	93
4.10	(a) Immersed domain for the Laplace's problem represented using cut-cells (b) Exact solution to Laplace's problem, $\psi_{exact} = \sin x \exp y$ . . . . .	95
4.11	(a) Error norms of $\psi$ for the solution to the Laplace's problem at different grid resolutions (b) Accuracy versus cost for the Laplace's problem with different orders of $k$ -exact reconstruction. . . . .	95
4.12	Streamlines for $Re_d=40$ flow over a cylinder for case $Re40_{80}$ with $k = 3$ . . .	98
4.13	Results for pressure coefficient with (a) $k = 2$ (b) $k = 3$ along the cylinder surface for $Re_d = 40$ compared with reference data from a boundary-fitted grid [17] (solid back dots) or cases: $-\cdot-\cdot Re40_{10}$ ; $-\cdot-\cdot Re40_{20}$ ; $—Re40_{40}$ ; $—Re40_{80}$ . . . . .	99
4.14	Results for skin friction coefficient with (a) $k = 2$ (b) $k = 3$ along the cylinder surface for $Re_d = 40$ compared with reference data from a boundary-fitted grid [17] (solid back dots) or cases: $-\cdot-\cdot Re40_{10}$ ; $-\cdot-\cdot Re40_{20}$ ; $—Re40_{40}$ ; $—Re40_{80}$ . . . . .	99

4.15	Vorticity iso-lines for $Re_d=100$ flow over a cylinder for case $Re_{40_{80}}$ with $k = 3$ . Solid lines denote positive vorticity and dotted lines denote negative vorticity. . . . .	100
4.16	Variation of drag coefficient over non-dimensional time for $Re_d = 100$ for various grid resolutions with: (a) $k = 2$ (b) $k = 3$ ; $--Re_{100_{10}}$ ; $---Re_{100_{20}}$ ; $—Re_{100_{40}}$ ; $—Re_{100_{80}}$ . . . . .	101
4.17	Variation of lift coefficient over non-dimensional time for $Re_d = 100$ for various grid resolutions with: (a) $k = 2$ (b) $k = 3$ ; $--Re_{100_{10}}$ ; $---Re_{100_{20}}$ ; $—Re_{100_{40}}$ ; $—Re_{100_{80}}$ . . . . .	101
4.18	Instantaneous snapshot of vorticity iso-lines showing the transitioning from (a) anti-phase to (c) in-phase regime in vortex shedding of the two cylinders using cut-cell scheme with cubic reconstruction ( $k=3$ ) (solid and dotted lines denote positive and negative vorticity, respectively). . . . .	104
4.19	Lift coefficient history for two side-by-side cylinders in a $Re_d = 100$ cross flow with: (a) $k=2$ (b) $k=3$ (c) Spectral difference method (figure taken from [127]). . . . .	105
4.20	Fast Fourier Transform of lift coefficient for $k=2$ and $k=3$ . . . . .	106
4.21	Instantaneous snapshot of (a) vorticity iso-lines showing a single bluff body vortex shedding pattern for two cylinders in close contact with the each other using cut-cell scheme with cubic reconstruction ( $k=3$ ) (solid and dotted lines denote positive and negative vorticity, respectively), and (b) Velocity vector plot near the narrow gap. . . . .	107
4.22	Drag and lift coefficient history for two side-by-side cylinders close to each other in a $Re_d = 100$ cross flow exhibiting an in-phase shedding regime. . .	108
4.23	Numerical mesh (a) in the vicinity of the corrugated airfoil (only every 4 points shown) and (b) zoomed in view to highlight the sharp geometrical discontinuities. . . . .	108
4.24	Instantaneous snapshot of vorticity iso-lines for flow over corrugated airfoil at different angles of attack using cut-cell scheme with cubic reconstruction ( $k=3$ ) (solid and dotted lines denote positive and negative vorticity, respectively). 110	
4.25	Time averaged (a) drag coefficient, $C_d$ and (b) lift coefficient $C_l$ at three different angles of attack, $\alpha=0, 5$ and $10^\circ$ compared with Experiments [132] ( $—■$ ) for $k=2$ ( $--▲$ ); $k=3$ ( $—◆$ ) and previous numerical study ( $—●$ ) [133]. 111	

4.26	Instantaneous streamlines for flow past a single sphere at:(a) $Re_d = 50$ (b) $Re_d = 150$ (c) $Re_d = 250$ shown in $x - y$ plane . . . . .	113
4.27	Iso-surfaces of Q-criterion colored with vorticity magnitude for $Re_d = 300$ flow past sphere. . . . .	114
4.28	(a) Distribution of the pressure coefficient, $C_p$ around the top and bottom sphere in the principal x-y plane (Filled dots - [6]). (b) Smooth spatial distribution of $C_p$ , on the surface of the top and bottom sphere. Also shown are flow streamlines in the principal plane. . . . .	116
4.29	(a) Distribution of the skin friction coefficient, $C_f$ , around the top and bottom sphere in the principal x-y plane (Filled dots - [6]). (b) Smooth spatial distribution of $C_f$ , on the surface of the top and bottom sphere. Also shown are flow streamlines in the principal plane. . . . .	116
4.30	Convergence rates in error of entropy for the case of smoothly expanding piston. . . . .	119
4.31	Grid convergence studies of (a) pressure, (b) density and (c) Mach no. profiles for the piston moving at Mach 2: $\Delta x = \text{---} L/2$ ; $\text{---} L/5$ ; $\text{---} L/10$ ; $\text{---} L/20$ (piston region colored with blue). . . . .	121
4.32	Comparison of (a) pressure, (b) density and (c) Mach no. profiles for the piston moving at Mach. 2 for $\Delta x = L/20$ with analytical results (piston region colored with blue). . . . .	122
4.33	(a) Shape of the membrane at various time instants and (b) the comparison of the average density with analytical value. . . . .	124
4.34	Contours of velocity magnitude (m/s) at various time instants for the moving cylinder problem in a viscous flow at Re 40 for the case $Re40_{80}$ . . . . .	125
4.35	(a) Comparison of the drag coefficient ( $C_d$ ) for the different grid resolutions (b) Zoomed in view showing reduction of oscillations with progressive mesh refinement: $\text{---} Re40_{10}$ ; $\text{---} Re40_{20}$ ; $\text{---} Re40_{40}$ ; $\text{---} Re40_{80}$ . . . . .	126
4.36	Comparison of the pressure coefficient ( $C_p$ ) and the skin friction coefficient ( $C_f$ ) with previous results from a body-fitted grid [17] (solid back dots) for the case of Re=40 moving cylinder in a viscous flow: $\text{---} Re40_{10}$ ; $\text{---} Re40_{20}$ ; $\text{---} Re40_{40}$ ; $\text{---} Re40_{80}$ . . . . .	128
4.37	Mach number plot for a moving cylinder at $M = 5.75$ in a quiescent flow. Top: Viscous flow at $Re_d = 15.9 \times 10^3$ , bottom: Inviscid flow. . . . .	129

4.38	Pressure distribution on the rear of the cylinder for the viscous and inviscid case compared with experimental data [140]. . . . .	130
4.39	Time series of the bow shock visualized by contours of gradient of pressure compared with analytical correlation Eq.(4.56) marked with red dots. . . .	131
4.40	Schlieren contours for shock-driven cylinder at various times. . . . .	132
4.41	Regions where the second order MUSCL is activated using the curvature based discontinuity detection switch is highlighted in grey at various time instants. . . . .	133
4.42	Force, velocity and position of the rigid cylinder as a function of grid compared against the reference solution of Henshaw & Schwendenman [43]. . .	134
5.1	Schematic of turbulent kinetic energy spectra. The multi-level filtering of a flow quantity $\phi$ and the associated wave number are also indicated. . . . .	136
5.2	Multi-level representation of a filtered quantity $\phi$ on a AMR mesh. . . . .	138
5.3	Schematic of the multi-level correction for $k^{sgs}$ on a AMR mesh. . . . .	143
5.4	AMR mesh for (a) coarse to fine and (b) fine to coarse case . . . . .	145
5.5	Instantaneous vorticity magnitude on the central XY plane for (a) coarse to fine and (b) fine to coarse case. . . . .	145
5.6	Resolved TKE spectrum near an AMR grid interface for (a) coarse to fine and (b) fine to coarse cases. . . . .	147
5.7	Averaged plot of resolved TKE, $\tilde{u}_i \tilde{u}_i$ for (a) coarse to fine scenario and (b) fine to coarse scenario: — fine with correction; — coarse with correction; ..... fine without correction; ..... coarse without correction; - - - uniform fine and - - - uniform coarse. . . . .	148
5.8	Averaged plot of resolved TKE, $\tilde{u}_i \tilde{u}_i$ for (a) coarse to fine scenario and (b) fine to coarse scenario: — fine with correction; — coarse with correction; ..... fine without correction; ..... coarse without correction; - - - uniform fine and - - - uniform coarse. . . . .	149
5.9	sgs budget for flow past an AMR grid discontinuity for (a) fine to coarse and (b) coarse to fine case. . . . .	150



5.10	Snapshot of local mesh refinement near cylinder surface for $Re_d = 3900$ flow past a cylinder. . . . .	151
5.11	Time history of drag ( $C_d$ ) and lift ( $C_l$ ) coefficient of $Re_d=3900$ flow past a cylinder. . . . .	152
5.12	Vortex structures visualization by iso-surface of Q-criterion colored with streamwise velocity. . . . .	153
5.13	Instantaneous snapshot of (a) vorticity magnitude (b) subgrid kinetic energy and (c) eddy viscosity ratio in the center x-y plane . . . . .	153
5.14	Time and spatially averaged (in homogeneous direction) data of (a) pressure coefficient $\overline{C_p}$ and (b) skin friction coefficient for $Re_d = 3900$ flow past cylinder. Block dots in (a) represent data from a past experimental study [147] and (b) represent data from a body fitted LES [145]. . . . .	155
5.15	Time average plots of (a) Streamwise velocity (b) Subgrid kinetic energy (c) LDKM parameter $C_\nu$ and (d) LDKM parameter $C_\epsilon$ in center x-y plane. . . .	155
5.16	Time averaged streamwise velocity along the cylinder centerline. Blue solid line - Cutcell-AMRLES, Black dotted line - Body-fitted LES [145], Black filled dots - Experimental [148], Black filled triangles - Experimental [149].	157
5.17	Snapshot of local mesh refinement near surface for $Re_d = 3700$ flow past a sphere. . . . .	157
5.18	Time history of drag ( $C_d$ ) and lift ( $C_l$ ) coefficient of $Re_d=3700$ flow past a sphere. . . . .	158
5.19	Vortex structures visualization by iso-surface of Q-criterion colored with streamwise velocity. . . . .	158
5.20	Instantaneous snapshot of (a) subgrid kinetic energy and (b) eddy viscosity ratio in the center x-y plane . . . . .	159
5.21	Time averaged data of (a) pressure coefficient $\overline{C_p}$ and (b) skin friction coefficient for $Re_d = 3700$ flow past cylinder. Solid blue line- Cutcell-AMRLES Block dots in (a) represent data from a past experimental study [147] and (b) represent data from a body fitted LES [145]. . . . .	160
5.22	Smooth distribution of pressure on the sphere surface for $Re_d = 3700$ flow past a sphere. . . . .	160

5.23	Time averaged streamwise velocity along the cylinder centerline. Blue - Cutcell-AMRLES, Black dots - Body-fitted unstructured DNS [150] . . . .	161
6.1	Schematic of the multi-level approach (a) and workflow (b) in the LEMLES and RRLES strategy. Subfigure (a) shows contours of progress variable on both the grids for a planar premixed flame configuration. . . . .	165
6.2	A schematic describing the gradient reconstruction of species scalar field at LEM level. . . . .	167
6.3	A schematic describing the multi-level RRLES closure for the filtered reaction rate. . . . .	168
6.4	A schematic of the turbulent premixed flame configuration (a) and the premixed flame regime diagram [158] (b) showing the cases considered in this study. Solid and open symbols indicate the initial state of the flame-turbulence interaction and the state at which analysis is performed, respectively. . . .	170
6.5	Contours of filtered temperature field overlaid with the flame brush extents in the central $x-y$ plane identified using the filtered progress variable (iso-lines of $\tilde{c} = 0.01$ and $\tilde{c} = 0.99$ ) [151]. . . . .	174
6.6	Conditional variation of the filtered reaction rate of $\text{CH}_4$ with respect to the progress variable [151]. . . . .	175
7.1	Schematic for the shock-turbulence interaction study. . . . .	178
7.2	Iso-surfaces of Q-criterion colored with pressure for the cases $STI_{DNS1}$ and $STI_{DNS2}$ . . . . .	180
7.3	Comparison of (a) axial and (b) transverse Reynolds stresses for case $STI_{DNS1}$ with DNS[171] . . . . .	180
7.4	Comparison of (a) axial and (b) transverse Reynolds stresses for case $STI_{LES1}$ with filtered DNS data . . . . .	181
7.5	Comparison of axial and transverse Reynolds stresses for case $STI_{DNS2}$ with a past DNS [167] . . . . .	182
7.6	$STI_{LES2f}$ : Comparison of axial and transverse Reynolds stresses for case LES of $M=1.5$ , $Re_\lambda = 40.0$ with filtered DNS data . . . . .	183

7.7	STI <sub>LES2c</sub> : Comparison of axial and transverse Reynolds stresses for case LES of M=1.5, $Re_\lambda = 40.0$ with filtered DNS data . . . . .	183
7.8	Comparison of the filtered $k^{sgs}$ with simulation predictions for the fine and coarse LES of M=1.5, $Re_\lambda = 40.0$ . . . . .	185
7.9	$k^{sgs}$ budget for the low and high Re cases. — $\langle D^{sgs} \rangle$ ; --- $\langle P^{sgs} \rangle$ ; - - - $\langle \frac{\partial \tilde{\rho u_i k^{sgs}}}{\partial x_i} \rangle$ ; - . - $\langle T^{sgs} \rangle$ ; — $\langle pd^{sgs} \rangle$ . . . . .	186
7.10	Time series of snapshot of AMR patches field at central XY plane for a Taylor blast. Red - 1 <sup>st</sup> level refinement, green - 2 <sup>nd</sup> level of refinement and blue - finest level of refinement. . . . .	188
7.11	Line plots for interaction of a blast with an isotropic turbulence $Re_\lambda = 40.0$ . . . . .	188
7.12	Comparison of radially averaged pressure profile at time = 1 ms with and without turbulence. . . . .	189
7.13	Plots of various quantities at t = 1 ms for the case of blast interacting with an isotropic turbulence. . . . .	190
7.14	Radially averaged sgs budget for the blast-turbulence interaction problem at t = 1.0 ms. — $\langle D^{sgs} \rangle$ ; --- $\langle P^{sgs} \rangle$ ; - - - $\langle \frac{\partial \tilde{\rho u_i k^{sgs}}}{\partial x_i} \rangle$ ; - . - $\langle T^{sgs} \rangle$ ; — $\langle pd^{sgs} \rangle$ . . . . .	191
8.1	Schematic of the JICF configuration. . . . .	195
8.2	Snapshot of the AMR mesh for JICF configuration (only every 4 mesh points shown). . . . .	196
8.3	Instantaneous snapshot of vortical structures identified by Q-criterion and colored with vorticity magnitude for jet velocities . . . . .	198
8.4	Eddy viscosity ratio for the $Re_j = 6000$ case . . . . .	199
8.5	Turbulent kinetic energy spectra . . . . .	199
8.6	Time averaged flow field contours for the Jet center $x - y$ plane . . . . .	200
8.7	Jet centerline trajectory comparisons scaled with only $r_m d$ . Solid black - $r_m = 2.9$ , dashed blue - $r_m = 2.2$ , dash-dot red - $r_m = 1.4$ , blue dots - Su Mungal [182], black squares - New <i>et al.</i> [191]. . . . .	201

8.8	Flow pattern in the near field of the jet inflow in the (a) x-y central plane and (b) x-z plane at $y = 0$ . . . . .	202
8.9	Instantaneous snapshot of vortical structures identified by Q-criterion and colored with vorticity magnitude for different jet Reynolds numbers. . . . .	204
8.10	Instantaneous temperature contours in the jet central x-y plane. . . . .	205
8.11	Instantaneous snapshot of (a) Heat Release Rate (HRR) and (b) scaled flame index for $Re_j=6000$ . . . . .	206
8.12	Scatter plot of $Da$ number and HRR colored with flame index. . . . .	207
8.13	Comparison of the magnitude of the baroclinic torque between reacting and non-reacting cases for $Re_j=200$ . . . . .	208
8.14	Mean temperature contours at jet center x-y plane for different cases. . . . .	209
8.15	Comparison of the mean jet behavior between the current simulations and DLR experimental data [189]. Experimental image taken from [193]. . . . .	210
8.16	Line plots of (a) mean streamwise velocity (b) rms of streamwise velocity and (c) mean temperature at various axial locations on x-y jet centerplane. Solid blue line - Cutcell-AMRLES, black dots - DLR experiments [189]. . . . .	211
8.17	Iso-volume of heat release rate clipped between 10 and 90 percent of the total heat release for the three cases. . . . .	212
9.1	1D profiles at various time instants (0 - 1.0 ms) for (a) the moving piston and (b) the static wall problem. Pressure values are shifted by 200 kPa every for each time instant for clarity. . . . .	217
9.2	Comparison of the pressure profile history between the moving and stationary reacting piston problem. . . . .	218
9.3	Comparison 1D profiles at (a) various time instants (0 - 1.0 ms) (b) zoomed in view at $t = 1.0$ ms for the two grid resolutions $\Delta x = 40 \mu m$ and $80 \mu m$ . . . . .	219
9.4	Time series of Schlieren image of the detonation front for the case of impulsive cylinder motion in a reacting mixture. . . . .	221
9.5	Visualization of cellular structures Left: Numerical soot foil from AMR simulations. Right: Open-shuttle photograph of a diverging cylindrical detonation[201] . . . . .	222

9.6	Time history of the velocity of propagation of the diverging detonation front.	223
9.7	Snapshot of the AMR mesh for the problem detonation initiation by a hypersonic projectile (only every four grid points shown). . . . .	224
9.8	Pseudocolor plots of temperature in Y-plane at the same time instants for various filling pressures ( $p_{filling} = 97.5, 96, 95$ and $90$ kPa) for the case of supersonic projectile shot into a stiochiometric $H_2/O_2$ mixture. . . . .	226
9.9	Different combustion regimes observed for various filling pressures (SIC - Shock induced combustion, ODW - Oblique Detonation Wave). . . . .	227
9.10	Schlieren snapshots from experiments [202] of the different combustion regimes observed for the case of supersonic projectile shot into a stiochiometric $H_2/O_2$ mixture (figure taken from [202] with permissions). . . . .	228
9.11	Instantaneous iso-surface of temperature colored with pressure for various filling pressures ( $p_{filling} = 90, 95, 96$ and $97.5$ Kpa) for the case of supersonic projectile shot into a stoichiometric $H_2/O_2$ mixture. . . . .	230

## SUMMARY

This thesis aims at developing numerical models and subgrid closures for Large Eddy Simulation (LES) of turbulent reacting flow problems in non-trivial geometries with moving boundaries. Many practical engineering devices involve moving boundaries interacting with a reacting flow. While Computational Fluid Dynamics (CFD) can be effectively employed to study and understand the functioning of these systems, existing numerical methods face several difficulties that have so far limited their use. The foremost problem with the conventional body conformal CFD approaches is that of grid generation especially for complex geometries and moving boundaries. In contrast, the grid generation is greatly simplified with Cartesian grid based Embedded Boundary (EB) methods due to which they are gaining popularity in recent years. However, to resolve the flow and reaction dynamics in complex flow systems, a high order of accuracy is often needed without which many critical flow phenomena cannot be captured. This requirement has been particularly challenging for IB methods as many of the existing schemes suffer from a lower order of accuracy specifically near the embedded boundaries. For moving boundaries, conservation of mass, momentum, and energy is not easy to enforce with existing IB methods.

In this thesis, a wholistic approach is taken to identify some of the key issues related to numerical simulation of moving boundary reacting flow problems, and several developments are done to address these problems. The need for local mesh refinement to resolve fine-scale flow features is addressed by performing block-structured adaptive mesh refinement by interfacing with a massively parallel open source library (BoxLib). A strictly conservative high-order Cartesian cut-cell method is developed to handle embedded boundaries. A novel cell clustering algorithm for handling the ‘small cell’ problem afflicting all the cut-cell methods is proposed. The developed cut-cell method is capable of smooth reconstruction of flow solution with upto fourth order accuracy. The cell clustering algorithm is also extended to enforce strict conservation for moving boundaries. Finally, subgrid closures for flow and

chemistry are developed adapted to the presence of block structured refinement and embedded boundaries.

There are several validation tests performed to demonstrate the accuracy and robustness of the developments in this thesis. The cost effectiveness of AMR is demonstrated by applying it to blast and detonation studies. It is shown that the cut-cell method can achieve design order of accuracy and also results in smooth near wall solution. For moving boundary problems, strict conservation is demonstrated by employing the extended cell clustering algorithm. The multi-level closure model, when applied with the cut-cell method, provides a consistent treatment for transitional turbulent flow problems. Improvements in model predictions are also demonstrated for the canonical problem of a flame interacting with turbulence, using the multi-level reacting rate based closure. The application of the AMR to study the interaction of turbulence with propagating shocks is described. The model and numerical method developments are then applied to practical configurations. The mechanisms of flame holding and stabilization in transverse reacting jet coming out of a pipe into a cross flow are studied. The other practical problem of detonation initiation by hypersonic projectiles in flight in a reacting mixture is investigated using the moving cut-cell method. Some important observations on the nature of detonation and flame stabilization for both the configurations are documented.

# **CHAPTER 1**

## **INTRODUCTION AND BACKGROUND**

There are many engineering devices with complex geometries that have moving or deforming surfaces in a compressible reacting flow environment. Examples of such applications include propulsion systems with moving components such as Internal Combustion (IC) engines, hypersonic propulsive devices such as Oblique Detonation Wave (ODW) engines, Ram accelerators [1] and solid rocket motors involving regressing propellant surfaces. In many cases, the reacting components may be integral to the functioning of these systems. Such as in IC engines, the motion of the valve regulates the flow into the cylinder, and the movement of the piston drives the engine. In some cases, the process of boundary deformation is a result of surface burning and regression as in the case of combustion of energetic materials or propellants [2]. Such problems are often characterized by complex interactions involving one or more of the following phenomenon: near-wall turbulence, unsteady shock motion and its impact on the surface, surface reactions and regression including fracture and particle ejections, and highly time-dependent transient motions. In other cases, the boundary motion can be a result of the interaction of hydrodynamic forces acting on the surface of the boundary such as in the case of ram accelerators. For some applications, the boundary motion can significantly alter the flow physics surrounding the body such as in the case of Explosively Formed Projectiles (EFP) [3]. The deformation of the surface of the projectile due to the impact of a detonating condensed phase has a significant effect on its aerodynamics characteristics and flight trajectory [4].

Also, there also exists several engineering applications where it is of interest to understand the flow over complex geometries with stationary boundaries. Examples include flow past finite airfoil, effusion holes in gas turbines, multi-injectors in a gas turbine, or a group of objects that are separated by narrow gaps, such as flow past heat exchangers [5], struts,



etc. Three-dimensional flow interactions between a group of droplets or solid particles are also relevant in many applications such as air pollution control, combustion systems, and chemical processes [6]. Some of these application problems of interest are illustrated via schematics or reproduced from other sources in 1.1. Numerical simulations can be effectively employed to study the performance and optimization of these systems.

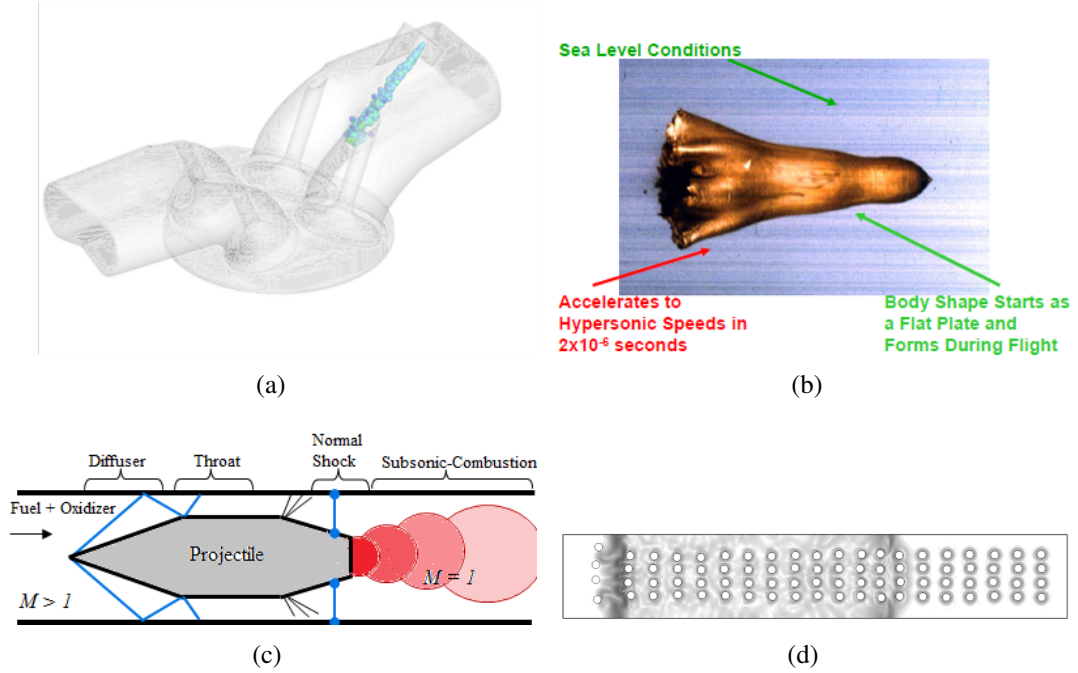


Figure 1.1: Schematic of the different application problems of interest a) direct ignition IC engines b) explosively formed projectile[3] c) super detonative ram accelerator d) Propellant grains in a gun barrel configuration

However, there are several challenges associated with the numerical simulation of flow problems with complex geometries and, with moving boundaries. These are briefly discussed in the next section.

## 1.1 Mathematical modeling of moving boundary problems

The various challenges associated to mathematical modeling of moving boundary problems are categorized under three topics: difficulties associated to grid generation, scheme and cost related problems and finally, the closure model issues related to turbulence modeling of

moving boundary reacting flow problems.

### Grid generation

Meshing complex surface topologies are especially challenging and in some cases impossible for body conformal structured approaches [7]. Another difficulty with structured approaches are the contradictory requirements of sufficient local resolution in the region of interest and minimizing the total number of overall grid points. The reason is, a refinement in a particular portion of the structured mesh will ‘bleed through’ the rest of mesh making it impossible to localize the refinement. Though moving mesh [8] technique can be used to represent moving boundaries on a structured grid, these methods are limited to small boundary displacements. In the case of larger displacements, the moving mesh approach can result in severe mesh distortion and tangling adversely affecting the accuracy of the flow solution[9].

Although the unstructured mesh methods [10, 11], on the other hand, can handle the complex geometries efficiently, managing the mesh connectivity is tedious requiring complicated data structures. Besides, developing high order schemes with the unstructured approach is problematic as many of these schemes are designed for a structured neighbor connectivity [7]. In the case of moving boundaries, periodic remeshing is needed to account for the surface motion. The quality of the remeshing region can quickly deteriorate with large scale boundary motion. As the solution is interpolated to the remeshed grid [12, 9], the accuracy of the solution can be highly compromised in such scenarios. Also, the remeshing in an unstructured approach is a global operation and is computationally expensive [9].

### Turbulence modeling of moving boundary reacting flow problems

Due to highly turbulent nature of most of the practical flows, resolving all scales of motion, as is done in a Direct Numerical Simulation (DNS), is not possible due to the high computational costs involved. The alternative is to employ Large Eddy Simulation (LES) in which only the most energy containing eddies are resolved by the numerical grid and effect of

small scales of motion on the larger scales is modeled. Development of subgrid closures for turbulent reacting flow problems is an active area of research with its own difficulties[13].

In addition, the introduction of unconventional numerical techniques such as embedded boundary methods [14, 15, 16, 17, 18] and Adaptive Mesh Refinement (AMR) can further complicate the closure problem for LES. The majority of sub-grid closures for LES have been developed for body-conformal, uniform grids without local refinement. The behavior of the closure models for unconventional methodologies such as dynamic mesh refinement [19] and embedded boundary techniques [20] is not completely understood. To the best of the author's knowledge, there have not been many studies in the area of LES with embedded boundary methods and dynamic refinement for reacting turbulent for moving boundary reacting flow problems.

#### Accuracy and computational cost of numerical schemes

In addition to grid generation challenges, an accurate prediction of all the physical phenomena related to moving boundary reacting flow problems requires adequate grid resolution. Due to high-speed nature of the flow in many of the propulsion applications, compressible features such as shocks, expansion waves, detonations, etc. are present in the system. Many of these features and their interactions results in multi-scale nature of flow solution. These fine scale flow features are much smaller than the overall scale of the problem. A uniform grid resolution without adopting to some form of local refinement would result in a prohibitively high computational cost. Instead, if a coarse back ground grid is employed and increased refinement is performed in only regions of interest, huge savings in the cost and the storage of simulation data can be achieved. This is demonstrated later in this thesis.

Additionally use of high-order methods (greater than second order) can result in gains in computational cost of the simulations [21]. As noted in [21], a common belief is that high-order methods are too costly to be applied for simulation of practical flow problems. Even though high-order methods are costlier than a corresponding low order method (order

of accuracy 2 or lower) for the same grid resolution, the required accuracy can be achieved at a much coarser grid resolution with a high-order method at a reduced cost. In the context of turbulence modeling using LES technique, the numerical error can strongly interact with the sub-grid closure models introducing a significant uncertainty in the simulation results [22]. Therefore use of high-order schemes becomes particularly relevant for LES as the truncation errors from lower order schemes can exceed the magnitude of the subgrid scale term [22].

## **1.2 Adaptive Mesh Refinement**

A wide range in scales of motion and flow features can be observed in the flow systems of practical devices. The multiscale nature of flow solution, therefore mandates some form of local mesh refinement for the overall computation to be even tractable. The term Adaptive Mesh Refinement (AMR) is used to refer to local mesh refinement, which dynamically changes as the regions of interest changes over time [23] such as in the case of shock hydrodynamics, simulation of detonations and blast waves, or simulation of unsteady flames such as in gas turbines or in moving boundary problems. More recently, many studies [24, 25, 26, 27, 28] have successfully employed AMR for embedded boundary methods. The local refinement can be performed using both structured [19, 29] and unstructured approach [30]. The specific focus of this thesis is on the structured refinement techniques and the following discussion is limited to the different methods related to the structured approach. An example of a locally refined mesh and a uniform mesh for resolving a sinusoidal front is shown in Fig. 1.2.

### 1.2.1 Cell based AMR

In a cell-based adaptive mesh refinement [29], the background mesh is made up of uniform Cartesian cells and each cell can be split locally into a quadtree/octree in two/three dimensions. Due to the cell based local refinement, the connectivity between the cells becomes unstructured. A tree-based data structure is often used to manage the hierarchical relation

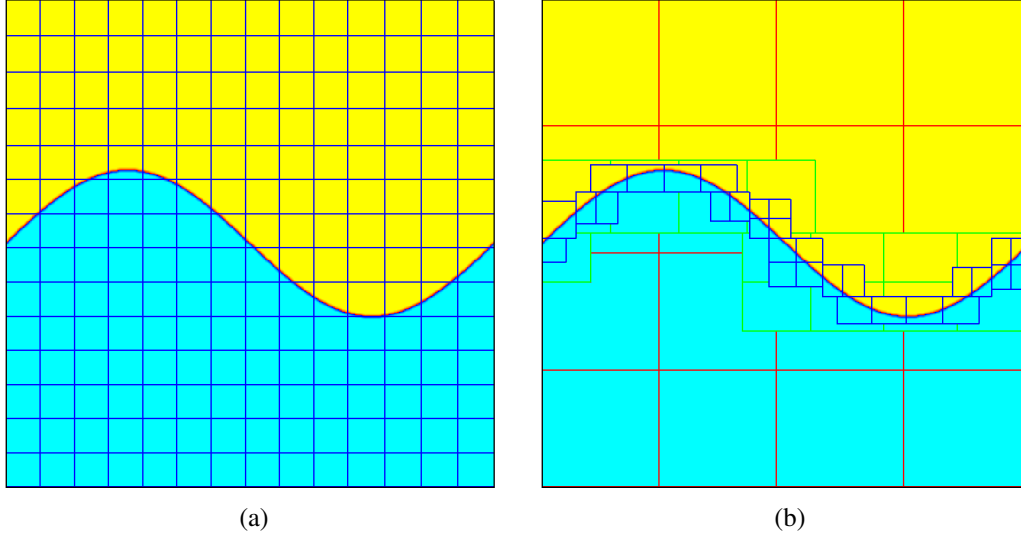


Figure 1.2: Comparison of (a) a uniform grid (b) an adaptively refined grid for capturing a sinusoidal front.

between a parent cell (of the background mesh) and its child cells (of the refined mesh). And, in some cases, the entire tree data structure has to be traversed through to access any particular cell. The computation of fluxes at the interfaces of a cell is similar to the unstructured mesh and require some form of linear least squares method.

The advantage of this method is that the refinement can be focused narrowly in the region of interest resulting in an optimal refinement with the most minimum cost. However, there are no known libraries for performing unstructured mesh refinement and can be tedious in implementation, especially when the underlying compressible solver is block structured.

### 1.2.2 Block structured patch based AMR

The patch based AMR is a block-structured adaptive mesh refinement, which is originally proposed by Berger and Collela [19]. The background mesh, as the name indicates is block structured and of coarser resolution. The regions of interest are stacked with series of nested blocks that are increasingly finer in their grid resolution. Ghost cells are built around each of the grid blocks to effect communication between adjacent blocks and across different levels

of refinement. Since the refinement is block based, the amount of the total number of grid points that is obtained from a particular refinement criteria is always more compared to the number grid points from an unstructured Cartesian AMR approach.

In contrary to the previous approach, however there are many open source libraries that are available for performing block-structured adaptive mesh refinement (BoxLib [31], Chombo[32], PARAMESH[33], SAMRAI [34], AMRCLAW[35], AMROC[36], etc.). The underlying base solver for compressible flows, that will be used in this thesis as described later, is a block structured solver (LESLIE) [37, 38, 39]. The block-structured patch based refinement approach is more suitable to the implement AMR and therefore, is the chosen approach in this thesis.

### **1.3 Existing numerical approaches for stationary and moving solid boundaries**

In order to deal with boundary motion, three main methodologies have been proposed in the literature. These are: body-conforming Arbitrary-Lagrangian-Eulerian (ALE) approaches [40, 41], overset grid techniques [42, 43] and embedded boundary methods [14, 15, 16, 17, 18]. Each approach has its own strengths and weakness. The differences in the approaches are mainly in the manner in which grid generation is performed to resolve the moving surface geometry.

In the first approach, the time varying computational domain is handled using a body-fitted approach and the numerical grid is updated every time the boundary moves. The majority of the ALE schemes are based on unstructured grid approach due to which mesh generation for complex geometries is relatively easy compared to the structured grid generation technique. The motion of the body surface is incorporated via a conservation equation written in a control volume formulation. Reynold transport theorem is then employed to account for the fluxes swept by a changing control volume. ALE schemes have been demonstrated to solve FSI problems with multicomponent compressible flow [44, 45]. The disadvantage, however, is that these schemes suffer from the poor accuracy of the solution due to mesh

tangling and, parallelization bottlenecks due to frequent remeshing in cases of significant deformation [46].

In the second class of methods, the embedded boundary is resolved by using a local structured mesh that overlay a background mesh. Multiple bodies are handled easily in this approach by providing each body its own body-conforming grid. Fluid state variables are exchanged between the overlapping grids, and the dynamic boundaries are handled by moving the upper associated mesh with it while the background mesh remains stationary. Henshaw and Schwendeman [43] employed the overset technique with success for simulation of moving boundaries in high-speed reactive and non-reactive inviscid flow. The main limitation of the overset technique is that it is restricted to only moving rigid boundaries and extension to deforming interfaces is more difficult. Also, since it is based on the identification of mesh intersection points and data interpolation on overlapping meshes, the quality of the solution is sensitive to the interpolation technique used. Besides, if the boundary shape is complex, the mesh generation difficulties persists affecting the grid quality, which can lead to stability and convergence issues in the numerical solver.

The last class of methods, the embedded boundary method (EB), consists of a background grid that does not conform to the body and special corrections are applied to the numerical scheme for solving the flow governing equations to the points or cells in close proximity to the boundary. Moving boundaries are easily handled using EB methods by repositioning the embedded surfaces in the fixed computational mesh [47, 48, 49, 50]. Also, narrow gaps between groups of bodies can be resolved without a major loss in grid quality. The embedded boundary methods can be classified as Immersed Boundary (IB) method [51] and Cartesian grid based method [52]. It must be noted that IB methods can also be employed for Cartesian grids and the distinction between IB and Cartesian methods is not very clear. For the purpose of this review, both these approaches are considered as Cartesian grid based methods. An excellent review of the existing methods to represent embedded boundaries within the background Cartesian mesh is provided by [20] and are known as Im-

mersed Boundary (IB) methods, in general, or more specifically, as Cartesian grid based IB methods. Due to the significant advantages posed by this class of method such as ease of grid generation, ease of handling moving boundaries and ability to incorporate high-order schemes, the Cartesian grid based EB methods are reviewed in more detail.

The first use of IB methods was reported by Peskin [51, 53] to simulate cardiac mechanics and associated blood flow. The entire simulation was performed on a Cartesian grid and a novel procedure was formulated for imposing the effect of an embedded boundary by adding a localized forcing function to the momentum transport equations. Since then, numerous modifications and refinements have been done to the basic formulation and various approaches have been developed in this area. All the existing approaches of IB methods can be broadly grouped into two major categories: continuous forcing and discrete forcing approach. Here, forcing is a formulation used to enforce the boundary condition at the embedded surface.

In the continuous forcing methods[53], a distributed global forcing function is added to the momentum equations to account for the interactions at the interface. The forcing function can be adapted to the flow configuration using model parameters. A number of extensions and adaptations of this basic method can be found [54, 55, 56, 53, 57]. While this approach is attractive for flows with elastic boundaries, rigid boundaries pose some challenges since the forcing terms do not behave well in the rigid limit leading to stability and accuracy issues [56, 58]. The other disadvantage of this approach is that sharp interfaces are smeared over an area corresponding to the local mesh width resulting in only first order accuracy [20].

The discrete forcing method, on the other hand, is based on applying a localized forcing function in the momentum equations for enforcing the interface conditions. This approach was followed in [59] and later in [60] along with a predictor and corrector formulation. The major advantage of such a discrete forcing concept, unlike the continuous forcing methods, is the absence of tunable parameters in the model and also an improvement in numerical stability. Balaras [61] reported flow past 2D and 3D bluff bodies using the discrete forcing



approach. This approach retains a sharp interface with no spreading and improved local accuracy near immersed boundary. The class of methods discussed so far are generally called as direct forcing methods. There are two other classes of discrete forcing IB methods which involve explicit representation of the boundary surface. These are the finite difference based ghost cell-based method [62, 63, 64]s and finite volume based cut-cell methods [65, 50]. Common to both the approaches is the modification of the numerical scheme used for integration of the flow governing equations near the embedded boundaries. They differ in the manner in which this modification is done to include the embedded boundary effects.

Additionally, the immersed interface methods (IIM) [66] and direct forcing are also categorized under discrete forcing methods. The key difference between the latter two and the former two methods is that in the latter approaches, the interface boundary conditions are implemented indirectly via jump conditions or forcing functions, whereas in the cut-cell and the GFM, the boundary conditions at the embedded surfaces are defined explicitly. Among the different Cartesian grid based methods, GFM and cut-cell are the most widely studied and are discussed in further detail in the following subsections.

### 1.3.1 Ghost fluid finite difference IB method

The Ghost Fluid Method (GFM) was originally developed for two-phase flows to achieve accurate discretization across the interface by Fedkiw *et al.* [67] and was later extended to handle solid embedded boundaries [17, 68]. GFM is a finite difference based and enforces boundary conditions at the embedded surfaces through the use of ghost nodes. The nodes on the solid side of the domain, which has at least, one of its neighbor node in the fluid side are referred to as ghost nodes. Standard finite difference operators can be used in Cartesian nodes away from the boundary for flow solution computation without any changes to the stencil. However, near to the boundary, the operator requires information from the ghost nodes that fall inside the solid. The state variables at the ghost nodes are interpolated from neighboring nodes so as to enforce the embedded wall boundary conditions [69, 55, 70,

71], [72], [73]. The main advantage of this class of methods is that they eliminate the time step restriction problem posed by the small cells, as the time step is only determined by the regular uncut cell size. These methods are attractive because of their simplicity. However, the major drawback of these methods is that strict conservation of mass and momentum are not observed in the vicinity of the boundaries [69, 55].

The non-conservation of mass, momentum, and energy can lead to spurious pressure oscillations, which are even more amplified as the boundary moves or deforms, whereby the fluid nodes change to solid nodes and vice-versa [74]. Also, the non-conservative nature of GFM can lead to an incorrect prediction of flow physics such as shock speed, detonation velocity, etc, in the case of high-speed flow problems. Many studies have been reported on applying the ghost fluid method along with different correction schemes to mitigate the oscillation issue and these are discussed below. There are a wide variety of studies, each focusing on a specific class of problems considering either one or more of the challenging aspects such as treatment of viscous fluxes, complex and moving geometries, turbulent flows, which are reviewed in the following couple of subsections.

Viscous flows using GFM: The GFM for viscous flows was first reported Tseng and Ferziger [17]. They employed a variant of the direct forcing method proposed in earlier studies [59, 16] by introducing a ghost cell inside to solid boundary to impose the momentum forcing. Ghias and Mittal [75] used ghost cell method to simulate wide a variety of compressible viscous flows including high Reynolds number flow past a circular cylinder and an airfoil. Recently Uddin [76] proposed a high-order IB method for viscous, compressible flows that is constructed on a partial difference equation based field extension of the boundary conditions into the solid region. The method was shown to achieve smooth reconstruction of pressure and wall shear stress solution. Although the scheme was set to achieve up to sixth-order accuracy away from the immersed boundaries, the solution dropped to second order at the boundaries.

Turbulence modeling using GFM: Turbulence modeling with ghost cell IB method on Cartesian grids is an active area of research. The difficulties essentially arise in suppressing spurious oscillations near the interface. Lee and Ruffin [77] used standard  $k - \epsilon$  model with a wall function treatment for Reynolds Averaged Navier-Stokes (RANS) turbulence closure, within the GFM, to solve flow over 3D rotorcraft airfields. A more recent interesting approach using a Normalized Ray Refinement (NRR) technique was proposed by Ruffin *et al.* [78] to perform cost effective RANS computations using IB technique. In their proposed approach, instead of refining completely along boundary, local refinement was restricted to narrow ‘rays’ originating from the boundary surface. Their NRR approach was shown to predict accurate skin friction and pressure distribution for 2D attached and separated high Reynolds number flows. Vanella *et al.* [79] presented a direct forcing approach which is a variant of the GFM approach for solving transitional and turbulent moving body problems. They simulated turbulent incompressible flow around two falling plates and also, LES of turbulent incompressible flow around a sphere. A dynamic viscosity model with a Lagrangian averaging procedure was employed for the LES subgrid closure.

Moving boundaries using GFM: Most of the work in employing ghost cell method for moving boundaries was done for inviscid flows [62, 63, 80] and [81]. Wang *et al.* [80] instead of relying exclusively on interpolation or extrapolation for the ghost nodes, proposed a method to enforce the appropriate value of fluid velocity at the wall and recover the value of fluid pressure using an exact solution of local 1D fluid-structure Riemann problems and demonstrated it for inviscid moving flow problems. Lee *et al.* used a GFM method for moving body problems in viscous, incompressible flow and identified two sources of spurious oscillations. The first is from the discontinuity in pressure field at grid points located on the immersed boundary and the second source is from the temporal discontinuity in the velocity field when a grid changes its state from fluid to solid due to boundary motion. In a later

work, Lee and You [82] used a fully implicit time integration along with mass source/sink algorithm so as to address both the sources of oscillations in GFM based methods that were identified by Lee *et al.* [74]. Another approach was adopted by Bergmann *et al.* [83] by using a penalty correction to impose the right pressure boundary conditions in the GFM and suppressed the oscillations by using face-centered velocity. They have applied their method for complex moving geometries in an incompressible medium. Mittal *et al.* [68] employed a multi-dimensional ghost-cell methodology, which was shown to simulate incompressible flow past 3D stationary, moving, as well as deforming bodies. One of the common problem in all the above studies associated with extending the GFM method to moving boundaries is the handling of the freshly cleared” nodes, i.e. nodes in the fluid region which were inside the solid region and got uncovered due to boundary motion [20]. These nodes do not have a time history of state variables and therefore require interpolation from their neighbors. However, the interpolation is non-conservative and results in loss of conservation near the moving boundary which can be amplified for high speed reacting flow problems.

Reacting flow using GFM The literature on using GFM for reacting flow problems is very sparse with only few reported studies. Deiterding [28] employed a finite volume based GFM for simulation of shock induced combustion for high speed inviscid flow problems in complex domains. The method is globally second order accurate but locally only first order accurate.

### 1.3.2 Cartesian grid based Cut-cell finite volume method

Clarke *et al.* [52] first introduced the cut-cell method in the context of Cartesian grid methods for inviscid flow computations. In this method, cells cut by the solid boundary are reshaped to conform to the shape of the interface. The cut-cell approach is designed to satisfy the underlying conservation laws for the cells near the interface. Strict global and local conservation of mass, momentum, and energy is guaranteed by resorting to a finite volume

discretization even for the cut cells. The Cartesian cut-cell finite volume methods [52, 84, 25] are, therefore, in comparison to finite difference ghost cell methods [55, 73], attractive as they enforce strict conservation and also can avoid generation of spurious pressure fluctuations that are observed typically with ghost fluid methods [85, 20, 86]. Nonetheless, there are two main problems that are often associated with cut-cell methods. The primary issue is the presence of very small cells, which results in an excessively small time step in case of an explicit scheme or a badly conditioned matrix in case of an implicit scheme. The other issue that often affects cut-cell schemes is the numerical oscillation of pressure and especially wall shear stress at the boundaries [87].

Several approaches have been suggested in the literature for the small cell problem such as (a) cell mixing/redistribution [88, 89], approach where the numerical fluxes from the small cells are mixed with the surrounding cells in a conservative manner, (b) the cell-merging approach [90, 91], wherein the small cells are physically merged with the neighbor cell to create a net cell composed of big and small cells, and (c) the cell linking approach [92], where the small cells are linked with a master neighbor cell to form a master/slave pair.

Among the different approaches for handling the small cell problem, the cell mixing is the easiest to implement as it does not require any changes to underlying cut-cell data structure [48]. The cell merging approach [93], on the other hand, require modifications in the way cut-cells are indexed and stored. Furthermore, the cell merging process introduces new cell topologies, which can severely complicate the finite volume discretization process [89]. The additional complexity with cell merging approach is in finding the appropriate neighbors for merging, which is non-trivial in three dimensions [89, 48]. In the cell linking approach, on the other hand, the cut-cell and the neighbor cell are linked as a master/slave pair, instead of merging them to form a single cell. The volumetric and surface information of the slave and master cells remain distinct. Although the cell-linking is well established for 2 D problems, its extensibility to 3D has not been studied well, where it would be required to link more than two cells. Moreover, the cell linking as well as merging procedures reduces the

order of the numerical scheme locally [94]. To the best of authors knowledge, none of the above small cell treatments have been shown in the past to be more than second-order accurate. Sources of the numerical noise in wall shear stress prediction were later analyzed by [95] and different near wall modeling solution approaches were suggested. They found that the numerical oscillations are caused by the presence of irregularities in the stencil spacing of the numerical grid adjacent to the boundaries and proposed wall models that can result in smooth reconstruction of wall shear stress. The existing literature studies on applying cut cell method in addressing different aspects of the application problems of interest are detailed in the following sections.

Viscous flows using cut-cell: The use of cut-cell method for viscous flows was first introduced by Udaykumar *et al.* [84] also, there were several other later studies by their group [65, 96, 90]. An assessment of Cartesian mesh based cut-cell approach for viscous flows is provided by Coirier and Powell [87]. They concluded that the non-positivity induced by the cut-cells in wall gradient data based derived quantities, such as skin friction and heat transfer, results in significant numerical noise in the solution although the integrated quantities such as the drag and lift coefficient agree well with past data. Hartman et al [94, 97, 25] in a series of papers presented a novel cut-cell method with ghost node implementation for modeling compressible viscous flows. They employed distance weighted convex averaging of cell centered gradients to compute surface gradients needed for viscous terms. The second order overall accuracy of the method was demonstrated for several 2D and 3D test cases for steady and unsteady flows. However, the accuracy and smoothness of the wall shear stress prediction using their approach were never demonstrated. Gao [98] extended the cut cell method to viscous incompressible flows, which was originally developed for inviscid flows, by Yang et al [14]. Botella and Cheny [99] employed a levelset based cut-cell method to solve incompressible viscous flows. Their method was based on symmetry preserving finite volume discretization. However, the only 2D studies were reported in the paper and applica-

bility of the approach for 3D flows is not clear. All the above studies except for Coirier and Powell [87] only report on the global integrated quantities such as drag and lift coefficient and do not look into surface shear stress distribution.

*Turbulence modeling using cut-cell:* To date, there have been only a few reported works on modeling turbulence using the cut-cell Cartesian method. Meyer [100] developed a conservative second order accurate immersed interface method suitable for LES of high Reynolds number incompressible flows. However, an implicit LES approach in the capacity of ALDM approach was employed for the turbulence closure. Essentially, the numerical dissipation of the scheme was assumed to mimic the physical dissipation due to action of small scale unresolved turbulence. In a recent article, Berger and Aftosmis [95] extensively analyzed modeling of steady viscous compressible flows using Cartesian cut cell finite volume method. They explored the use of wall models for laminar and turbulent flows to suppress numerical oscillations in the second derivatives used for viscous flux computations.

*Moving boundaries using cut cell:* There have been a limited number of studies reported on applying the cut-cell method to moving boundaries. Yang and Causon [101, 102], in a series of two papers, described a Cartesian cut cell method applicable to compressible inviscid flows around stationary and moving bodies. A unique feature of their method is the use of cell merging technique to address both the issues of time step restriction due to small cells and the problem of "freshly-cleared" cells. The approach adopted was to use the cell merging technique to populate the flow state variables in cells that are exposed due to interface motion. The only caveat was that the surface was not allowed to sweep across more than one local cell width thereby restricting the time step. Hu and Khoo [48] employed a level set description for the interface and a mixing procedure to circumvent the time step restriction for the small cells to solve for flow around moving boundaries. The interface conditions for the boundary points are obtained using an interface interaction

method [103]. Schneiders et al. [50, 104] extended the work done by Hartmann *et al.* [25] to moving boundaries. They employed a variant of the flux redistribution technique previously developed by Pember *et al.* [105] for handling the small cell problem. The blending of a stable non-conservative update based on interpolation, with an unstable conservative update based on time integration, was done to achieve stability of the small cells and achieve a smooth temporal variation of surface forces on the boundary. The mass deficit/surplus due to the non-conservative update is distributed to the neighboring cells. However, the effect of flux distribution on the accuracy of the surface shear stress predictions was not discussed. Moreover, the cases demonstrated were mostly restricted to bodies moving at low subsonic velocities. The capability of the method to handle large displacements at high speed was not addressed.

#### **1.4 Summary of the existing numerical capabilities**

A summary of various techniques with respect to the grid generation for complex and moving boundaries are listed in Table. 1.1 and the key features comparing the two main EB methods are provided in Table.1.2. Overall, the highlights of the existing numerical capabilities are summarized in the following points:

Based on survey of existing approaches, an overview of the different solver schemes that are used to simulate moving boundary problems by overcoming some of the associated challenges (highlighted earlier), is shown in Fig. 1.3. Although there are several approaches used in the past for the class of problems mentioned earlier, the discussion in this thesis is restricted to the most popular approaches that apply to viscous, high Reynolds number, high speed reacting flow problems.

- Among the three numerical solver schemes, only the Cartesian cut-cell method and GFM IB method can perform automatic mesh generation for complex and moving boundaries. Other body-conforming approaches have limitations when employed for moving boundary problems.



Table 1.1: Comparison of various numerical techniques with respect to grid related aspects

<b>Method</b>	<b>Grid type</b>	<b>Grid generation for complex geometries</b>	<b>Main challenge</b>	<b>Difficulty in moving boundary application</b>
Overset(structured)	curvi-linear	tedious for complex geometries	trade-off bw adequate resolution and number of grid points	mesh tangling
ALE (unstructured)	polyhedral	easy	mesh connectivity, extension to high-order schemes	periodic remeshing with interpolation
EB methods	Cartesian	easy	resolving the boundary with accuracy	ensuring conservation, oscillations in shear stress, heat transfer rate, etc.

Table 1.2: Comparison of embedded boundary methods

Feature	Ghost cell	Cut cell
a) Discretization scheme	finite difference	finite volume
b) Conservative property	no	yes
c) Enforcing boundary conditions	using ghost nodes	modifying the stencil
d) Time step restriction	no	yes, via small cell volume
e) Main challenge	spurious numerical oscillations near boundaries esp. for viscous flows	small cell treatment, numerical noise in near wall solution
f) Studies on viscous flows	[17],[59], [16],[75], [77], [79]	[84],[65],[96], [87],[14],[99], [100], [95]
g) Studies on moving bodies	[62][63],[80],[81] [106],[82],[20] [83][80]	[101][102],[48], [103], [50],[104], [25], [105] [107]
h) Studies on reacting flows with moving bodies	[28]	

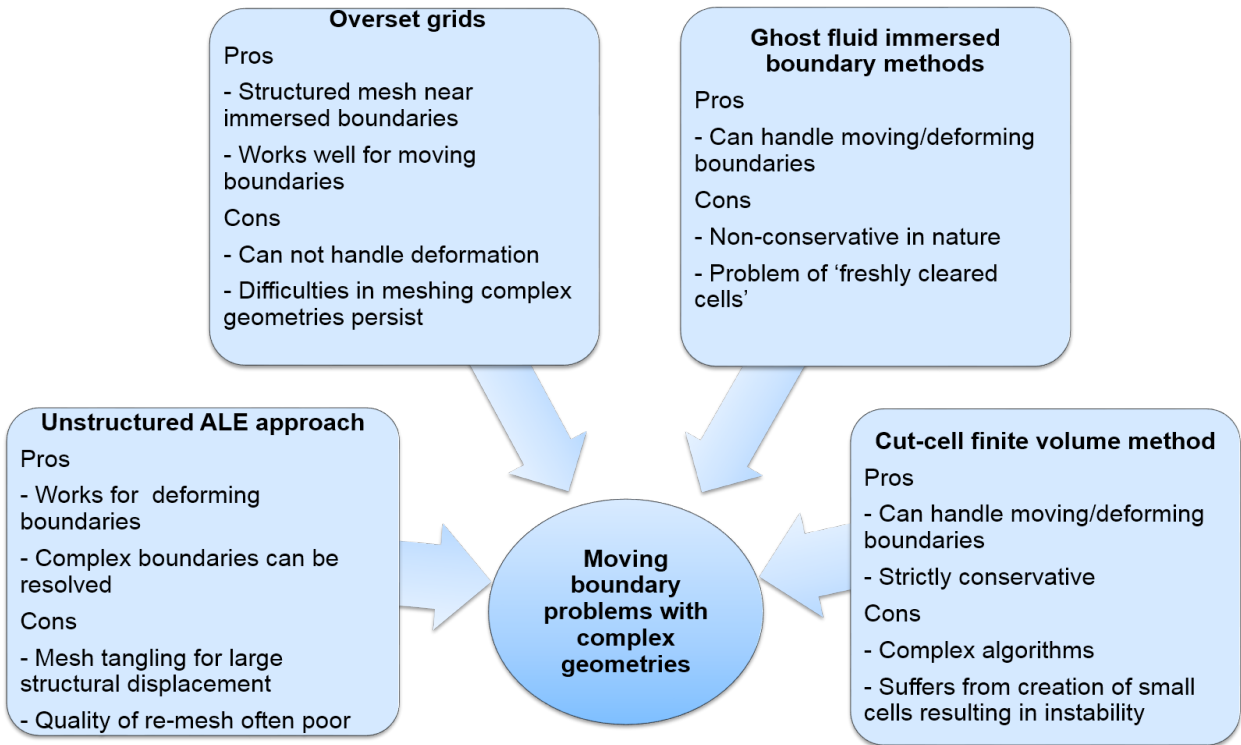


Figure 1.3: Block diagram summarizing different approaches to solve moving body problems involving complex geometries

- Between the embedded boundary approaches, the GFM IB methods are not conservative and can produce spurious numerical oscillations due to mass loss issues. The loss of conservation becomes more severe for moving boundaries when employing GFM techniques.
- Although the cut cell method, ensures strict conservation, it also has problems in ensuring a robust treatment for small cells and, a noise free reconstruction of wall shear stress. The cell-merging and the cell-linking algorithms reported in the literature for small cell treatment have been demonstrated for mostly simple geometries. Extension to complex 3D geometries is not well studied.
- Only very few studies have been reported for reacting flow problems using embedded boundary approaches although there are several engineering applications that can be mathematically modeled using such a capability.
- All the methods reported are utmost globally second order accurate and in some cases the accuracy reduces to first order near immersed boundaries.

## **1.5 Thesis objectives**

The long term application problems that are of interest in this thesis involve high speed, reacting and turbulent flows over/through complex geometries, which may be having either static or moving boundary. A successful strategy for the simulation these problems must address both the numerical scheme and model development aspects. The existing approaches are either not robust or inaccurate when dealing these class of problems (i.e., moving boundaries). Other issues related to the past approaches such as numerical artifacts at the boundary and loss of conservation have to be resolved. The desired properties of the proposed strategy are summarized below:

- Ability to perform local mesh refinement - *Adequate grid resolution is needed without huge cost overhead and without compromising the accuracy of the simulation*

- Robustness of the method when dealing with complex and moving boundaries- *The method must be applicable to practical geometries with narrow gaps and sharp edges*
- High-order of accuracy near embedded boundaries - *Uniform accuracy required both at the boundaries and in the interior especially for turbulent flows.*
- Have good conservation properties - *required when the problem involves compressible effects such as shocks and detonations*
- Be time accurate - *To resolve the highly transient flow physics involved in reacting flow moving boundary problems*
- Be flexible to incorporate sub-grid closures in the context of LES - *The numerical schemes must be able to work efficiently with minimal changes to existing LES subgrid closures*

The overarching goal of this thesis is thus to develop the required numerical and model framework, with all the above properties as well as subgrid closures that are required for LES of turbulent reacting high speed flow problems in complex geometries with stationary/moving boundaries. A block diagram including the workflow between the different components of the proposed numerical framework is illustrated in Fig.1.4. The specific technical objectives for this thesis, the justifications and the associated tasks are detailed below.

#### 1.5.1 Development of numerical approach for simulation of moving boundary reacting flow problems

The major contribution of the thesis is a numerical framework for performing adaptive multi-scale simulations with a high order strictly conservative embedded boundary method. To this end, several approaches were identified based on extensive survey of past literature. Ability to perform local mesh refinement for increased accuracy at manageable overall cost is identified as one of the requirement for simulation of application problems of interest. To

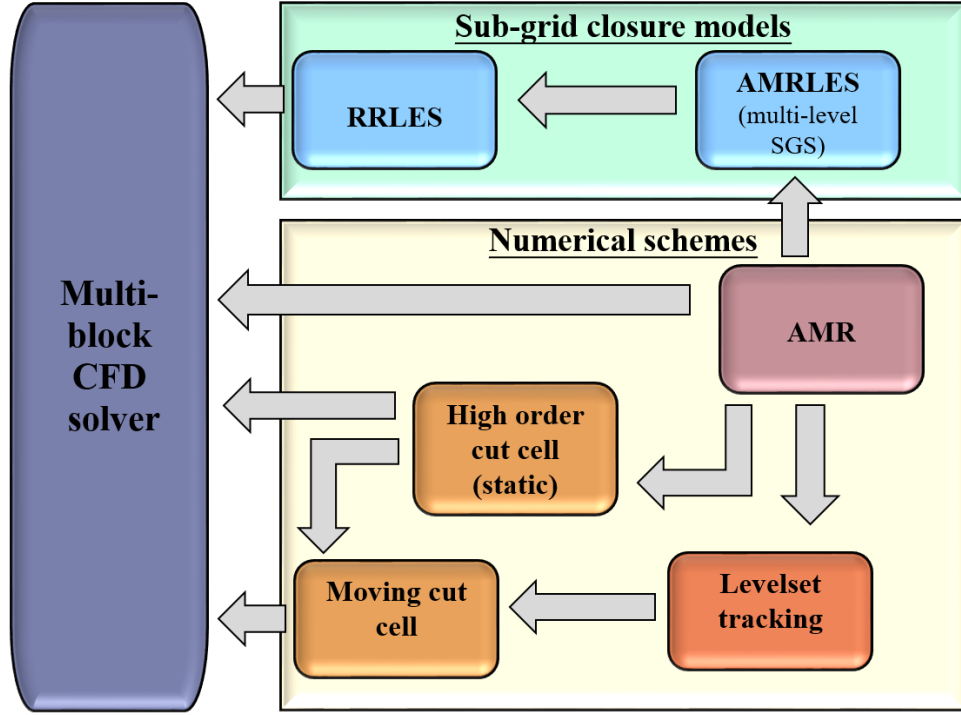


Figure 1.4: Workflow between the different components of the proposed numerical framework

resolve stationary and moving boundaries, a high-order (greater than second order) method that is strictly conservative and can provide accurate results for compressible viscous flow problems is also required since viscous effects are significant in many application problems. To address the above requirements, the two major numerical techniques that are developed are the capability to perform block structured adaptive mesh refinement and treatment of embedded boundaries using a high-order cut-cell approach. The specific tasks under this objective are discussed below:

- **Adaptive Mesh Refinement** strategy using a block structured approach is developed by interfacing an in-house high fidelity compressible flow solver, LESLIE [37] with BoxLib, [31] an open source massively parallel library developed at Lawrence Berkley National Lab (LBNL) to address the computational needs of the problems of interest. As LESLIE is a block structured compressible flow solver, using block-structured AMR to perform refinement is determined to be more appropriate and efficient. New

interfacing algorithms for synchronizing communication between BoxLib and LESLIE are developed. The algorithm and methodology used are generalized so that they apply to interfacing any generic multi-block structured code and a library for block structured refinement.

- **A high order accurate cut-cell method** that can deal with complex geometries involving moving boundaries is developed. The method is demonstrated to achieve fourth order accuracy for inviscid flow problems, third order accuracy for viscous flow problems. For moving boundaries, the method is second order accurate. The cut-cell embedded boundary approach also involved developing cell clustering algorithm, a new "small cell" treatment that can preserve the order of accuracy at the boundaries, both when the body is stationary as well as during its movement. The "small cell" treatment also robustly handles complex boundaries with narrow gaps, sharp edges, etc. The method also ensures noise free reconstruction of skin friction coefficient and heat transfer rate, which is critical for the accurate prediction of various physics related to near-wall effects. Some other notable aspects of the approach are: a robust neighbor finding algorithm for the cell clustering approach (that works with complex geometrical features such as narrow gaps, sharp edges, etc.), extension of the small cell algorithm to enforce strict conservation for moving boundaries and ability to achieve arbitrary orders of accuracy.
- **Verification and validation of AMR/cut-cell approach** are performed extensively with various appropriately designed canonical test cases. The accuracy of the proposed cut-cell method is verified for both static and moving boundary problems. The accuracy and the cost effectiveness of the AMR framework is demonstrated by studying various 2D and 3D test cases.

### 1.5.2 Development of sub-grid closures for turbulent reacting flow in the presence of local refinement and embedded boundaries

The numerical framework that is developed (as part of the previous objective) also requires consistent subgrid closures, as most of the existing sub-grid closures that are designed for body conformal approaches and single level grids, can not be directly applied. As the cut-cell method introduces irregularities in the stencil at the wall of the boundaries, the sub-grid closures have to be modified so that it can be applied to the new stencil. In addition, the deployment of AMR introduces multi-levels of refined meshes. Therefore, corrections to the sub-grid closures are developed so that the closures are consistent and applicable across the various mesh levels. In specific, the focus of the model development are:

- **A multi-level subgrid closure** is developed and validated by extending the existing one equation subgrid kinetic energy closure [37] for AMR/cut-cell approach (henceforth called as Cut-cell/AMRLES).
- **A multi-level reaction rate based closure** for reacting flows is also developed and demonstrated by extending the existing Linear Eddy Model (LEM)[108] for LES of turbulent reacting flow when used with AMR/cut-cell approach (henceforth called as multi-level RRLES)

### 1.5.3 Application studies involving high speed turbulent reacting flow problems with complex/moving geometries

The developed framework is applied to some chosen applications of interest. Three application studies are performed, each focusing and making use of multiple aspects of the developed numerical framework.

- **Interaction of turbulence with stationary and propagating shocks** is investigated, which is of fundamental interest in many high-speed applications. Two configurations are chosen for the study: the canonical problem of a planar shock interacting with a

isotropic turbulence with different Reynolds numbers and a Taylor blast interacting with ambient isotropic turbulence. In these studies, both DNS and LES studies are performed with the AMR based code. AMRLES is used to accurately capture statistically stationary and propagating shocks. For the shock turbulence interaction study, DNS is performed to assess the accuracy of the AMR approach in handling turbulent flow. LES of the same configurations is performed to highlight multi-level closure performance and study the dynamical behavior of closure model across refinement interfaces. The LES study is then extended to analyze interaction of a strong Taylor blast wave with surrounding isotropic turbulence. Comparison with past studies are also used for validation.

- **Flame interaction with turbulence in simple and complex configurations** are studied, where the cut-cell/AMR along with the developed sub-grid closures for both flow and reaction chemistry are also utilized. The multi-level closure for chemistry is validated for a canonical configuration of a freely propagating flame interacting with decaying turbulence. Flame anchoring mechanism in a reacting transverse jet in a cross flow (JICF) are investigated using LES at different jet/crossflow velocity ratios where the cut-cell method is used for resolving the jet inflow pipe and bottom wall boundary. These cases are chosen since previous data from experiments exists for comparison.
- **Detonation initiation and stabilization by moving projectiles** are investigated as an application involving moving bodies. The problem of detonation initiation by projectiles moving at hypersonic speed is of fundamental interest in hypersonic propulsion systems. In this study, cut-cell the method is deployed for the moving body along with dynamic mesh refinement using AMR. The different modes of combustion and the effect of pressure on these modes are analyzed to understand the physical mechanisms behind the detonation stabilization. Comparison with experimental data is used to demonstrate the accuracy of the proposed method.



All of the application problems are chosen carefully so as to represent best the various flow characteristics encountered in practical engineering devices. The studies also provide some insight into the various physics related questions that remains to be answered in the above class of problems.

## **1.6 Thesis organization**

The organization of the thesis is as follows. In Chapter 2, the governing equations and mathematical formulation employed for all the numerical simulations presented in this thesis are described. The integration of an external open source library with the inhouse CFD solver to perform block structured adaptive mesh refinement is described and appropriate validation cases are provided in Chapter 3. The high-order cut-cell based embedded boundary method to handle static/moving or deforming boundaries is then introduced in Chapter 4. The algorithm to handle the "small cell" problems common to all cut-cell techniques is also described in this chapter. In addition, the verification and validation of the cut-cell embedded boundary method are discussed by studying several test cases. The details of a new multi-level subgrid closure for flow based on the one equation based subgrid scale kinetic energy model is described in Chapter 5. The proposed closure is investigated for several test cases with local mesh refinement and embedded boundaries handled using the cut-cell approach in the same chapter. In Chapter 6, an extension of the Linear Eddy Model (LEM) to AMR grids is proposed and assessment of the closure is performed for the problem of a freely propagating flame interacting with isotropic turbulence. The application AMR to the canonical problem of shock-turbulence interaction and blast turbulence interaction is performed in Chapter 7. In the next Chapter, 8, the problem of a reacting jet in cross flow is studied using the combination of the cut-cell method and AMR. Finally, detonation initiation by hypervelocity projectiles is presented in Chapter 9. Conclusion emphasizing the contributions of this thesis and directions for the future research and recommendations for extending current capabilities are summarized in the final Chapter 10.

## CHAPTER 2

### GOVERNING EQUATIONS AND MATHEMATICAL FORMULATION

In this chapter, the governing equations used for simulation of all the problems relevant to this thesis and the details of closure modeling for LES of reacting flow problems are first discussed. The mathematical formulation used for discretization of the governing equations and numerical approaches employed for evaluation of the fluxes are then described.

#### 2.1 Governing equations

Multi-component, reacting, compressible Navier-Stokes equations are solved in both the unfiltered form without employing any closure models and with the filtered form with subgrid closure models for LES to obtain the various results reported in this thesis. These equations are described along with the various associated sub-classes of equations and models in the following sections.

##### 2.1.1 Unfiltered Navier-Stokes equation

The compressible Navier-Stokes equations in its conservative form are given by:

$$\frac{\partial \mathbf{U}}{\partial t} + \frac{\partial \mathbf{F}_{\text{inv},i}}{\partial x_i} + \frac{\partial \mathbf{F}_{\text{vis},i}}{\partial x_i} = \mathbf{Q}, \quad i = 1, 2, 3, \quad (2.1)$$

where  $\mathbf{U}$  is the vector of conservative variables  $\mathbf{U} = [\rho, \rho u_1, \rho u_2, \rho u_3, \rho E, \rho Y_k]^T$  with  $\rho$  being the density,  $u_i$  denoting the velocity components,  $p$  denoting the pressure,  $E$  being the total energy per unit mass defined as the sum of internal energy,  $e$  and kinetic energy:

$$E = \frac{1}{2} u_i u_i + e. \quad (2.2)$$

The internal energy of a multicomponent system is defined as:

$$e = \sum_{k=1}^{N_s} Y_k e_k, \quad (2.3)$$

where  $e_k$  and  $Y_k$  are sensible energy and the mass fraction of the  $k^{th}$  species, respectively. In Eq. (2.1),  $\mathbf{F}_{\text{inv},i}$ ,  $\mathbf{F}_{\text{vis},i}$  and  $\mathbf{Q}$  are the vectors of the inviscid, viscous fluxes and source terms, respectively in the  $i^{th}$  direction and are given as follows:

$$\mathbf{F}_{\text{inv},i} = \begin{pmatrix} \rho u_i \\ \rho u_i u_1 + p \delta_{i1} \\ \rho u_i u_2 + p \delta_{i2} \\ \rho u_i u_3 + p \delta_{i3} \\ (\rho E + p) u_i \\ \rho u_i Y_k \end{pmatrix}, \mathbf{F}_{\text{vis},i} = - \begin{pmatrix} 0 \\ \tau_{i1} \\ \tau_{i2} \\ \tau_{i3} \\ u_j \tau_{ij} - q_i \\ Y_k V_{i,k} \end{pmatrix}, \text{ and } \mathbf{Q} = \begin{pmatrix} 0 \\ 0 \\ 0 \\ 0 \\ 0 \\ \dot{\omega}_k \end{pmatrix}, \quad (2.4)$$

where  $\dot{\omega}_k$  is the mass production rate of  $k^{th}$  species,  $\tau_{ij}$  and  $q_i$  are the stress tensor and the heat flux vector respectively, and  $V_{i,k}$  is the diffusion velocity for the  $k^{th}$  species. The inviscid and viscous flux vectors are identified separately to facilitate the discussion of numerical procedures associated to compute these fluxes. The different terms in Eq. (2.1) will be described in more detail as follows:

### *Equation of state*

The equation of state for a thermally perfect gas is given by:

$$P = \rho RT, \quad (2.5)$$

with  $R$  being the mixture gas constant defined as:

$$R = \mathcal{R}_u \sum_k^{N_s} \frac{Y_k}{MW_k}. \quad (2.6)$$

In Eq. (2.6),  $\mathcal{R}_u$  is the universal gas constant expressed in per mole and  $MW_k$  is the molecular weight of the  $k^{th}$  species. Based on the equation of state defined by Eq. (2.6), for a thermally perfect gas, the sensible energy of  $k^{th}$  species and thus the total internal energy of the mixture can be shown to be strictly a function of temperature only and is given as follows:

$$e = \rho \sum_{k=1}^{N_s} Y_k e_k = \rho \sum_{k=1}^{N_s} Y_k \left( e_k^0 + \int_{T_0}^T c_{v,k}(T') dT' \right), \quad (2.7)$$

where  $c_{v,k}(T)$  is the specific heat at constant volume of  $k^{th}$  species, which is a function of Temperature  $T$ . and  $e_k^0$  is the reference energy of the species  $k$  evaluated at temperature  $T_0$ . In many of the thermodynamic databases, polynomial curve fits are available for the specific heat at constant pressure,  $c_{p,k}(T)$ . This motivates rewriting Eq. (2.7) in terms of the sensible enthalpy of the species, which is a function of  $c_{p,k}(T)$ . This is done by using the state relation,  $e = h + p/\rho$  where  $h$  is the sensible enthalpy of the mixture. The sensible enthalpy of  $k^{th}$  species is given the following equation:

$$h_k = h_k^0 + \int_{T_0}^T c_{p,k}(T') dT', \quad (2.8)$$

where  $h_k^0$  is the sensible enthalpy at reference temperature  $T_0$  for species  $k$ . The specific heat at constant volume ( $c_{v,k}$ ) and constant pressure ( $c_{p,k}$ ) are related by:

$$c_{p,k} = c_{v,k} + \frac{\mathcal{R}_u}{MW_k}. \quad (2.9)$$

Using Eqs. (2.8) and (2.9), the thermodynamic state of the mixture is completely defined along with the equation of state if the  $c_{p,k}$  of each species  $k$  is known.

### *Viscous stress tensor*

In this work, the fluid is assumed to be Newtonian and accordingly the viscous stress tensor is expressed as:

$$\tau_{ij} = \mu \left( \frac{\partial u_i}{\partial x_j} + \frac{\partial u_j}{\partial x_i} \right) + \lambda \frac{\partial u_k}{\partial x_k} \delta_{ij}, \quad (2.10)$$

where  $\mu$  is the kinematic viscosity,  $\lambda$  is the bulk viscosity and  $\delta_{ij}$  is the Kronecker delta function given as:

$$\delta_{ij} = \begin{cases} 1 & \text{if } i = j \\ 0 & \text{otherwise.} \end{cases} \quad (2.11)$$

The value of bulk viscosity is set as  $\lambda = -2/3\mu$  following Stoke's hypothesis which states that the sum of normal viscous stresses is zero i.e., the trace of stress tensor is zero. This assumption generally holds in practice for a wide range flows and is used for all the simulations in this study. The stress tensor can then be written as:

$$\tau_{ij} = 2\mu (S_{ij} - 2/3\delta_{ij}S_{ll}) \quad (2.12)$$

where  $S_{ij} = 1/2 \left( \frac{\partial u_i}{\partial x_j} + \frac{\partial u_j}{\partial x_i} \right)$  is the strain rate tensor. For all the non-reacting cases, the kinematic viscosity which is a function of temperature only is computed using a power-law of the form:

$$\mu = \mu_0 \left( \frac{T}{T_0} \right)^n, \quad (2.13)$$

where  $\mu_0$  and  $T_0$  are the reference values and  $n$  is the power law exponent. For reacting case studies, the viscosity is a function of both temperature and mixture composition and computed using mixture-averaged rules

### *Heat flux vector*

The heat flux vector,  $q_i$ , present in the energy equation, can be given using the Fourier's law of heat conduction and also from the contribution to sensible enthalpy due to species diffusion:

$$q_i = -\kappa \frac{\partial T}{\partial x_i} + \rho \sum_{k=1}^{N_s} h_k Y_k V_{i,k}, \quad (2.14)$$

where  $\kappa$  is the thermal conductivity,  $\mu$  is dynamic viscosity,  $h_k$  is the specific enthalpy and  $V_{i,k}$  is the diffusion velocity for the  $k^{th}$  species. Similar to the dynamic viscosity,  $\kappa$  can be computed using a power law expression or from mixture averaged formulation. A common practice is to relate  $\mu$  and  $\kappa$  using a non-dimensional number known as Prandtl number ( $Pr$ ) as follows:

$$Pr = \frac{C_p \mu}{\kappa}, \quad (2.15)$$

and is assumed to be  $Pr = 0.7$  for non-reacting cases and  $Pr = 0.72$  for the reacting cases.

### *Species diffusion velocity*

The diffusion velocity,  $V_{i,k}$  is modeled using Fickian diffusion approximation as:

$$V_{i,k} = -D_k \frac{1}{X_k} \frac{\partial X_k}{\partial x_i} + \frac{1}{W} \sum_{k=1}^{N_s} D_k W_k \frac{\partial X_k}{\partial x_i}, \quad (2.16)$$

where  $W$  is the mixture molecular weight,  $D_k$  and  $X_k$  are the diffusion coefficient and the mole fraction of the  $k^{th}$  species, respectively. Soret effects are neglected in the above model. Note that the above formulation satisfies the condition  $\sum V_{i,k} = 0$  without which the mass conservation would be violated. For the reacting cases reported in this thesis,  $V_{i,k}$  is computed using the mixture averaged formulation.

### 2.1.2 Filtered Navier-Stokes equation for LES

The Navier-Stokes equations can be solved using DNS in which the complete range of scales of motions are resolved. The computational cost of DNS, however can go up significantly especially for turbulent flows. Through simple dimensional analysis, it can be shown that the number of degrees of freedom in space and time required for a DNS is related to the flow Reynolds number as [109]:

$$\frac{l}{\eta} = Re_l^{3/4}, \quad (2.17)$$

$$\frac{\tau_l}{\tau_\eta} = Re_l^{2/4}. \quad (2.18)$$

where  $l$  is the integral length scale,  $\eta$  is the Kolmogorov length scale,  $\tau_l$  and  $\tau_\eta$  are the integral and Kolmogorov time scales, respectively and  $Re_l$  is the Reynolds number based on the integral length scale. The number of points  $N$  required to resolve  $\eta$  and  $l$  is given by  $N = \frac{l}{\eta}$ . The total number of points required in 3D is  $N^3$  and scales as  $Re_l^{9/4}$ . The number of time steps required to resolve an integral time scale scales as  $N_t = Re_l^{2/4}$ . Therefore the total cost of the simulation which involves solving  $N^3$  points for  $N_t$  time steps would scale as  $N^3 \times N_t = Re_l^{11/4}$ . It can be seen that the cost grows roughly cubically with Reynolds number. For practical flows, which are generally at high Reynolds numbers, the cost becomes prohibitively high. The alternative is to employ Large Eddy Simulation (LES) strategy in which only the most energy containing scales of motion are resolved by the numerical discretization. The effect of unresolved small scales motion on the represented scales

is modeled using subgrid closures.

The basic idea behind LES is to perform a spatial filtering operation and decompose the flow variables into the resolved and subgrid scales. For any flow variable,  $\phi$  the filtering operation results in:

$$\phi = \bar{\phi} + \phi''.$$
 (2.19)

In Eq. (2.19),  $\bar{\phi}$  is the resolved part and  $\phi''$  represents the unresolved subgrid part. The separation of the resolved and unresolved scales is done by applying a filtering operator,  $\mathcal{G}$  over the numerical domain,  $\Omega$ :

$$\bar{\phi}(\mathbf{x}) = \int_{\Omega} \mathcal{G}(\mathbf{x} - \mathbf{x}') \phi(\mathbf{x}') d\mathbf{x}',$$
 (2.20)

where  $\mathbf{x}$  and  $\mathbf{x}'$  are position vectors. The filtering operation  $\mathcal{G}$  is often expressed a product of one dimensional filter kernels performed over the three coordinate directions:

$$\mathcal{G}(\mathbf{x}') = \prod_{i=1}^3 g(x_i - x_i').$$
 (2.21)

The one-dimensional filter kernel takes the following for a box-filter:

$$g(x_i - x_i') = \begin{cases} 1/\Delta_i & \text{if } |x_i - x_i'| < \Delta_i/2 \\ 0 & \text{otherwise.} \end{cases}$$
 (2.22)

The filter width,  $\Delta$  size in three dimensions can be notionally considered as:

$$\Delta = (\Delta_1 \Delta_2 \Delta_3)^{1/3}.$$
 (2.23)

It has to be noted that for LES without an explicit filtering, the numerical grid acts as the filter and the filter width is same as the local grid size. For compressible and variable density flows,



a more convenient form of density weighted filtering known as *Favre* filtering is performed on the flow variables as follows:

$$\tilde{\phi} = \frac{\overline{\rho\phi}}{\rho}. \quad (2.24)$$

After Favre filtering, the compressible, multicomponent N-S equations, has the following form:

$$\frac{\partial}{\partial t} \begin{pmatrix} \bar{\rho} \\ \bar{\rho}\tilde{u}_j \\ \bar{\rho}\tilde{E} \\ \bar{\rho}\tilde{Y}_k \end{pmatrix} + \frac{\partial}{\partial x_j} \begin{pmatrix} \bar{\rho}\tilde{u}_i \\ \bar{\rho}\tilde{u}_i\tilde{u}_j + \bar{p}\delta_{ij} - \tilde{\tau}_{ij} + \tau_{ij}^{sgs} \\ (\bar{\rho}\tilde{E} + \bar{p})\tilde{u}_j - \tilde{u}_i\tilde{\tau}_{ij} + \bar{q}_j + H_j^{sgs} + \sigma_j^{sgs} \\ \bar{\rho}\tilde{u}_j\tilde{Y}_k - \tilde{Y}_k\tilde{V}_{j,k} + Y_{j,k}^{sgs} + \theta_{j,k}^{sgs} \end{pmatrix} = \begin{pmatrix} 0 \\ 0 \\ 0 \\ \bar{\omega}_k \end{pmatrix}. \quad (2.25)$$

The total resolved energy,  $\tilde{E}$  is the sum of filtered internal energy, resolved kinetic energy and subgrid kinetic energy,  $k^{sgs}$ :

$$\tilde{E} = \tilde{e} + \frac{1}{2}\tilde{u}_i\tilde{u}_i + k^{sgs}, \quad (2.26)$$

with the subgrid kinetic energy defined as:

$$k^{sgs} = \frac{1}{2}\widetilde{u_i u_i} - \tilde{u}_i\tilde{u}_i. \quad (2.27)$$

The filtered equation of state for a thermally perfect gas is:

$$\bar{p} = \bar{\rho} \left( \tilde{R}\tilde{T} + T^{sgs} \right), \quad (2.28)$$

where  $\tilde{R}$  is the mixture gas constant and is given as:

$$\tilde{R} = \sum_{k=1}^{N_s} \tilde{Y}_k \frac{\mathcal{R}_u}{W_k}. \quad (2.29)$$

The filtered viscous stress tensor,  $\bar{\tau}_{ij}$ , and the filtered heat-flux vector,  $\bar{q}_i$  are modeled as:

$$\bar{\tau}_{ij} = 2\mu(\tilde{T}) \left( \tilde{S}_{ij} - \frac{1}{3}\tilde{S}_{kk}\delta_{ij} \right), \quad (2.30)$$

$$\bar{q}_i = -\kappa(\tilde{T}) \frac{\partial \tilde{T}}{\partial x_i} + \bar{\rho} \sum_{k=1}^{N_s} \tilde{h}_k \tilde{Y}_k \tilde{V}_{i,k} + \sum_{k=1}^{N_s} q_{i,k}^{\text{sgs}}. \quad (2.31)$$

Here,  $\tilde{S}_{ij}$  is the resolved rate of strain, given as:

$$\tilde{S}_{ij} = \frac{1}{2} \left( \frac{\partial \tilde{u}_i}{\partial x_j} + \frac{\partial \tilde{u}_j}{\partial x_i} \right) \quad (2.32)$$

Finally,  $\tilde{V}_{i,k}$  is the filtered diffusion velocity for the  $k^{\text{th}}$  species, and is modeled as

$$\tilde{V}_{i,k} = -\bar{D}_k \frac{1}{\tilde{X}_k} \frac{\partial \tilde{X}_k}{\partial x_i} + \frac{1}{W} \sum_{k=1}^{N_s} \bar{D}_k W_k \frac{\partial X_k}{\partial x_i}. \quad (2.33)$$

In the above equations, all the subgrid-scale terms, indicated with a *sgs* superscript, are unclosed, and therefore, require modeling. These terms are summarized below:

$$\tau_{ij}^{\text{sgs}} = \bar{\rho} (\widetilde{u_i u_j} - \tilde{u}_i \tilde{u}_j), \quad (2.34)$$

$$H_i^{\text{sgs}} = \bar{\rho} (\widetilde{E u_i} - \tilde{E} \tilde{u}_i) + (\overline{u_i P} - \tilde{u}_i \bar{P}), \quad (2.35)$$

$$\sigma_i^{\text{sgs}} = (\overline{u_j \tau_{ij}} - \tilde{u}_j \bar{\tau}_{ij}), \quad (2.36)$$

$$Y_{i,k}^{\text{sgs}} = \bar{\rho} (\widetilde{u_i Y_k} - \tilde{u}_i \tilde{Y}_k), \quad (2.37)$$

$$\theta_{i,k}^{\text{sgs}} = \bar{\rho} (\widetilde{V_{i,k} Y_k} - \tilde{V}_{i,k} \tilde{Y}_k), \quad (2.38)$$

$$q_{i,k}^{\text{sgs}} = \bar{\rho} (\widetilde{h_k Y_k V_{i,k}} - \tilde{h}_k \tilde{Y}_k \tilde{V}_{i,k}), \quad (2.39)$$

$$T^{\text{sgs}} = \widetilde{RT} - \tilde{R} \tilde{T}, \quad (2.40)$$

$$E_k^{\text{sgs}} = \widetilde{Y_k e_k(T)} - \tilde{Y}_k e_k(\tilde{T}) \quad (2.41)$$

Models for  $\tau_{ij}^{\text{sgs}}$ ,  $H_i^{\text{sgs}}$ ,  $\sigma_i^{\text{sgs}}$ ,  $Y_{i,k}^{\text{sgs}}$ ,  $\theta_{i,k}^{\text{sgs}}$ , and  $\bar{\omega}_k$  are presented in the next section. The

other terms,  $E_k^{sgs}$ ,  $T^{sgs}$ , and  $q_i^{sgs}$  are neglected based on a previous study [110].

The subgrid model used in this thesis is based on a past work by Kim and Menon [111] and a compressible form of the same subgrid closure later extended by Genin and Menon [37]. The model is based on solving for the evolution of the subgrid turbulent kinetic energy  $k^{sgs}$ . The details of closure model for the base case without any AMR refinement are explained in this section. The extension of the model to handle block adaptive mesh refinement and embedded boundaries is discussed later in chapters 5 and 6.

The *sgs* subgrid terms in the momentum equations are closed by employing the Boussinesq eddy viscosity assumption which postulates that the momentum transfer due to action of turbulent eddies is analogous to that caused by molecular viscosity. Accordingly, the eddy viscosity and the subgrid stress tensor are modeled as:

$$\nu_t = C_\nu \sqrt{k^{sgs}} \Delta, \quad (2.42)$$

$$\tau_{ij}^{sgs} = -2\bar{\rho}\nu_t \left( \tilde{S}_{ij} - \frac{1}{3}\tilde{S}_{kk}\delta_{ij} \right) + \frac{2}{3}k^{sgs}\delta_{ij}, \quad (2.43)$$

where  $\Delta$  is the grid filter width set same as the local grid size. the two unclosed terms in the energy equation,  $H_i^{sgs}$  and  $\sigma_i^{sgs}$  are modeled together as[37]:

$$H_i^{sgs} + \sigma_i^{sgs} = (\bar{\rho}\nu_t + \mu) \frac{\partial k^{sgs}}{\partial x_i} + \frac{\bar{\rho}\nu_t c_p}{Pr_t} \frac{\partial \tilde{T}}{\partial x_i} + \tilde{u}_j \tau_{ij}^{sgs}. \quad (2.44)$$

The subgrid kinetic energy,  $k^{sgs}$  is obtained by solving a transport equation for its evolution:

$$\frac{\partial \bar{\rho} k^{sgs}}{\partial t} + \frac{\partial}{\partial x_i} (\bar{\rho} \tilde{u}_i k^{sgs}) = \mathcal{T}_{k^{sgs}} + p d_{k^{sgs}} + P_{k^{sgs}} - D_{k^{sgs}}, \quad (2.45)$$

where  $\mathcal{T}_{k^{sgs}}$  denotes the transport of  $k^{sgs}$  due to diffusion effects,  $p d_{k^{sgs}}$  is the pressure dilatation correlation,  $P_{k^{sgs}}$  is the subgrid kinetic energy production and  $D_{k^{sgs}}$  is the subgrid kinetic energy dissipation. The closure formulation of the each of these terms are summa-

ized below:

$$\mathcal{T}_{k^{sgs}} = \frac{\partial}{\partial x_i} \left[ (\bar{\rho}\nu_t + \mu) \frac{\partial k^{sgs}}{\partial x_i} + \frac{\bar{\rho}\nu_t \tilde{R}}{Pr_t} \frac{\partial \tilde{T}}{\partial x_i} \right], \quad (2.46)$$

$$pd_{k^{sgs}} = \alpha_{pd} M_t^{sgs2} \left( \frac{\bar{\rho} \tilde{S} k^{sgs}}{D^{sgs}} \right)^2 (P_{k^{sgs}} - D_{k^{sgs}}), \quad (2.47)$$

$$P_{k^{sgs}} = \tau_{ij}^{sgs} \tilde{S}_{ij}, \quad (2.48)$$

$$D_{k^{sgs}} = \bar{\rho} C_\epsilon (k^{sgs})^{3/2} / \bar{\Delta}. \quad (2.49)$$

In Eq. (2.45), the pressure dilatation term  $pd_{k^{sgs}}$  which is a model for effect pressure fluctuations on the subgrid kinetic energy production is relevant only for flows with significant compressibility effects i.e.  $M_t > 0.1$ . where  $M_t$  is the turbulent Mach number given by  $M_t = \sqrt{q}/\bar{c}$  with  $q = \tilde{u}_i \tilde{u}_i$  and  $\bar{C}$  is the filtered speed of sound. Similarly the diffusion of the  $k^{sgs}$  due to temperature gradients in  $\mathcal{T}_{k^{sgs}}$  is also negligible for low speed flows.

The coefficients  $C_\nu$  and  $C_\epsilon$  can be computed using a local dynamic approach originally developed by Kim and Menon [111]. Extension of the dynamic approach for determining compressibility corrections terms  $Pr_t$  and  $\alpha_{pd}$  was then later performed by Genin and Menon [37].

## 2.2 Mathematical formulation

### 2.2.1 Finite volume approach for moving boundary problems

The finite volume scheme is described for the unfiltered multi-component compressible Navier-Stokes (N-S) equation without loss of any generality. The same procedure applies for the filtered N-S equations with appropriate modifications to include the  $sgs$  terms. The N-S governing equations are discretized using the finite volume formulation based on the integral form of Eq. (2.1) over a control volume  $V(t)$  whose boundary surfaces are moving

with a velocity  $\mathbf{u}_s$ . For a moving reference frame, using the Reynolds Transport theorem:

$$\int_{v(t)} \frac{\partial}{\partial t} \mathbf{U} dv = \frac{\partial}{\partial t} \int_{v(t)} \mathbf{U} dv + \int_{s(t)} \mathbf{F}_s(\mathbf{U}) \cdot \mathbf{n} ds, \quad (2.50)$$

where  $\mathbf{F}_s$  is the flux due to the boundary motion. Reformulating the above equation using Eq. (2.1) results in:

$$\frac{\partial}{\partial t} \int_{v(t)} \mathbf{U} dv + \int_{s(t)} (\mathbf{F}_{\text{inv}}(\mathbf{U}) + \mathbf{F}_{\text{vis}}(\mathbf{U})) \cdot \mathbf{n} ds = \int_{v(t)} \mathbf{Q} dv. \quad (2.51)$$

The inviscid flux function  $\mathbf{F}_{\text{inv}}$  is modified taking into account  $\mathbf{F}_s(\mathbf{U})$  and therefore is in terms of the contra-variant velocity vector,  $\mathbf{v} = \mathbf{u} - \mathbf{u}_s$ , where  $\mathbf{u}_s$  is the surface velocity vector. The complete flux formulation for  $\mathbf{F}_{\text{inv}}$  for moving control volume is:

$$\mathbf{F}_{\text{inv},i} = \begin{pmatrix} \rho(u_i - u_{s,i}) \\ \rho(u_i - u_{s,i})u_1 + p\delta_{i1} \\ \rho(u_i - u_{s,i})u_2 + p\delta_{i2} \\ \rho(u_i - u_{s,i})u_3 + p\delta_{i3} \\ (\rho E + p)(u_i - u_{s,i}) + pu_{s,i} \\ \rho(u_i - u_{s,i})Y_k \end{pmatrix}, \quad (2.52)$$

where  $u_{s,i}$  is the velocity of the boundary surface,  $S(t)$  of the control volume  $V(t)$  in  $i^{\text{th}}$  direction. Note that the background Cartesian mesh is always stationary, even in the case of a moving boundary, therefore  $\mathbf{u}_s = 0$  at all the regular cell faces. However, at the boundary surface  $\mathbf{u}_s$  is nonzero and is the velocity vector of the moving boundary. The only change in flux evaluation of moving boundary problems is restricted to the inviscid part. The viscous and the source term formulation remain invariant in a moving reference frame.

Applying volume averaging of the Eq. (2.51) over a computational cell with a volume  $V$  and discretely approximating the surface integral over the surface  $\Gamma$  of the computational

cell would result in the following semi-discrete form:

$$\frac{\partial}{\partial t}(V\bar{\mathbf{U}}) = \left( \sum_{m=1}^M \sum_{l=1}^{n_g} w_l \mathbf{F}_{\text{inv}}(\mathbf{U}) \cdot \mathbf{n} + \sum_{m=1}^M \sum_{l=1}^{n_g} w_l \mathbf{F}_{\text{vis}}(\mathbf{U}) \cdot \mathbf{n} \right), \quad (2.53)$$

where

$$\bar{\mathbf{U}} = \frac{1}{V} \int_v \mathbf{U} dV, \quad (2.54)$$

represents the volume average of a conservative quantity  $\mathbf{U} = (\rho, \rho u_i, E)$  in the computational cell  $(i, j, k)$ . Here  $M$ ,  $w_l$ , and  $n_g$  denote the face number, quadrature weights and the number of quadrature points used for flux integration along each of the  $M$  faces with a unit normal vector  $\mathbf{n}$ , respectively. The finite volume scheme described is applied to both the regular Cartesian cells and also for partially cell partially cut by the solid embedded boundaries.

A sketch of a normal cell and a cut-cell in two-dimensions with the relevant parameters used in Eq. (2.53) is shown in Fig. 2.1. To evaluate the inviscid and viscous fluxes, Mac-

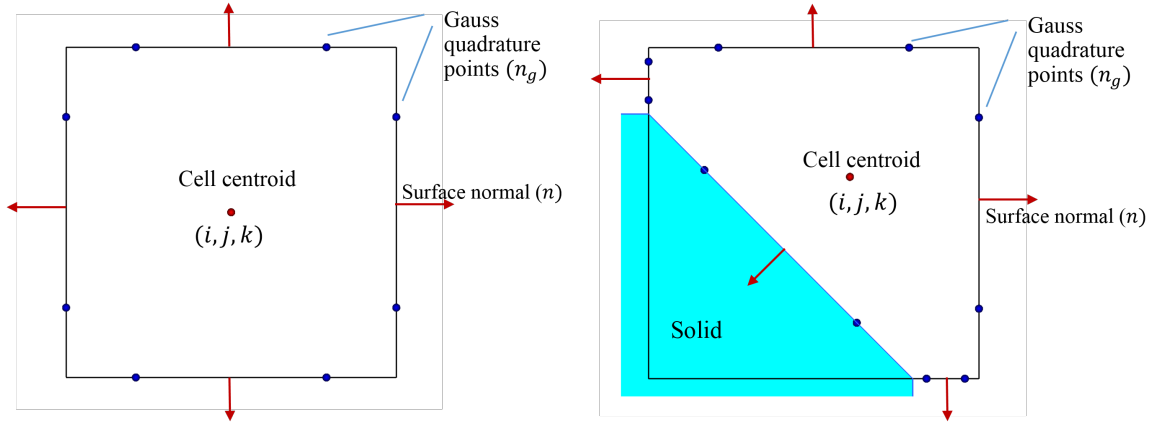


Figure 2.1: Schematic of a (a) 2D normal cell and (b) 2D cut-cell.

Cormack's predictor-corrector [112] method is employed on full cells away from the embedded boundaries. The finite volume version of the MacCormacks method couples the time and

spatial integration schemes. First order or second order extrapolation of cell-averaged values that alternates between the downwind and the upwind direction at each step is performed to compute the fluxes on the cell faces. This results in a second-order accurate scheme in both time and space. A higher order extrapolation can increase the accuracy of the scheme to fourth order. For cut-cells, an alternative formulation is used for computing the fluxes and is described below.

### 2.2.2 Inviscid flux evaluation

The inviscid flux  $\mathbf{F}_{\text{inv}}$  at each cell interface is evaluated as the solution of a local Riemann problem with the initial discontinuous data defined by the left and the right reconstructed states  $\mathbf{U}_L$  and  $\mathbf{U}_R$  [113], and is given as:

$$\mathbf{F}_{\text{inv}}(\mathbf{U}) \cdot \mathbf{n} = \mathbf{f}_{\text{inv}}(\mathbf{U}_L, \mathbf{U}_R, \mathbf{n}), \quad (2.55)$$

where  $\mathbf{f}_{\text{inv}}$  is the solution to the Riemann problem in the direction defined by the surface normal  $\mathbf{n}$ . In this work, Hartmann-Lax-VanLeer family of approximate Riemann solvers (HLL and HLLC) [113] are employed to solve the Riemann problem. The left and the right solution states,  $\mathbf{U}_L$  and  $\mathbf{U}_R$ , are reconstructed based on a  $k$ -exact higher order piecewise polynomial approximation of  $\mathbf{U}$  described in more detail in Section 4.1.1. For a  $k$ -order exact reconstruction, a  $(k+1)$ -order accurate spatial discretization is achieved for smooth hyperbolic problems [114].

### 2.2.3 Viscous flux evaluation

The viscous flux  $\mathbf{F}_{\text{vis}}$  in the direction  $\mathbf{n}$  at each cell interface  $m$ , is computed from the cell interface values of the conservative state  $\mathbf{U}$  and its gradient  $\nabla \mathbf{U}$ , and can be defined in terms of the viscous flux function  $\mathbf{f}_{\text{vis}}$  as:

$$\mathbf{F}_{\text{vis}}(\mathbf{U}) \cdot \mathbf{n} = \mathbf{f}_{\text{vis}}(\mathbf{U}, \nabla \mathbf{U}, \mathbf{n}). \quad (2.56)$$

Both the cell interface solution,  $\mathbf{U}$  and its gradient  $\nabla\mathbf{U}$ , must be known for evaluating the viscous flux function  $\mathbf{f}_{\text{vis}}$ . As detailed in Ivan and Groth [114], an unlimited, cell centered,  $k$ -exact, higher order polynomial reconstruction is employed to obtain  $\mathbf{U}$  and its gradient  $\nabla\mathbf{U}$  is obtained from the direct differentiation of the  $k$ -exact polynomial. Overall, the viscous flux evaluation is  $k$ -order accurate for a  $k$ -order polynomial reconstruction. Thus, for example, for  $k=3$ , the proposed scheme is fourth order accurate for inviscid fluxes and third order accurate for viscous fluxes. A stable central scheme results by taking average of the left and the right reconstructed states,  $\mathbf{U}_L, \mathbf{U}_R$ , and their gradients,  $\nabla\mathbf{U}_L, \nabla\mathbf{U}_R$  for evaluating the viscous flux at the cell interface [114].

The number of Gauss quadrature point,  $n_g$ , employed for the integration of the numerical fluxes at each cell interface is selected to match the order of reconstruction. In general, a  $n_g$  point Gauss quadrature rule yields an exact result for a polynomial of degree  $2n_g - 1$ . Accordingly, a single quadrature point ( $n_g = 1$ ) is used for quadratic reconstruction and two quadrature points ( $n_g=2$ ) are employed for cubic reconstruction.



## CHAPTER 3

### BLOCK STRUCTURED ADAPTIVE MESH REFINEMENT

The implementation and validation of block structured Adaptive Mesh Refinement into a multi-block CFD solver, are discussed in this chapter. Some basic concepts of block structured refinement are first described. The details of interfacing an AMR library with a multi-block structured CFD solver is then discussed. Results for several validation cases are reported to demonstrate the computational efficiency and accuracy of performing block structured AMR.

#### 3.1 Basic concepts of block structured AMR

To facilitate the further discussion of various AMR related scheme and model development implemented in this thesis, some of the basic concepts of block structured refinement are discussed and appropriate notations are provided in this section. To simplify the discussion, the notations are developed assuming a two dimensional coordinate system. Extension to the three dimensions is quite direct and the overall hierarchical grid index system developed here is used later for discussion of three dimensional scheme and model development. The basic concept of patch based AMR and the notations developed are described through the schematics Fig. 3.1 and Fig. 3.2.

The numerical domain is given is denoted as  $\mathcal{D}$  and is a represented by a block structured AMR grid,  $G$ . The grid is comprised by various subgrids  $G_l$  at different refinement levels,  $l = 1, 2, 3, \dots, NL_{max}$ . In mathematical notation this is given by:

$$\mathcal{G} := G_l : l \in N, 1 \leq l \leq NL_{max}. \quad (3.1)$$

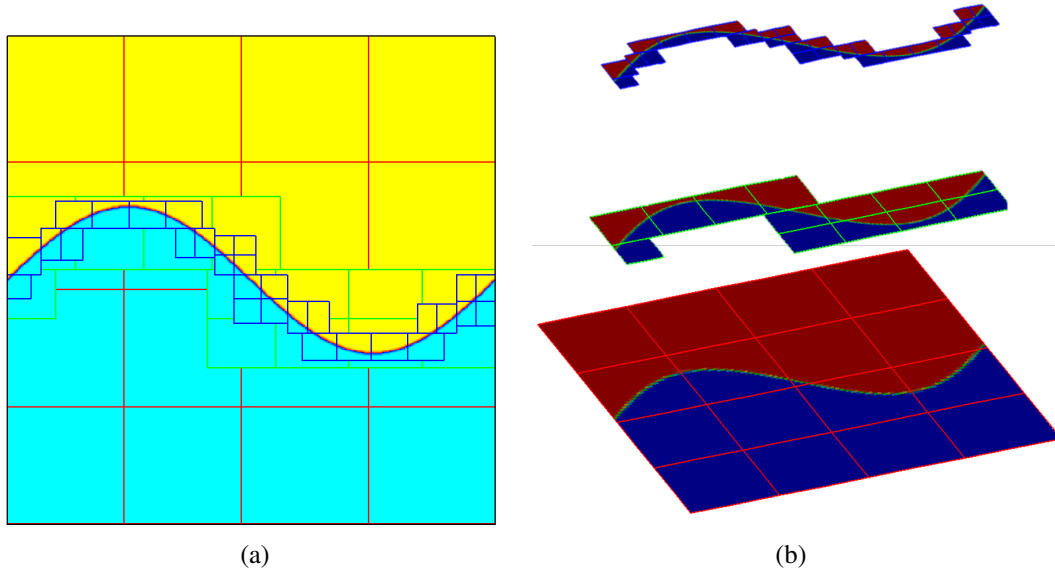


Figure 3.1: Schematic of block based refinement for a front (a) flattened view (b) hierarchical view.

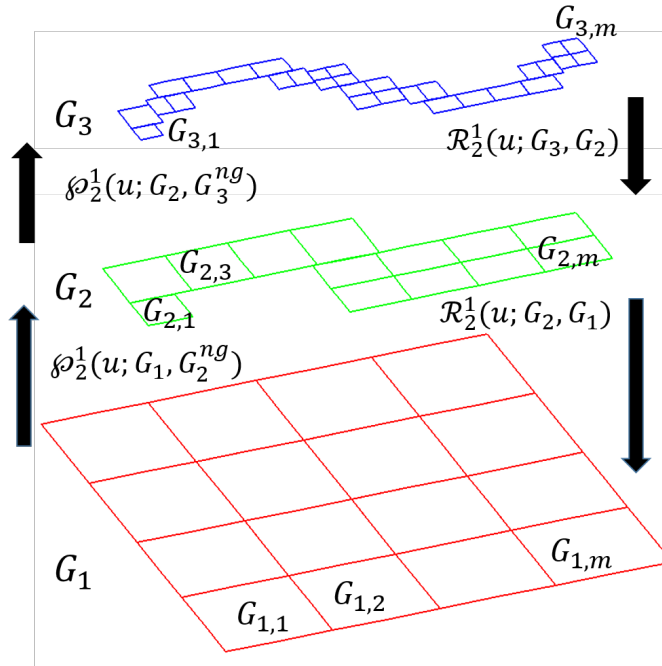


Figure 3.2: Schematic for AMR nomenclature and different data operations.

At each refinement level, the subgrids  $G_l$  is a union of blocks  $G_{l,m}$  where  $m = 1, 2, \dots, M_l$  with  $M_l$  being the number of blocks at level,  $l$ . Accordingly,

$$G_l := \bigcup_{m=1}^{M_l} G_{l,m}. \quad (3.2)$$

An additional constraint is implied on the block structured grid topology which is the *nest-  
edness* of the various levels which requires:

$$G_l \subseteq G_{l-1}. \quad (3.3)$$

The implication of Eq. (3.3) is that a grid level,  $G_l$  is wholly contained by its immediately coarser grid level,  $G_{l-1}$ . Proper nesting makes sure all the cells of a finer level,  $l$  are completely covered by the cells of all the coarser levels from 1 to  $l - 1$ . This ensures all the internal cells of level  $l$  can only be adjacent to all the internal cells in level  $l - 1$  and  $l + 1$ . Properly nested block structured topology is strictly required for correctness of interpolation of flow solution between various levels. Additionally grid blocks of a subgrid at certain refinement level are non-overlapping, adjacent but may not be contiguous.

The size of each grid level,  $G_l$  defined in terms of number of cells in each direction,  $(Ni_l, Nj_l)$ , can be determined from the base grid resolution as:

$$(Ni_l, Nj_l) = (r^{l-1}Ni_1, r^{l-1}Nj_1), \quad (3.4)$$

where  $r$  is the refinement ratio between two successive refinement levels and  $(Ni_1, Nj_1)$  is the base grid resolution. In this work, unless mentioned, all the simulations employ a refinement ratio of  $r = 2$ . Each grid block,  $G_{l,m}$  can be uniquely identified with a global index given by:

$$N(G_{l,m}) = \sum_{k=1}^{l-1} M_k + m \quad (3.5)$$

The computational index extents of a grid level can be determined given the size of the grid level:

$$CG_l = \{(i, j) : 0 \leq i < Ni_l, 0 \leq j < Nj_l\}. \quad (3.6)$$

The co-ordinate system defined in Eq. (3.6) is used to index all the cells contained by grid level,  $G_l$ . The computational indexing of each of the grid block  $G_{l,m}$  requires the starting index in the  $CG_l$  coordinate system. and the size of each of grid block  $(Ni_{l,m}, Nj_{l,m})$ . A size distribution of the all the blocks in the level is denoted by:

$$S(G_l) = \{(Ni_{l,k}, Nj_{l,k}) : k = 1, 2, \dots, M_l\},$$

$$\sum_k^{M_l} Ni_{l,k} \leq Ni_l \text{ and } \sum_k^{M_l} Nj_{l,k} \leq Nj_l. \quad (3.7)$$

The size distribution for a level,  $S(G_l)$  is constrained by three inputs:  $MAX\_SIZE$ ,  $Cl\_width$  and  $Cl\_fac$ . These inputs are the maximum number of cells allowed for a grid block, the minimum width of the grid block in any direction and the factor with the sizes must exist i.e.  $Ni_{l,m}, Nj_{l,m} = i \times Cl\_fac, j \times Cl\_fac : i, j \in \mathcal{N}$ . Another input that determine the distribution of the blocks on a certain refinement level is the tagging criteria:

$$T(G_l) = \{(itag, jtag) : 0 \leq itag < Ni_l, 0 \leq jtag < Nj_l\}. \quad (3.8)$$

The tagging criteria  $T(G_l)$  is provided in terms of a distribution of coordinate indices which are marked for refinement. Based on the  $T(G_l)$  and  $S(G_l)$ , the number and size of grid blocks in a certain level are determined. Once these two parameters are known, the individual block identity can be found at in terms of its coordinate extents as:

$$CG_{l,m} = \{i, j : loi_{l,m} \leq i < hii_{l,m}, loj_{l,m} \leq j < hij_{l,m}\}, \quad (3.9)$$

where  $(loi_{l,m}, loj_{l,m})$  and  $(hii_{l,m}, hij_{l,m})$  are the beginning and starting index of a grid block  $m$  at level  $l$ . To facilitate communication and application of boundary condition, a halo of ghost cell of thickness  $ng$  is created around each block. According the grid block,  $G_{l,m}$  is now augmented by ghost cells and is denoted as  $G_{l,m}^\sigma$  with coordinate extents:

$$CG_{l,m}^\sigma = \{i, j : -ng + loi_{l,m} \leq i < hii_{l,m} + ng, -ng + loj_{l,m} \leq j < hij_{l,m} + ng\}, \quad (3.10)$$

The layer ghost layer cells for the entire grid at level  $l$  has the following computational extents:

$$\begin{aligned} CG_{l,m}^{ng} := & \{i, j : -ng \leq i < loi_{l,m}, -ng \leq j < loj_{l,m}\} \\ & \cup \{i, j : hii_{l,m} \leq i < hii_{l,m} + ng, -ng \leq j < loj_{l,m}\}, \\ & \cup \{i, j : -ng \leq i < loi_{l,m}, hij_{l,m} \leq j < hij_{l,m} + ng\}, \\ & \cup \{i, j : hii_{l,m} \leq i < hii_{l,m} + ng, hij_{l,m} \leq j < hij_{l,m} + ng\}. \end{aligned} \quad (3.11)$$

The corresponding halo grid of the grid level  $G_l$  is identified as  $G_l^{ng}$ . The main operations involved in a multi-block structure AMR and their respective nomenclatures are discussed in the following sections.

### 3.2 AMR data operations

Operations involving interpolation, extrapolation and communication of data between various refinement levels of AMR hierarchy is necessary to enable AMR in any flow solver. One of the aspects of block structured AMR is that the data is operated independently at different levels. A reconciliation step is necessary to ensure consistency and integrity of data. The various data operations ensure that the data is represented consistently across the AMR grid hierarchy.

The operation in which the data is filtered from the finer level to the coarser levels is

known as restriction, **R**. And the operation of interpolating from the coarse level to finer levels is known as prolongation or projection, **P**. The restriction of data between any two levels  $l$  and  $l - 1$ , is generally done for all the cells in the interior of the the two levels. This operation between two levels is defined in this thesis as  $\mathcal{R}_l^{l-1}(u; G_l, G_{l-1})$ , where  $u$  is any flow data such as mass, momentum or energy. The restriction operation across the entire grid hierarchy, denoted as **R**( $u$ ), is summarized by the Algorithm 1.

**R**( $u$ ), restriction of data  $u$  across  $\mathcal{G}$  :

```

for  $i \leftarrow NL_{max}$  to 2 do
    Perform  $\mathcal{R}_i^{l-1}(u; G_l, G_{l-1})$ 
end

```

**Algorithm 1:** Restriction of interior data across AMR levels

The prolongation of data between any two levels  $l$  and  $l + 1$ , is generally done to fill the ghost cells of level  $l + 1$  with information from the interior cells of a coarser level,  $l$ . This operation is defined as  $\mathcal{P}_l^{l+1}(u; G_l, G_{l+1}^{ng})$ . And the prolongation operation across the entire grid hierarchy, **P**<sup>ng</sup>( $u$ ) is summarized by the Algorithm 2.

**P**<sup>ng</sup>( $u$ ), prolongation of data  $u$  across  $\mathcal{G}$  :

```

for  $i \leftarrow 1$  to  $NL_{max} - 1$  do
    Perform  $\mathcal{P}_i^{l+1}(u; G_l, G_{l+1}^{ng})$ 
end

```

**Algorithm 2:** Prolongation of ghost cell data across AMR levels

In certain situations, the prolongation operation may be applied to all the cells, both interior and the ghost cells between two levels and accordingly defined as  $\mathcal{P}_l^{l+1}(u; G_l, G_{l+1})$ . The prolongation operation on the entire grid for data  $u$  denoted as **P**( $u$ ) is then given by Algorithm 3.

**P(u), prolongation of data  $u$  across  $\mathcal{G}$  :**

**for**  $i \leftarrow 1$  **to**  $NL_{max} - 1$  **do**  
    Perform  $\mathcal{P}_l^{l+1}(u; G_l, G_{l+1})$

**end**

**Algorithm 3:** Prolongation of interior and ghost cell data across AMR levels

Finally, the data communication operation between ghost cells of various blocks within the same level is denoted as  $\mathcal{C}(u; G_l, G_l^{ng})$  and the communication for the whole grid is summarized in Algorithm 4

**C(u), communication of data  $u$  for  $\mathcal{G}$  :**

**for**  $i \leftarrow 1$  **to**  $NL_{max}$  **do**  
    Perform  $\mathcal{C}_l(u; G_l^\sigma, G_l^{ng})$

**end**

**Algorithm 4:** Communication of data between various blocks across AMR levels

Suppose we consider a problem of the form:

$$\mathcal{H}(u) = 0, \tag{3.12}$$

where  $\mathcal{H}(u)$  can be an ordinary differential equation, the procedure for performing the numerical solution to this problem using AMR is reported in the following algorithm:

**Sequence of steps for solution of  $\mathcal{H}(u)$  in an AMR grid hierarchy,  $G$ :**

**for**  $i \leftarrow 1$  **to**  $NL_{max}$  **do**

**for**  $m \leftarrow 1$  **to**  $M$  **do**

        Solve for  $\mathcal{H}(u)$  on  $G_{i,m}$

**end**

**end**

**Communicate** using  $\mathbf{C}(u)$  to fill information in the interior ghost cells;

**Restrict** using  $\mathbf{R}(u)$  to filter data from finest grid to coarser grids;

**Prolongate** using  $\mathbf{P}^{ng}(u)$  to fill ghost cells at fine/coarse or coarse/fine AMR boundaries

**Algorithm 5:** General procedure for numerical solution to a problem with AMR  
As described in the above Algorithm 5, the first step in the solution to  $\mathcal{H}(u) = 0$  is to solve the numerical discretization of the equation in each of the grid blocks  $G_{l,m}$  across all the levels. The data from a given grid block is then communicated to the ghost cells of the neighboring grid blocks. The communication needs to be done since many of the simulations of problems studied in this thesis are performed on modern parallel computing clusters. A restriction operation is then performed that filters data from the finest AMR grid blocks to underlying coarser grid blocks. Finally, data from regions of coarser grid blocks that are covered by finer grid ghost cells are prolonged initialize valid data at the coarse/fine and fine/coarse interfaces. The sequence of above steps is repeated if a time integration of governing equations needs to be performed on an AMR grid hierarchy.

### 3.3 Implementation of AMR into a multi-block CFD solver

The BoxLib library[31] developed by Lawrence Berkeley National Laboratory (LBNL) is used to perform local adaptive mesh refinement for all the simulations presented in this thesis. The BoxLib library contains all the functionalities for managing the hierarchical AMR grids and has been shown to scale well in parallel computing environment [31]. BoxLib



provides the software framework (building blocks) for building massively parallel block-structured AMR codes for solving time-dependent Partial Differential Equations. The library consists of a hybrid C++/Fortran90 version as well as pure Fortran90 version and is publicly available ([ccse.lbl.gov/BoxLib](http://ccse.lbl.gov/BoxLib)). The BoxLib library contains extensive software support for 1D/2D/3D grid-based and particle-mesh operations on adaptive hierarchical meshes and supports data on cell centers, faces and nodes. Also the software architecture of BoxLib is very similar to that of LESLIE. The version control of the code repository is managed using GIT version control system [115] for both the codes (LESLIE and BoxLib). Similarly, CMake [116] is used for building the libraries and executables associated with the code. For these reasons, the block structured implementation using BoxLib was chosen from among the multiple open source AMR libraries.

Though BoxLib library provides all the functionalities for writing a AMR based CFD solver, often the requirement would be to add the AMR capability to an existing CFD solver code base. This is a non-trivial task as the data layout, code design, and data communication used by the multi-block CFD solver are often very different from those employed by an external library such as BoxLib. In this section, the framework for performing block structured refinement with a multi-block structured CFD code such as LESLIE is discussed.

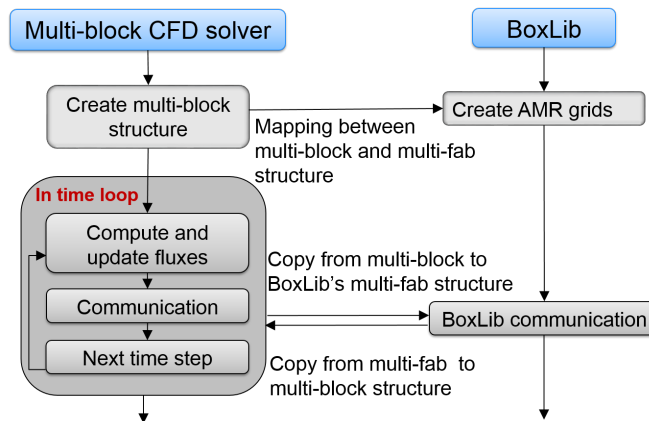


Figure 3.3: Process flow describing implementation of AMR using BoxLib into a multi-block CFD solver

Every time a regridding is performed for dynamic refinement, the mapping between the AMR and the multi-block structure must be reestablished.

### *Mapping between AMR data structure and a multi-block data structure*

One of the most important step of the coupling between a multi-block solver and BoxLib is to establish the mapping between the data layouts of the solver and AMR library. This is briefly discussed in this section. The Fig. 3.4 illustrates how the blocks across the different AMR

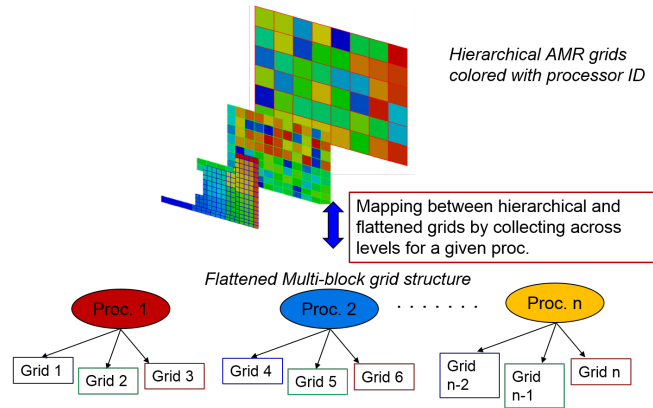


Figure 3.4: Creation of the mapping between the multi-block data structure and BoxLib hierarchical AMR data structure

levels are collected for a given processor and mapped to an equivalent multi-block structure. The hierarchical AMR data layout is flattened to create the multi-block data layout. As is the case for any scientific code, the basic units of the data structures are the multi-dimensional arrays. If the order of dimensions of the application CFD code conforms to the the order of dimensions of the hierarchical data structures, duplication of memory allocation can be avoided. But in cases, such as in the LESLIE code, since the order of the multidimensional arrays is different than the BoxLib order, data is copied every timestep from the multi-block structure to BoxLib structure. This is an overhead that can be avoided if the data layout of multidimensional arrays (mainly the arrays used for holding the conservative quantities) is made the same in LESLIE. Generally, the cost of the memory copy is only a fraction of the overall computational cost, but can become significant under certain conditions (such

as if the number of processors on which the simulations are run is increased). Any data communication and multi-level operations is done on the hierarchical data sets and any CFD solver operations are performed on the multi-block structure. Once the mapping is created, data can be transferred back and forth between the two data sets. If a regridding operation is performed, the mapping between the two data structures must be recreated.

### 3.4 Refinement criteria

Flow sensors are employed to detect physical flow phenomena, based on which grid refinement is performed where appropriate. Grid adaptation along discontinuities is achieved by evaluating gradients multiplied by the local grid size (scaled gradients) in all directions. A cell is flagged for refinement if any of the following conditions are satisfied:

$$\begin{aligned}\nabla\rho\Delta x &> \epsilon_\rho, \\ \nabla p\Delta x &> \epsilon_p, \\ \nabla Y_k\Delta x &> \epsilon_{Y_k},\end{aligned}\tag{3.13}$$

where  $\epsilon_\phi$  is the threshold constant for the scaled gradient of any quantity. This constant is set dynamically for each refinement step as,

$$\epsilon_\phi = f\overline{(\nabla\phi\Delta x)^2},\tag{3.14}$$

with the parameter  $f$  set to 0.75 using numerical experiments. The species mass fraction based refinement criteria is used only for reacting cases. By default, only the pressure based and density based refinement criteria is employed. Additional criteria can also be easily added. Similar criteria has been used in the past [28] for performing refinement for compressible reacting flows.

Table 3.1: Summary of AMR test cases and their motivation.

Case	Reacting/Non-reacting	Motivation
1D shock tube problem	Non-reacting	Is a basic test case for a numerical method
2D Riemann problem	Non-reacting	Validation for 2D
2D/3D Sedov blast problem	Non-reacting	Validation of AMR for strong propagating shocks
3D Blast studies	Non-reacting	Validation for NM and TNT charge detonation
2D Detonation propagation	Reacting	Validation for a reacting problem

### 3.5 Validation of AMR for non-reacting/reacting problems

The block structured AMR implementation into LESLIE multi-block solver is validated through several test problems listed in Table 3.1. The purpose of each of the test case is also summarized in the table.

#### 3.5.1 1D shock tube studies

Two shock tube problems are considered. The first test is a variation of the Sod Riemann problem. The initial interface forms a right-moving shock, a left-moving rarefaction fan, and an intermediate contact discontinuity. Specifically, the rarefaction fan contains as sonic point, a physical feature that some linearized solvers can not resolve correctly. The initial discontinuity is formed by the following left and right states:

$$q_L = \begin{bmatrix} \rho_L \\ u_L \\ v_L \\ w_L \\ p_L \end{bmatrix} = \begin{bmatrix} 1.0 \\ 0.75 \\ 0.0 \\ 0.0 \\ 1.0 \end{bmatrix}, \quad q_R = \begin{bmatrix} \rho_R \\ u_R \\ v_R \\ w_R \\ p_R \end{bmatrix} = \begin{bmatrix} 0.125 \\ 0.0 \\ 0.0 \\ 0.0 \\ 0.1 \end{bmatrix} \quad (3.15)$$

The one-dimensional domain,  $0.0 < x < 1.0$ , is discretized by 100 computational points with the flow discontinuity located at  $x = 0.3$  m. A simple extrapolation boundary condition is imposed at the ends of the shocktube. The results are compared to an exact solution of the Riemann problem at a final time of 0.2 seconds.

For the second test, the initial interface forms a right-moving shock, a left-moving rarefaction fan, and an intermediate contact discontinuity, which is stationary during the simulation. The initial discontinuity is formed by the following left and right states:

$$q_L = \begin{bmatrix} \rho_L \\ u_L \\ v_L \\ w_L \\ p_L \end{bmatrix} = \begin{bmatrix} 1.0 \\ -19.59745 \\ 0.0 \\ 0.0 \\ 1000.0 \end{bmatrix}, \quad q_R = \begin{bmatrix} \rho_R \\ u_R \\ v_R \\ w_R \\ p_R \end{bmatrix} = \begin{bmatrix} 1.0 \\ -19.59745 \\ 0.0 \\ 0.0 \\ 0.01 \end{bmatrix} \quad (3.16)$$

The initial the flow discontinuity is located at  $x = 0.8$  m. The adiabatic index is 1.4. The left-boundary is a supersonic outflow boundary and the right is a supersonic inflow boundary. The results are compared to an exact solution of the Riemann problem at a final time of 0.012 seconds. Both the cases were run with a base grid resolution of (100 X 100) cells with three AMR levels. As observed in Figs 3.5 and 3.6, there is an excellent agreement between the simulation results and the exact solution.

### 3.5.2 2D Riemann problem

The 2D Riemann problem consists of solving four initially discontinuous flow states in a (1 x 1) unit computational domain. The four quadrants of the domain are initially assigned different flow and thermodynamic states. Depending upon the type of the initial data, different geometric flow patterns formed by shocks, rarefactions, slip lines, and contacts, can be observed with the evolution of the solution. The initial data for the Riemann problem is set

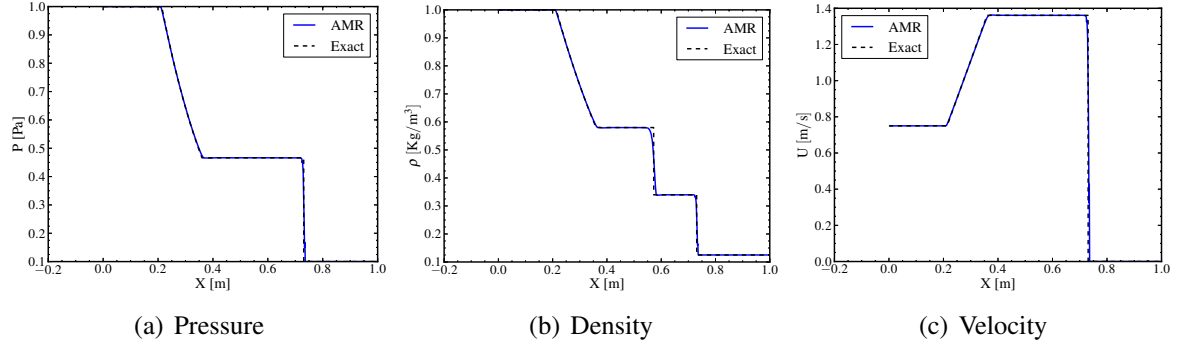


Figure 3.5: Profiles for shock testtube configuration 1.

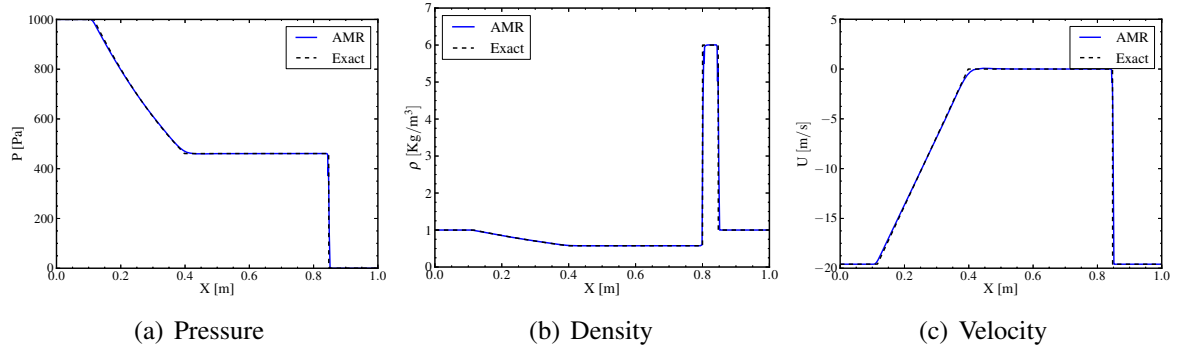


Figure 3.6: Profiles for shock testtube configuration 2.

as follows:

$$(p, \rho, u, v)(x, y, 0) = \begin{pmatrix} (p1, \rho1, u1, v1), x > 0.5, y > 0.5 \\ (p2, \rho2, u2, v2), x < 0.5, y > 0.5 \\ (p3, \rho3, u3, v3), x < 0.5, y < 0.5 \\ (p4, \rho4, u4, v4), x > 0.5, y < 0.5 \end{pmatrix} \quad (3.17)$$

There are several configurations with different set of values for the four sections of the domain. Here, one of the configurations with the following initial data is simulated:

$$p1 = 1, \rho1 = 2, u1 = -0.75, v1 = -0.5$$

$$p2 = 1, \rho2 = 2, u2 = -0.75, v2 = 0.5$$

$$p3 = 1, \rho3 = 1, u3 = 0.75, v3 = 0.5$$

$$p4 = 1, \rho4 = 3, u4 = 0.75, v4 = -0.5$$

A base grid resolution of (100 x 100) cells with three AMR levels is employed such that the effective resolution is (400 x 400) cells. The results are compared with that of a uniform mesh with the same effective resolution as the finest AMR level.

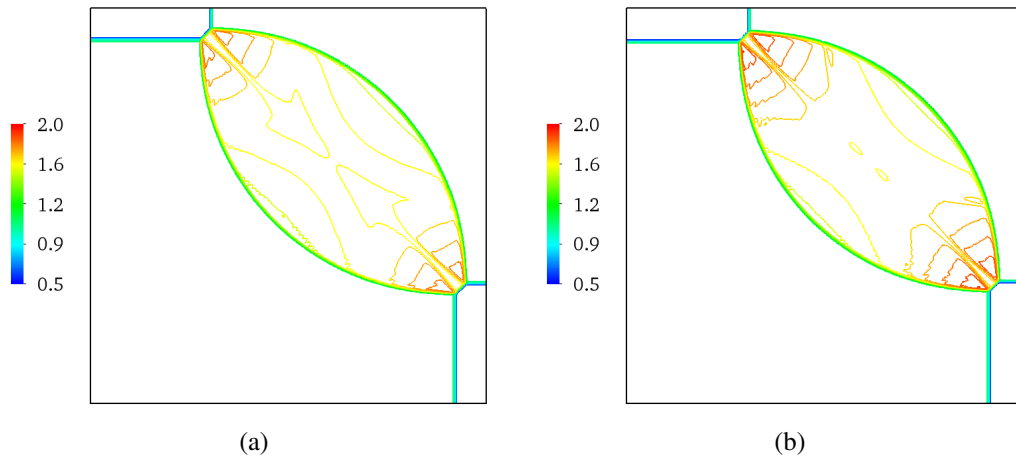


Figure 3.7: Comparison of density contours between (a) AMR and (b) uniform mesh at  $t = 0.25$ .

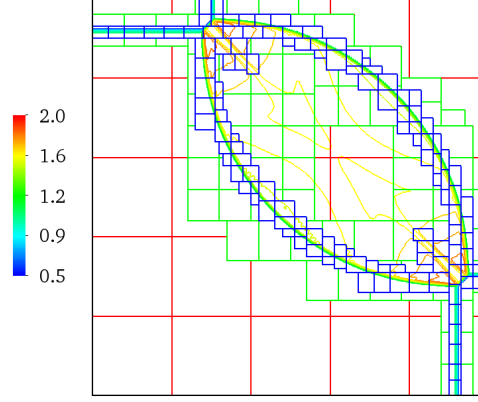


Figure 3.8: Snapshot of the block structure refinement at  $t = 0.25$ . Red - coarsest level, green - finer level, blue - finest level.

Since exact solutions are not available for the 2D Riemann problems, the result of the simulation with AMR is compared with that from using a uniform fine mesh. The density contours at  $t = 0.25$  units for both the cases are compared in Fig. 3.7 and a good agreement in the results can be observed. The refinement of the density gradients by the three AMR levels can be seen in Fig. 3.8.

### 3.5.3 Sedov blast studies

In this problem, a high-pressure blob is allowed to expand in an open domain. The objective of this test is to validate AMR for a 2D and 3D blast problem. Sedov, in a seminal work [117], demonstrated that the blast solution becomes self-similar sufficiently far away from the center of a strong blast. He quantified the blast evolution and showed that the radius of the outwards-going blast front follows  $R(t) \propto t^2/(n+2)$ , where  $n = 1$  for a planar explosion,  $n = 2$  for a cylindrical one, and  $n = 3$  for a spherical explosion.

Simulations are conducted using a uniform fine mesh and an AMR mesh with three levels such that both have the same effective grid resolution of  $dx = 5 \times 10^{-4}$  units. The computational domain is of  $(0.512 \times 0.512)$  units with initial blast located in the center of the domain. For 3D simulations, only a quadrant of the full domain is simulated taking advantage of the symmetry of the solution. Symmetry condition is imposed on the lower  $x$ ,



y and z planes and supersonic outflow condition is prescribed on the other boundaries.

The evolution of the pressure field for the 2D Sedov problem is shown in Fig. 3.9 and it can be seen that the blast remains circular at all times mainly because the blast front is well resolved by local refinement. The radially averaged pressure field for the 2D Sedov problem with AMR is compared with that of the uniform fine mesh case in Fig. 3.10(b). Although there are some differences in the results especially near the smaller pressure peak early in the simulation, the results agree very later when the two pressure peaks merge. The scaling of the blast radius with time follows a  $2/4^{th}$  in 2D and  $2/5^{th}$  in 3D as seen in Fig. 3.10(a) and Fig. 3.11.

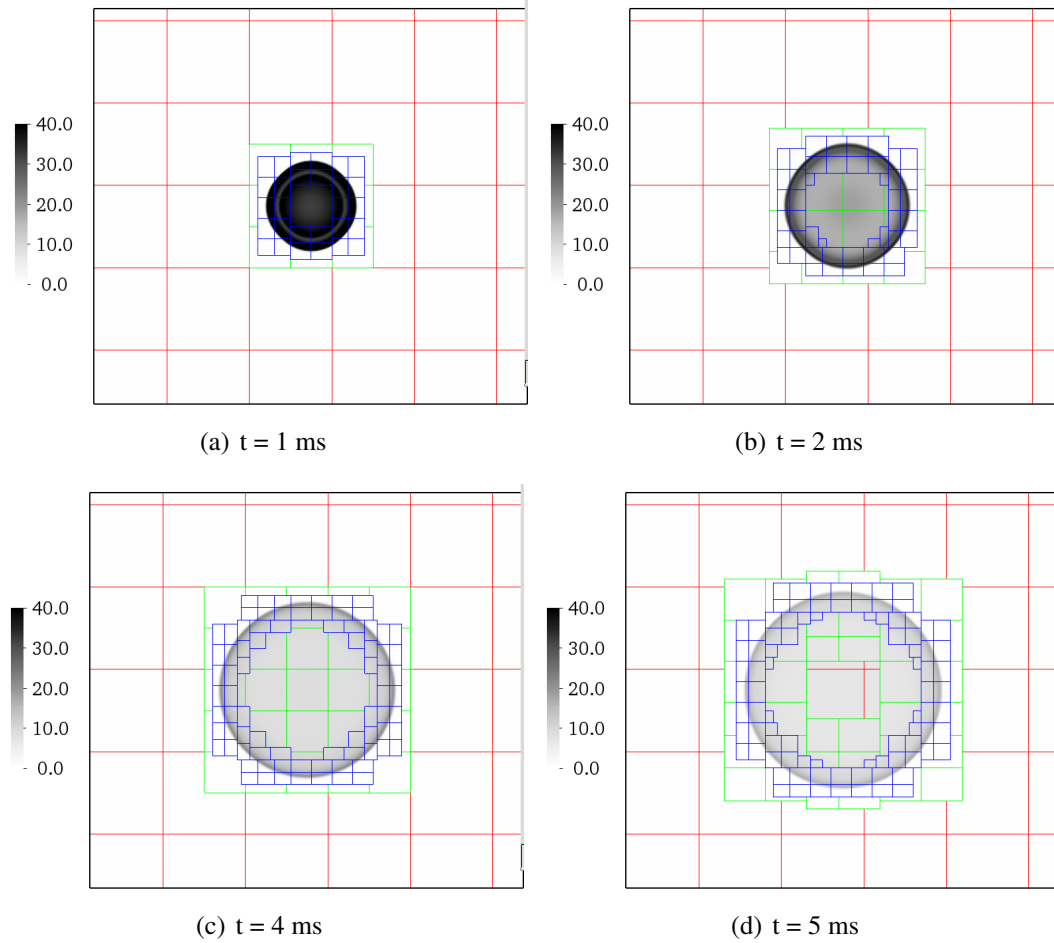


Figure 3.9: Pressure contours at various time instants for the 2D sedov test case

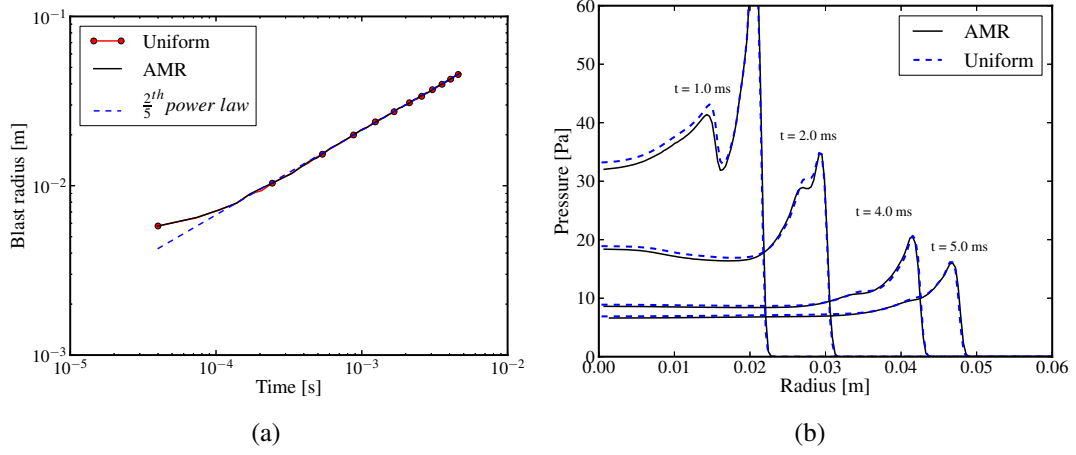


Figure 3.10: Comparison of the blast characteristics (a) blast radius and (b) radially averaged pressure profile between AMR and uniform mesh for 2D Sedov problem.

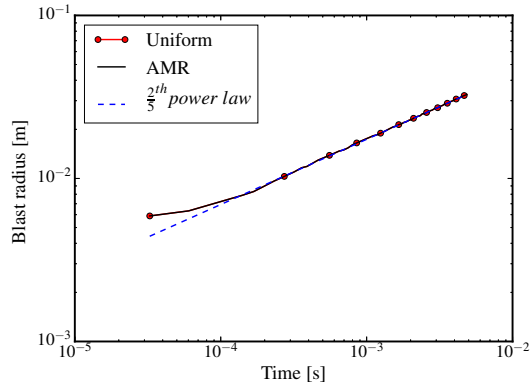


Figure 3.11: Comparison of the blast radius evolution between AMR and uniform mesh for 3D Sedov problem.

### 3.5.4 2D detonation propagation

High resolution 2D simulation of a detonation propagating in a channel is performed for stoichiometric ethylene/oxygen gaseous mixture diluted with argon. A single step chemistry with Arrhenius kinetics of the form

$$\dot{\omega} = -A\rho Y \exp -\frac{E_a}{RT} \quad (3.18)$$

is employed to model the reaction occurring at the detonation front. The parameters  $A$  and  $E_a$ , which are the pre-exponential factor and activation energy respectively, are chosen from past studies [118] for the same mixture.

Computations are performed on a  $(0.018 \times 0.006) \text{ m}^2$  2D domain with three AMR levels and a base resolution of  $(216 \times 72)$ . The channel width is chosen to capture a single regular detonation cell. Inflow and outflow conditions are set in the  $x$ -direction and periodic boundary condition is used in the transverse direction.

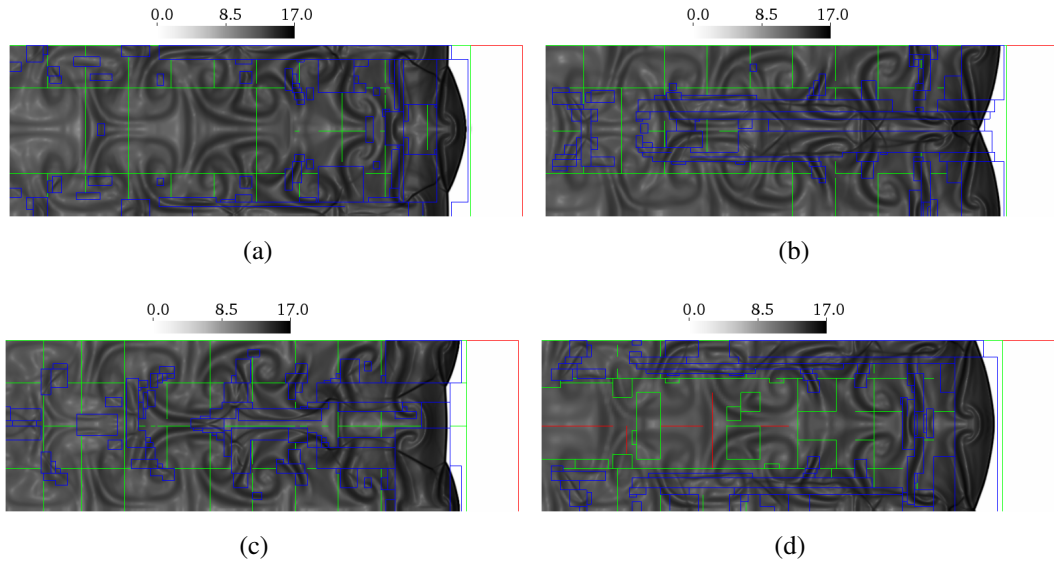


Figure 3.12: Instantaneous snapshot of the detonation front at various stages of the triple point motion along the leading shock front.

Past studies have reported that the leading shock at the detonation front is wrinkled and

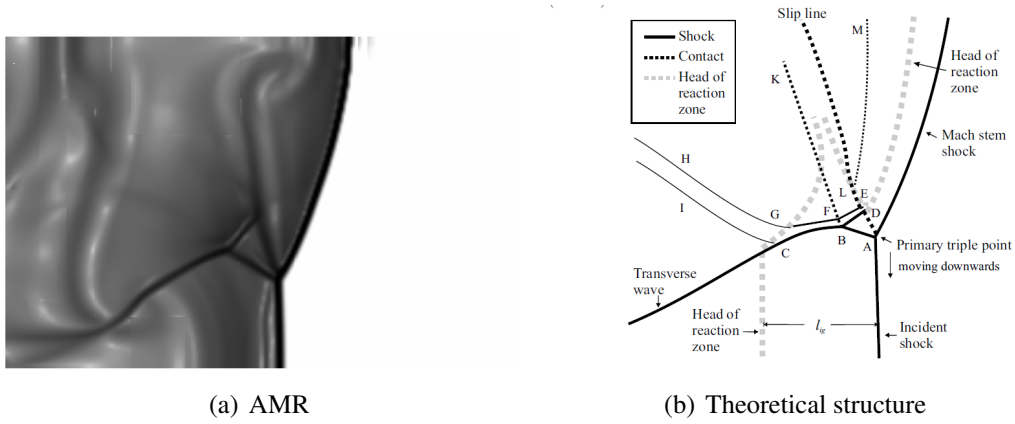


Figure 3.13: Comparison of the triple point structure with theory.

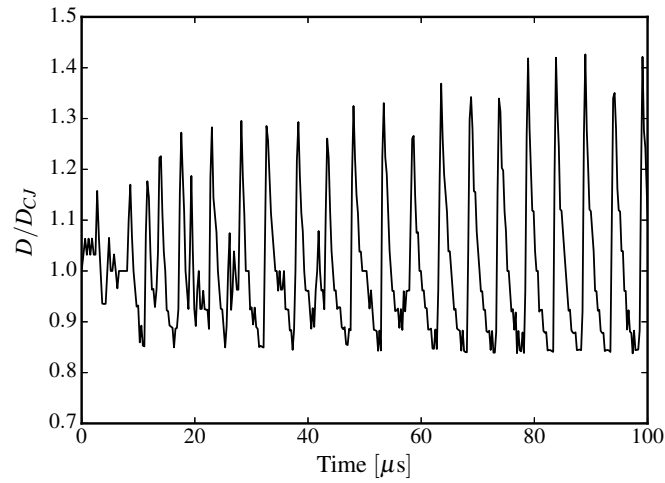


Figure 3.14: Regular oscillation of the detonation velocity,  $D$  tracked using temporal history of triple point.

comprises of alternate strong Mach stems and weak incident shocks. Triple points formed at the junctions of the transverse waves and leading shock front propagates along the detonation front as it moves forward. Sufficient mesh resolution is required to resolve the transverse waves structures that generates this characteristic cellular pattern. Without the use of AMR, a high mesh resolution would be required for the entire domain to resolve a highly localized flow feature such as detonation front. Dynamic AMR can be effectively used for such cases to accurately resolve all the relevant flow characteristics.

The simulations are performed in a frame attached to the moving detonation front. After an initial period, solutions exhibit regular oscillatory cellular behavior. Shown in Fig. 3.12 are snapshots of the front at various time instants. The comparison of the triple point structure from with the theoretical structure is shown in Fig. 3.13. A remarkable resolution of the various features such as the leading Mach stem, incident shock, transverse wave and slip line is achieved by the simulations and matches their description from the theoretical structure. The regular oscillation of the detonation front velocity with time is shown in Fig. 3.14. After some initial transience, the detonation velocity on an average matches with that given by the Chapman-Jouget [119] conditions.

### 3.5.5 3D blast studies

In this 3D test problem, blast wave propagation corresponding to an initial charge of 11.8 cm diameter of TNT and Nitro Methane is tracked with AMR. The grid resolution and initial detonation profile is used from a previous study [120]. Taking advantage of the symmetry of the problem, the simulation is performed for a quadrant of the complex 3D domain. The domain is a cubic box of size  $4\text{m} \times 4\text{m} \times 4\text{m}$  with a base grid resolution of (250 X 250 X 250) and 4 levels of AMR are employed resulting in an effective resolution of 2mm.

Figure 3.15 presents the logarithm of density field at various time instants. The evolution of the primary blast, the formation of the secondary shock and its subsequent reflection can be clearly observed from the results. The ensuing hydrodynamic instability can also be noted

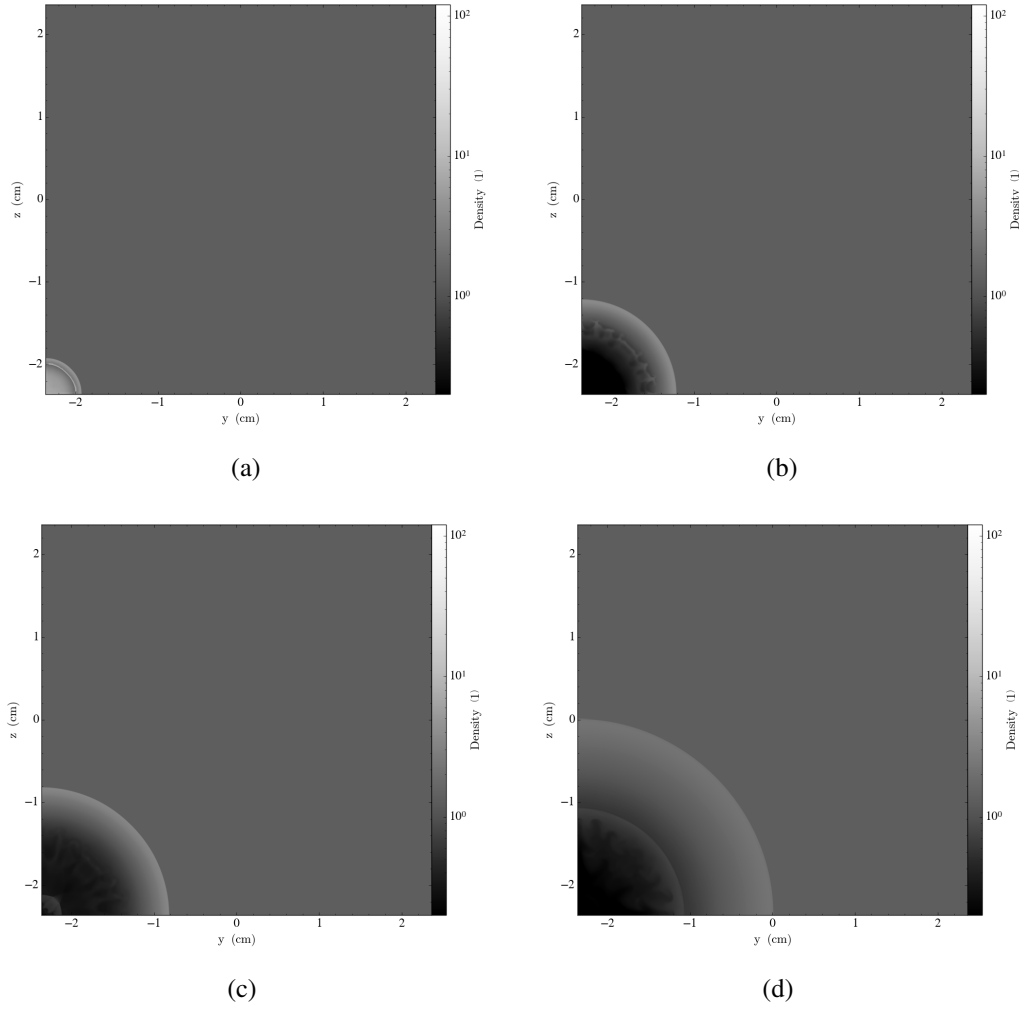


Figure 3.15: Instantaneous snapshots of  $\log(\rho)$  at the x-y plane for 3D NitroMethane blast.

in the later stages of the blast evolution. More quantitative analysis of the blast characteristics is studied by comparing the blast radius evolution and the overpressure with previous studies in Fig. 3.16 for both the explosives. There is an excellent match of the primary blast evolution and overpressure with past data. However, the current simulations predict stronger secondary shock which propagates faster. This might be because, the origin is exactly represented in the current approach. Whereas in the previous study [120] employed a sector grid in which the origin is a singularity and can not be resolved. As discussed in [120], a small cut-off radius equal to one cell width is introduced. The differences in the treatment of the origin could be resulting in differences in the dynamics of the secondary shock. A snapshot of the AMR levels for the NM blast problem is shown in Fig. 3.17. The refinement near both the primary and the secondary blast front can be clearly seen.

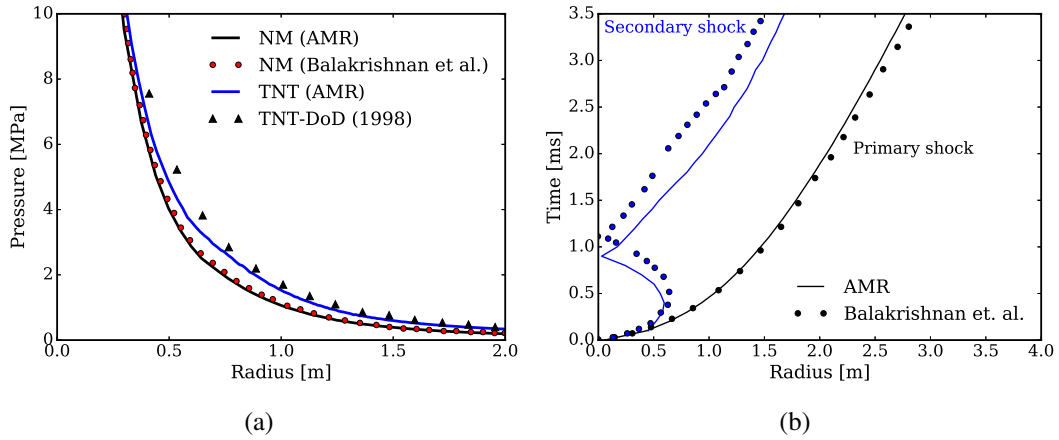


Figure 3.16: Comparison of (a) blast overpressure for TNT and NitroMethane charges and (b) blast radius evolution for a NitroMethane charge with past studies.

### 3.6 Performance of block structured AMR implementation

One of the main goals of employing AMR is computational cost reduction. This is achieved by reduction of the total number of grid points required for the simulation through local refinement. As mentioned before, this can result in an order of magnitude savings in terms of computational costs and also the storage space required for the results of the simulation. The

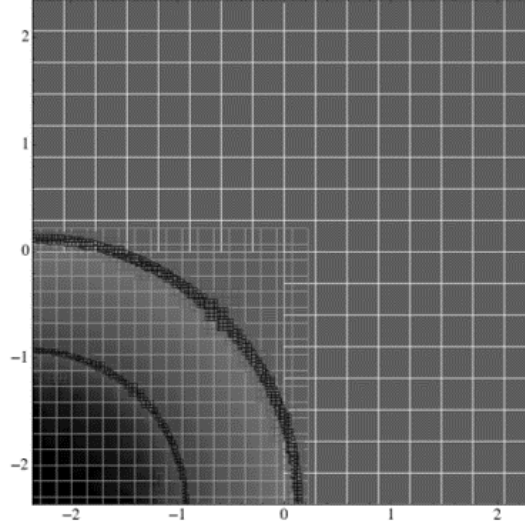


Figure 3.17: Snapshot of the AMR levels for the free blast of Nitro Methane.

computational gains of using AMR is demonstrated by comparing the above metrics with that obtained from using a uniform fine mesh with the same effective resolution as AMR, for the 3D Sedov blast problem. The cost and space comparisons are reported in Fig. 3.18 for two different grid resolutions. All the computations were performed on 64 cores of a Linux cluster with Intel(R) Xeon(R) CPU E5-2670 @ 2.6GHz and 32 GB of RAM. The data for the uniform case for  $512^3$  is projected from the timing results for the  $256^3$  case as the problem was too big to be run on 64 processors.

As seen in Fig. 3.18, there is an order of magnitude gain in employing AMR and the space required for storing a single restart checkpoint simulation file also comes down significantly with AMR. The gains are much higher for the  $512^3$  case in comparison to the  $256^3$  case. It must be noted that these comparisons are specific to this case and there might be other cases where the benefits of using AMR may not be this high. To further understand the computational performance of AMR, the cost distribution of different solver operations are reported in Fig. 3.19. The majority of time spent by the solver is from the flux evaluation. The communication overhead which includes the copying of data from the multi-block structure to the BoxLib data structure is around five %. The other significant solver step that



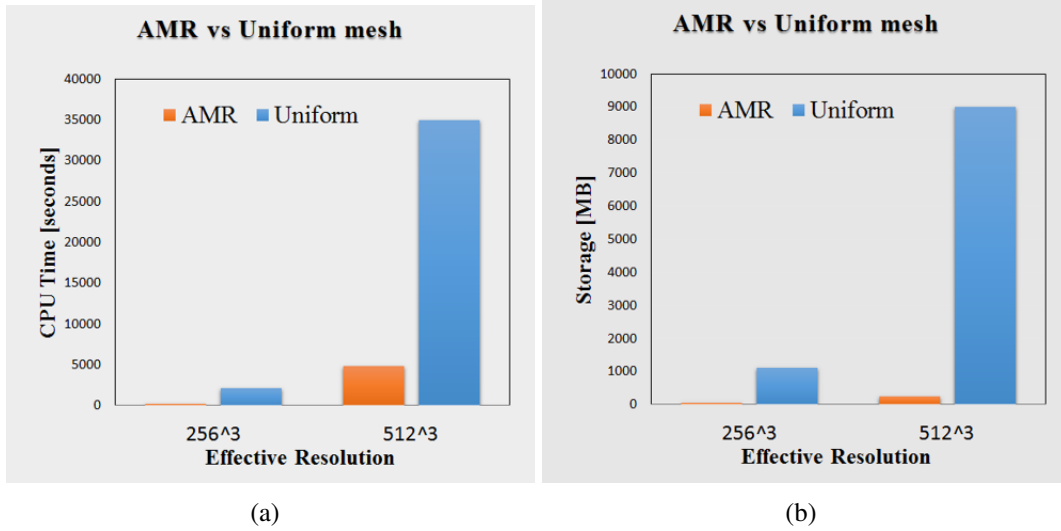


Figure 3.18: Comparison of (a) computational cost and (b) storage space required for the 3D Sedov problem.

takes around 22 % of the computational time is the regridding step. The regridding, as seen from the results, is a computationally costly step and therefore care must be taken to perform the dynamic regridding only when required.

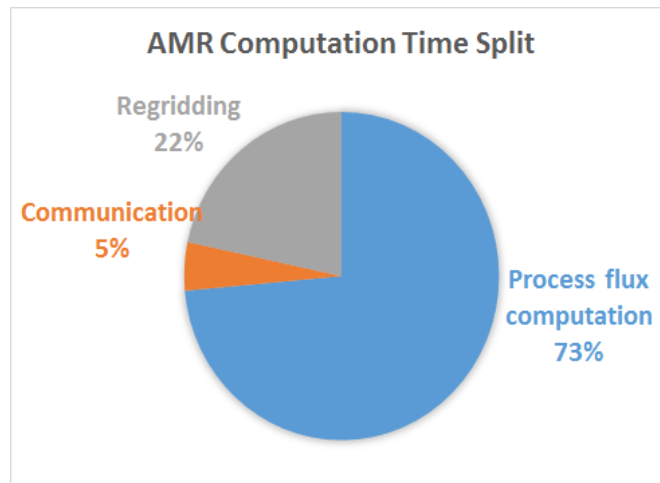


Figure 3.19: Time taken by various solver steps for the 3D Sedov problem for the  $256^3$  case.

## CHAPTER 4

### CARTESIAN BASED CUT-CELL EMBEDDED BOUNDARY METHOD

A Cartesian based strictly conservative cut-cell method is developed in this thesis to resolve solid embedded boundaries. The details of the formulation of the high-order (up to 4th order) cut-cell method for stationary boundaries and a second order cut-cell method for moving boundaries are described in this chapter. Extensive validation of the approach is performed, and accuracy of the method is demonstrated through several 1D, 2D, and 3D test problems. The formulation and results for the stationary cut-cell approach described here are from a published work by the thesis author [26] and are repeated here with appropriate permissions.

#### 4.1 Formulation and implementation of cut-cell method

Cut-cell method [94, 14] is used in this work to represent embedded boundaries on a Cartesian grid. Information for defining the cut-cells at the embedded boundary is extracted from a levelset field description. Levelset, as defined by Osher and Sethian [121, 122], is a continuous scalar field having values  $\phi > 0$  in the fluid region,  $\phi < 0$  in the solid region and  $\phi = 0$  at the interface. Once the levelset field is described completely, all the cut-cell metrics can be computed.

To create a cut-cell, the levelset field is assumed to be piecewise linear in a cell and is given as:

$$\begin{aligned}\phi(x, y, z) &= \sum_{p1=0}^1 \sum_{p2=0}^1 \sum_{p3=0}^1 x^{p1} y^{p2} z^{p3} a_{p1,p2,p3}, \\ (p1 + p2 + p3) &\leq 1\end{aligned}\tag{4.1}$$

in which the coefficients,  $a_{p1,p2,p3}$ , are determined based on the nodal values,  $\phi_i$ ,  $i = 1, 8$  for a given computational cell. The embedded boundary surface is defined by the function

$\phi(x, y, z) = 0$ . The boundary equation along with the linear system of equations representing the cut-cell edges are solved simultaneously to provide the points of intersection of the boundary with the edges. The process of finding the cut surface is illustrated in Fig. 4.1(a). As shown, the embedded surface is approximated by a planar cut in a given computation cell  $(i, j, k)$ .

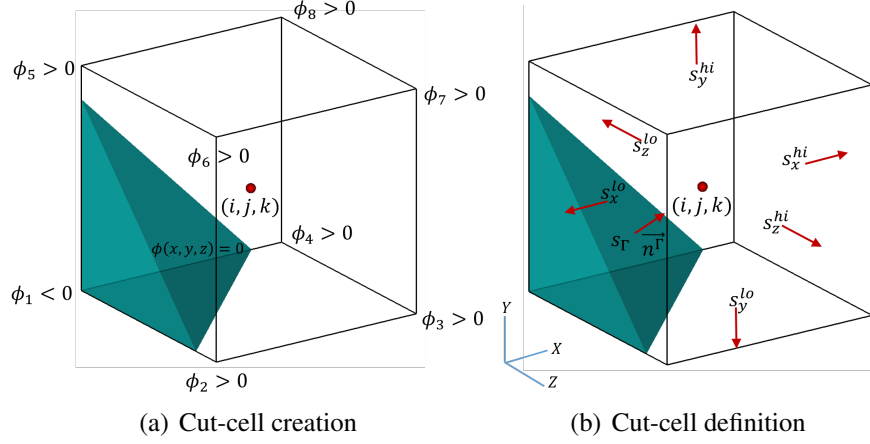


Figure 4.1: Schematic of a three dimensional cut-cell: (a) creation from levelset description  $\phi$  with cut-surface described by  $\phi(x, y, z) = 0$ . (b) Various geometric variables for defining a cut-cell to represent an embedded boundary.

Once the intersection points are determined, the available face area in each of the coordinate directions  $(x, y, z)$ :  $s_x^{hi}$ ,  $s_x^{lo}$ ,  $s_y^{hi}$ ,  $s_y^{lo}$ ,  $s_z^{hi}$  and  $s_z^{lo}$ , as shown in Fig. 4.1(b), are determined using fifth-order accurate Gauss-Legendre quadrature rules. Here, the suffices *lo* and *hi* denote the positive and negative direction along a coordinate direction, respectively. Using the computed cut areas, the cut surface area of the embedded boundary,  $s_\Gamma$  and the cell normal vector,  $n_\Gamma$  are obtained following the procedure detailed in [14] and are given as:

$$s_\Gamma = \sqrt{(s_x^{hi} - s_x^{lo})^2 + (s_y^{hi} - s_y^{lo})^2 + (s_z^{hi} - s_z^{lo})^2}, \quad (4.2)$$

$$n_{\Gamma,x} = \frac{1}{s_\Gamma}(s_x^{hi} - s_x^{lo}), \quad (4.3)$$

$$n_{\Gamma,y} = \frac{1}{s_\Gamma}(s_y^{hi} - s_y^{lo}), \quad (4.4)$$

$$n_{\Gamma,z} = \frac{1}{s_\Gamma}(s_z^{hi} - s_z^{lo}). \quad (4.5)$$

As the cut-cells have a reduced volume, the cell centroid for the cut-cells  $(x_c, y_c, z_c)$  is adjusted to its new position  $(\hat{x}_c, \hat{y}_c, \hat{z}_c)$  according to:

$$\hat{x}_c = \frac{1}{V} \int x dv, \quad \hat{y}_c = \frac{1}{V} \int y dv, \quad \hat{z}_c = \frac{1}{V} \int z dv, \quad (4.6)$$

where  $V$  is the cut-cell volume of cell  $(i, j, k)$  and can be evaluated by using Gauss divergence theorem [94].

#### 4.1.1 Higher order $k$ -exact least squares reconstruction

The main idea behind achieving a higher order accuracy at the embedded boundaries is use of a piece-wise high order polynomial approximation of cell centered flow quantities as proposed by Ivan and Groth [114]. Accordingly, the following reconstruction polynomial of order  $k$  for any conservative or primitive flow quantity  $u$  in a given cell  $i$  is defined as follows:

$$u_i^k(x, y, z) = \sum_{p_1=0}^k \sum_{p_2=0}^k \sum_{p_3=0}^k (x - x_{c,i})^{p_1} (y - y_{c,i})^{p_2} (z - z_{c,i})^{p_3} D_{p_1,p_2,p_3}^k, \quad (4.7)$$

$$p_1 + p_2 + p_3 \leq k$$

where  $(x_{c,i}, y_{c,i}, z_{c,i})$  are the cell center coordinates and  $D_{p_1,p_2,p_3}^k$  are coefficients of  $k^{th}$  order approximation of  $u$ , which can be proved to be scalar multiples of derivatives of  $u$  using Taylor series expansion. Once these coefficients are determined, the above polynomial approximation in Eq. (4.7) can be employed to reconstruct, anywhere within the cell  $i$ , the quantity  $u$  and its  $p^{th}$  derivative with the order of accuracy  $(k + 1)$  and  $(k - p + 1)$ , respectively. Using the volume averaged values of the current cell  $\overline{u}_i$ ,

$$\overline{u}_i = \frac{1}{V} \int_v \sum_{p_1=0}^k \sum_{p_2=0}^k \sum_{p_3=0}^k (x - x_{c,i})^{p_1} (y - y_{c,i})^{p_2} (z - z_{c,i})^{p_3} D_{p_1,p_2,p_3}^k dv, \quad (4.8)$$

and the neighboring cell  $\overline{u}_j$ , the coefficients  $D_{p_1, p_2, p_3}^k$  can be found by solving a system of linear equations defined as follows:

$$\begin{aligned} \overline{u}_j - \overline{u}_i &= \sum_{p_1=0}^k \sum_{p_2=0}^k \sum_{p_3=0}^k (\widehat{x^{p_1} y^{p_2} z^{p_3}})_{ij} D_{p_1, p_2, p_3}^k \mid j = 1..n_p, \\ p_1 + p_2 + p_3 &\leq k \end{aligned} \quad (4.9)$$

where  $n_p$  represents the number of neighbors that are required to solve the  $i^{th}$  cell centered quantity and depends on the order of reconstruction. In Eq. (4.9),  $\widehat{x^{p_1} y^{p_2} z^{p_3}}$  is the geometric moment of  $j^{th}$  cell about  $i^{th}$  cell center given by:

$$(\widehat{x^{p_1} y^{p_2} z^{p_3}})_{ij} = \int_{v_j} (x - x_{c,i})^{p_1} (y - y_{c,i})^{p_2} (z - z_{c,i})^{p_3} dv. \quad (4.10)$$

For a given order of reconstruction  $k$ , the number of unknowns  $N$  that are solved in the above system of equations Eq. (4.9), for example in 3D is given by:

$$N = \frac{1}{6}(k+1)(k+2)(k+3) - 1. \quad (4.11)$$

In the current work, as suggested by Ivan and Groth [114], additional neighbors are included to make the reconstruction more robust in the presence of cut-cells. Accordingly, the central stencil for reconstruction uses 8 nearest neighbors in 2D and 27 nearest neighbors in 3D for  $k=2$ . For  $k=3$ , 24 nearest neighbors in 2D and 124 nearest neighbors in 3D are used for reconstruction. The number of neighbors needed for  $k > 3$  will depend on the number of unknowns as given by Eq. (4.11). For example, for  $k = 4$ , the number of unknowns in 3D would be 34 which implies that a stencil width spanning 124 nearest neighbors is sufficient for the linear least square reconstruction. The stencil width in case of 2D cut-cell geometry is illustrated through a schematic in Fig. 4.2. For achieving  $k$ -th order accuracy,  $k + 1$  ghost cells are added to the block boundaries. This is due to the stencil width required for the least-squares reconstruction as described in Fig. 2. For  $k$ -th order accurate scheme,  $k - 1$

ghost cells are required for the reconstruction. Two additional cells are added for building the cut-cells at the boundary.

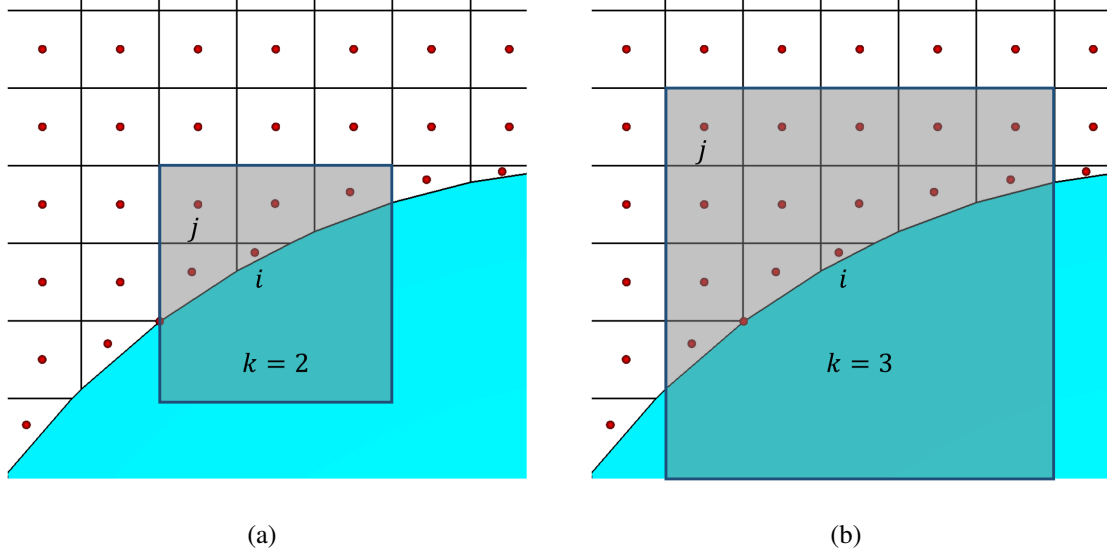


Figure 4.2: Illustration of the  $k$ -exact reconstruction stencil used for (a)  $k=2$  and (b)  $k=3$ . Stencil highlighted by the gray shaded region. Subscript  $i$  denotes the cell for which  $k$ -exact reconstruction is done and  $j$  is one of the neighbor cells.

As  $n_p \geq N$  in general, Eq. (4.9) is often an over determined system of linear equations to ensure stability of the solution to the system of linear equations. The Eqs. (4.9)-(4.10) need to be computed for each neighbor cell  $j$  and this evaluation is computationally very intensive. Hence, a strategy to compute the geometric moments that was originally developed by Gooch and Alten [123] is employed whereby differences  $(x - x_{c,i})$ ,  $(y - y_{c,i})$  and  $(z - z_{c,i})$  are replaced with  $(x - x_{c,j}) + (x_{c,j} - x_{c,i})$ ,  $(y - y_{c,j}) + (y_{c,j} - y_{c,i})$  and  $(z - z_{c,j}) + (z_{c,j} - z_{c,i})$ , respectively. This modification expresses the geometric moments of  $j^{th}$  cell about  $i^{th}$  cell center as in Eq. (4.10) as a function of the geometric moment about  $j^{th}$  (its own) cell center. The integral in Eq. (4.10) can, therefore be approximated by the following binomial expansion:

$$(\widehat{x^{p_1} y^{p_2} z^{p_3}})_{ij} = \sum_{l=0}^{p_1} \sum_{r=0}^{p_2} \sum_{t=0}^{p_3} \binom{p_1}{l} \binom{p_2}{r} \binom{p_3}{t} \Delta x_{ij}^l \Delta y_{ij}^r \Delta z_{ij}^t (\overline{x^{p_1-l} y^{p_2-r} z^{p_3-t}})_j, \quad (4.12)$$

where  $\Delta x_{ij} = (x_{c,i} - x_{c,j})$ ,  $\Delta y_{ij} = (y_{c,i} - y_{c,j})$ ,  $\Delta z_{ij} = (z_{c,i} - z_{c,j})$  and  $(\overline{x^{p_1-l} y^{p_2-r} z^{p_3-t}})_j$  is a geometric moment of cell  $j$  about its own cell center.

The overdetermined linear system of equations given by Eq. (4.9) can be written as:

$$\mathbf{A}\mathbf{x}=\mathbf{b}=\mathbf{e}, \quad (4.13)$$

where the coefficient matrix  $\mathbf{A}$  depends only on the mesh,  $\mathbf{b}$  contains the volume averaged solution values in each cell and  $\mathbf{x}$  is the vectors of coefficients  $D_{p_1,p_2,p_3}^k$  needed for the  $k$ -exact reconstruction. The vector,  $\mathbf{e}$  represents the residual error that must be minimized. The overdetermined system of Eq. (4.13) is solved in the current study using a least-squares approach. Each row of Eq. (4.13) is multiplied with a geometric weight that is the inverse of the distance between the current cell  $i$  and each of the neighbor cell  $j$  (Refer Fig. 4.2 for more details) to improve the accuracy of the reconstruction. The weighted least-squares problem of Eq (4.13) is solved using Singular Value Decomposition (SVD) [124] by which the pseudo-inverse matrix,  $A^\dagger$  can be found. The solution to the least-squares problem is then given by  $\mathbf{x} = A^\dagger \mathbf{b}$  [125]. The pseudo-inverse matrix  $A^\dagger$ , like  $\mathbf{A}$ , depends only on the mesh and therefore is precomputed and stored in a pre-processing step.

#### 4.1.2 Boundary conditions at embedded surfaces

Boundary conditions are enforced by introducing constraint equations into the system of linear equations, Eq. (4.9). Velocity fields are prescribed with Dirichlet boundary condition and remaining flow variables, i.e., pressure, density, and temperature are prescribed with Neumann condition. For a Dirichlet condition, the following system of equations are added:

$$u(x_l, y_l, z_l)_j - \bar{u}_i = \sum_{p_1=0}^k \sum_{p_2=0}^k \sum_{p_3=0}^k ((x_l - x_{c,i})^{p_1} (y_l - y_{c,i})^{p_2} (z_l - z_{c,i})^{p_3} - (\overline{x^{p_1} y^{p_2} z^{p_3}})_i) D_{p_1,p_2,p_3}. \quad (4.14)$$

Here,  $(x_l, y_l, z_l)_j$  are coordinates of the Gauss quadrature points on cut-cell face of  $j^{th}$  cell. To specify Neumann condition for variables such as pressure, density and temperature, a Neumann boundary constraint are of the following form:

$$\begin{aligned} \nabla u_n(x_l, y_l, z_l)_j = & \sum_{p_1=0}^k \sum_{p_2=0}^k \sum_{p_3=0}^k (p_1(x_l - x_{c,i})^{p_1-1} (y_l - y_{c,i})^{p_2} (z_l - z_{c,i})^{p_3} n_{\Gamma,x} \\ & + p_2(x_l - x_{c,i})^{p_1} (y_l - y_{c,i})^{p_2-1} (z_l - z_{c,i})^{p_3} n_{\Gamma,y} \\ & + p_3(x_l - x_{c,i})^{p_1} (y_l - y_{c,i})^{p_2} (z_l - z_{c,i})^{p_3-1} n_{\Gamma,z}) D_{p_1,p_2,p_3}, \end{aligned} \quad (4.15)$$

with,

$$\begin{aligned} \nabla u_n(x_l, y_l, z_l)_j = & (\nabla u_x(x_l, y_l, z_l) n_{\Gamma,x} + \\ & \nabla u_y(x_l, y_l, z_l) n_{\Gamma,y} + \nabla u_z(x_l, y_l, z_l) n_{\Gamma,z})_j, \end{aligned} \quad (4.16)$$

where  $n_{\Gamma,x}$ ,  $n_{\Gamma,y}$  and  $n_{\Gamma,z}$  are the boundary normals in  $x$ ,  $y$  and  $z$  direction, respectively as shown in Fig. 4.1(b). The boundary constraint equations (Eqs. (4.14) and (4.15)) are added to the system of linear equations (Eq. (4.9)) and solved using linear least squares method.

### 4.1.3 Flux computation near embedded surfaces

#### *Inviscid flux evaluation at cut faces*

The evaluation of the inviscid flux at cut faces is based on the formulation of Ingram *et. al.* [126]. The pressure  $p_n$  at a boundary quadrature point  $(x_l, y_l, z_l)$  for  $j^{th}$  cell is evaluated using the higher order polynomial expression as follows.

$$p_n(x_l, y_l, z_l) = \sum_{p_1=0}^k \sum_{p_2=0}^k \sum_{p_3=0}^k (x_l - x_{c,i})^{p_1} (y_l - y_{c,i})^{p_2} (z_l - z_{c,i})^{p_3} D(p)_{p_1,p_2,p_3}, \quad (4.17)$$



where  $D(p)_{p_1,p_2,p_3}$  are the coefficients of polynomial expansion of pressure field. The inviscid fluxes  $F^{\text{inv}}$  at the cut-cell surface  $s$  are then evaluated as follows.

$$\mathbf{F}_{\Gamma,\text{inv}} \begin{pmatrix} \rho \\ \rho u_i \\ \rho E \\ \rho Y_k \end{pmatrix} = \begin{pmatrix} 0 \\ \sum_{l=1}^{n_g} w_l p_n(x_l, y_l, z_l) A_i^\Gamma \\ u_{s,i} p_n(x_l, y_l, z_l) \\ 0 \end{pmatrix}, \quad (4.18)$$

where  $A_i^\Gamma$  is the projected area of the cut surface along direction  $i$ ,  $w_l$  is the quadrature weight,  $n_g$  is the number of quadrature points, and  $u_{s,i}$  is the surface velocity in  $i$  direction.

#### *Wall shear stress evaluation*

At the cut-faces, the wall shear stress is evaluated from the derivatives of velocity components that are reconstructed from the piecewise polynomial expansion at the boundary face  $\Gamma$  as :

$$\frac{1}{V} \int_s \mathbf{F}_{\text{vis}} \cdot \mathbf{n} ds = \frac{1}{V} \sum_{l=1}^{n_g} w_l \tau_{ij}(x_l, y_l, z_l) A_j^\Gamma ds. \quad (4.19)$$

In Eq. (4.19),  $V$  is the cell volume,  $w_l$  is the quadrature weight,  $n_g$  is the number of quadrature points,  $A_j^s$  is the projected area of cut surface  $s$  in  $j$  direction, and  $(x_l, y_l, z_l)$  are the Gauss quadrature points. The derivatives at each of the quadrature point at the wall is obtained by differentiating the high order polynomial approximation and are given by:

$$\frac{\partial u}{\partial x}(x_l, y_l, z_l) = \sum_{p_1=0}^k \sum_{p_2=0}^k \sum_{p_3=0}^k p_1 (x_l - x_{c,i})^{p_1-1} (y_l - y_{c,i})^{p_2} (z_l - z_{c,i})^{p_3} D(u)_{p_1,p_2,p_3}, \quad (4.20)$$

$$\frac{\partial v}{\partial x}(x_l, y_l, z_l) = \sum_{p_1=0}^k \sum_{p_2=0}^k \sum_{p_3=0}^k p_2 (x_l - x_{c,i})^{p_1} (y_l - y_{c,i})^{p_2-1} (z_l - z_{c,i})^{p_3} D(v)_{p_1,p_2,p_3}, \quad (4.21)$$

$$\frac{\partial w}{\partial x}(x_l, y_l, z_l) = \sum_{p_1=0}^k \sum_{p_2=0}^k \sum_{p_3=0}^k p_3(x_l - x_{c,i})^{p_1}(y_l - y_{c,i})^{p_2}(z_l - z_{c,i})^{p_3-1} D(w)_{p_1,p_2,p_3}. \quad (4.22)$$

In Eqs.( 4.20)-(4.22),  $D(u)_{p_1,p_2,p_3}$ ,  $D(v)_{p_1,p_2,p_3}$  and  $D(w)_{p_1,p_2,p_3}$  represent the coefficients of polynomial approximation for  $u$ ,  $v$  and  $w$  velocity fields, respectively. It is important to note that the shear stress evaluation using the above method is higher order accurate and also results in smooth reconstruction of shear stress even if the distance between the cut-face quadrature points and cell centroid changes irregularly. It is noted that, many of the previous studies with cut-cell employed a first order formulation of derivatives for evaluating shear stress, which besides a loss of accuracy, is known to result in a very 'noisy' wall shear stress [95, 87].

#### 4.1.4 Cell clustering algorithm for small cell treatment

During the creation of cut-cells from boundary crossings on a Cartesian mesh, arbitrary cells of very low volume can also be generated. Low cell volume of these cells considerably increases the stiffness of the system of governing equations and results in numerical instability. This is a well-known problem in all the cut-cell based immersed boundary schemes and has been addressed in the past using several approaches such as: cell merging approach [90, 91], cell linking approach [92], cell mixing/redistribution [88, 89] and mixed approaches[85].

As pointed out earlier, the cell mixing approach is easiest to implement due to its inherent simplicity. However, when the classical cell mixing algorithm along with the  $k$ -exact reconstruction for viscous flow over embedded boundaries was used, significant numerical oscillations in the solution were observed at the boundaries destroying the smoothness of the reconstruction procedure. The oscillations were particularly accentuated for the wall shear stress as it involves reconstruction of the gradients. The distributions of the pressure coefficient ( $C_p$ ) and the skin friction coefficient ( $C_f$ ) over a cylinder surface in a cross flow of

diameter based Reynolds number,  $Re_d = 40$  are shown in Fig. 4.3. Note, a comparatively fine grid resolution is used based on a previous study with the cut-cell approach that used cell merging technique [94]. Although a reasonably smooth distribution for pressure was obtained using cell merging technique in [94], the behavior of the skin friction coefficient is not known as the data was not reported.

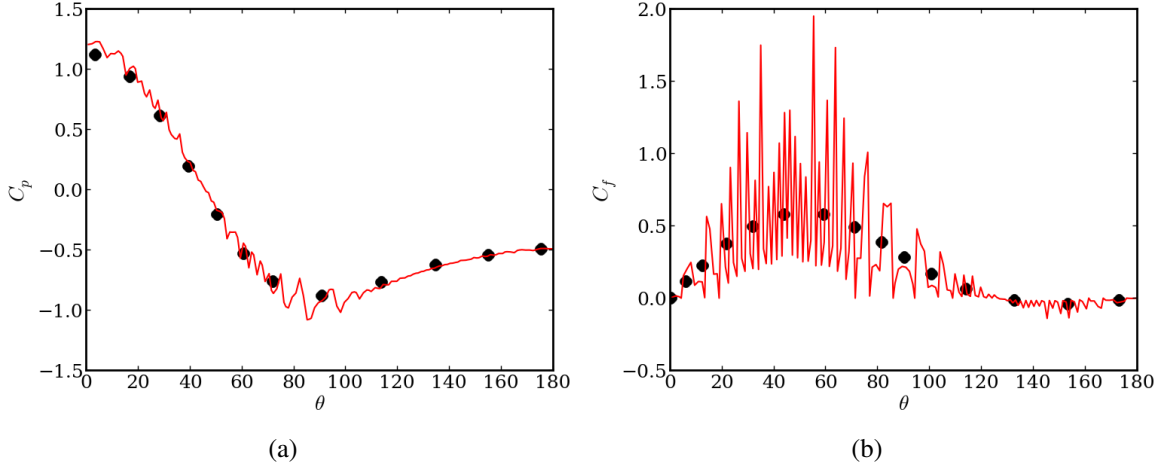


Figure 4.3: Numerical oscillations in the pressure coefficient and the skin friction coefficient on a cylinder surface placed in a  $Re_d = 40$  cross flow. Cell-mixing algorithm [100] was used for the small cell treatment and the grid resolution used was based on a previous study using cut-cells [94] (Solid black dots indicate data from a previous study [17] with body-fitted grid).

The problem of oscillatory behavior of the flow solution along the embedded boundary is due to the irregular stencil employed for the  $k$ -exact CENO reconstruction and also degradation of solution accuracy due to local cell mixing of conservative quantities. This problem has been reported even for other cut-cell methods with lower order schemes [87, 95]. Clearly, the advantage of using a high-order scheme is nullified at the boundaries because of the problem of irregularity in the stencil used for reconstructing the flow solution and its gradients using the  $k$ -exact CENO scheme. To address the stability of the small volume cut-cells and also at the same time maintain the design order of accuracy, a new cell clustering algorithm is proposed.

The central idea of the cell clustering technique is to employ the  $k$ -order, polynomial

piecewise approximation of the flow solution to a cluster of cells. The reconstruction polynomial for the cluster is based on the common centroid of the cell cluster and is given as:

$$u_c^k(x, y, z) = \sum_{p_1=0}^k \sum_{p_2=0}^k \sum_{p_3=0}^k (x - x_c)^{p_1} (y - y_c)^{p_2} (z - z_c)^{p_3} D_{p_1, p_2, p_3}$$

$$p_1 + p_2 + p_3 \leq k, \quad (4.23)$$

where ,

$$(x, y, z)_c = \frac{\sum_{n=1}^{n_c} (x, y, z)_n V_n}{\sum_{n=1}^{n_c} V_n} \quad (4.24)$$

with  $(x, y, z)_c$  and  $(x, y, z)_n$  being the cell centroid coordinates for the cluster  $c$  and cell  $n$  respectively,  $n_c$  is the number of small cells in the cluster, and  $V_n$  is the volume of cell  $n$ . A single polynomial approximation for the cell cluster, as given by Eq. (4.23), is employed for evaluation of the inviscid and the viscous fluxes for all the cells belonging to the cluster. The geometric moments of the cluster  $(\widehat{x^{p_1} y^{p_2} z^{p_3}})_c$  is computed from the individual cell geometric moments about the cluster cell centroid and is given as:

$$(\widehat{x^{p_1} y^{p_2} z^{p_3}})_c = \frac{\sum_{n=1}^{n_c} (\widehat{x^{p_1} y^{p_2} z^{p_3}})_{(n,c)} V_n}{\sum_{n=1}^{n_c} V_n}, \quad (4.25)$$

where  $(\widehat{x^{p_1} y^{p_2} z^{p_3}})_{(n,c)}$  is the geometric moment of cell  $n$  about the cluster centroid  $c$ . The operation in Eq. (4.25) can shown to be consistent by the following steps. Invoking the Divergence to transform the volume integral into surface integrals results in:

$$\begin{aligned} (\widehat{x^{p_1} y^{p_2} z^{p_3}})_{(n,c)} &= \frac{1}{V_n} \int_V (x - x_c)^{p_1} (y - y_c)^{p_2} (z - z_c)^{p_3} dV, \\ &= \frac{1}{V_n(p_1 + 1)} \int_V \nabla \cdot ((x - x_c)^{p_1+1} (y - y_c)^{p_2} (z - z_c)^{p_3} \hat{i}) dV, \\ &= \frac{1}{V_n(p_1 + 1)} \int_s (x - x_c)^{p_1+1} (y - y_c)^{p_2} (z - z_c)^{p_3} n_{\Gamma_s, x} ds. \end{aligned} \quad (4.26)$$

Eq. (4.26) can be numerically approximated as:

$$(\widehat{x^{p_1} y^{p_2} z^{p_3}})_{(n,c)} = \frac{1}{V_n(p_1 + 1)} \sum_{m=1}^M \sum_{l=1}^{n_g} w_l (x - x_c)^{p_1+1} (y - y_c)^{p_2} (z - z_c)^{p_3} n_{\Gamma_m, x} A_{\Gamma_m, x}, \quad (4.27)$$

where  $n_{\Gamma_m, x}$  is a unit normal of surface  $m$  in x-direction. The summation of the geometrical moments of individual cells performed for according to Eq. (4.25) then reduces to:

$$(\widehat{x^{p_1} y^{p_2} z^{p_3}})_c \sum_{n=1}^{n_c} V_n = \frac{1}{(p_1 + 1)} \sum_{n=1}^{n_c} \sum_{m=1}^M \sum_{l=1}^{n_g} w_l (x - x_c)^{p_1+1} (y - y_c)^{p_2} (z - z_c)^{p_3} n_{\Gamma_m, x}^n A_{\Gamma_m, x}^n. \quad (4.28)$$

It should be noted that for the common face  $m$  of the two neighboring cells  $(n, n + 1)$ ,  $n_{\Gamma_m, x}^n = -n_{\Gamma_m, x}^{n+1}$ . This leads to cancellation of the terms for common interior faces except for the outer surfaces bounding the cluster resulting in effective geometric moments of the cluster  $c$ .

In contrast to cell merging techniques used in the past [94, 85], the individual identities of the cells are maintained retaining the full geometric resolution of the embedded surface in the current cell clustering approach. The process of forming the cell cluster of small cells having a volume fraction,  $\alpha$  less than the allowed volume fraction,  $\alpha_{lim}$  is described in the following algorithm:

**Cluster cells less than a limiting volume fraction  $\alpha_{lim}$ :**

*First pass to find immediate cluster neighbors;*

```

for  $i \leftarrow 1$  to  $N_{cut-cells}$  do
    if  $\alpha_i < \alpha_{lim}$  then
        Find  $j$  along greatest component of cut surface normal of  $i$  ;
        Add  $i$  as a cluster neighbor to  $j$ ;
        Add  $j$  as a cluster neighbor to  $i$ ;
        Increment no. of cluster neighbors of cells  $j$  and  $i$ 
    end
end

Second pass to link all cluster cells to each other;

for  $i \leftarrow 1$  to  $N_{cut-cells}$  do
    if  $neighbor\ count(i) > 0$  then
        for  $j \leftarrow 1$  to  $neighbor\ count(i)$  do
            Add neighbors of  $j^{th}$  neighbor cell to  $i$ 
        end
        Update neighbor count( $i$ )
    end
end

```

#### **Algorithm 6:** Cell clustering algorithm

All the cluster properties from Eq. (4.23)-(4.25) can be computed for each cluster group and stored in each cell belonging to the cluster group by looping over the list of neighbors of a given cut-cell. The stencil for high-order  $k$ -exact least-square reconstruction (as described in Fig. 2) of the cluster is centered around the cell that is closest to the cluster centroid. Since an inverse distance weighing is used, all the neighbors of the cell belonging to the same cluster will be discarded in the polynomial least-square reconstruction procedure. This is because the individual cell centroids are corrected with the cluster centroid resulting in zero weights for the neighbor cells belonging to the same cluster. The reconstruction procedure

is performed for only one cell belonging to the cluster and for all the other cells, the cluster properties are copied. Cell clustering for the case of viscous flow over a cylinder is shown in Fig. 4.4 for different values of limiting volume fraction,  $\alpha_{lim}$  allowed for a cut-cell.

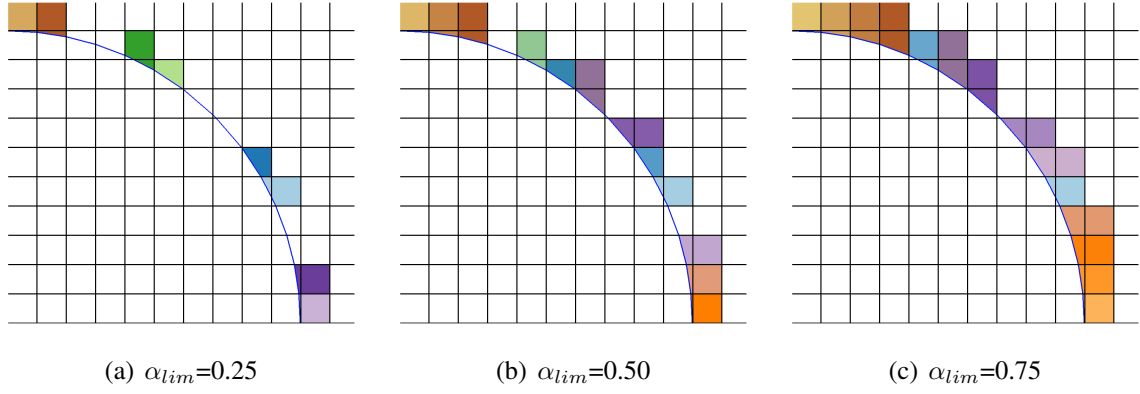


Figure 4.4: Cell cluster groups colored based on cluster number for the case of viscous flow 2D cylinder. Clusters are shown for various values of limiting volume fraction  $\alpha_{lim}$ .

Algorithm 6 is robust and stable in finding cell clusters for any value of limiting volume fraction  $\alpha_{lim} = 0 - 1$ . The  $k^{th}$ -order, piecewise polynomial reconstructed for each cluster using Eq. (4.23), is then employed for evaluating the inviscid and the viscous fluxes according to Eq. (2.55) and Eq. (2.56), respectively, at each of the cut-cell faces belonging to the cell cluster. In essence, the surface-flux reconstruction is performed on all the cells in the same exact manner. However, since the polynomial coefficients of the cluster are copied into all the cells belonging to the cluster, these cells will be using the cluster based reconstruction polynomial. The conservative quantities,  $\mathbf{U}$  in all normal cells and small cells are updated by integrating Eq. (2.53) and at the end of time integration, a conservative volume averaging is performed over each cell cluster according to:

$$\overline{\mathbf{U}}_c = \frac{\sum_{n=1}^{n_c} \overline{\mathbf{U}}_n V_n}{\sum_{n=1}^{n_c} V_n}. \quad (4.29)$$

The conservative averaging overwrites the flow variables on all cells belonging to the cluster with the cluster-averaged values. For the time integration of Eq. (2.53), the time step is

calculated based on the CFL condition based on the normal cells having volume fraction greater than the limiting volume fraction ( $\alpha > \alpha_{lim}$ ).

The improvement in reconstruction of the pressure coefficient and the skin friction coefficient ( $C_f$ ) is clearly observable in Fig. 4.5. The solution for  $C_p$  and  $C_f$  is quite smooth and matches very well with the previous studies using body-fitted approaches for the same problem. Additionally, the smoothness in the solution is not affected by the increase in the minimum small cell volume allowed. This is an excellent property of the approach described here as the minimum allowable time step based on CFL condition can be significantly improved without compromising the accuracy of the solution. For the current case, an increase of close to 60% in the time step is observed by increasing the limiting volume fraction  $\alpha_{lim}$  from 0.25 to 0.75. It must be noted that for the pressure and skin friction coefficient distribution not to be affected by the limiting volume fraction  $\alpha_{lim}$ , the flow gradients must be adequately resolved. The results shown in Fig. 4.5 are for a grid resolving the diameter of the cylinder by 80 cells. At a lower grid resolution using 20 cells, the pressure and the skin friction coefficient are found to have a weak dependence on  $\alpha_{lim}$  as seen in Fig. 4.6. For all the cases in the current study, a conservative value of  $\alpha_{lim}=0.33$  is used that is consistent with many past studies [85, 94] using the cut-cell approach.

#### 4.1.5 Corrections near moving boundaries using cell clustering method

The modification of the cell clustering algorithm to accommodate moving boundaries is described in this section. It is important to emphasize here that the conservative averaging though may appear to be first order at the boundaries, along with the application of a cluster based polynomial approximation as given by Eq.(4.24), provides a high order accuracy for the flux evaluations. For the time integration of Eq. (2.53), the time step is calculated based on the CFL condition based on the normal cells having volume fraction greater than the limiting volume fraction ( $\alpha > \alpha_{lim}$ ). A most noteworthy feature of the cell clustering algorithm as detailed above, is the ability to achieve large limiting volume fractions without losing out



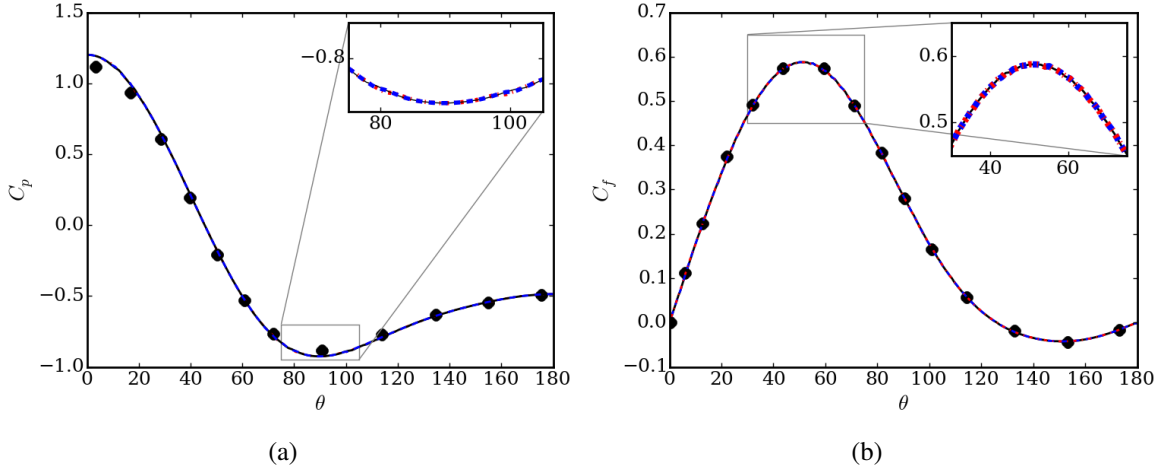


Figure 4.5: Plot of (a) co-efficient of pressure ( $C_p$ ) and (b) skin friction co-efficient ( $C_f$ ) for different values of limiting volume fraction  $\alpha_{lim}$  with the proposed cell clustering method:  $\alpha_{lim} = 0.25$  ;  $\alpha_{lim} = 0.50$  ;  $\alpha_{lim} = 0.75$  demonstrating that the smoothness of solution is not affected by changing  $\alpha_{lim}$  (Solid black dots indicate data from a previous study [17] with body-fitted grid).

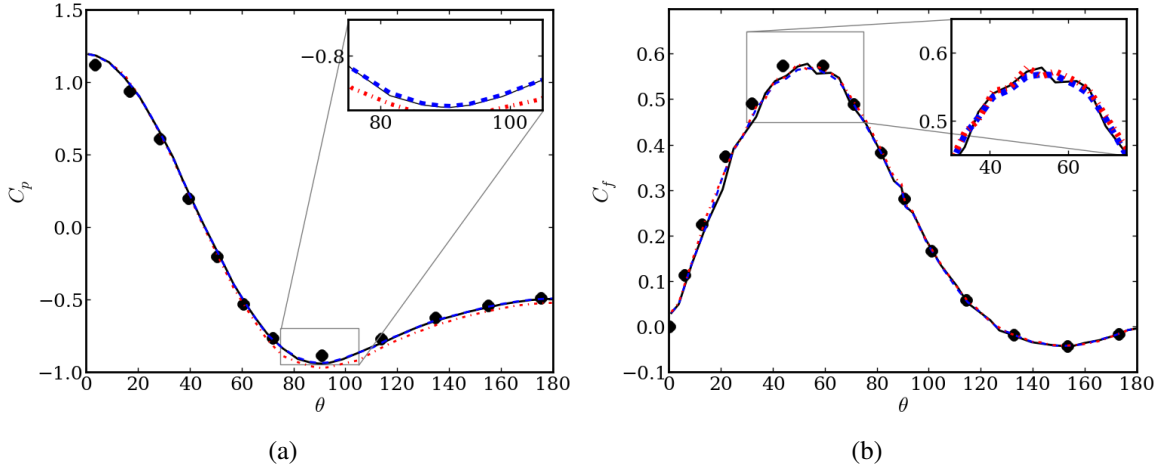


Figure 4.6: Plot of (a) co-efficient of pressure ( $C_p$ ) and (b) skin friction co-efficient ( $C_f$ ) for different values of limiting volume fraction  $\alpha_{lim}$  with the proposed cell clustering method:  $\alpha_{lim} = 0.25$  ;  $\alpha_{lim} = 0.50$  ;  $\alpha_{lim} = 0.75$  for a coarser grid using 20 cells for resolving the cylinder (Solid black dots indicate data from a previous study [17] with body-fitted grid).

on the accuracy as demonstrated in [26].

The details on how newly emerging fluid cells and cells that turn into solid are handled are provided below. For the sake of clarity, a single time update for a cell,  $k$ , of the following form:

$$(V\mathbf{U})_k^{n+1} = (V\mathbf{U})_k^n - \Delta t \left( \sum_{m=1}^M \mathbf{H}(\mathbf{U})_m^n A_m^n - (V\mathbf{Q}(\mathbf{U}))_k^n \right), \quad (4.30)$$

is considered. In the case of newly emerging cells,  $V_k^n = 0$  and  $V_k^{n+1} > 0$ . Whereas, when the cell,  $k$ , turns into a solid,  $V_k^n > 0$  and  $V_k^{n+1} = 0$ . Both the possible scenarios are shown in Fig. 4.7. The time update in Eq. (4.30) is valid only for cells with  $V_k^{n+1} > 0$  as the conservative update of  $\mathbf{U}_k^{n+1}$  requires dividing the right hand side of Eq. (4.30) with  $V_k^{n+1}$ . The following time update is used for vanishing cells which along with the cell clustering corrections described in Sections 4.1.5 and 4.1.5 ensures strict conservation:

$$V_k^n (\mathbf{U})_k^{n+1} = (V\mathbf{U})_k^n - \Delta t \left( \sum_{m=1}^M \mathbf{H}(\mathbf{U})_m^n A_m^n - (V\mathbf{Q}(\mathbf{U}))_k^n \right). \quad (4.31)$$

In the above Eq. (4.31), the state of a vanishing cell,  $k$  is not physically defined. Rather, including the time update for the vanishing cells as given in Eq. (4.31) facilitates transfer of correct mass, momentum and energy to neighboring cluster cells using the following corrections.

### *Correcting for vanishing cells*

During boundary movement, a cell can get progressively covered by the moving boundary and eventually vanish. To account for the mass of the cells that turn into a solid cell, explicit redistribution of the cell mass to its cluster neighbors is performed as follows:

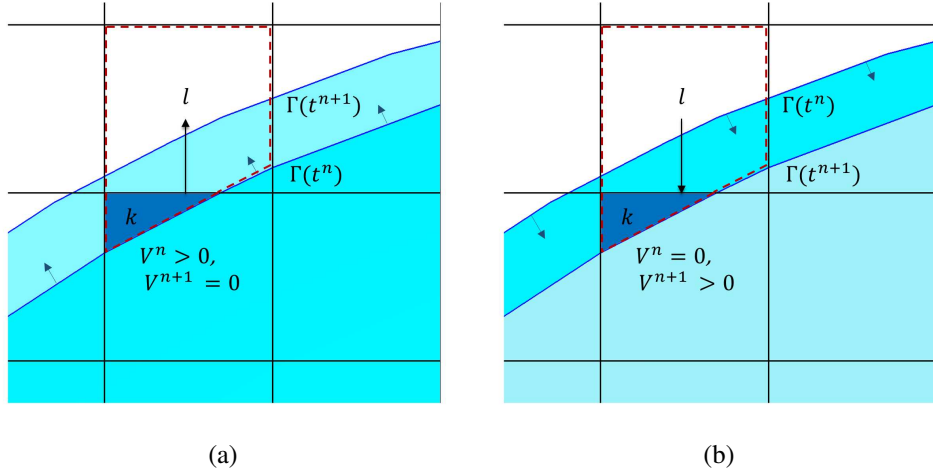


Figure 4.7: Schematic depicting (a) a fluid cell vanishing and (b) a new fluid cell emerging because of boundary motion. The thick arrow indicates the direction of transfer of mass, momentum and energy between a cell and its neighbor.

$$\overline{\mathbf{U}}_k^{n+1} = \overline{\mathbf{U}}_k^{n+1,*} + \frac{\sum_{i=1}^{n_v} \overline{\mathbf{U}}_i^{n+1,*} (V_i)^n}{\sum_{i=1}^{n_c} V_i^{n+1}}, k = 1, 2, \dots, n_c \quad (4.32)$$

Here,  $n_v$  is the number of vanishing cells in the cluster,  $c$  at time level  $n$  and  $n_c$  is the total number of cells in the cluster. The subscripts,  $n$  and  $n+1$  denote the current and the next time step. The cell averaged quantity before the clustering update is given by  $\overline{\mathbf{U}}_k^{n+1,*}$  and after update is given by  $\overline{\mathbf{U}}_k^{n+1}$ . The above Eq. (4.32) takes up the mass of all the vanishing cells in a given cluster and redistribute it to all the other cluster neighbors in a volume weighted manner.

#### *Correction for newly emerging cells*

When a moving boundary uncovers new fluid cells, it's initial state before a time update is undefined. In such a case, the newly emerged cell is made as a part of the cell cluster. This is enforced by the making sure that the boundary motion does not exceed the volume limit required to form a cell cluster. As described in Eq. (4.37), the characteristic cell length

is computed as  $h^n = \sqrt[3]{\alpha_{lim} V^n}$ , with  $\alpha_{lim}$  being the limiting cell volume fraction. This constraint ensures that the cell is always clustered with its neighbors when the boundary crosses a cell and thereby uncovers the cell. A similar approach was employed in [14] for a small cell linking strategy. The main difference in the current approach is that the cell clustering allows linking with multiple neighbors of a small cell and allows a higher value of the limiting volume fraction whereas in [14], the number of neighbors of a small cell is restricted to one. Thus the current cell clustering methodology is valid for complex changes in grid topologies where it is often difficult to find unique pairs of small cell and a neighboring bigger cell. Once the clusters are formed for the newly emerging cell, a cell clustering correction of the following form:

$$\overline{\mathbf{U}}_k^{n+1} = \frac{\sum_{i=1}^{(n_c - n_e)} \overline{\mathbf{U}}_i^{n+1,*} (V_i)^{n+1}}{\sum_{i=1}^{n_c} V_i^{n+1}}, k = 1, 2, \dots, n_c \quad (4.33)$$

is applied to all the cells of the cluster,  $c$ , formed at time level  $n+1$ . Note that all the cells that are newly emerging ( $V_n = 0$ ) has no history of flow solution and hence must be discarded in the summation on the numerator of Eq. (4.33). This ensures that all the newly emerged cells are set with a consistent value of the conservative variables  $\mathbf{U}$  after boundary motion. Note that many of previous approaches [104, 50] resort to some form of a correction in addition to the small cell technique used. For example, in [104], the newly emerged cells are linked for a single time step with a neighboring cell and delinked later. Such corrections increase the complexity of the algorithm and implementation. In contrast, the cell clustering technique can handle all the scenarios related to moving boundaries and hence is much more simpler to implement.

#### *Equation of motion for rigid bodies*

For problems where the body motion is driven by hydrodynamic forces, the Newton's equations of motion are solved to determine the boundary velocity. Accordingly, the forces acting

on the surface of a rigid boundary are stored and the following equations are solved at every sub-time step:

$$F_i = \int_{\Gamma} F_{s,i} A_i ds, \quad (4.34)$$

$$v_i^{n+1} = v_i^n + \frac{F_i}{m} dt, \quad (4.35)$$

where  $F_{s,i}$  is the force acting normal to the boundary  $\Gamma$  in the direction  $i$  with  $A_i$  being the projected boundary area in the  $i^{th}$  direction. The interface velocities at time steps  $n$  and  $n+1$  along a given direction are denoted by  $v$  and  $m$  is the mass of the rigid body.

#### 4.1.6 Time integration for moving boundary problems

The time integration of the moving boundary needs special attention as the domain volume is allowed to change during a time step. Figure 4.8 shows the change in volume of a cut-cell due to boundary motion between time steps  $t^n$  and  $t^{n+1}$ . Note that this is in contrast with some of the recent studies where the domain volume is frozen during a time integration step [104]. A first order error in time can be incurred for high speed flow problems because the surface motion and the flow solution integration is not coupled during a single time integration step. An even large departure of the solution is possible if the frozen volume approach is used for fluid-structure interaction problems where the surface motion is due to the hydrodynamic forces exerted on the surface.

In this work, a second order Runge-Kutta scheme modified to accommodate deforming/moving boundaries during a solution step is employed and is given as:

$$\begin{aligned} (V\mathbf{U})^{n+1/2} &= (V\mathbf{U})^n - \frac{\Delta t}{2} \left( \sum_{m=1}^M \mathbf{H}(\mathbf{U})_m^n A_m^n - (V\mathbf{Q}(\mathbf{U}))^n \right), \\ (V\mathbf{U})^{n+1} &= (V\mathbf{U})^n - \Delta t \left( \sum_{m=1}^M \mathbf{H}(\mathbf{U})_m^{n+1/2} A_m^{n+1/2} - (V\mathbf{Q}(\mathbf{U}))^{n+1/2} \right), \end{aligned} \quad (4.36)$$

where  $V$  is the volume of the cell,  $n, n+1/2$ , and  $n$  represent the time step indices,  $\mathbf{H}(\mathbf{U})$  de-

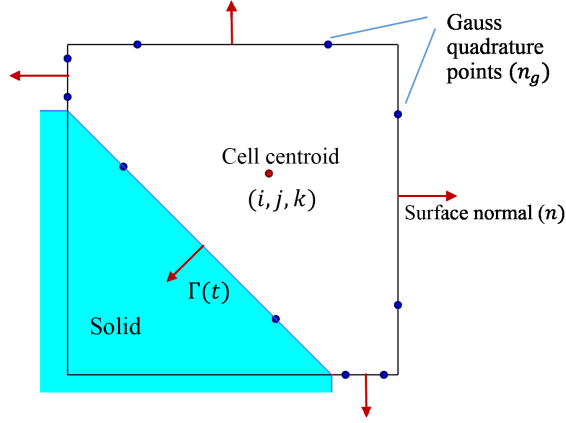


Figure 4.8: Schematic of a 2D cut-cell undergoing a volume change due to boundary motion.

notes flux function including both the inviscid fluxes,  $\mathbf{F}_{\text{inv}}(\mathbf{U})$  and the viscous fluxes  $\mathbf{F}_{\text{vis}}(\mathbf{U})$ . Note that the volume of the cell,  $V$  is allowed to change within the time step. In the above Eq. (4.36), the quadrature points are dropped for clarity. The time step is computed globally as:

$$\Delta t = \min_{n \in D} \left\{ \frac{\text{CFL } h^n}{|\mathbf{u}|^n + a^n + \frac{2\nu^n}{h^n}} \right\}, \quad (4.37)$$

where  $h^n$  is the characteristic length of the cell,  $n$ , computed as  $h^n = \sqrt[3]{\alpha_{\text{lim}} V^n}$  with  $V$  being the volume of the cell,  $\alpha_{\text{lim}}$  is the limiting volume fraction (explained in Section. 4.1.5), below which cells are clustered,  $|\mathbf{u}|$  is the velocity magnitude,  $a$  is the speed of sound and  $\nu$  is the kinematic viscosity, all of which are computed locally for a cell  $n$ . The constraint  $h^n = \sqrt[3]{\alpha_{\text{lim}} V^n}$  ensures that the solid boundary does not cross a given cell before it has formed a cluster with a neighboring fluid cell.

For stationary boundaries, the time step is computed globally as:

$$\Delta t = \min_{n \in D} \left\{ \frac{\text{CFL } h^n}{|\mathbf{u}|^n + a^n + \frac{2\nu^n}{h^n}} \right\}, \quad (4.38)$$

A CFL number of 0.5 is used for all moving and stationary boundary problems.

### *Algorithm for moving boundary simulations*

The implementation of the current method for simulation of moving boundary problems using the adaptive cut-cell technique is summarized by the following steps:

- **Step 1:** Prescribe initial conditions for the flow  $\mathbf{U}^0$  and the levelset field,  $\phi^0$  to define the embedded boundary
- **Step 2:** Compute the geometrical properties of the cut-cell from the levelset description
- **Step 3:** Begin time stepping loop
- **Step 4:** Mark regions of strong flow discontinuity based on the curvature sensor
- **Step 5:** Compute or prescribe surface velocities at embedded boundaries
- **Step 6:** Compute the fluxes on all the regular and cut-cell faces with a high-order unlimited CENO reconstruction in smooth regions and a limited second order MUSCL in regions of flow discontinuity
- **Step 7:** Update the levelset field based on the computed or prescribed surface velocities
- **Step 8:** Recompute the geometric properties of cut-cell and update cell volumes
- **Step 9:** Update flow solution,  $(\mathbf{UV})^{n+1}$  from  $(\mathbf{UV})^n$  using Eq. (4.36) for the time step  $t^{n+1}$
- **Step 10:** Apply the small cell correction using Eq. (4.29) and corrections for change of state of a cell (from fluid to solid and vice versa) using Eqs. (4.32) and (4.33)
- **Step 11:** Repeat **Step 5-10** for all the sub stages of a Runge-Kutta scheme and time integrate till end of time

The surface motion of the embedded boundary can be prescribed or can be driven by the interaction with hydrodynamic forces. In either case, the same procedure described above is followed. The differences in the procedure appear only in the step where the surface velocities of the embedded boundaries are computed.

#### 4.1.7 Hybridization of flux computation in regions of flow discontinuity

For problems with high speed effects such as shocks and other compressible flow features, a high-order  $k$ -exact reconstruction can not be used in the regions of strong flow discontinuity. Instead in these regions, a monotonized central limited second order MUSCL scheme [14] is used. As in a previous work [37], curvature of pressure and density is used for detection of the strong shocks or high gradients in flow solution. For any face  $(i + 1/2, j, k)$ , the inviscid flux function  $F_{\text{inv}}(\mathbf{U})_{i+1/2,j,k}^n$  is evaluated in the near field of the embedded boundary as:

$$\mathbf{F}_{\text{inv}}(\mathbf{U})_{i+1/2,j,k}^n = \lambda_{i+1/2,j,k} \mathbf{F}_{\text{inv}}(\mathbf{U})_{i+1/2,j,k}^{n,CENO} + (1 - \lambda_{i+1/2,j,k}) \mathbf{F}_{\text{inv}}(\mathbf{U})_{i+1/2,j,k}^{n,MUSCL}, \quad (4.39)$$

where  $\lambda_{i+1/2,j,k}$  is a Heavside step function switch at face  $(i + 1/2, j, k)$  computed as:

$$\lambda_{i+1/2,j,k} = \begin{cases} 1 & \text{if } \max(S_{\psi,i}, S_{\psi,i+1}) \leq 0 \\ 0 & \text{otherwise.} \end{cases} \quad (4.40)$$

In Eq. (4.40),  $S_{\psi,i}$  is the smoothness parameter of the flow quantities  $\psi = p, \rho$  computed according to:

$$S_{\psi,i} = \begin{cases} \frac{|\psi_{i+1,j,k} - 2\psi_{i,j,k} + \psi_{i-1,j,k}|}{|\psi_{i+1,j,k} - \psi_{i,j,k}| + |\psi_{i,j,k} - \psi_{i-1,j,k}|} - S^{th} & \text{if } |\psi_{i+1,j,k} - 2\psi_{i,j,k} + \psi_{i-1,j,k}| > \epsilon_{\psi} \psi_{i,j,k} \\ -S^{th} & \text{otherwise.} \end{cases} \quad (4.41)$$



Based on a previous study [37], The coefficients,  $\epsilon_p$  and  $\epsilon_\rho$  are taken to be equal to 0.05 and 0.1, respectively. The parameter,  $S^{th}$  is the threshold value of the pressure or density field after which the curvature value is computed and is taken to be equal to 0.5 and 0.25, respectively. The same procedure is repeated for the  $j$  and  $k$  directions.

## 4.2 Validation of high-order cut-cell for stationary boundaries

Various test cases are chosen to verify and validate the current cut-cell method for laminar compressible flow problems. The different test cases and the motivation for each of the cases are summarized in Table 4.1. The order of accuracy in reconstruction of any flow field quantity and its derivative on immersed boundaries is verified in case 1. The effect of small cell mixing on the order of accuracy of the  $k$ -exact scheme for cut-cells is investigated in the second test case (case 2). The third test case, (case 3) is that of laminar flow over a single cylinder at two different Reynolds number and the results are compared with established data from literature. The more complex case of flow past two cylinders in cross flow at different pitch ratios and incidence angles is studied in the next test case. For one of the configurations, (with  $Re_d=100$ ) the results are compared with a past numerical study [127] performed using a body-fitted spectral difference scheme. The sensitivity of the vortex flow patterns observed for this case on the order of the scheme is also reported. The cut-cell scheme is then used to investigate the flow vortex patterns when the cylinders are placed very close to each other with a narrow gap between them. The problem of low Reynolds number flow over a corrugated airfoil at different angles of attack is then investigated. The results from the cut-cell scheme are compared with previous experimental and numerical studies for a similar configuration. The motivation for this case is to assess the performance of the solver in handling complex geometrical features. Finally, results are presented for laminar flow over single and multiple spheres to demonstrate the consistency and accuracy of the three dimensional cut-cell method.

Table 4.1: Summary of test cases and their motivation.

Case	Motivation
$k$ -exact scalar and gradient reconstruction	Check accuracy of $k$ -exact reconstruction
2D elliptic problem	Check accuracy with cell clustering method
Flow over single cylinder	Verify scheme for 2D flows.
Flow over two side-by-side cylinders	Investigate vortex shedding patterns for complex configurations involving narrow gaps.
Flow over a corrugated airfoil	Demonstrate the robustness of the solver in handling sharp geometrical features.
Flow over two side-by-side spheres	Verify 3D cut-cell scheme and investigate complex flow interactions between pair of solid spheres.

#### 4.2.1 Order of accuracy analysis for scalar and its gradient reconstruction

To verify the order of accuracy of the proposed  $k$ -exact reconstruction, consider a scalar field  $\psi$  in a 2D domain  $(x, y) \in [1, 1]$  given by:

$$\psi(x, y) = \sin(\pi x) \sin(\pi y) \quad (4.42)$$

A circular boundary of radius 0.1 m, is resolved using cut-cells on a 2D Cartesian mesh. Both, the variable  $\psi$  and its gradient  $|\nabla\psi|$  are evaluated at the circular boundary for various grid sizes: 0.025 m, 0.0125 m, 0.00625 m, and 0.003125 m. The initial solution is integrated and stored for each computational cell using a fifth-order accurate Gauss-Legendre quadrature rule. The errors are computed on the surface as follows.

$$e_\psi = \psi_\Gamma - \psi_{exact} \quad (4.43)$$

$$e_{\nabla\psi} = \nabla\psi_\Gamma - \nabla\psi_{exact} \quad (4.44)$$

where subscript  $\Gamma$  denotes the reconstructed value of  $\psi$  and  $\nabla\psi$  at the boundary and subscript *exact* denotes the corresponding analytical solution, respectively. While the error  $e_\psi$  is in-

Table 4.2: Error in reconstruction of a scalar  $\psi$  and order of accuracy at the embedded boundary using a quadratic reconstruction( $k=2$ ).

Grid	$L^1$ norm	$L^1$ order	$L^2$ norm	$L^2$ order	$L^\infty$ norm	$L^\infty$ order
40 x 40	$6.83 \times 10^{-6}$	-	$1.03 \times 10^{-5}$	-	$1.66 \times 10^{-5}$	-
80 x 80	$7.26 \times 10^{-7}$	<b>3.23</b>	$1.05 \times 10^{-6}$	<b>3.29</b>	$1.65 \times 10^{-6}$	<b>3.33</b>
160 x 160	$7.69 \times 10^{-8}$	<b>3.24</b>	$1.09 \times 10^{-7}$	<b>3.26</b>	$2.05 \times 10^{-7}$	<b>3.08</b>
320 x 320	$7.21 \times 10^{-9}$	<b>3.40</b>	$1.02 \times 10^{-8}$	<b>3.41</b>	$2.11 \times 10^{-8}$	<b>3.28</b>

Table 4.3: Error in reconstruction of gradient of a scalar,  $|\nabla\psi|$  and order of accuracy at the embedded boundary using a quadratic reconstruction( $k=2$ ).

Grid	$L^1$ norm	$L^1$ order	$L^2$ norm	$L^2$ order	$L^\infty$ norm	$L^\infty$ order
40 x 40	$7.86 \times 10^{-4}$	-	$1.06 \times 10^{-3}$	-	$1.18 \times 10^{-3}$	-
80 x 80	$2.11 \times 10^{-4}$	<b>1.90</b>	$2.51 \times 10^{-4}$	<b>1.90</b>	$2.47 \times 10^{-4}$	<b>2.26</b>
160 x 160	$6.57 \times 10^{-5}$	<b>1.68</b>	$7.54 \times 10^{-5}$	<b>1.68</b>	$8.74 \times 10^{-5}$	<b>1.50</b>
320 x 320	$1.51 \times 10^{-5}$	<b>2.12</b>	$1.71 \times 10^{-5}$	<b>2.12</b>	$1.97 \times 10^{-5}$	<b>2.15</b>

dicative of the accuracy of inviscid terms discretization,  $e_{\nabla\psi}$  is representative of the accuracy of viscous terms reconstruction. The  $L^p$  norms of the errors are computed as:

$$L^p(e_{\psi,|\nabla\psi|}) = \left( \frac{1}{\sum_i A_\Gamma^i} \sum_i A_\Gamma^i |e_{\psi,|\nabla\psi|}^i|^p \right)^{\frac{1}{p}}, \quad (4.45)$$

where  $A_\Gamma^i$  and  $e^i$  are the area of the cut surface and error in reconstruction for  $i^{th}$  cell, respectively. The errors  $e_{\psi,|\nabla\psi|}$  are reported in Tables 4.2, 4.3, 4.4 and 4.5 for different orders of reconstruction along with the convergence rates.

The convergence rates for  $\psi$  and  $\nabla\psi$  are also shown in Fig. 4.9. As seen in the tables

Table 4.4: Error in reconstruction of a scalar  $\psi$  and order of accuracy at the embedded boundary using a cubic reconstruction( $k=3$ ).

Grid	$L^1$ norm	$L^1$ order	$L^2$ norm	$L^2$ order	$L^\infty$ norm	$L^\infty$ order
40 x 40	$2.07 \times 10^{-6}$	-	$2.44 \times 10^{-6}$	-	$2.86 \times 10^{-6}$	-
80 x 80	$1.44 \times 10^{-7}$	<b>3.85</b>	$1.63 \times 10^{-7}$	<b>3.90</b>	$2.05 \times 10^{-7}$	<b>3.80</b>
160 x 160	$7.57 \times 10^{-9}$	<b>4.25</b>	$9.17 \times 10^{-9}$	<b>4.15</b>	$1.51 \times 10^{-8}$	<b>3.76</b>
320 x 320	$4.38 \times 10^{-10}$	<b>4.11</b>	$5.64 \times 10^{-10}$	<b>4.02</b>	$1.05 \times 10^{-9}$	<b>3.85</b>

Table 4.5: Error in reconstruction of gradient of a scalar,  $|\nabla\psi|$  and order of accuracy at the embedded boundary using a cubic reconstruction( $k=3$ ).

Grid	$L^1$ norm	$L^1$ order	$L^2$ norm	$L^2$ order	$L^\infty$ norm	$L^\infty$ order
40 x 40	$4.49 \times 10^{-4}$	-	$5.90 \times 10^{-4}$	-	$6.45 \times 10^{-4}$	-
80 x 80	$6.75 \times 10^{-5}$	<b>2.73</b>	$7.64 \times 10^{-5}$	<b>2.95</b>	$1.05 \times 10^{-4}$	<b>2.61</b>
160 x 160	$8.75 \times 10^{-6}$	<b>2.95</b>	$9.62 \times 10^{-6}$	<b>2.99</b>	$1.28 \times 10^{-5}$	<b>3.03</b>
320 x 320	$1.10 \times 10^{-6}$	<b>2.93</b>	$1.22 \times 10^{-6}$	<b>2.98</b>	$1.96 \times 10^{-6}$	<b>2.70</b>

and the figure, the reconstruction scheme has excellent consistency across the different  $L^p$  norms and the order represents the true order of the reconstruction both locally and globally. Formally third order with  $k=2$  and fourth order with  $k=3$  for inviscid terms and formally second order with  $k=2$  and third order with  $k=3$  for is derivatives is achieved the boundaries. This is an improvement over the earlier studies using cut-cell [94, 86] where the accuracy degraded to first order at the wall boundaries.

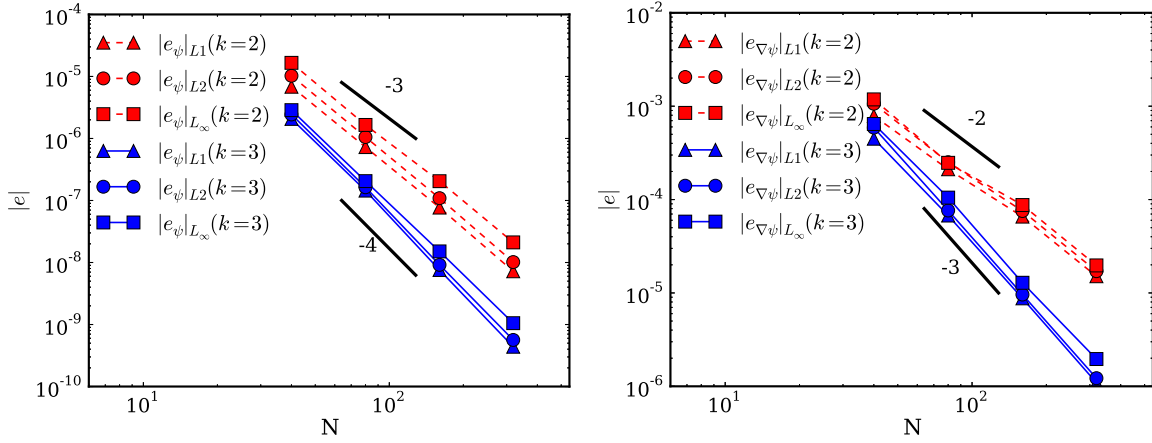


Figure 4.9: Error norms in reconstruction of a scalar  $\psi$  and its gradient  $\nabla\psi$  on a immersed boundary. Solid black lines indicate the design order of accuracy

#### 4.2.2 Order of accuracy analysis for a 2D elliptic problem

The accuracy of the cut-cell finite volume scheme is demonstrated by solving for the Laplace's problem:

$$\frac{\partial^2 \psi}{\partial x^2} + \frac{\partial^2 \psi}{\partial y^2} = 0, \quad (4.46)$$

on a series of successively refined grids and with two different orders of reconstruction:  $k=2$  and  $k=3$ . The exact solution of Eq. (4.46) is:  $\psi_{exact} = \sin x \exp y$ . Although, a high order accurate reconstruction of the flow field quantities and their derivatives are obtained using the  $k$ -exact approach, the solution accuracy degrades due to the aforementioned cell mixing process. Particularly for viscous flow problems, the classical cell mixing method, achieves numerical stability in computations but causes significant noise in the reconstruction of the derivative quantities, e.g, shear stress and heat flux (as seen in Fig. 4.3).

The proposed small cell treatment scheme is now assessed for this Laplace's problem on a domain,  $D$  with a embedded boundary,  $\Gamma$ . The boundary is defined by a levelset description  $\phi$  on a  $1 \times 1$  unit domain given by:

$$\phi_1(x, y) = 1 - \sqrt{\frac{(x - x_c)^2}{r_1^2} + \frac{(y - y_c)^2}{r_2^2}}, \quad (4.47)$$

$$\phi_2(x, y) = 1 - \sqrt{\frac{(x - x_c)^2}{r_2^2} + \frac{(y - y_c)^2}{r_1^2}}, \quad (4.48)$$

$$\phi(x, y) = \min(\phi_1, \phi_2) \quad (4.49)$$

where  $(x_c, y_c)$  is set at  $(0.5, 0.5)$  and  $r_1 = 0.3, r_2 = 0.5$ . The boundary represented by the above levelset description is shown in the following Fig. 4.10(a).

Equation Eq. (4.46) is solved using the finite volume approach described in Section 2.2. All the conserved quantities are frozen and an additional scalar equation is solved for  $\psi$  with a Dirichlet boundary condition  $\psi(x_\Gamma, y_\Gamma) = \psi_{exact}$  imposed at the immersed boundaries. The  $L^1$ ,  $L^2$  and  $L^\infty$  norm of the errors are computed as  $L^p(e_\psi) = \left( \frac{1}{\sum_i v_i} \sum_i v_i |e_\psi|^p \right)^{\frac{1}{p}}$  with  $v_i$  being the volume of cell,  $p$  is error norm and  $|e_\psi| = |\psi - \psi_{exact}|$ . The error norms are reported for different mesh sizes and for  $k=2$  and  $k=3$  in Table 4.6. The plot of the error

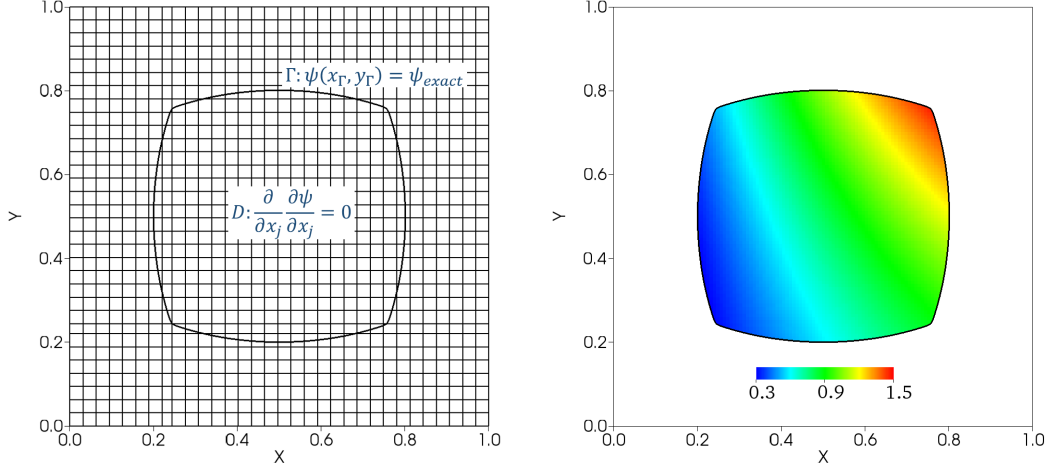


Figure 4.10: (a) Immersed domain for the Laplace's problem represented using cut-cells (b) Exact solution to Laplace's problem,  $\psi_{exact} = \sin x \exp y$ .

norms along with the design order of accuracy is shown in Fig. 4.11(a).

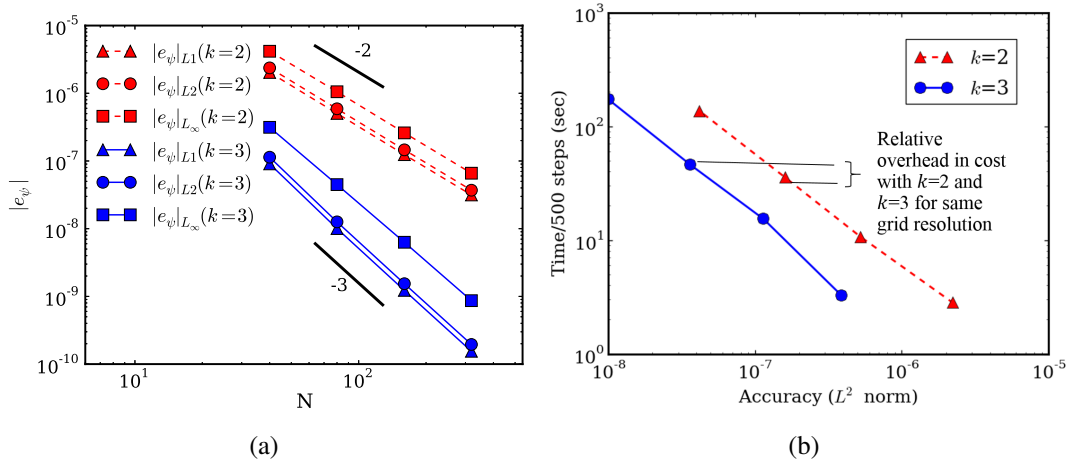


Figure 4.11: (a) Error norms of  $\psi$  for the solution to the Laplace's problem at different grid resolutions (b) Accuracy versus cost for the Laplace's problem with different orders of  $k$ -exact reconstruction.

The error in the solution includes the effects of small cell clustering and mixing. With the cell clustering algorithm, the design order of accuracy is achieved for both  $k=2$  and  $k=3$ . Previous studies employing cut-cell [25, 85] have only reported the reconstruction error which does not account for the small cell effects. It is noted that in the current approach, higher or-

Table 4.6: Error norms for solution to Laplace equation for different orders of  $k$ -exact reconstruction.

$k = 2$						
Grid	$L^1$ norm	order	$L^2$ norm	order	$L^\infty$ norm	order
$40^2$	$2.03 \times 10^{-6}$	-	$2.37 \times 10^{-6}$	-	$4.173 \times 10^{-6}$	-
$80^2$	$5.04 \times 10^{-7}$	<b>2.01</b>	$5.90 \times 10^{-7}$	<b>2.0</b>	$1.053 \times 10^{-6}$	<b>1.99</b>
$160^2$	$1.24 \times 10^{-7}$	<b>2.02</b>	$1.46 \times 10^{-7}$	<b>2.01</b>	$2.60 \times 10^{-7}$	<b>2.02</b>
$320^2$	$3.15 \times 10^{-8}$	<b>1.98</b>	$3.70 \times 10^{-8}$	<b>1.98</b>	$6.59 \times 10^{-8}$	<b>1.98</b>
$k = 3$						
Grid	$L^1$ norm	order	$L^2$ norm	order	$L^\infty$ norm	order
$40^2$	$9.06 \times 10^{-8}$	-	$1.14 \times 10^{-7}$	-	$3.14 \times 10^{-7}$	-
$80^2$	$1.0 \times 10^{-8}$	<b>3.17</b>	$1.26 \times 10^{-8}$	<b>3.17</b>	$4.48 \times 10^{-8}$	<b>2.81</b>
$160^2$	$1.23 \times 10^{-9}$	<b>3.03</b>	$1.54 \times 10^{-9}$	<b>3.03</b>	$6.30 \times 10^{-9}$	<b>2.83</b>
$320^2$	$1.55 \times 10^{-10}$	<b>2.99</b>	$1.95 \times 10^{-10}$	<b>2.98</b>	$8.65 \times 10^{-10}$	<b>2.86</b>

der accuracy is achieved both locally and globally. When compared with error norms for only the reconstruction shown in Fig. 4.9, it appears that the effect of cell clustering is to increase the error in the solution locally but the method is still able to maintain the design order of convergence. This clearly indicates the robustness of the proposed cell clustering approach in handling complex surface topologies and still achieve higher order. The Laplace's problem is representative of the class of viscous flow problems since it involves elliptic, diffusion like term and therefore, the inferences made on order of accuracy for this simple problem should be applicable to compressible viscous flow problems in general.

All the computations were performed on a Intel(R) Xeon(R) CPU E5345 @ 2.33GHz processor with 4 MPI threads. The cost is measured as the time taken to compute 500 steps and is plotted against the accuracy measured in terms of the  $L^2$  norm error in Fig. 4.11(b). As seen in the figure, to achieve a given accuracy, the high order  $k=3$  scheme requires lesser number of grid points and is always less costlier than the lower order  $k=2$  scheme. And for a given a grid resolution, though there is a overhead in using the cubic  $k$ -order ( $k=3$ ) reconstruction compared to the quadratic reconstruction ( $k=2$ ), the gain in accuracy is in orders of magnitude. This simple test provides some insight into the cost incurred versus the accuracy gained in employing a higher order reconstruction.

Table 4.7: Various grid resolutions used for viscous flow over cylinder case.

$Re_d$	Case	Levels of local refinement	$D/\Delta x$
40	$Re40_{10}$	2	10
40	$Re40_{20}$	3	20
40	$Re40_{40}$	4	40
40	$Re40_{80}$	5	80
100	$Re100_{10}$	2	10
100	$Re100_{20}$	3	20
100	$Re100_{40}$	4	40
100	$Re100_{80}$	5	80

#### 4.2.3 Laminar flow over a single cylinder

The case of laminar flow past a cylinder has been extensively studied both experimentally and numerically [55, 128] and used for validation of many IB schemes in the past. Results are reported for two Reynolds numbers with  $Re_d = 40$  and  $Re_d = 100$  where  $Re_d$  is the Reynolds number based on diameter of the cylinder,  $d$  and free stream velocity,  $u_\infty$ . For both the cases, Mach number of the free stream is set to  $M_\infty = 0.2$ . The domain size for both is  $30d \times 30d$ . A characteristic inflow boundary condition is employed to the left side while a non-reflecting characteristic outflow is set on the top, bottom and right. All the simulated cases that are run are summarized in Table 4.7. The last column in the Table 4.7 denotes the number of grid points resolving the diameter of the cylinder,  $d$ .

At this low Reynolds number of  $Re_d=40$ , the flow remains steady and the cylinder wake is characterized a symmetric pair of vortices that are attached to the cylinder. A re-circulation region behind the wake develops which eventually breaks with the increase in flow Reynolds number. The streamline plot at the finest resolution with cubic reconstruction is shown in Fig. 4.12. At this resolution (case  $Re40_{80}$ ), it is found that there are no apparent differences in the streamlines with  $k = 2$  and  $k = 3$ . But at the lowest resolution, minor differences especially in the recirculation region are noticeable with different orders of reconstruction (figure not shown).

More quantitative comparisons of the improvement in the solution with increase in order



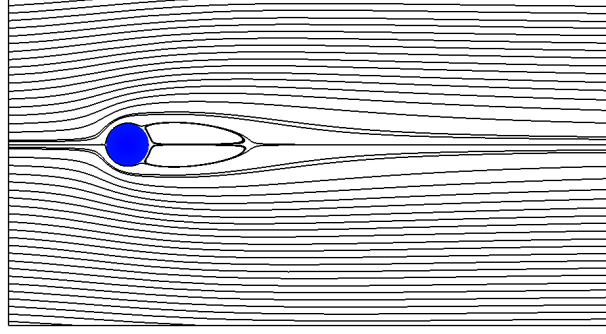


Figure 4.12: Streamlines for  $Re_d=40$  flow over a cylinder for case  $Re40_{80}$  with  $k=3$ .

of reconstruction are be done by analyzing the pressure coefficient  $C_p$  computed as  $C_p = (p - p_\infty)/\rho U_\infty^2$  and the skin friction coefficient computed as  $C_f = 2\tau_f/\rho u_\infty^2$  along the cylinder surface. Here,  $\tau_f$  is the skin friction on the surface of the cylinder. The  $C_p$  and  $C_f$  are plotted in Figs. 4.13 and 4.14 for the different grid resolutions given in Table 4.7 and for  $k=2$  and  $k=3$ . As seen in the figures, there is a very good agreement between the current results and the data from previous study [17] with a body-fitted grid. A smooth reconstruction of both inviscid and viscous fluxes is achieved at the cut-cell boundary resulting in a smooth pressure and shear stress distribution at the solid boundaries with a very low effective grid resolution. A clear improvement in the  $C_p$  and  $C_f$  distribution can be noticed by increasing the order of reconstruction from  $k=2$  to  $k=3$ . Even with just 10 points per diameter of the cylinder, the correct pressure and shear stress distribution is recovered with  $k=3$  that almost matches with the fine resolution case having 80 points per diameter of the cylinder. The deviations noted at  $\theta \approx 90^\circ$  in  $C_p$  and  $\theta \approx 50^\circ$  in  $C_f$  can be due to errors in the surface approximation using cut-cells rather than from the accuracy of the scheme. A better approximation of the surface with multiple planar cuts could potentially improve the solution even more. The results demonstrates the superiority of the proposed scheme over previous cut-cell based approaches.

On increasing the Reynolds number of the cross flow to  $Re_{D,critical} > 49$ , the re-circulation region in the wake of the cylinder becomes unstable [129] and above this critical Reynolds

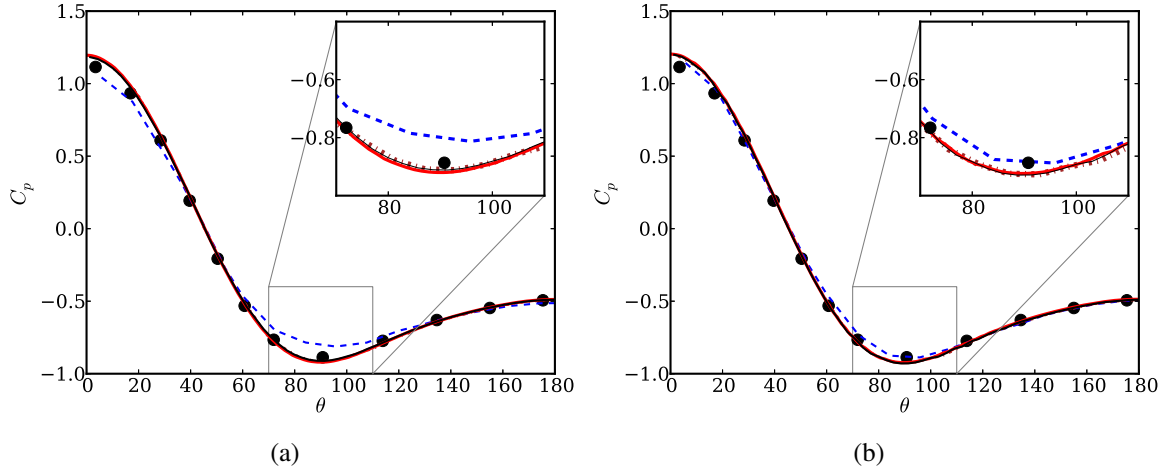


Figure 4.13: Results for pressure coefficient with (a)  $k = 2$  (b)  $k = 3$  along the cylinder surface for  $Re_d = 40$  compared with reference data from a boundary-fitted grid [17] (solid back dots) or cases:  $--Re_{40_{10}}$  ;  $-\cdot- Re_{40_{20}}$  ;  $—Re_{40_{40}}$  ;  $—Re_{40_{80}}$ .

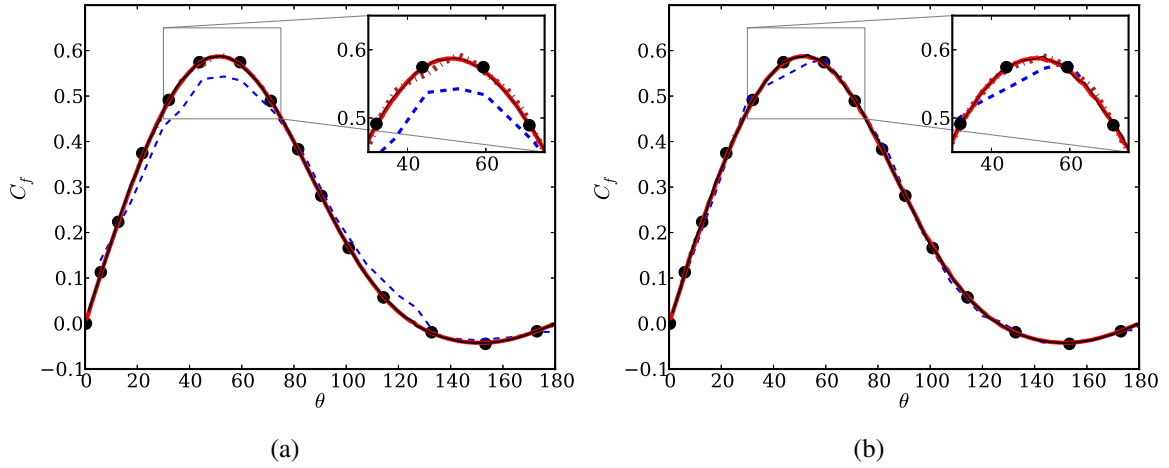


Figure 4.14: Results for skin friction coefficient with (a)  $k = 2$  (b)  $k = 3$  along the cylinder surface for  $Re_d = 40$  compared with reference data from a boundary-fitted grid [17] (solid back dots) or cases:  $--Re_{40_{10}}$  ;  $-\cdot- Re_{40_{20}}$  ;  $—Re_{40_{40}}$  ;  $—Re_{40_{80}}$ .

number, the wake begins to oscillate. Periodic alternating vortices are shed exhibiting the well known von Kármán vortex street. This can be observed from the vorticity iso-lines shown in Fig. 4.15 at  $Re_d = 100$  again for the finest resolution with  $k = 3$  reconstruction. No differences are observed with  $k = 2$  reconstruction in the vortex patterns at this resolution. As for the steady case, the higher order of reconstruction is found to only marginally improve resolution of the wake vortical structures at lower resolutions (figure not shown).

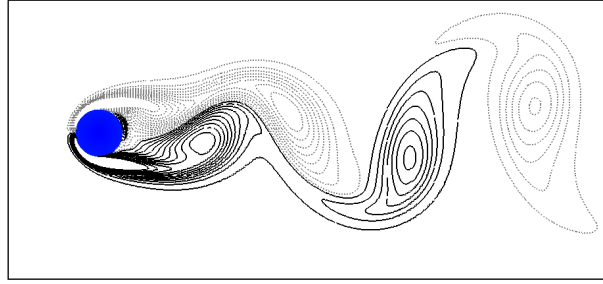


Figure 4.15: Vorticity iso-lines for  $Re_d=100$  flow over a cylinder for case  $Re40_{80}$  with  $k = 3$ . Solid lines denote positive vorticity and dotted lines denote negative vorticity.

The variation of the drag coefficient  $C_d = F_{drag}/(0.5\rho u_\infty^2)$  with time is shown in Fig. 4.16 for various resolutions. A rapid convergence to the fine grid solution is noted for  $k=3$  compared to  $k=2$ . A similar plot for the lift coefficient  $C_l = 2F_{lift}/\rho u_\infty^2$  over time is presented in Fig. 4.17. The amplitude of the lift coefficient is better predicted using  $k=3$  whereas with  $k=2$ , the peak amplitude is off by 33%.

The drag coefficient,  $C_d$  at different grid resolutions for  $Re_d = 40$  are listed in Table 4.15. Also reported in the table are the  $C_d$  data from a previous study employing cut-cell method. As seen, the drag coefficient rapidly converges to the fine grid value. In comparison, the prior study [25] employing cut-cell scheme exhibits a slower convergence. Similar behavior is observed for the average coefficient of drag  $\bar{C}_d$  and Strouhal number,  $St = Df_s/u_\infty$ , where  $f_s$  is the shedding frequency, for  $Re_d = 100$  as seen in Table 4.9. The values of  $C_d$ ,  $\bar{C}_d$  and  $St$  reported by previous studies are reported in Table 4.10 along with values obtained using the present cut-cell method for the finest resolution cases ( $Re40_{80}$  and  $Re100_{80}$ ) and

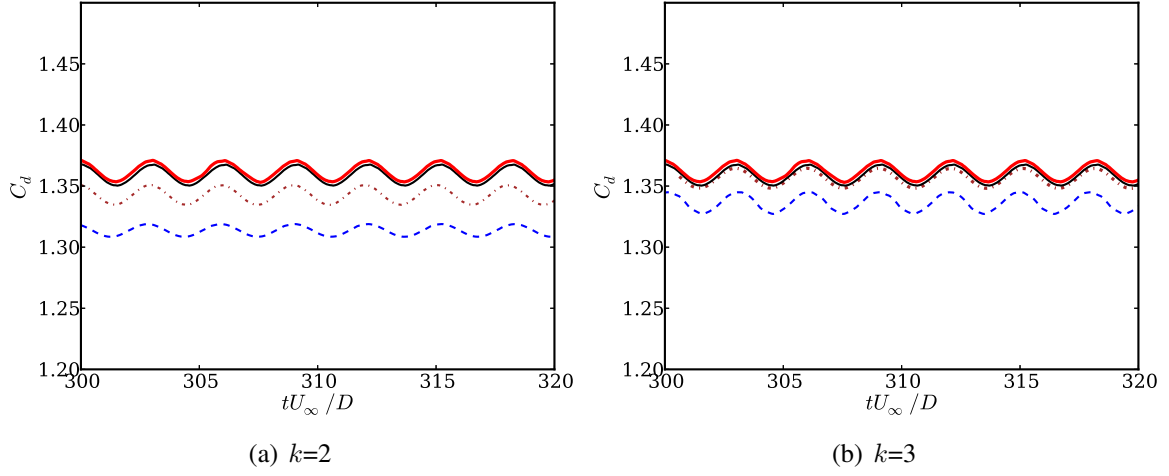


Figure 4.16: Variation of drag coefficient over non-dimensional time for  $Re_d = 100$  for various grid resolutions with: (a)  $k = 2$  (b)  $k = 3$ ;  $--Re100_{10}$  ;  $-\cdot- Re100_{20}$  ;  $—Re100_{40}$  ;  $—Re100_{80}$ .

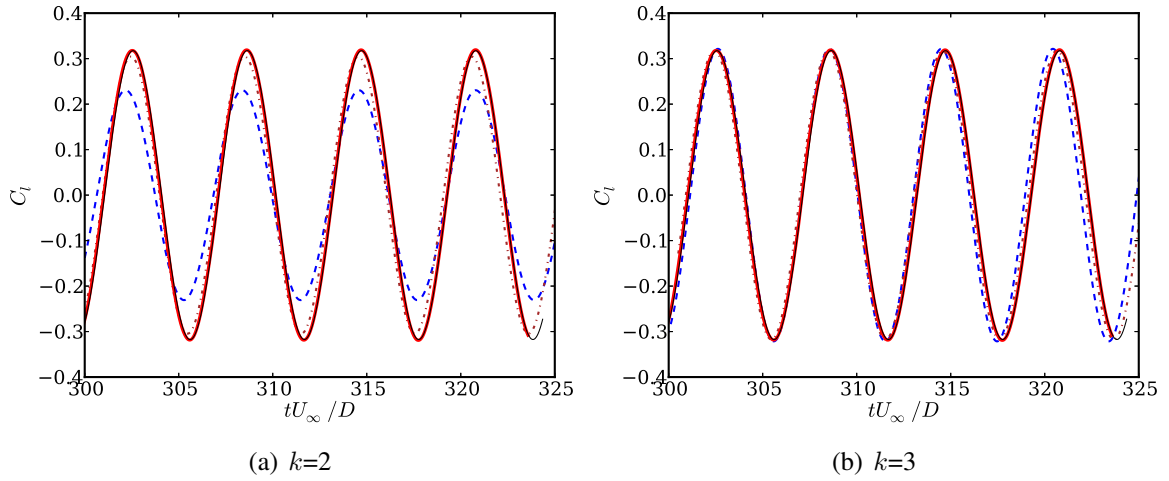


Figure 4.17: Variation of lift coefficient over non-dimensional time for  $Re_d = 100$  for various grid resolutions with: (a)  $k = 2$  (b)  $k = 3$ ;  $--Re100_{10}$  ;  $-\cdot- Re100_{20}$  ;  $—Re100_{40}$  ;  $—Re100_{80}$ .

Table 4.8: Grid convergence of  $C_d$  for  $Re_d = 40$ 

Effective res. ( $D/\Delta x$ )	$Re_d = 40$		
	$C_{d,k=2}$	$C_{d,k=3}$	$C_d$ (Past study [25])
10	1.545	1.551	1.428
20	1.558	1.559	1.488
40	1.558	1.559	1.513
80	1.559	1.560	1.521

Table 4.9: Grid convergence of  $\bar{C}_d, St$  for  $Re_d = 100$ 

Effective res. ( $D/\Delta x$ )	$Re_d = 100$			
	$\bar{C}_d, k=2$	$\bar{C}_d, k=3$	$St, k=2$	$St, k=3$
10	1.314	1.336	0.163	0.165
20	1.340	1.356	0.165	0.166
40	1.359	1.359	0.166	0.167
80	1.361	1.361	0.166	0.167

with  $k=3$ . The predicted values from the simulation agree well with the data from existing studies.

Note that the skin friction coefficient and the pressure coefficient converges to the fine grid value at a grid resolution of  $D/\Delta x = 20$  (See Table 4.8) with the current approach. The values of the relevant derived quantities ( $C_d, St$ ) also converged to the second decimal at relatively low grid resolution as seen in Table 4.9. In comparison, previous studies [94] required much higher grid resolution (4 times more) to predict even first order quantities such as pressure. The results suggests the potential of the current formulation to maintain good accuracy even at a relatively lower grid resolution.

Table 4.10: Comparison with past studies: Left -  $C_d$  for  $Re_d = 40$ , Right -  $\bar{C}_d$  and  $St$  for  $Re_d = 100$ 

Contribution	$C_d$	Contribution	$\bar{C}_d$	$St$
Tritton [128]	1.58	Tseng and Ferziger [17]	1.42	0.164
Tseng and Ferziger [17]	1.53	Kim <i>et al.</i> [55]	1.33	0.165
Chung [91]	1.54	Chung[91]	1.39	0.172
<b>Current work</b>	<b>1.56</b>	<b>Current work</b>	<b>1.36</b>	<b>0.167</b>

#### 4.2.4 $Re_d=100$ flow over two side-by-side cylinders in cross-flow

The new approach is now applied to a more complex problem of a  $Re_d = 100$  flow over two side by side cylinders with a free stream Mach number of  $M = 0.2$ . The two cylinders are placed apart from each other with a center to center distance of  $P = 2.5D$  where  $P$  is generally defined as the pitch between cylinders. This case was earlier investigated using a fourth-order spectral difference method with a body-fitted mesh [127] and an IB method employing discrete momentum forcing [130]. This is a challenging test case as the wake pattern of the two cylinders initially are in anti-phase, but later exhibits a transition from anti-phase vortex shedding to an in-phase vortex shedding. A less accurate numerical scheme would not be able to accurately capture the transition and predict the wake pattern behavior. The phase transition phenomenon has been noted in the past [127, 130] for pitch ratio of  $P/D = 2.5$ . The process of the vortex synchronization and pairing between the vortices of opposite signs of the gap between the cylinders resulting in two von Kármán vortex streets that are in anti-phase is also noted in experiments [131]. It must be noted that for the vortex pairing process to occur, there must be a small difference in the shedding frequencies of the upper and lower cylinders. In reality, flow irregularities causes instantaneous differences in the vortex shedding frequencies of the upper and lower cylinder. This facilitates the vortices of opposite signs to pair up and synchronize. In the current study, as in [130], the flow was initialized with a random state, whereby a numerical noise of magnitude 5% of the freestream velocity was added to both the streamwise and spanwise velocity components.

A domain of  $45D \times 30D$  was used for this case and the boundary conditions are the same as employed for the single cylinder study. Five AMR levels of local grid refinement over a base resolution of  $0.3D$  is used resulting in an effective resolution of  $0.01875D$ , which is comparable to grid resolution used in the previous spectral difference study [127]. Simulations are performed for two different orders of reconstruction ( $k=2$  and  $k=3$ ). The phase transition from antiphase shedding pattern to inphase, because of pairing of vortices on either side of the gap between cylinders, is shown in Fig. 4.18.

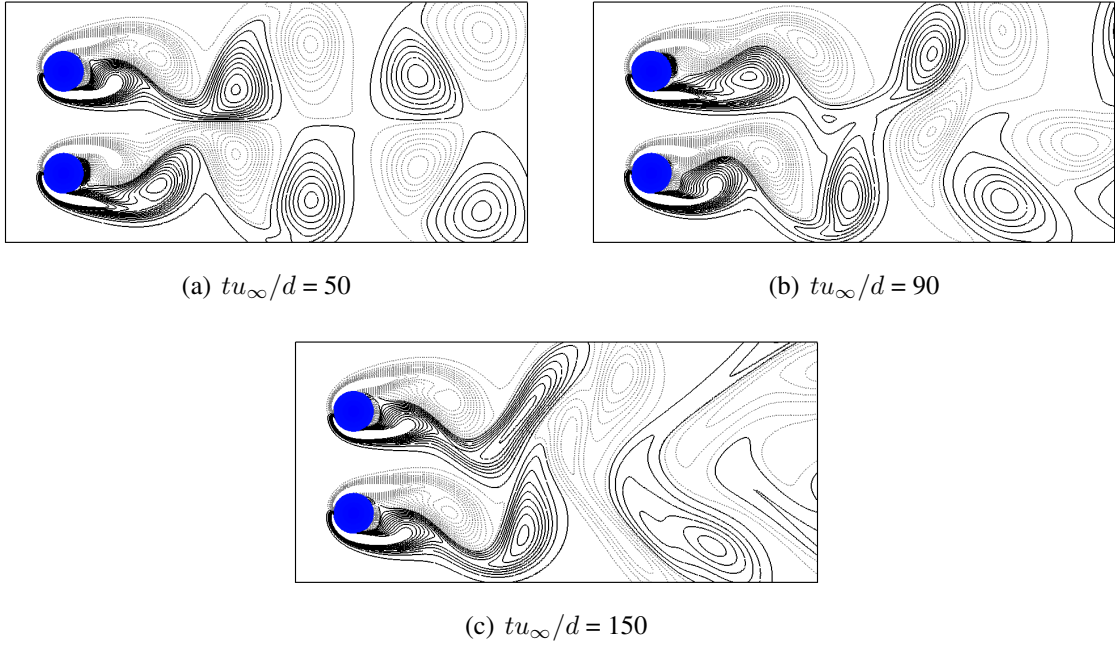


Figure 4.18: Instantaneous snapshot of vorticity iso-lines showing the transitioning from (a) anti-phase to (c) in-phase regime in vortex shedding of the two cylinders using cut-cell scheme with cubic reconstruction ( $k=3$ ) (solid and dotted lines denote positive and negative vorticity, respectively).

The results of the time history of lift coefficients for the upper and the lower cylinder are shown in Fig. 4.19 for  $k = 2$  and  $k = 3$  and compared with the earlier spectral difference study [127].

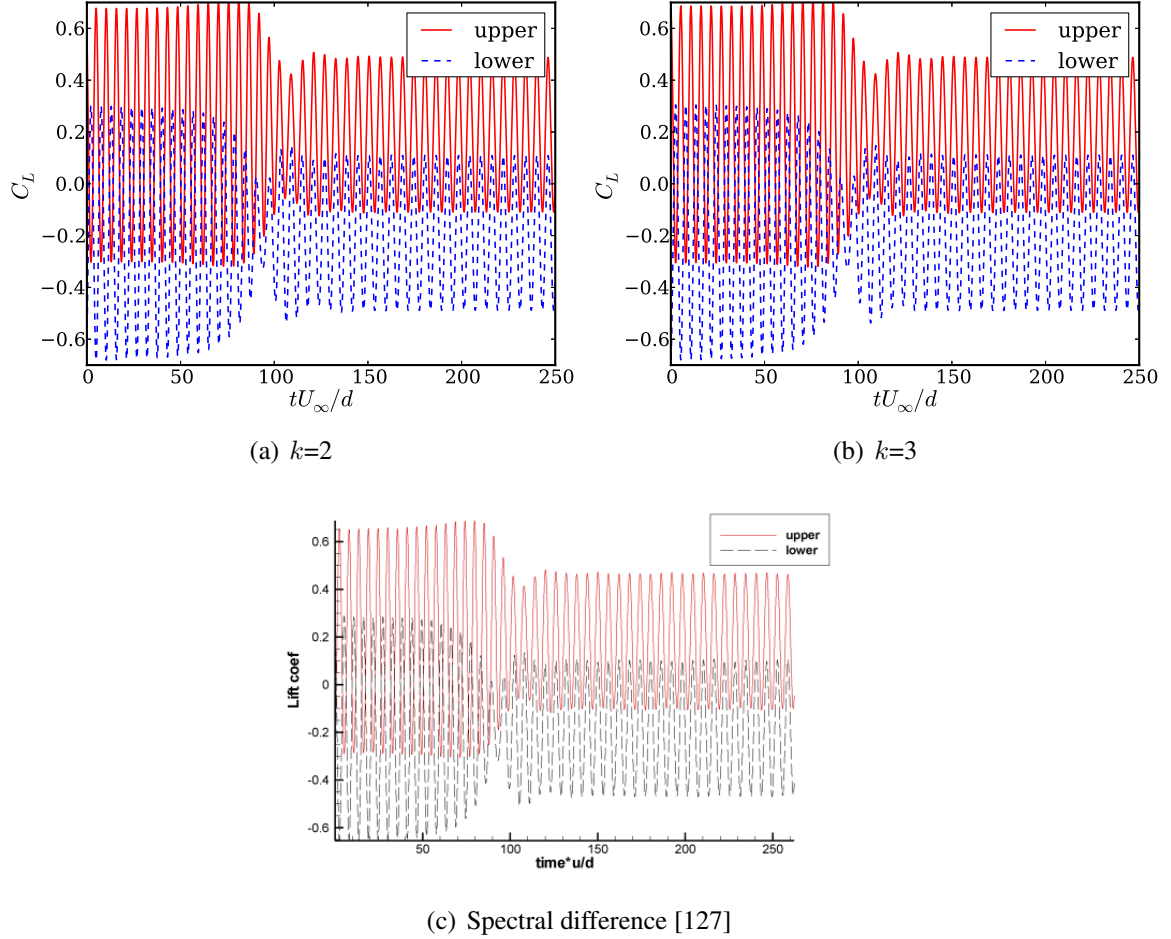


Figure 4.19: Lift coefficient history for two side-by-side cylinders in a  $Re_d = 100$  cross flow with: (a)  $k=2$  (b)  $k=3$  (c) Spectral difference method (figure taken from [127]).

As seen in Fig. 4.19, the transition in the wake pattern is captured accurately by the present method with both  $k=2$  and  $k=3$ . The lift coefficient history is in fact almost identical for both the second-order and third-order schemes implying that the near cylinder wall physics is accurately captured even with the second-order scheme. As seen from the results of the single cylinder studies in Section 4.2.3, the higher order reconstruction improves the solution only for a coarse mesh. For a relatively well resolved mesh as used in this case, the



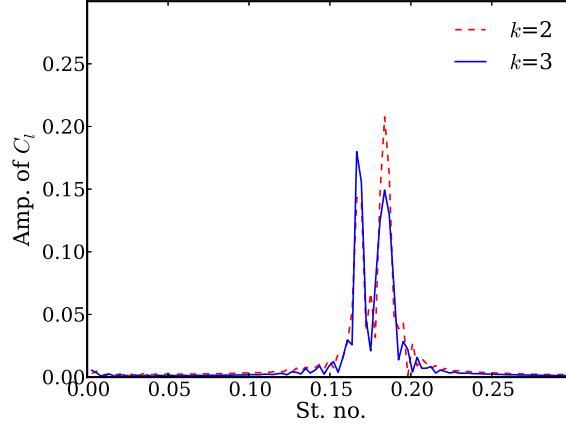


Figure 4.20: Fast Fourier Transform of lift coefficient for  $k=2$  and  $k=3$ .

predictions are not expected to improve between  $k=2$  and  $k=3$ . The Fast Fourier Transform (FFT) of the lift coefficient of the top cylinders is presented in Fig. 4.20. The peaks correspond to the shedding pattern before and after transition. First peak corresponding to the inphase vortex shedding is occurring at around  $St \approx 0.167$  with both  $k=2$  and  $k=3$  and is close to the value reported by Kang [130].

Further, to analyze the performance of the proposed scheme for geometries involving narrow gaps, the wake pattern behind the two cylinders is also investigated when they are very close to each other. The same configuration used in the previous case is employed but the cylinders are now placed close to each other separated by a narrow gap of  $\Delta=0.01875D$  which corresponds to a single numerical grid for the chosen resolution. Such a configuration is difficult to simulate for any scheme and to the best of authors knowledge, is not investigated in the past using body-fitted or IB methods. This is essentially due to the difficulty in achieving a good numerical grid resolving the narrow gap between cylinders. The particular interest in this case is the behavior of the higher order  $k$ -exact reconstruction near narrow gaps and therefore  $k=3$  cubic reconstruction is employed. Due to lack of experimental or numerical data for this configuration, only qualitative assessment of the results are made.

The vorticity patterns in the wake of the two cylinders as seen in Fig. 4.21 clearly shows a single vortex street behind the cylinders. The time history of the lift coefficients for the upper

and the lower cylinder are shown in Fig. 4.22 and confirm the in-phase nature of the vortex shedding. Since the two cylinders are almost in contact with each other with  $P/D \approx 1.0$ , the flow patterns exhibits behavior seen for a single bluff body. The vortex shedding frequency is different from that of a single cylinder, but only a single von Kármán vortex street is observable. These characteristics were also noticed in the experiments [131] in which flow patterns were studied when two staggered cylinders are placed in a cross-flow. When the two cylinders are separated by a small gap, the flow bleeds through the gap and affects the vortex shedding process. Even though only a single von Kármán vortex street is observed, the length of the wake region extends because of the presence of the base bleed.

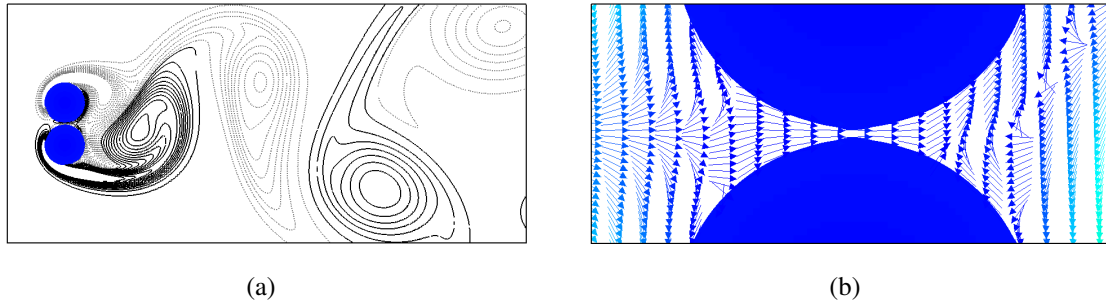


Figure 4.21: Instantaneous snapshot of (a) vorticity iso-lines showing a single bluff body vortex shedding pattern for two cylinders in close contact with the each other using cut-cell scheme with cubic reconstruction ( $k=3$ ) (solid and dotted lines denote positive and negative vorticity, respectively), and (b) Velocity vector plot near the narrow gap.

#### 4.2.5 Low Reynolds number flow over a corrugated airfoil

One of the main advantages of employing sharp interface schemes such as cut-cell method is that sharp and irregular bodies can be accurately resolved. To demonstrate that the proposed high order cut-cell scheme can work with abrupt geometrical discontinuities without loss of accuracy, the results are presented for the problem of flow over a corrugated airfoil of chord length  $c$  at a chord based Reynolds number of  $Re_c = 10,000$ . The airfoil represents the cross-section located at the mid-section of the forewing of a dragonfly (*Aeshna cyanea*). Three different angles of attack,  $\alpha = 0, 5$  and  $10$  degrees are considered for this study.

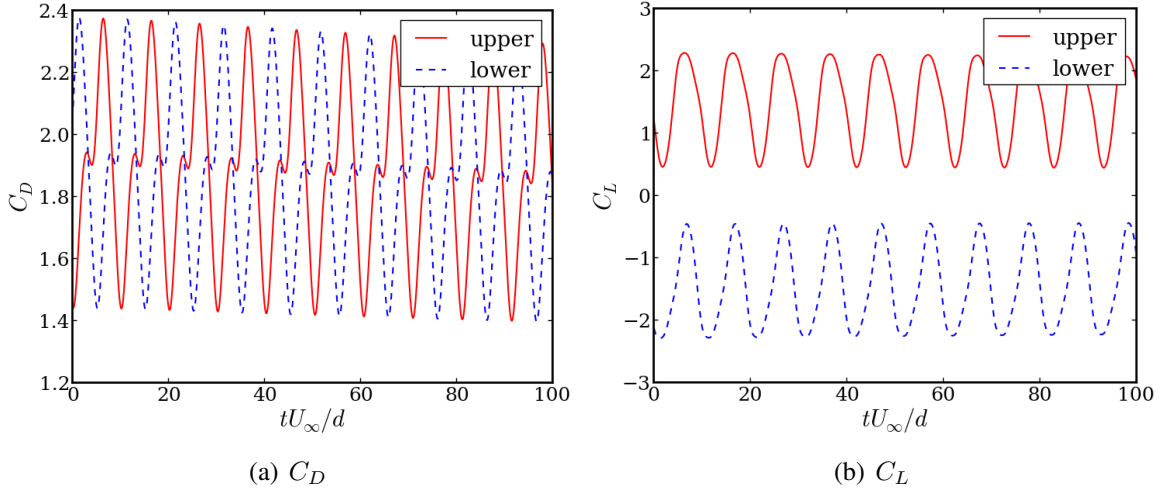


Figure 4.22: Drag and lift coefficient history for two side-by-side cylinders close to each other in a  $Re_d = 100$  cross flow exhibiting an in-phase shedding regime.

This specific profile of the airfoil was experimentally investigated by Kesel, [132] and was also numerically studied by Vargas *et al.*, [133]. Both  $k = 2$  and 3 reconstruction are used for this study. The domain and grid resolution is based from the previous numerical study of Vargas *et al.*, [133]. The domain size is  $12c \times 6c$  with the airfoil located at the center. An effective grid resolution of  $0.0834t$ , where  $t$  is the thickness of the airfoil, is used by employing AMR with 5 levels of refinement. The mesh in the close proximity of the airfoil is shown in Fig. 4.23.

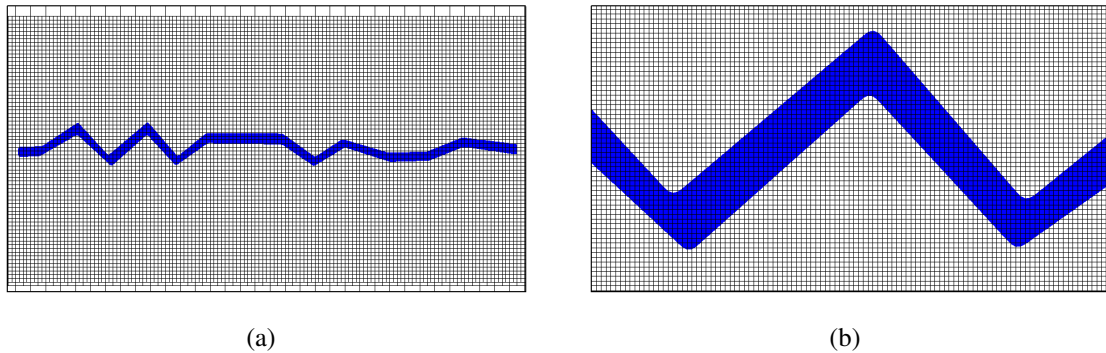


Figure 4.23: Numerical mesh (a) in the vicinity of the corrugated airfoil (only every 4 points shown) and (b) zoomed in view to highlight the sharp geometrical discontinuities.

In comparison with a profiled airfoil, the corrugated airfoil can achieve higher lift at the same flight conditions [132]. The corrugation prevents large-scale flow separation and airfoil stall at low Reynolds numbers. This is because the protruding corners of the corrugated airfoil generates unsteady vortex structures to promote the transition of the separated boundary-layer flow from laminar to turbulent. Experimental studies of Hu and Tamai [134] showed that the unsteady vortex structures trapped in the valleys of the corrugated cross section can bring in high speed fluid flow from the outer section into the corrugations which results in increase of the kinetic energy of the near-wall flow preventing flow separation and stall. Therefore accurate resolution of the sharp corners is of paramount importance for any numerical scheme in accurately predicting of aerodynamic performance of corrugated airfoils. This generally is not easy to achieve with traditional methods due to mesh singularity near corners and inability of some numerical schemes to handle abrupt geometrical discontinuities.

The instantaneous plots of the vorticity iso-lines for the three different angles of attack at a same time instant is shown in Fig. 4.24. Consistent with past observations [133], there is a considerable amount of flow separation and reattachment in the valleys of the corrugation. At  $\alpha = 10^\circ$ , there is a large scale vortex role up as evident in the instantaneous plots.

The comparison of the time averaged plot of the lift and drag coefficients for the different angles of attack with the past data are presented in Fig. 4.25. As in the previous study [133], the data for the first 5 time units is ignored and the time averaging is done over next 15 time units for  $\alpha = 0^\circ$ , 20 time units for  $\alpha = 5^\circ$  and 40 time units for  $\alpha = 10^\circ$ . A time unit is the non-dimensionalised time using the free stream velocity,  $U_\infty$  and the chord length,  $c$  and is given as  $t^* = tU_\infty/c$ . Good agreement with the experimental results is observed for the drag coefficient,  $C_d$ . The lift coefficient,  $C_l$ , is over predicted by around 28 % at  $\alpha = 10^\circ$ , but for the other two angles of attack, matches well with the experiment. The discrepancy in the lift coefficient can be attributed to possible modification of pressure and shear forces on the airfoil due to the end effects from tunnel walls and this effect can become more pronounced

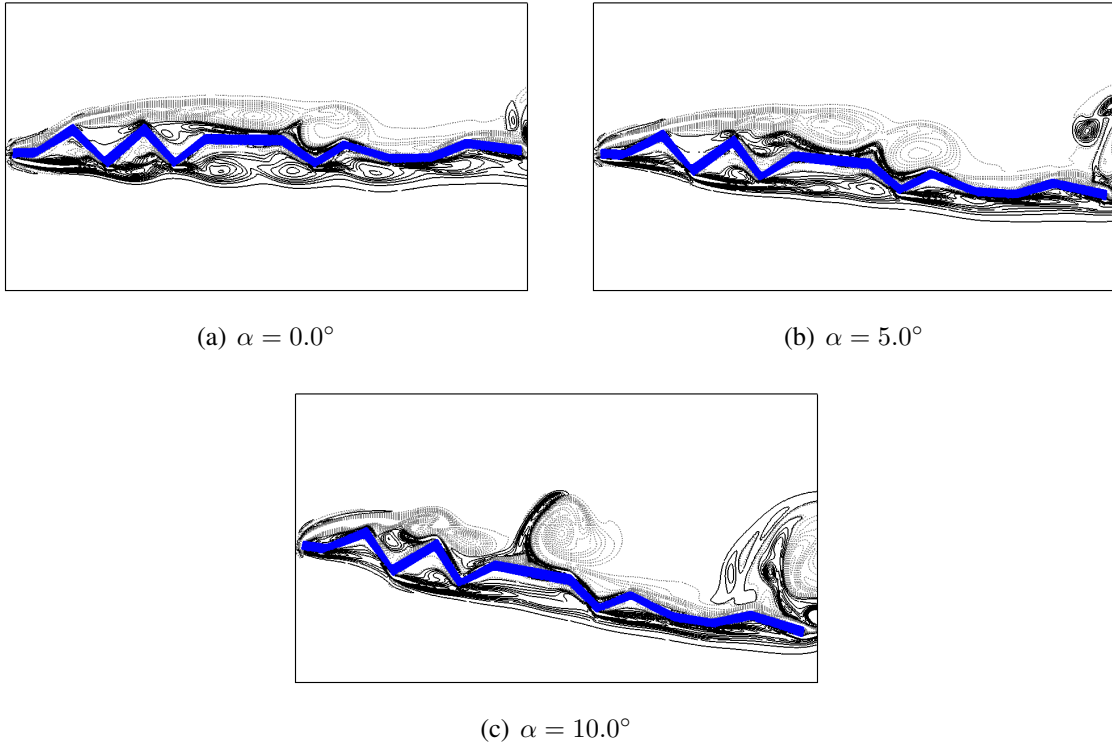


Figure 4.24: Instantaneous snapshot of vorticity iso-lines for flow over corrugated airfoil at different angles of attack using cut-cell scheme with cubic reconstruction ( $k=3$ ) (solid and dotted lines denote positive and negative vorticity, respectively).

at higher angles of attack [133]. The general trend is however well predicted by the cut-cell scheme. It can be observed from Fig. 4.25 that there are noticeable differences in the lift and drag prediction between the past numerical study which employed a finite difference based IB method and the current work. One reason that can be attributed to the differences in the results, is that the sharp corners of the airfoil are more accurately represented using the cut-cell approach. Whereas, in the past study, the airfoil shape was considerably smoothed out to remove the sharp edges for the purpose of reducing resolution requirements of the simulation. Note that the same mesh resolution is used in the present study, but the airfoil geometry is well resolved preserving the sharp edges that are critical to the aerodynamic performance. The lift and drag coefficient results are almost the same using both  $k=2$  and 3. This indicates that the flow is well resolved for this Reynolds number.

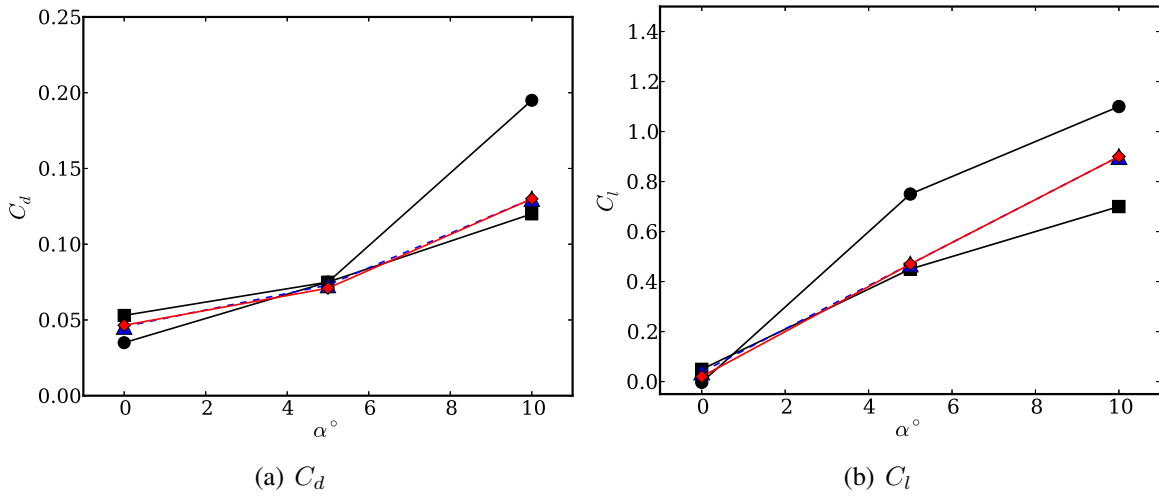


Figure 4.25: Time averaged (a) drag coefficient,  $C_d$  and (b) lift coefficient  $C_l$  at three different angles of attack,  $\alpha=0, 5$  and  $10^\circ$  compared with Experiments [132] (—■) for  $k=2$  (-.-▲);  $k=3$  (—◆) and previous numerical study (—●) [133].

#### 4.2.6 Three dimensional flow over single and multiple spheres in cross-flow

In this final study, a Mach 0.2 laminar flow over a single sphere at various Reynolds numbers are simulated along with the flow over two side-by-side spheres at  $Re_d=100$ . The purpose

of these simulation is to demonstrate that the proposed cut-cell method remains robust and accurate for 3D flows as well. The simulation results with current scheme are compared with some of the earlier experimental and simulation data [135, 136, 55, 25] for flow over a single sphere. Although seemingly simple, this is a challenging case for IB methods as all possible angles of intersection between the embedded boundary and the Cartesian grid occur.

All the three-dimensional cases were run with quadratic polynomial reconstruction ( $k=2$ ). A reasonably fine mesh resolution of 40 points per diameter of the sphere is used for all the cases ( $D/\Delta x = 40$ ). It was observed from the studies on single cylinder presented in Section 4.2.3 that for this resolution,  $k=3$  did not significantly improve the results. Thus for all the three-dimensional cases, a quadratic reconstruction with  $k=2$  is employed. Higher order reconstruction for three-dimensional flows will be performed for high Reynolds number flows in near future. For both, the single sphere and multiple spheres cases, A domain of size  $32D \times 32D \times 32D$  with 5 levels of local mesh refinement performed from a base resolution of  $0.8D$  is used resulting in an effective resolution of  $0.025D$ . The choice of grid resolution is based on the numerical grid convergence studies for flow past a single cylinder conducted earlier and reported (see Section 4.2.3).

Streamline plots for flow over a single sphere for various Reynolds numbers is shown in Fig. 4.26. As noted in the past studies [135, 55], the flow remains steady until  $Re_d \approx 270$  and at Reynolds numbers ranging between 270 to 300, an onset of unsteady motion occurs that causes periodic vortex shedding. Since the Reynolds number of the flow is less than the critical Reynolds number, the flow is steady for all the cases. As noted in Fig. 4.26, the wake pattern remains symmetric and an increase in the Reynolds number is resulting in a progressively bigger re-circulation region. The results of the computations for the steady regime are summarized in Table 4.11 and compared with past data from literature. As observed, there is a very good agreement between the current study and the past studies. The Table 4.12 compares the results of the cut-cell simulations for  $Re_d= 300$  with data from previous studies. At this Reynolds number, the wake becomes unsteady resulting in complex three dimensional

hairpin-like structures. The mean drag, lift coefficient and Strouhal number predictions agree well for also this unsteady case with the past results. The Q-criterion [137] is generally used to identify the vortex structures in numerical simulations and is defined as:

$$Q = \frac{1}{2} (\Omega_{i,j}\Omega_{i,j} - S_{i,j}S_{i,j}), \quad (4.50)$$

where  $\Omega_{i,j} = \frac{1}{2}(\frac{\partial u_i}{\partial x_j} - \frac{\partial u_j}{\partial x_i})$  is the rotation rate and  $S_{i,j} = \frac{1}{2}(\frac{\partial u_i}{\partial x_j} + \frac{\partial u_j}{\partial x_i})$  is the strain rate. The iso-surface of Q-criterion with  $Q > 0$  will identify regions where the rotation rate dominates the strain rate and thus visualizing the vortex regions. The vortex structures identified by iso-surface of Q-criterion for the  $Re_d = 300$  flow past sphere is shown in Fig. 4.27. The hairpin-like flow structures are clearly identifiable in the wake of the sphere.

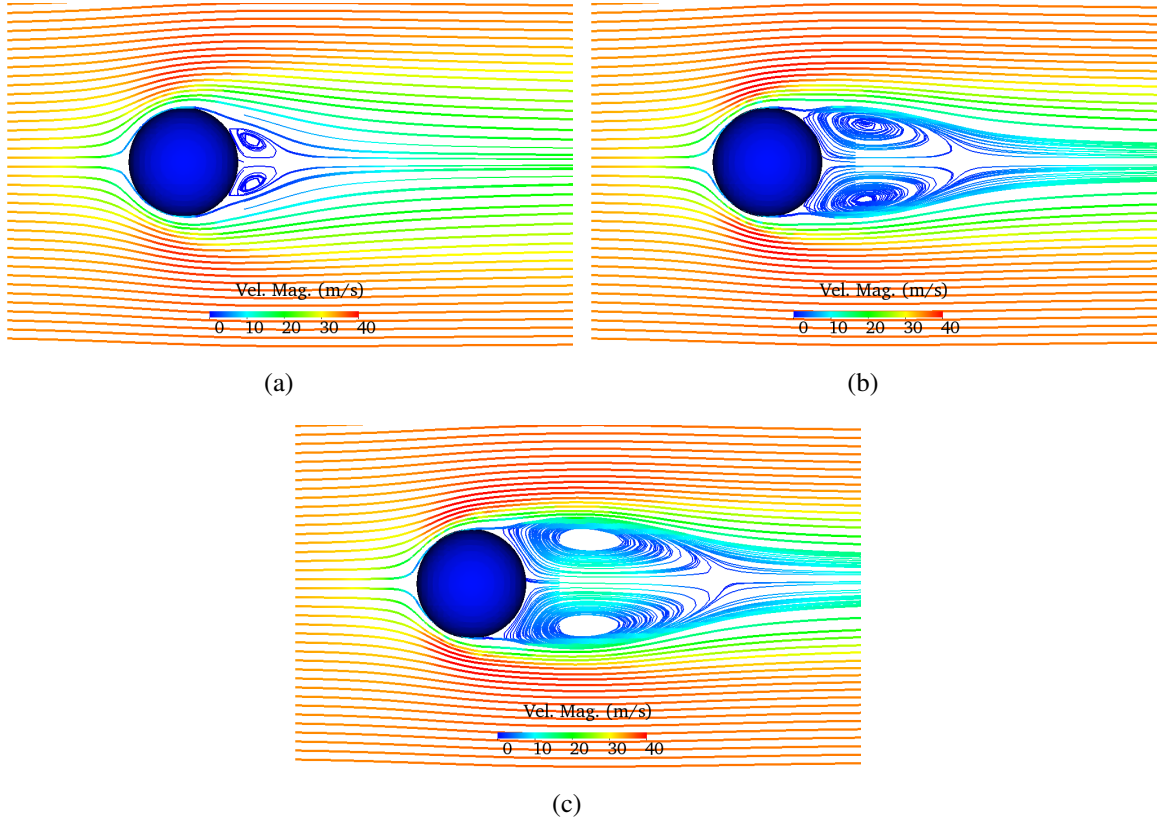


Figure 4.26: Instantaneous streamlines for flow past a single sphere at:(a)  $Re_d = 50$  (b)  $Re_d = 150$  (c)  $Re_d = 250$  shown in  $x - y$  plane



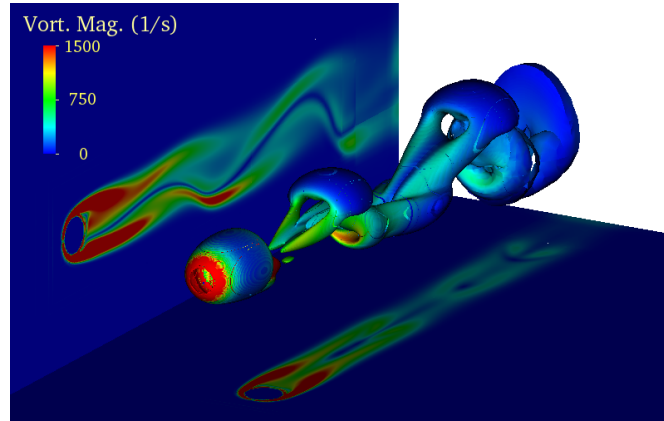


Figure 4.27: Iso-surfaces of Q-criterion colored with vorticity magnitude for  $Re_d = 300$  flow past sphere.

Table 4.11: Drag coefficients for flow over sphere at different  $Re_d$ .

Contribution	$C_d, Re_d=50$	$C_d, Re_d=150$	$C_d, Re_d=250$
<b>Present</b>	<b>1.56</b>	<b>0.88</b>	<b>0.69</b>
Johnson and Patel [135]	1.57	0.9	-
Marella <i>et al.</i> [136]	1.56	0.85	-
Kim <i>et al.</i> [55]	-	-	0.70
Hartmann <i>et al.</i> [25]	1.57	0.88	0.0

Table 4.12: Drag, lift coefficients and Strouhal number for flow over sphere at  $Re_d = 300$ .

Contribution	$\overline{C_d}$	$\overline{C_l}$	St. no.
<b>Present</b>	<b>0.52</b>	<b>-0.063</b>	<b>0.131</b>
Johnson and Patel [135]	0.656	-0.069	0.137
Kim <i>et al.</i> [55]	0.657	-0.067	0.134
Hartmann <i>et al.</i> [25]	0.657	-0.069	0.135

The case of  $Re_d=100$  flow over two spheres separated from each other with center to center pitch to diameter ratio of  $P/D = 0.75$  was previously investigated by Kim *et al.* [6] using a body-fitted structured grid approach to understand the three-dimensional flow interactions between droplets and solid particles. Generating a good grid is considerably complex in the vicinity of multiple spheres and in the prior study [6], a symmetry condition was imposed on the plane separating the two spheres and only a single sphere was actually simulated. The limitation with the approach is that only steady state flow with low Reynolds number can be investigated. In the current approach, the complete grid involving both the spheres is generated and hence the approach allows study of both steady and unsteady flow over multiple spheres.

Figure 4.28(a) shows the pressure coefficient,  $C_p$ , around the top sphere in the principal x-y plane and the results agree well with the previous numerical study [6]. As seen in the figure, due to the presence of another sphere in the vicinity, the pressure on the top part of the sphere is, on an average, higher than the bottom sphere contributing to a positive lift force, which is absent in case of flow past a single sphere. The spatial pressure coefficient distribution along the surface of the spheres is shown in Fig. 4.28(b) along with the flow streamlines in the principal plane. Note the smooth distribution of the pressure coefficient along the surface of the spheres. In Fig. 4.29(a), the skin friction coefficient,  $C_f$ , is shown in the same principal plane as in Fig. 4.28(a). The presence of a neighboring sphere makes the distribution of  $C_f$  asymmetric between the top and bottom surfaces of the sphere. An interesting feature of the shear stress plot is the differences in the angle at which the shear stress vanishes ( $C_f = 0$ ) for the top and bottom surface indicating different separation points. There is a very good agreement of the  $C_f$  distribution with the previous study [6]. Especially, the flow separation angles are in excellent agreement. There is a minor difference in the magnitude of the peak shear stress, nevertheless the smoothness in  $C_f$  distribution on the top and bottom surfaces (Fig. 4.29(b)) and the earlier results of  $C_p$  shows that the current implementation is accurate and models the near wall region very well.

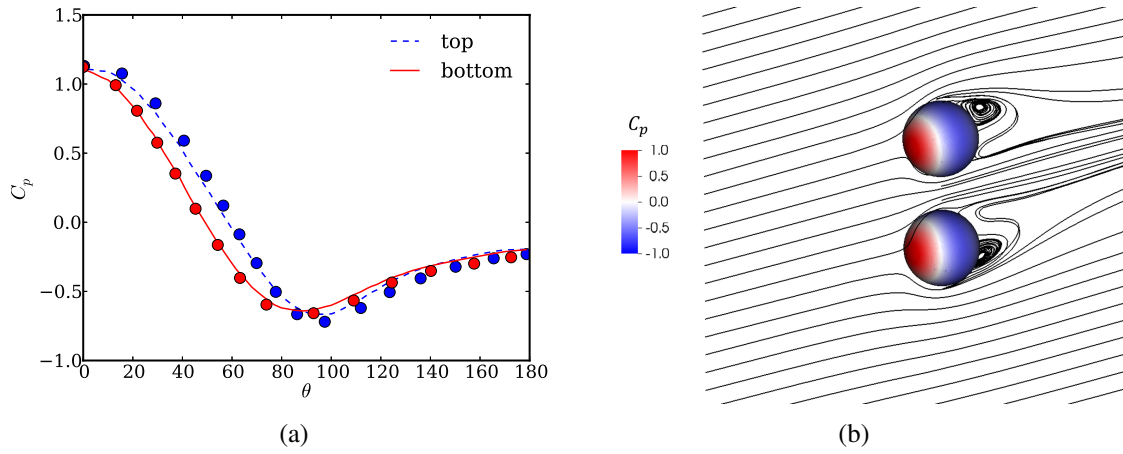


Figure 4.28: (a) Distribution of the pressure coefficient,  $C_p$  around the top and bottom sphere in the principal x-y plane (Filled dots - [6]). (b) Smooth spatial distribution of  $C_p$ , on the surface of the top and bottom sphere. Also shown are flow streamlines in the principal plane.

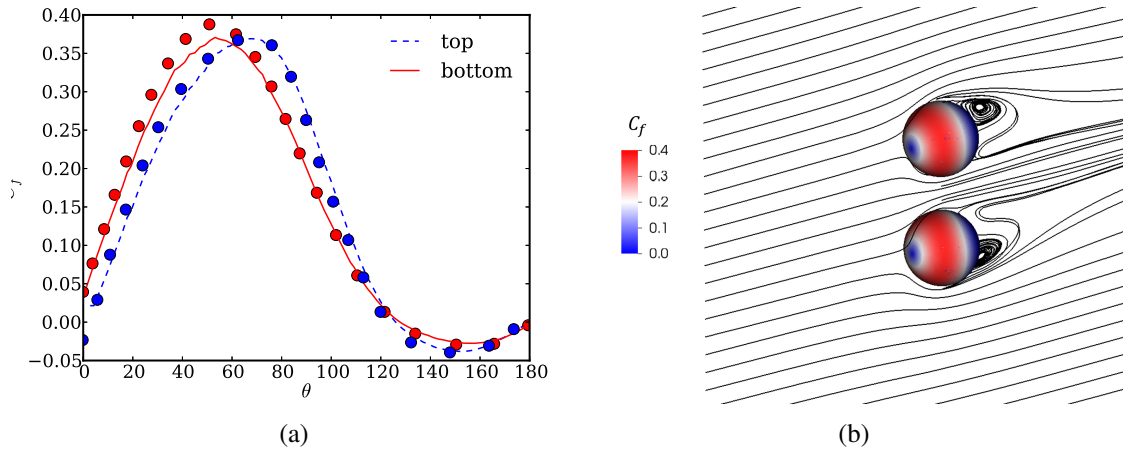


Figure 4.29: (a) Distribution of the skin friction coefficient,  $C_f$ , around the top and bottom sphere in the principal x-y plane (Filled dots - [6]). (b) Smooth spatial distribution of  $C_f$ , on the surface of the top and bottom sphere. Also shown are flow streamlines in the principal plane.

### 4.3 Validation of second order cut-cell method for moving boundaries

The order of accuracy of the moving cut-cell method is assessed by studying isentropic expansion of a gas confined between two reflecting walls. The validation of the new cut-cell method for moving boundary problems is then performed by studying a piston moving at Mach 2 in a quiescent ambient air. The grid convergence of the shock location is reported for various grid resolutions. To demonstrate the strict mass conservative property of the current scheme, results are reported for flow inside an oscillating membrane. Next, comparison of surface pressure and wall shear stress distribution is presented for the case of a cylinder moving at subsonic and supersonic velocities in a stationary fluid with an equivalent static boundary problem with moving fluid and stationary cylinder. The ability of the method to handle coupled fluid and rigid body motion is demonstrated by studying the problem of shock driven cylinder motion. Validation studies are then presented for the case of a moving piston in a reacting flow at supersonic velocities and the results are compared with an equivalent static boundary problem. Finally, the developed cut-cell scheme is applied to study the complex problem of detonation initiation and propagation by a hypervelocity projectiles shot into a detonable mixture. All the test cases and their motivations are listed in Table 4.13.

All the simulations, unless mentioned, use a time step based on a CFL number of 0.5 and  $\alpha_{lim} = 0.75$  such that the time step restrictions are close to the ones based on the full cell volume. This value of limiting volume fraction,  $\alpha_{lim}$ , is much higher than the usual value of 0.5 used in most of the previous cut-cell approaches. A quadratic reconstruction  $k = 2$  is employed for all the cases. This provides a third order accuracy in the computation of inviscid fluxes and second order accuracy for viscous fluxes evaluation in regions of smooth solution. Finally, the hybrid cut-cell scheme using the high-order CENO reconstruction in smooth regions of flow and a second order limited MUSCL reconstruction in regions of flow discontinuities is used for the all the simulations.

Table 4.13: Summary of test cases and their motivation.

Case	Motivation
Smoothly expanding piston	Assess the order of accuracy of the cut-cell method for moving boundaries
Non-reacting moving piston with prescribed supersonic motion	Check accuracy and strict mass conservation property of scheme
Flow inside an oscillating membrane	Demonstrate strict mass conservation even for deforming bodies
Moving subsonic/supersonic cylinder in a viscous flow	Compare solution accuracy with static cases and demonstrate smooth reconstruction of shear stress for moving boundaries
Shock driven cylinder motion	Demonstrate the accuracy and robustness of scheme for coupled fluid/rigid body interactions

#### 4.3.1 Smoothly expanding piston

A one-dimensional test case in which a non-reacting gas is confined between two reflecting walls located at  $x_l = 0.0$  and  $x_r = 0.5 + v_r t$ , where the right most wall is moving at a velocity  $v_r$  is considered. The initial conditions for the flow field variables are given as:

$$[\rho(x), u(x), p(x)]^T = [1 + 0.2 \cos(\pi - 2\pi x), 2v_r(1 - x), \rho(x)^\gamma]^T. \quad (4.51)$$

The entropy for the initial state is constant, i.e,  $s(x, 0) = p(x, 0)/\rho(x, 0)^\gamma = 1.0$  and remains constant with time as long as the solution is smooth. Since the flow is subsonic, discontinuities such as shocks are absent in the flow field, and the solution is expected to remain smooth. The error in entropy is thus an effective measure of the numerical error induced by the scheme. The  $L_\infty$  and  $L_1$  error norms for the entropy are reported after a time of  $t_e = 0.5$  secs in Fig. 4.30. The formal order of accuracy of the moving cut-cell method appears to be only second order accurate even with  $k = 2$  for which a third-order convergence is expected. The drop in order of convergence might be related to the corrections given by Eqs. (4.32) and (4.33) which enforce strict conservation during cell emerging and vanishing events. Though the formal order of accuracy is only second order, the drop in magnitude of

the error with an increase in the order of reconstruction can be clearly observed. Thus more accuracy is obtained by high-order reconstruction even though the formal order of accuracy of the moving cut-cell method is only second order.

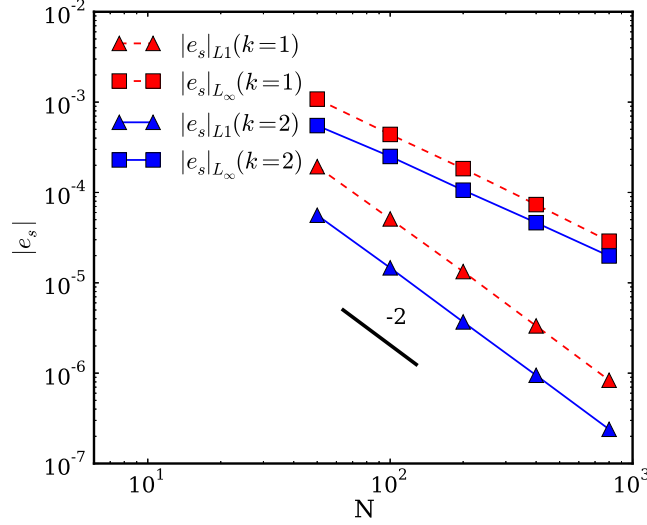


Figure 4.30: Convergence rates in error of entropy for the case of smoothly expanding piston.

#### 4.3.2 Non-reacting piston with prescribed supersonic motion

In this first example, a piston is moved at a constant speed of Mach 2 in a quiescent fluid. The piston of thickness  $L$  is initially centered at  $x = 64L$  in a 2D domain of length  $128L \times 4L$ , where  $L$  is a reference length. As the piston moves, a compression shock is formed ahead and a rarefaction wave results behind the piston. The flow solution at the front and the back of the piston can be treated as two independent Riemann problems for which exact analytical solutions are available [138]. As noted in the past studies of the same case [139, 104], strict conservation of mass, momentum and energy is essential for predicting the correct shock speed and the structure of the expansion region.

Computations for this case are done on a series of grid resolutions:  $\Delta x = L/2, L/5, L/10$  and  $L/20$  respectively. The coarsest resolution is chosen such that the piston is resolved by at least two cells. Slip walls are employed in the axial and transverse directions. The piston,

which is initially at rest, is given a sudden acceleration to a Mach number of 2 based on the initial fluid conditions. The computations are performed till a time unit of  $t = 25L/v_p$ , where  $v_p$  is the speed of the piston, after which the solutions at various grid resolutions, are compared.

The normalized pressure, density and the Mach number profiles at  $t = 25L/v_p$ , for the different grid resolutions are shown in Fig. 4.31. It can be seen that the flow solutions look converged even at the lowest grid resolution. The comparison of the profiles for the finest resolution case with the analytical solutions is shown in Fig. 4.32. There is an excellent agreement of the solution for the shock and the expansion region with the analytical results. A lesser accurate or a lesser robust scheme would not be able to produce correct results for this case especially even at the lowest resolution. It must be noted for cases of this nature, where a shock or expansion results due to a high-speed body in motion, the conservative nature of the scheme is most important. The fact that our scheme is conservative can be confirmed from the observation that the position of the shock is the same for different grid resolutions. This is an important asset of the method which guarantees exact prediction of high-speed flow features around moving interfaces even at a relatively coarse grid resolution.

#### 4.3.3 Oscillating membrane

The strict conservative property of the cut-cell scheme for deforming boundaries is verified by studying flow in an oscillating membrane. For a time period of oscillation given by  $T_p$ , the instantaneous location of the membrane surface satisfies:

$$\frac{x^2}{a^2} + \frac{y^2}{b(t)^2} = 1, \quad (4.52)$$

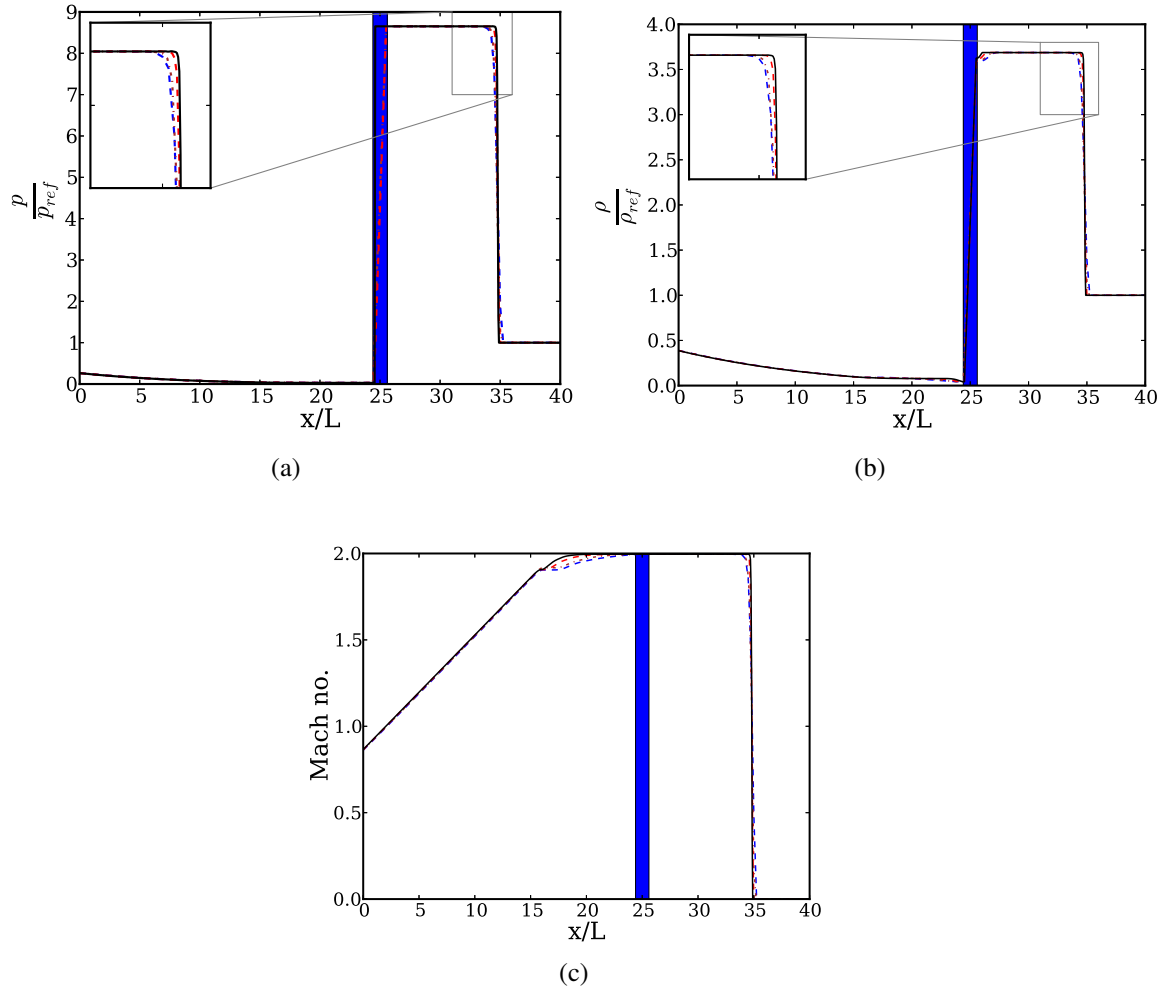


Figure 4.31: Grid convergence studies of (a) pressure, (b) density and (c) Mach no. profiles for the piston moving at Mach 2:  $\Delta x =$   $-\cdot-\cdot L/2$  ;  $-\cdot-\cdot L/5$  ;  $— L/10$  ;  $— L/20$  (piston region colored with blue).



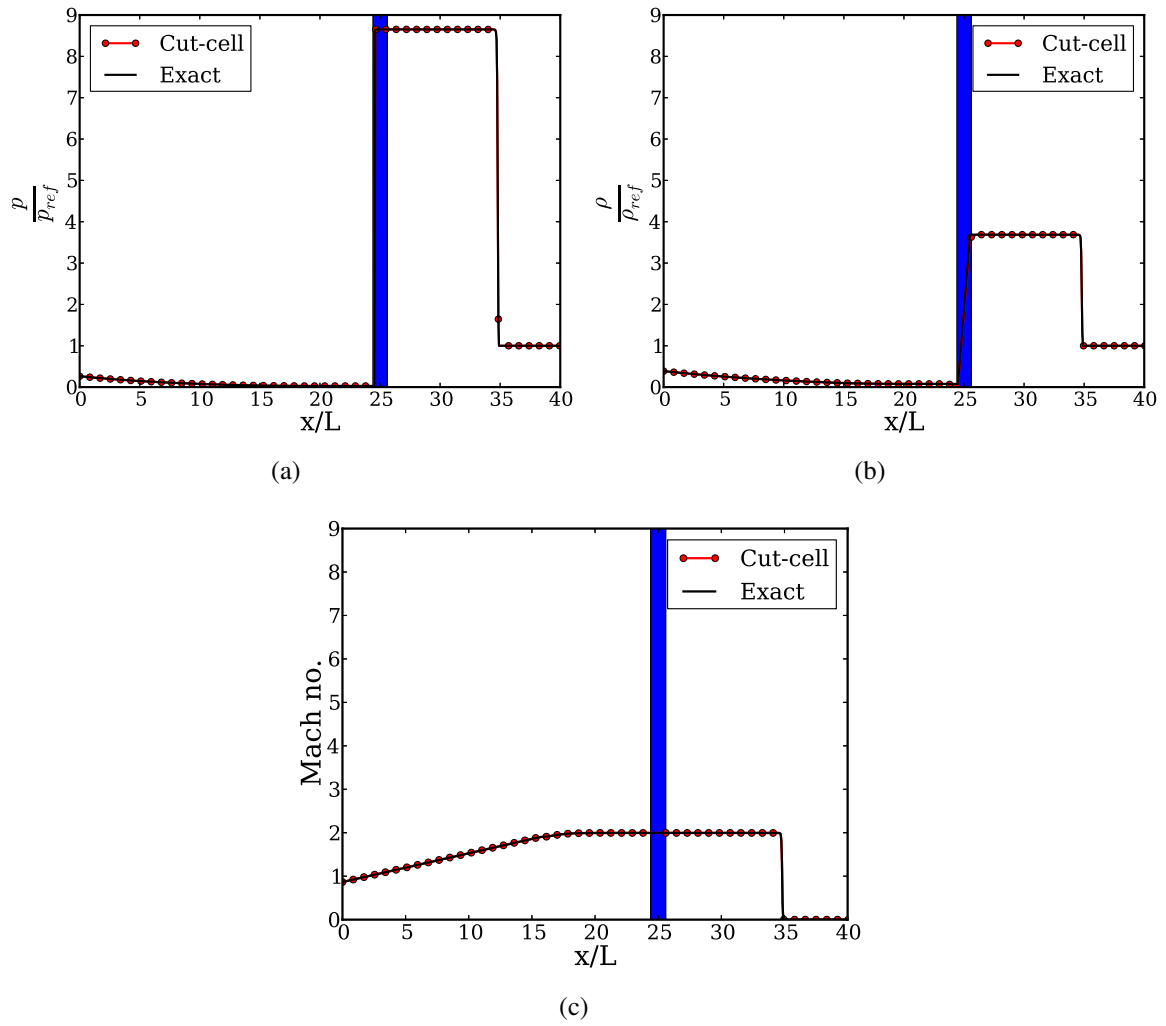


Figure 4.32: Comparison of (a) pressure, (b) density and (c) Mach no. profiles for the piston moving at Mach. 2 for  $\Delta x = L/20$  with analytical results (piston region colored with blue).

where  $a = 0.1$  and  $b(t) = a \left( 1 + 0.5 \sin\left(\frac{2\pi t}{T_p}\right) \right)$ . The surface velocity is then given by:

$$\frac{dy}{dt} = \begin{cases} +\frac{\pi a}{T} \cos\left(\frac{2\pi t}{T} \sqrt{1 - \frac{x^2}{a^2}}\right) & \text{if } y > 0, \\ -\frac{\pi a}{T} \cos\left(\frac{2\pi t}{T} \sqrt{1 - \frac{x^2}{a^2}}\right) & \text{if } y < 0. \end{cases} \quad (4.53)$$

Slip conditions are imposed on the surface of the membrane. Atmospheric conditions are assumed for the initial fluid state in the membrane. The membrane oscillation is simulated for two time periods during which the surface locations of the membrane change at various time instants of oscillation as shown in Fig. 4.33(a). Since the membrane is oscillating, the volume change results in progressive compression and expansion of the fluid medium. The average density ratio at any instant of time,  $t$ , can be found both numerically and analytically as:

$$\left(\frac{\bar{\rho}}{\rho_0}\right)_{ana} = \frac{\pi a^2}{\pi a b(t)}, \quad (4.54)$$

$$\left(\frac{\bar{\rho}}{\rho_0}\right)_{num} = \frac{\sum_{n=1}^N V_n \rho_n}{\sum_{n=1}^N V_n \rho_0}, \quad (4.55)$$

where  $N$  corresponds to the total number of cells in the numerical mesh,  $\rho_0$  is the initial density of the fluid under atmospheric conditions and  $V_n$  is the volume of the  $n^{th}$  grid cell.

The comparison of the instantaneous average density ratio  $\frac{\bar{\rho}}{\rho_0}$  from the simulation with the exact analytical value is shown in Fig. 4.33(b). The differences in the values were of the order of  $O(10^{-16})$  and is constant throughout the simulation implying that the mass conservation is enforced up to machine precision using the current scheme. Grid convergence studies are also conducted for this case but the results did not show any sensitivity to the grid resolution and therefore not shown.

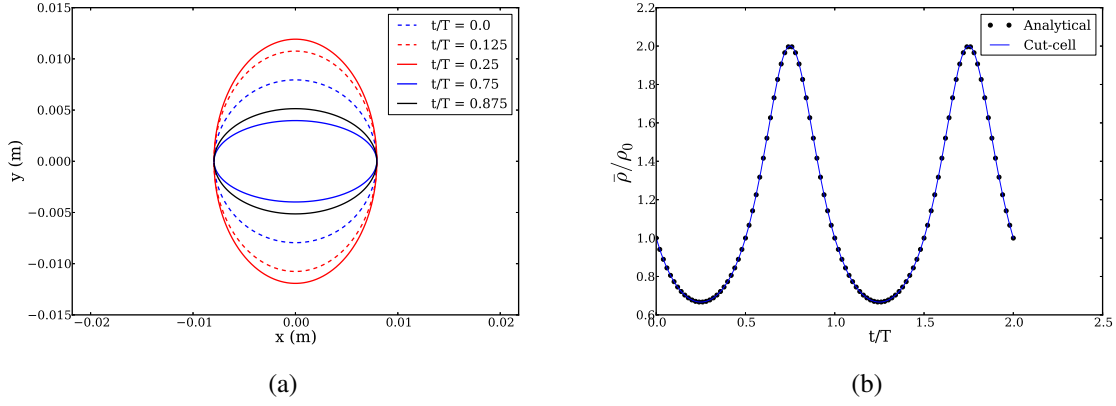


Figure 4.33: (a) Shape of the membrane at various time instants and (b) the comparison of the average density with analytical value.

#### 4.3.4 Moving cylinder in a viscous flow under subsonic conditions

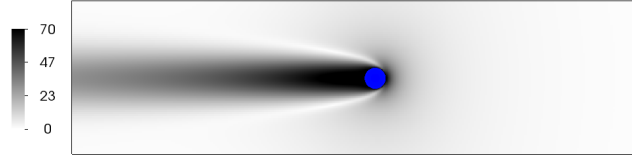
The canonical problem of a moving cylinder in a stationary viscous flow is considered for evaluating the moving cut-cell method for viscous flow problems. Extensive studies for this case have been performed both experimentally and numerically [55, 128] in the past and are used for validating the current cut-cell scheme for simulating moving boundaries in a viscous flow. The initial fluid conditions are atmospheric and the cylinder, initially at rest, is instantaneously accelerated to a uniform velocity of  $u_c$  such that the Mach number based on the initial fluid conditions is  $M = 0.2$  and the Reynolds number based on the diameter,  $D$ , is  $Re_d = 40$ . A domain size of  $80D \times 16D$  is used with the cylinder initially located at  $1.5D$  from the left boundary. Subsonic characteristics based outflow conditions are used on all the boundaries while a no-slip condition is imposed on the moving boundary of the cylinder. Computations are performed for a flight time of 65 non-dimensional time units,  $t^* = tu_c/D$ , during which the cylinder moves through a distance of  $78.5D$ . It is ascertained that the change in the drag and lift coefficients are less than 0.1 % for the last 20 time units. A series of grids are employed with progressive refinement in resolution in the near field of the cylinder and are summarized in Table. 4.14. The last column denotes the number of grid points resolving the diameter of the cylinder,  $D$ .

Table 4.14: Various grid resolutions used for the moving cylinder at  $Re=40$  case.

Case	Levels of local refinement	$D/\Delta x$
$Re40_{10}$	2	10
$Re40_{20}$	3	20
$Re40_{40}$	4	40
$Re40_{80}$	5	80



(a)  $t^*=36$



(b)  $t^*=46$



(c)  $t^*=57$

Figure 4.34: Contours of velocity magnitude (m/s) at various time instants for the moving cylinder problem in a viscous flow at  $Re 40$  for the case  $Re40_{80}$ .

For the given Mach and Reynolds number, the wake behind the moving cylinder is steady. A symmetric pair of vortices attached to the cylinder develop in the wake and the recirculation region which initially increases, attains a constant size later. The plots of the contours of the velocity magnitude at various time instants during the flight of the cylinder are shown in Fig. 4.34. Figure 4.35(a) plots the temporal history of the drag coefficient,  $C_d = 2F_{drag}/\rho u_c^2$ , for various grid resolutions that are given in Table 4.14. An immediate observation from the plot is the presence of numerical oscillations in  $C_d$  even though the mean looks converged. But these oscillations which are around 2 % for case  $Re40_{10}$  drops to 0.2 % for the finest resolution case  $Re40_{80}$ . The zoomed in view of these oscillations is shown in the Fig. 4.35(b). The reason for the presence of these oscillations may be related to the numerical approximations in the surface properties of the grid which diminishes with higher grid resolution. This is strongly supported by the almost linear reduction of the fluctuations with the grid refinement as noted in Table 4.14. The occurrence of new cell emerging events and grid cells turning into solid can result in instantaneous changes in the local flow quantities and can also be one of the reasons for the presence of the numerical perturbations. Also, the frequency of these oscillations does seem to have a high correlation with the grid spacing.

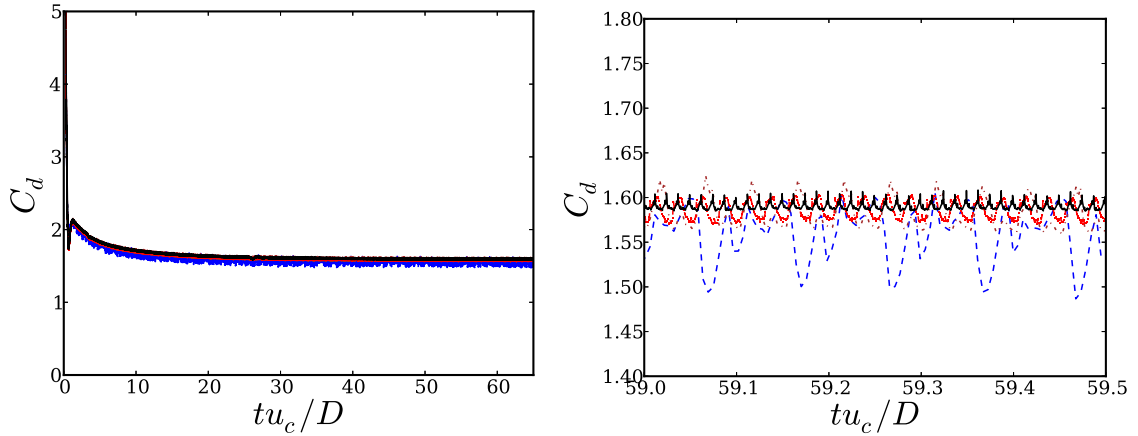


Figure 4.35: (a) Comparison of the drag coefficient ( $C_d$ ) for the different grid resolutions (b) Zoomed in view showing reduction of oscillations with progressive mesh refinement:  $--Re40_{10}$  ;  $-\cdot- Re40_{20}$  ;  $—Re40_{40}$  ;  $—Re40_{80}$ .

Table 4.15: Grid convergence of  $C_d$  for  $Re_d = 40$ 

Eff. res. ( $D/\Delta x$ )	$\overline{C_d} \pm \sigma_{C_d}$ , Moving (current)	$C_d$ , static [26]	$(\Delta C_d)_{err}$ (current)	order
10	$1.556 \pm 0.0325$	1.551	0.033	-
20	$1.582 \pm 0.0167$	1.559	0.007	<b>2.23</b>
40	$1.587 \pm 0.0099$	1.559	0.002	<b>1.81</b>
80	$1.589 \pm 0.0038$	1.560	-	

In order to further assess the accuracy of the moving cut-cell method, the pressure coefficient,  $C_p$ , computed as  $C_p = (p - p_\infty)/\rho u_c^2$  and the skin friction coefficient computed as  $C_f = 2\tau_f/\rho u_c^2$  along the cylinder surface are analyzed. Here,  $\tau_f$ , is the skin friction on the surface of the cylinder. The results for  $C_p$  and  $C_f$  at different grid resolutions after 60 units of non-dimensionalized flight time are presented in Fig. 4.35(a). Similar to trend observed for flow over static cylinder cases reported in an earlier work by the authors [26], the match with a body-fitted grid results are excellent even at a relatively low resolution of  $\Delta x = D/20$ . It can thus be concluded that all the attributes of the high order adaptive cut-cell method are retained even for the moving boundary cases. The minor numerical oscillations on the integrated quantities though present does not in any manner affect the accuracy of the near wall solution. It has to be noted that, to the best of authors knowledge, the current cut-cell scheme is the only method to predict a smooth skin friction coefficient prediction for moving bodies using an immersed boundary method.

Table 4.15 reports the drag coefficient,  $C_d$ , for the different cases. The  $C_d$  values for the all the cases are averaged over the final 20 time units. Results are also presented for the flow over a static cylinder for same Reynolds number. There is a good correspondence in the values computed for the moving cylinder in a static fluid case with the static cylinder in a moving flow problem. The minor differences could be due to different domain sizes employed for the two cases. The convergence rates of the error in the drag coefficient prediction computed as  $(\Delta C_d)_{err} = |C_{d,n} - C_{d,80}|$  where  $n = 10, 20, \text{ and } 40$ , suggests a quadratic trend implying the present method is second order accurate.

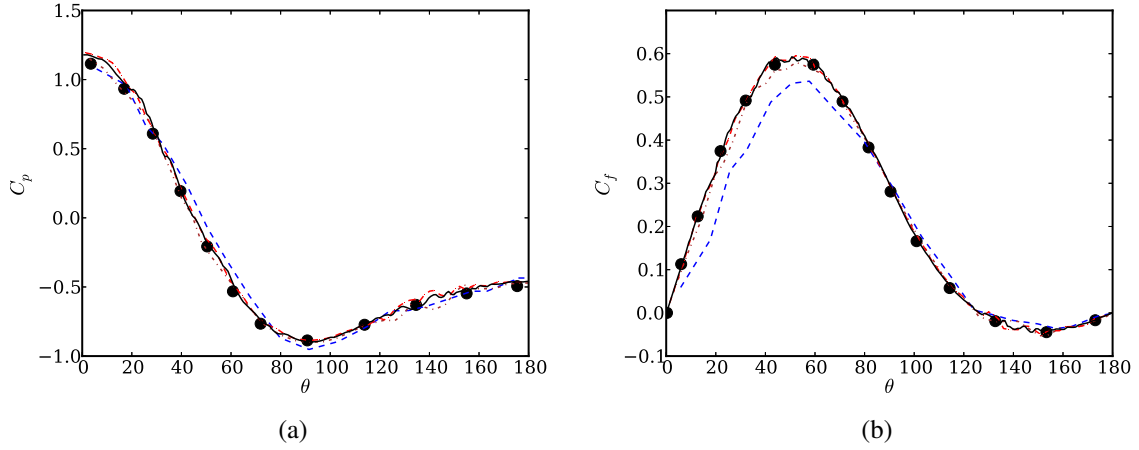


Figure 4.36: Comparison of the pressure coefficient ( $C_p$ ) and the skin friction coefficient ( $C_f$ ) with previous results from a body-fitted grid [17] (solid back dots) for the case of  $Re=40$  moving cylinder in a viscous flow:  $Re40_{10}$  ;  $Re40_{20}$  ;  $Re40_{40}$  ;  $Re40_{80}$ .

#### 4.3.5 Moving cylinder in a viscous flow under supersonic conditions

The new approach is applied to studying the problem of a cylinder moving at supersonic velocities in a viscous fluid medium. This case tests the performance of the method of simulating high speed moving boundaries in compressible viscous flows. The Mach number and the Reynolds number based on the free stream conditions are  $M = 5.75$  and  $Re_d = 15.9 \times 10^3$ , respectively. The same case was previously studied experimentally [140] and the data are available for comparison with the current results. A rectangular two-dimensional domain of size  $80D \times 16D$  is considered with the cylinder initially placed at  $(1.5D, 8D)$ . The problem is solved using both viscous and inviscid flow assumption to determine the significance of viscous effects on flow features. The Mach number plot of the flow field after a flight distance of  $60D$ , by which all the flow features are fully developed, is shown in Fig. 4.38(a) for both the viscous and inviscid cases. The near wall grid resolution with the 5 levels of refinement used is  $\Delta x = D/80$  which is just sufficient to resolve the boundary layer. It can be observed from Fig. 4.38(a) that the simulation captures all the essential flow features of the problem. A bow shock is formed ahead of the cylinder. The subsonic region behind the

shock expands and accelerates to supersonic flow which separates in the rear of the cylinder. A strong recirculation region is formed trapped between the separating supersonic flow. All these features were also noted in the past wind tunnel experiments of supersonic cylinders in viscous compressible flow [140]. The flow features ahead of the cylinder look identical for both viscous and inviscid cases. However, there are striking differences in the flow solution near the rear of the cylinder. Particularly, the separation is much delayed for the inviscid case. This results in a shift of the recompression shock and an increased thickness of the neck region between the shocks.

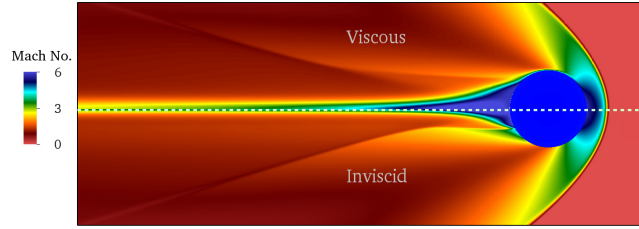


Figure 4.37: Mach number plot for a moving cylinder at  $M = 5.75$  in a quiescent flow. Top: Viscous flow at  $Re_d = 15.9 \times 10^3$ , bottom: Inviscid flow.

The comparison of pressure ratio,  $p/p_0$ , where  $p_0$  is the stagnation pressure, on the surface of the cylinder for viscous and inviscid computation with the corresponding experimental data [140], for the same Reynolds and Mach number, is shown in Fig. 4.38(a). It can be seen that there are reasonable agreement in the separation point and the pressure distribution predictions in the rear of the cylinder with the experimental data. An important observation to make is that the flow separation in the wake of the cylinder happens much earlier for the viscous case in comparison with the inviscid case and is closer to the experimental separation point. The current results highlight the importance of resolving near wall viscous effects in supersonic flow problems, especially if the wake effects are important. The development of the bow shock with time, visualized by contours of gradient of pressure, is shown



in Fig. 4.39(a). The shock shape is compared with the analytical correlation [141] given by:

$$x = R + \Delta - R_c \cot^2 \theta \left[ \left( 1 + \frac{y^2 \tan^2 \theta}{R_c^2} \right)^{1/2} - 1 \right], \quad (4.56)$$

where  $\Delta$  is the shock stand-off distance,  $R_c$  is the vertex radius of curvature and  $\theta$  is the asymptotic shock angle. Empirical correlations for the shock stand-off distance and radius of curvature are available for hypersonic flows and are given as:  $\Delta/R = 0.386 \exp(4.67/M^2)$  and  $R_c/R = 1.386 \exp(1.8/(M-1)^{3/2})$  with  $R$  being the radius of the cylinder and  $M$ , is the Mach number. The analytical shock shape is shifted with time to correspond to the position of the center of the cylinder as it moves through the fluid. From the Fig. 4.39(a) it can be observed that the bow shock structure once established, matches well with the analytical correlation and remains unchanged with cylinder motion. These results confirm the accuracy of the scheme in simulating high speed moving bodies in a compressible viscous flow.

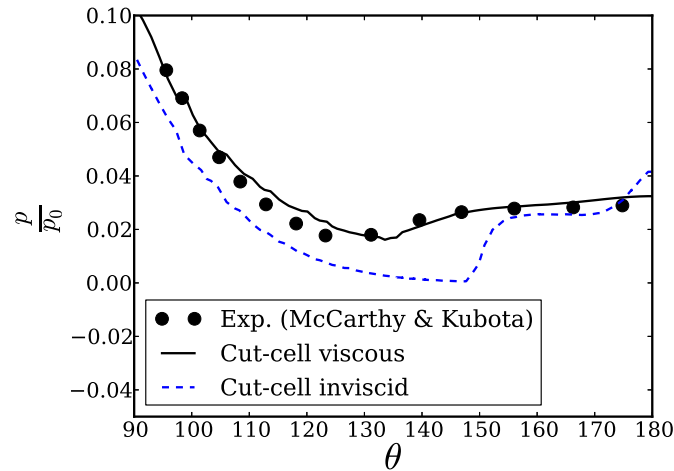


Figure 4.38: Pressure distribution on the rear of the cylinder for the viscous and inviscid case compared with experimental data [140].

#### 4.3.6 Cylinder driven by shock impact

In this problem, the interaction of a planar shock with a rigid cylinder is studied. This case was studied earlier using an overset grid technique and due to lack of an analytical solution

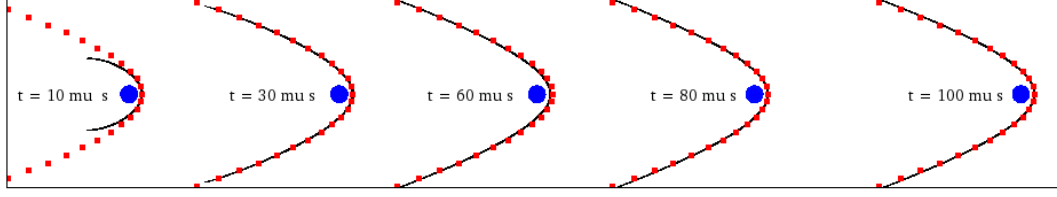
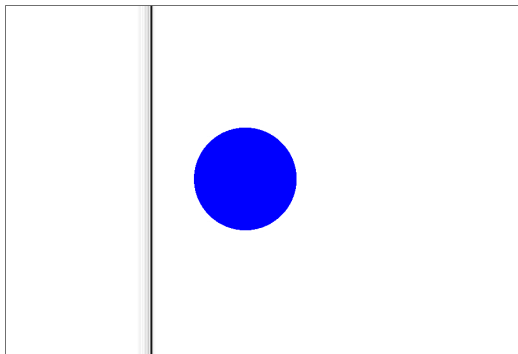


Figure 4.39: Time series of the bow shock visualized by contours of gradient of pressure compared with analytical correlation Eq.(4.56) marked with red dots.

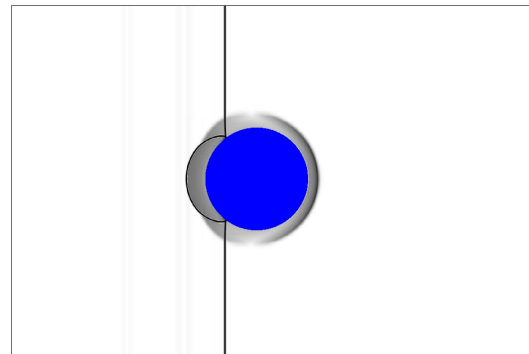
for this problem, the current results are compared with the data from the previous study [43]. A cylinder of mass  $m = 0.25$  kg, initially at rest at a position of  $x = -1/2$  and  $y = 0$  in a channel of extents  $|x| = 2$  and  $|y| = 2$ , is hit by a planar shock wave of Mach number 1.5, which is initially located at  $x = -1.5$ . The surface forces exerted by the shock wave drives the cylinder forward and are computed based on Eq. (4.34) and the cylinder velocity is updated using Eq. (4.35). The initial condition of the flow ahead of the shock is set to be  $\rho_0 = \gamma = 1.4$ ,  $p_0 = 1$  and post shock is determined by the normal shock jump conditions  $\rho_1 = 2.6069$ ,  $u_1 = 0.6944$ ,  $v_1 = 0$ ,  $p_1 = 2.4583$ . Computations are performed on a grid with three levels of dynamic refinement with an effective resolution of  $\Delta x = 2.5 \times 10^{-3}$ , which is same as the one used in a past study [43].

The Schlieren density contours at different time instants are shown in Fig. 4.40. The shock impact drives the cylinder forward which in turn generates a reflected shock in the back. The forward motion of the cylinder also creates a compression wave in the flow upstream which later develops into a bow shock. The incident shock on diffracting around the cylinder, generates a Mach-stem like shock which later interacts with the bow shock developed in front of the cylinder and the reflected shock at the back to form two pairs of three intersections. All of the above complex highly transient flow phenomena are accurately captured in the numerical solution. The regions where the limited second order MUSCL scheme is activated for this problem is shown in Fig. 4.41.

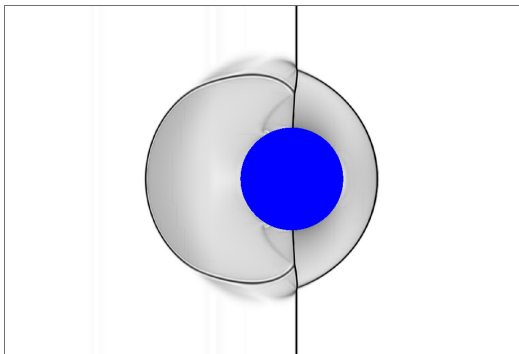
In a previous study [43], the authors employed the overlapping grids concept to solve



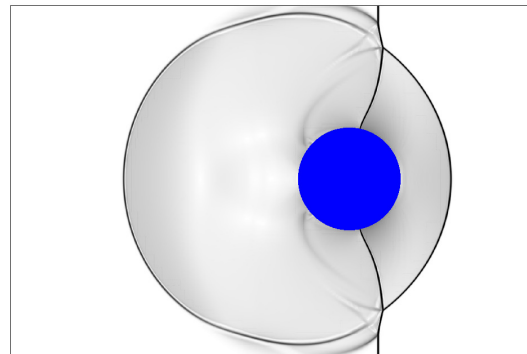
(a)  $t=0.0$



(b)  $t=0.5$



(c)  $t=1.0$



(d)  $t=1.5$

Figure 4.40: Schlieren contours for shock-driven cylinder at various times.

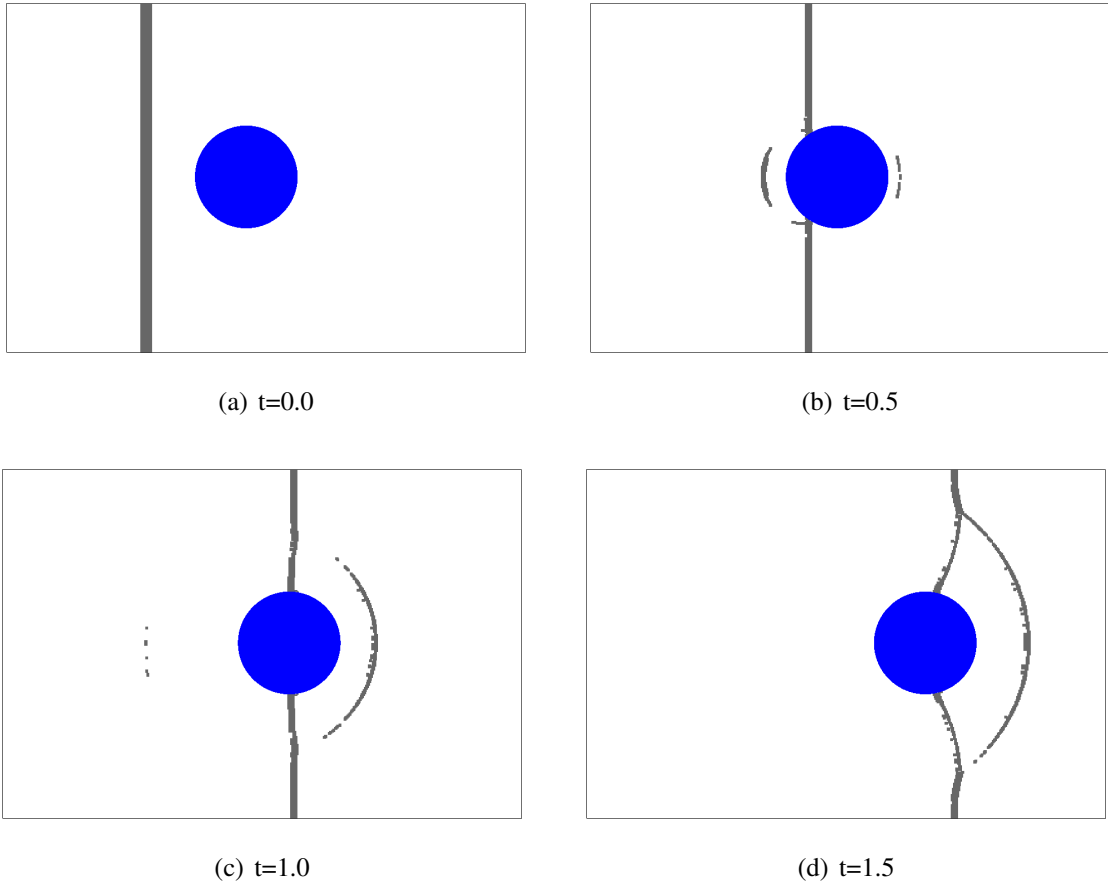


Figure 4.41: Regions where the second order MUSCL is activated using the curvature based discontinuity detection switch is highlighted in grey at various time instants.

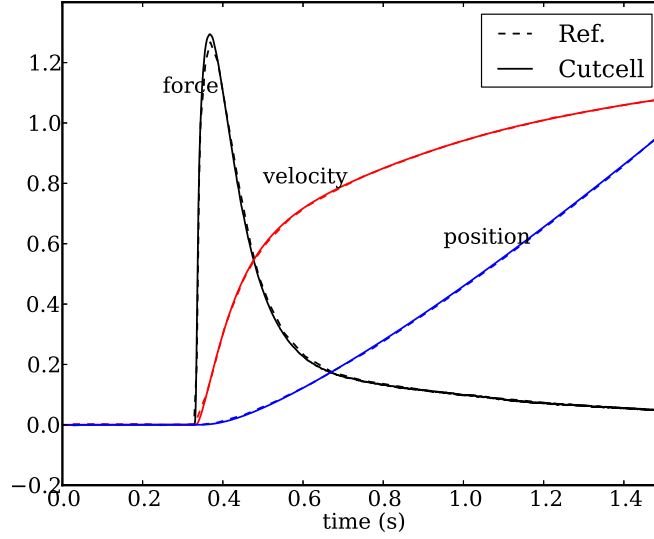


Figure 4.42: Force, velocity and position of the rigid cylinder as a function of grid compared against the reference solution of Henshaw & Schwendenman [43].

the same problem and the numerical solution computed from the adaptive cutcell method is compared against the solution reported [43] in Fig. 4.42. The  $x$ -component of force, velocity and position of the center of the cylinder are plotted as a function of time. The  $y$ -component of the force was close to zero within the round-off error, thereby confirming the symmetry of the flow solution. As observed from Fig. 4.42, results show excellent agreement with the past reference solution [43]. This case validates the capability of the current method to perform accurate computations of the coupled fluid driven rigid body motion.

## CHAPTER 5

### MULTI-LEVEL SUBGRID KINETIC ENERGY BASED CLOSURE

In this chapter, a multi-level formulation for the subgrid closure for unclosed  $sgs$  terms is described. The formulation is an extension of the transport equation based subgrid kinetic energy closure [37] for AMR grids. The main objective of the proposed formulation is to be able to perform LES in the presence locally refined mesh and embedded boundaries. Both these scenarios (with AMR for local refinement and cut-cell for embedded boundaries) are investigated using the multi-level closure.

#### 5.1 Multi-level nomenclature

Some additional notations pertaining to a multi-level grid for LES are developed in this section. These notations are useful for describing the proposed multi-level  $k^{sgs}$  closure and are adopted from a previous work [142]. The filtering operation described in Eq. (2.20) has the following modification for an AMR system:

$$\bar{\phi}^l(\mathbf{x}) = \int_{G_l} \mathcal{G}_l(\mathbf{x} - \mathbf{x}') \phi(\mathbf{x}') d\mathbf{x}', \quad (5.1)$$

where  $\mathcal{G}_l$  is the filtering operation associated to level  $l$  which can vary from  $l = 1, 2, \dots, N$  with  $N$  being the maximum level of refinement. The filter size for the operation,  $\Delta^n$  is same as the local grid size. Accordingly:

$$\Delta^1 > \Delta^2 > \dots > \Delta^N, \quad (5.2)$$

$$k_1 < k_2 < \dots < k_N, \quad (5.3)$$

where  $k_l$  is the wave number resolved by the grid at level  $l$ . The multi-level filtering operation, denoted by  $\overline{\overline{\phi}}^l$  can then be defined as:

$$\overline{\overline{\phi}}^l = \mathcal{G}_l * \mathcal{G}_{l+1} * \dots * \mathcal{G}_N \phi. \quad (5.4)$$

The double bar denotes the filtering obtained using recursive filtering operation. The relation between the filtered variables at various refinement levels is as follows:

$$\overline{\overline{\phi}}^N = \overline{\phi}^N, \quad (5.5)$$

$$\overline{\overline{\phi}}^{N-1} = \mathcal{G}_{N-1} \overline{\overline{\phi}}^N, \quad (5.6)$$

$$\vdots, \quad (5.7)$$

$$\vdots, \quad (5.8)$$

$$\overline{\overline{\phi}}^1 = \mathcal{G}_1 * \mathcal{G}_2 * \dots * \mathcal{G}_N \phi. \quad (5.9)$$

The representation of the filtered quantity on a multi-level AMR grid is shown in Fig. 5.1. The wavenumber corresponding to each AMR level and the corresponding filtered quantity at that level is indicated in the figure.

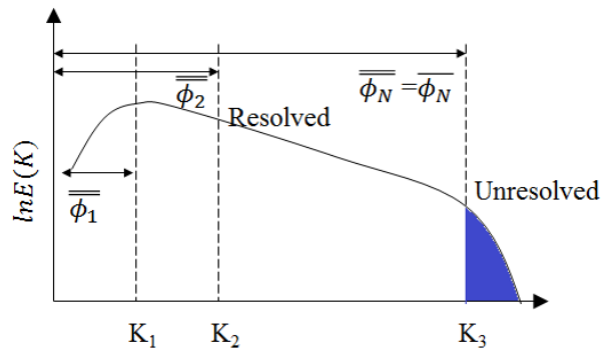


Figure 5.1: Schematic of turbulent kinetic energy spectra. The multi-level filtering of a flow quantity  $\phi$  and the associated wave number are also indicated.

Generally, the filter width  $\overline{\overline{\Delta}}^l$  associated with the filtered field  $\overline{\overline{\phi}}^l$  is not same as the local

filter width  $\Delta^l$  because of the successive filtering operation. But for a box filter, the filter width is same as the local filter width for that level implying atleast for all the cases in this study:

$$\overline{\overline{\Delta}}^l = \Delta^l. \quad (5.10)$$

The discrete representation of the recursive filtering operation, based on the notations described in Section 3.1 can be defined as the following:

$$\phi^l = \mathcal{R}_{l+1}^l(\mathcal{R}_{l+2}^{l+1}(\dots \mathcal{R}_N^{N-1}(D^N(\phi))\dots)). \quad (5.11)$$

In the above Eq. (5.11),  $\mathcal{R}_l^{l-1}$  is the restriction operation performed between grid levels  $G_l$  and  $G_{l-1}$ . The grid levels are dropped in the above equation for clarity. The operator  $D^N(\phi)$  is the implicit filtering operation by the grid level N.

**Remark** Note that for an AMR grid, there will be some regions of a given grid level,  $l$  covered with finer grids and there might be also some regions that are not covered with a finer mesh. In such a scenario, the multi-level representation of the filtered field for unrefined regions is given by:

$$\phi^l = D^l(\phi). \quad (5.12)$$

The multi-level representation of the filtered field is described more clearly in the schematic Fig. 5.2.

For compressible flows, the equivalent representation of the Favre filtering operation is:

$$\tilde{\phi}^l = \frac{\overline{\overline{\rho\phi}}^l}{\overline{\overline{\rho}}^l}. \quad (5.13)$$



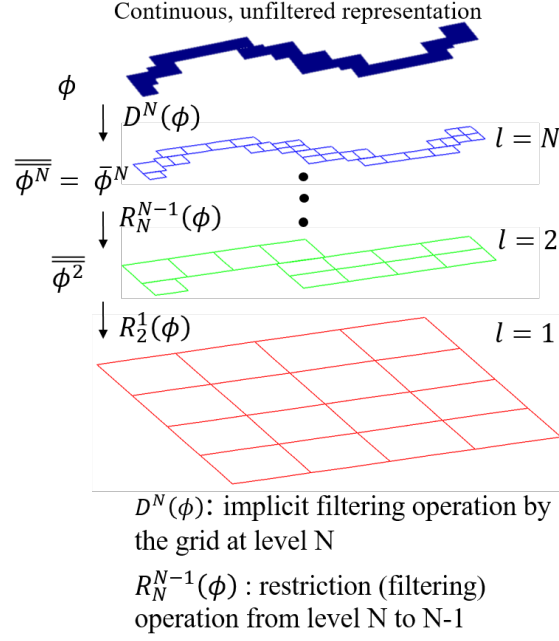


Figure 5.2: Multi-level representation of a filtered quantity  $\phi$  on a AMR mesh.

The filtered governing equations for a multi-level AMR grid then becomes:

$$\frac{\partial}{\partial t} \begin{pmatrix} \overline{\rho}^l \\ \overline{\rho}^l \tilde{u}_j^l \\ \overline{\rho}^l \tilde{E}^l \\ \overline{\rho}^l \tilde{Y}_k^l \end{pmatrix} + \frac{\partial}{\partial x_j} \begin{pmatrix} \overline{\rho}^l \tilde{u}_i^l \\ \overline{\rho}^l \tilde{u}_i^l \tilde{u}_j^l + \overline{p}^l \delta_{ij} - \tilde{\tau}_{ij}^l + \tau_{ij}^{sgs,l} \\ (\overline{\rho}^l \tilde{E}^l + \overline{p}^l) \tilde{u}_j^l - \tilde{u}_i^l \tilde{\tau}_{ij}^l + \overline{q}_j^l + H_j^{sgs,l} + \sigma_j^{sgs,l} \\ \overline{\rho}^l \tilde{u}_j^l \tilde{Y}_k^l - \tilde{Y}_k^l \tilde{V}_{j,k}^l + Y_{j,k}^{sgs,l} + \theta_{j,k}^{sgs,l} \end{pmatrix} = \begin{pmatrix} 0 \\ 0 \\ 0 \\ \overline{\dot{\omega}}_k^l \end{pmatrix} \quad (5.14)$$

for a grid level,  $G_l$ . The Favre average for single level will be replaced with the multi-level filtering operation  $\tilde{\cdot}$  in Eqs. (2.26) - (2.41) and are not repeated.

The superscripts  $sgs, l$  denote the unclosed subgrid terms in the governing equation corresponding to level  $l$ .

## 5.2 Subgrid closure modeling for multi-level LES

The approach proposed in this thesis for closure of the  $sgs$  terms in Eq. (5.14) is to employ the standard single level closures for each level independently. The only difference is in the

treatment of the subgrid turbulent kinetic energy  $k^{sgs,l}$  for which an additional correction is performed. The closure models for each of the  $sgs, l$  terms are summarized below:

$$\nu_t^l = C_\nu^l \sqrt{k^{sgs,l}} \Delta^l, \quad (5.15)$$

$$\tau_{ij}^{sgs,l} = -2\bar{\rho}^l \nu_t^l \left( \tilde{S}_{ij}^l - \frac{1}{3} \tilde{S}_{kk}^l \delta_{ij} \right) + 2/3 \bar{\rho}^l \bar{k}^{sgs,l} \delta_{ij}, \quad (5.16)$$

and

$$H_i^{sgs,l} + \sigma_i^{sgs,l} = - \left( \bar{\rho}^l \nu_t^l + \mu^l \right) \frac{\partial \bar{k}^{sgs,l}}{\partial x_i} - \frac{\bar{\rho}^l \nu_t^l c_p^l}{Pr_t^l} \frac{\partial \tilde{T}^l}{\partial x_i} + \tilde{u}_j^l \tau_{ij}^{sgs,l}. \quad (5.17)$$

The transport equation for the subgrid kinetic energy also becomes the following:

$$\frac{\partial \bar{\rho} k^{sgs,l}}{\partial t} + \frac{\partial}{\partial x_i} \left( \bar{\rho}^l \tilde{u}_i^l k^{sgs,l} \right) = \mathcal{T}_{k^{sgs,l}} + pd_{k^{sgs,l}} + P_{k^{sgs,l}} - D_{k^{sgs,l}}, \quad (5.18)$$

with the different closure terms in the  $k^{sgs}$  equation taking the following form:

$$\mathcal{T}_{k^{sgs,l}} = \frac{\partial}{\partial x_i} \left[ \left( \bar{\rho}^l \nu_t^l + \mu \right) \frac{\partial k^{sgs,l}}{\partial x_i} + \frac{\bar{\rho}^l \nu_t^l \tilde{R}^l}{Pr_t^l} \frac{\partial \tilde{T}^l}{\partial x_i} \right], \quad (5.19)$$

$$pd_{k^{sgs,l}} = \alpha_{pd}^l M_t^{sgs,l2} \left( \frac{\bar{\rho}^l \tilde{S}^l k^{sgs,l}}{D^{sgs,l}} \right)^2 (P_{k^{sgs,l}} - D_{k^{sgs,l}}), \quad (5.20)$$

$$P_{k^{sgs,l}} = \tau_{ij}^{sgs,l} \tilde{S}_{ij}^l, \quad (5.21)$$

$$D_{k^{sgs,l}} = \bar{\rho}^l C_\epsilon^l (k^{sgs,l})^{3/2} / \Delta^l. \quad (5.22)$$

The Eqs. (5.16) - (5.22) are in fact exact equivalents of Eqs. (2.43) - (2.49) with the single level flow variables now replaced with their multi-level representation. The coefficients,  $C_\nu^l$ ,  $C_\epsilon^l$ ,  $\alpha_{pd}^l$  and  $Pr_t^l$  are computed still computed dynamically for each level after employing a test filter with twice the local grid size and using a least square approach. More details on the dynamic approach near coarse/fine and fine/coarse AMR boundaries are discussed later

in this section.

Consider the flow solution by solving the governing equations in a time advanced manner. Once the filtered governing equations are solved using a numerical scheme for each grid level,  $G_l$ , a restriction operation is performed according to Eq. (5.11). Suppose that this solution to the flow governing equations based on single level formulations is denoted as  $\overline{\phi}^l$  with  $\phi$  representing any conserved quantity such as mass, momentum or energy. The restriction operation,  $\mathbf{R}(\phi)$ , overwrites  $\overline{\phi}^l$  solved at a coarser level,  $l$  with the filtered value,  $\overline{\overline{\phi}}^l$  from finer levels covering it. This filtered field for  $\phi$  is then used to solving the filtered governing equations for the next time step on each grid level.

The above procedure is consistent as long as flow quantity that is filtered is conservative i.e. the filtering operation satisfies Eq. (5.4). This is true of the mass, momentum and total energy, but the quantity,  $\rho k^{sgs}$  is non-conservative across a multi-level system. This is proved as follows by considering filtering of  $k^{sgs,l+1}$  to  $k^{sgs,l}$  by a restriction operation:

$$\begin{aligned}
\overline{k^{sgs,l+1}} &= \mathcal{R}_{l+1}^l(k^{sgs,l+1}) \\
&= \mathcal{R}_{l+1}^l(\widetilde{u_i u_i}^{l+1} - \widetilde{u_i}^{l+1} \widetilde{u_i}^{l+1}) \\
&= \mathcal{R}_{l+1}^l(\widetilde{u_i u_i}^{l+1}) - \mathcal{R}_{l+1}^l(\widetilde{u_i}^{l+1} \widetilde{u_i}^{l+1}) \\
&= \mathcal{R}_{l+1}^l(\widetilde{u_i u_i}^{l+1}) - \mathcal{R}_{l+1}^l(\widetilde{u_i}^{l+1}) \mathcal{R}_{l+1}^l(\widetilde{u_i}^{l+1}) + \\
&\quad (\mathcal{R}_{l+1}^l(\widetilde{u_i}^{l+1}) \mathcal{R}_{l+1}^l(\widetilde{u_i}^{l+1}) - \mathcal{R}_{l+1}^l(\widetilde{u_i}^{l+1} \widetilde{u_i}^{l+1})) \\
&= \widetilde{u_i u_i}^l - \widetilde{u_i}^l \widetilde{u_i}^l + \\
&\quad (\mathcal{R}_{l+1}^l(\widetilde{u_i}^{l+1}) \mathcal{R}_{l+1}^l(\widetilde{u_i}^{l+1}) - \mathcal{R}_{l+1}^l(\widetilde{u_i}^{l+1} \widetilde{u_i}^{l+1})) \\
&= k^{sgs,l} + (\widetilde{u_i}^l \widetilde{u_i}^l - \mathcal{R}_{l+1}^l(\widetilde{u_i}^{l+1} \widetilde{u_i}^{l+1})).
\end{aligned} \tag{5.23}$$

Rearranging terms in Eq. (5.23) results in the following relation between the subgrid kinetic energies at two levels:

$$k^{sgs,l} = \mathcal{R}_{l+1}^l(k^{sgs,l+1}) + \overline{\delta}^{sgs,l}, \tag{5.24}$$

where  $\bar{\delta}^{sgs,l} = (\mathcal{R}_{l+1}^l(\tilde{u}_i^{l+1}\tilde{u}_i^{l+1})) - \tilde{u}_i^l\tilde{u}_i^l$  is the correction term that needs to be added to the filtered subgrid kinetic energy field from level,  $l + 1$ . Identifying that the same relation is applicable between levels  $l + 1 / l + 2$  and so on, till  $N - 1/N$ , the relation in Eq. (5.24) can be generalized as:

$$k^{sgs,l} = \overline{\overline{k^{sgs}}}^l + \bar{\delta}^{sgs,l}. \quad (5.25)$$

The multi-level correction in Eq. (5.25) is therefore:

$$\bar{\delta}^{sgs,l} = \overline{\overline{u_i u_i}}^l - \tilde{u}_i^l \tilde{u}_i^l. \quad (5.26)$$

For a compressible formulation, the Favre filtered form of the above correction would be:

$$\overline{\bar{\rho}} k^{sgs,l} = \overline{\overline{\rho k^{sgs}}}^l + \overline{\bar{\rho}} \bar{\delta}^{sgs,l}, \quad (5.27)$$

$$\overline{\bar{\rho}} \bar{\delta}^{sgs,l} = \overline{\overline{\rho u_i u_i}}^l - \frac{\overline{\overline{\rho u_i}}^l \overline{\overline{\rho u_i}}^l}{\overline{\bar{\rho}}^l}. \quad (5.28)$$

The discrete formulation of the multi-level correction  $\overline{\bar{\rho}} \bar{\delta}^{sgs,l}$  is given as:

$$\overline{\bar{\rho}} \bar{\delta}^{sgs,l} = \frac{R_N^l(\rho^N \tilde{u}_i^N \tilde{u}_i^N)}{R_N^l(\bar{\rho}^N)} - \frac{R_N^l(\rho^N \tilde{u}_i^N) R_N^l(\rho^N \tilde{u}_i^N)}{R_N^l(\bar{\rho}^N) R_N^l(\bar{\rho}^N)}. \quad (5.29)$$

It can be noted that the correction for  $k^{sgs}$  with  $\overline{\bar{\rho}} \bar{\delta}$  is the unresolved turbulent kinetic energy that is resolved by a grid level finer than the current grid level. So in essence, the correction ensures consistency of the total represented kinetic energy at any grid level. The entire solution procedure is described through the following algorithm:

**A single time iteration for solving  $\bar{\bar{\mathbf{U}}}$  with the multi-level sgs closure:**

**for**  $i \leftarrow 1$  **to**  $NL_{max}$  **do**

**for**  $m \leftarrow 1$  **to**  $M$  **do**

        Solve for filtered governing equations on  $G_{i,m}$

**end**

**end**

**Communicate** using  $\mathbf{C}(\bar{\bar{\mathbf{U}}})$  to fill information in the interior ghost cells;

**Restrict** using  $\mathbf{R}(\bar{\bar{\mathbf{U}}})$  to filter data from finest grid to coarser grids;

**Prolongate** using  $\mathbf{P}^{ng}(\bar{\bar{\mathbf{U}}})$  to fill ghost cells at fine/coarse or coarse/fine AMR

boundaries

**Correct** for the total represented turbulent kinetic energy using Eq. (5.28) and adding the correction  $\overline{\overline{\rho\delta}}^{sgs}$

**Algorithm 7:** Single solution step for the multi-level sgs closure

The multi-level correction procedure is illustrated in Fig. 5.3. For unrefined regions, the single-level transport equation based closure is employed. But for the refined regions indicated by yellow and blue color, the correction described by Eq. (5.28) is applied.

The multi-level formulation can be seen as a mixed model that employs, the transport equation based sgs model at the finest resolution and adding a correction based on the explicit filtering of represented turbulent kinetic energy on the grid resolution finer than the current level. Common to mixed model formulation is the issue of Galilean invariance. Consider a new reference frame with  $u_i^* = u_i + V_i$  where  $V_i$  is the velocity of the reference frame. It can be shown that:

$$\frac{1}{2} \left( \overline{\overline{\rho \tilde{u}_i^N \tilde{u}_i^N}} - \overline{\overline{\rho \tilde{u}_i^N}} \overline{\overline{\rho \tilde{u}_i^N}} / \overline{\overline{\rho}}^n \right) = \frac{1}{2} \left( \overline{\overline{\rho \tilde{u}_i^{*,N} \tilde{u}_i^{*,N}}} - \overline{\overline{\rho \tilde{u}_i^{*,N}}} \overline{\overline{\rho \tilde{u}_i^{*,N}}} / \overline{\overline{\rho}}^n \right). \quad (5.30)$$

Thus the proposed correction is Galilean invariant.

*Remark:* The interpretation of the local dynamic procedure for computing the coeffi-

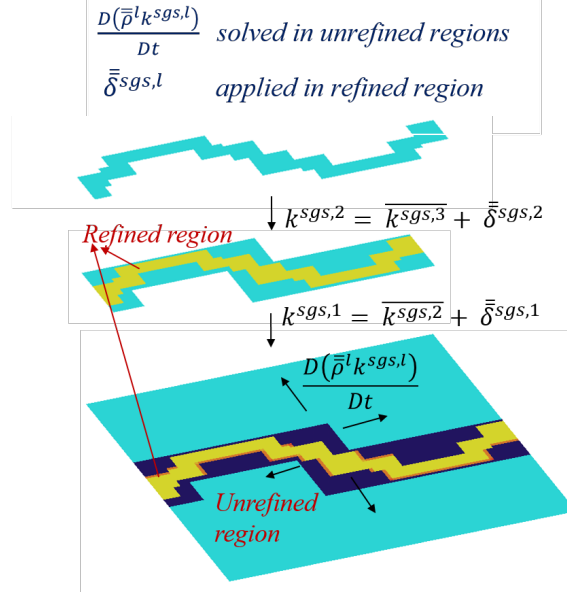


Figure 5.3: Schematic of the multi-level correction for  $k^{sgs}$  on a AMR mesh.

cients:  $C_\nu^l$ ,  $C_\epsilon^l$ ,  $\alpha_{pd}^l$  and  $Pr_t^l$  for a AMR grid may not be direct especially at the coarse/fine and fine/coarse interface and more details of this step are discussed here. For a given grid cell index  $CG_l(i, j)$ , the local dynamic procedure involves a test filter of size  $2\Delta^l$  applied to the neighboring cells  $CG_l(i \pm 1, j \pm 1)$ . In the interior of the grid, this operation is perfectly defined. But along the first layer of cells adjacent to the boundary, the filtering operation may appear to be ill defined especially along a coarse/fine or fine/coarse boundary. On a more careful consideration, it becomes apparent that the filtering operation is still defined as for any general grid block,  $G_{l,m}$ , a halo layer of ghost cells,  $G_{l,m}^{halo} = G_{l,m}^{mg} \hat{G}_{l,m}$  exists. A projection operation,  $\mathbf{P}(\phi)$  defined in Section 3.1 is used to fill all the ghost cells at a coarse/fine or fine/coarse interface.

### 5.3 Assessment of multi-level AMRLES

To assess the performance of the multi-level closure, two cases are considered. In the first case, the behavior of the closure model when a turbulent flow convects past an AMR grid interface is studied. The flow solution and the closure model behavior is then investigated for

the case of turbulent flow past a cylinder and sphere represented by the cut-cell embedded boundary approach.

### 5.3.1 LES of homogeneous turbulence convecting across coarse/fine AMR interface

The problem of a turbulent flow past an AMR grid refinement interface is generally encountered in the simulation of many practical engineering flow systems. In many applications when AMR is applied to resolve features such as flames, shocks, and detonations, the turbulent flow invariably crosses a coarse/fine AMR interface. Here we consider a basic test problem involving advection of a decaying isotropic turbulence past a coarse/fine and fine/coarse interface. The test domain is a channel of dimensions  $(-2\pi, 2\pi)$  in the x-direction and of  $(0, 2\pi)$  in y and z-direction. Homogeneous turbulence of  $Re_\lambda = 400$  and  $M_t = 0.05$  is advected from left to right with a convective Mach number of  $M = 1.5$  and periodic boundary conditions are employed along the spanwise directions. This configuration is same as the one employed in previous studies for analyzing the effect of grid discontinuity on turbulent flow statistics [143, 144]. Both the scenarios, when the flow passes through from a coarse to fine grid and from a fine to the coarse grid are considered. All the cases for this problem are summarized in Table 5.1. The inflow turbulence is precomputed using the same subgrid model as is used for the simulation in a  $(2\pi \times 2\pi \times 2\pi)$  box with periodic boundary conditions and is brought in using Taylor’s frozen turbulence hypothesis.

For cases  $CF - WC$  and  $CF - NC$ , the left side of the block of size  $(2\pi, 2\pi, 2\pi)$  is coarser and has  $64 \times 64 \times 64$  cells and the right block of the same size is fine with  $128 \times 128 \times 128$  cells. This case was setup to study the coarse to fine transition. The other cases  $FC - WC$  and  $FC - NC$  has the coarse and fine blocks interchanged to study fine to coarse transition. The goal of the study is to understand the behavior of the various turbulent flow quantities such as the vorticity magnitude, resolved turbulent kinetic energy and the subgrid turbulent kinetic energy across an AMR grid discontinuity.

When a turbulent flow convects past an AMR interface, some abrupt changes in its char-

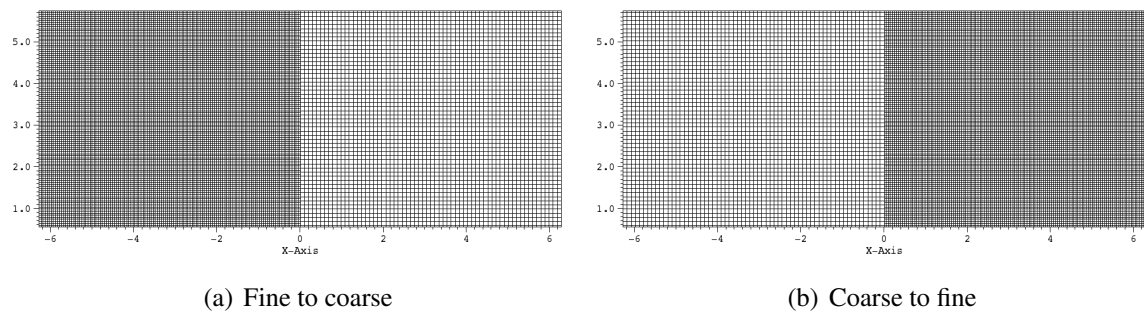


Figure 5.4: AMR mesh for (a) coarse to fine and (b) fine to coarse case

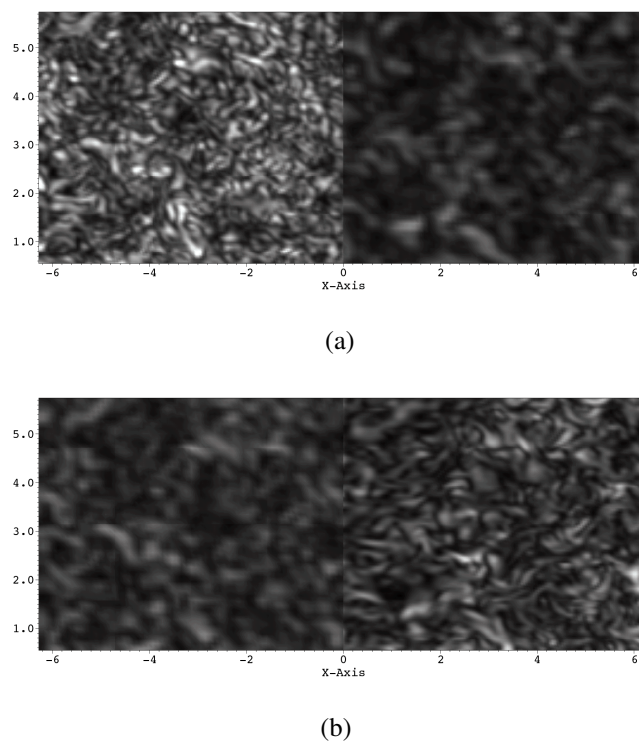


Figure 5.5: Instantaneous vorticity magnitude on the central XY plane for (a) coarse to fine and (b) fine to coarse case.



Table 5.1: LES of advection of homogeneous turbulence across a AMR grid discontinuity

Case	Grid	No. of points	Multi-level sgs corr.
UC	Uniform-coarse	$2 \times 64^3$	N/A
UF	Uniform-fine	$2 \times 128^3$	N/A
CF-WC	Coarse to fine	$64^3 + 128^3$	Present
FC-WC	Fine to coarse	$128^3 + 64^3$	Present
CF-NC	Coarse to fine	$64^3 + 128^3$	Not present
FC-NC	Fine to coarse	$128^3 + 64^3$	Not present

acteristics can be expected due to the sudden change in the grid size. This change in the flow features can be observed in the instantaneous vorticity magnitude plots shown for both the coarse/fine interface and fine/coarse interface in Figs. 5.5(a) and 5.5(b). For the coarse/fine case, there is a sudden coarsening of the turbulent structures downstream of grid discontinuity. Whereas, in the fine/coarse case, it can be seen that there is a gradual recovery of small-scale structures as the turbulence advects into the fine downstream mesh from the coarser upstream mesh. The transition length required for the small scales to get populated depends on the convective and the eddy turn around time scale. From the plot, it can be seen that the recovery of small-scale structures is quite evident immediately after the interface. For the fine to a coarse case, the behavior of the resolved turbulence is basically inverse to that seen for the coarse to the fine case. As seen in Fig. 5.5(b), the sudden coarsening, which translates to a sudden change in the filter size, leads to abrupt loss of small-scale structures. The effect of the lost small scales of motion on the flow post the discontinuity must be adequately modeled by the subgrid closure.

The spectra of the resolved turbulent kinetic energy taken at two locations just before and after the AMR grid interface are shown in Fig. 5.6. The spectra is obtained by collecting y-z plane data over one flow-through time. Any artifact introduced by a grid discontinuity is expected to shown up prominently in the turbulent kinetic energy spectra. For the coarse to fine case, when the turbulence enters the fine region, the wave number support increases. Due to the interpolation from the coarse grid ghost cells, there are some high wave number modes introduced into the spectra which is taken at y-z plane of the first fine grid cell. But

after few grid points, the non-linear convective processes and vortex stretching introduce small-scale structures which relax the spectra to a more physical state. The fine-coarse case shows a behavior analogous to an operation of a box filter on the fine mesh flow solution. High wave number modes disappear and there is also some damping noticeable at the higher wave numbers that are resolvable on the coarse mesh. This is a typical characteristic of a box filter which does not perform a sharp spectral cut-off and has infinite support in the spectral space. The energy pile up problem noted by Vanella *et al.* [143] before a fine to coarse interface is not present in the current results. This is believed due to the conservative nature of handling the total resolved turbulent kinetic energy,  $\widetilde{u_i u_i} = \widetilde{u_i} \widetilde{u_i} + k^{sgs}$ , across a grid discontinuity.

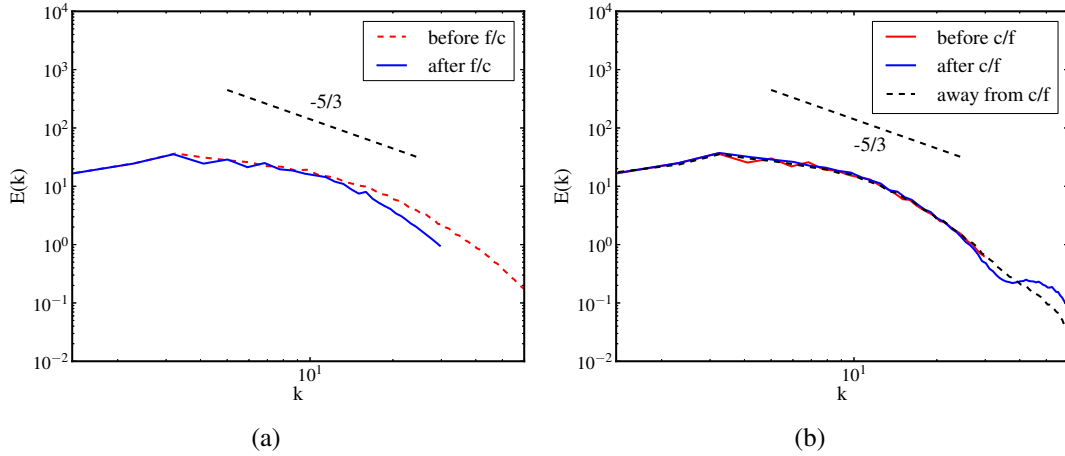


Figure 5.6: Resolved TKE spectrum near an AMR grid interface for (a) coarse to fine and (b) fine to coarse cases.

One of the main interests of the study is to understand the behavior of sgs terms across a grid interface. In fact, a sudden change in the size of the grid which acts as a filter, is expected to most significantly affect the sgs contributions. The predicted subgrid kinetic energy,  $k^{sgs}$ , is spatially averaged along the homogeneous directions and also averaged over two convective flow-through times and its variation along the axial direction is plotted in Figs. 5.7(a) and 5.7(b) for both the cases. The subgrid kinetic energy has a monotonically increasing relationship with the filter size. A sudden increase in the filter size must result in

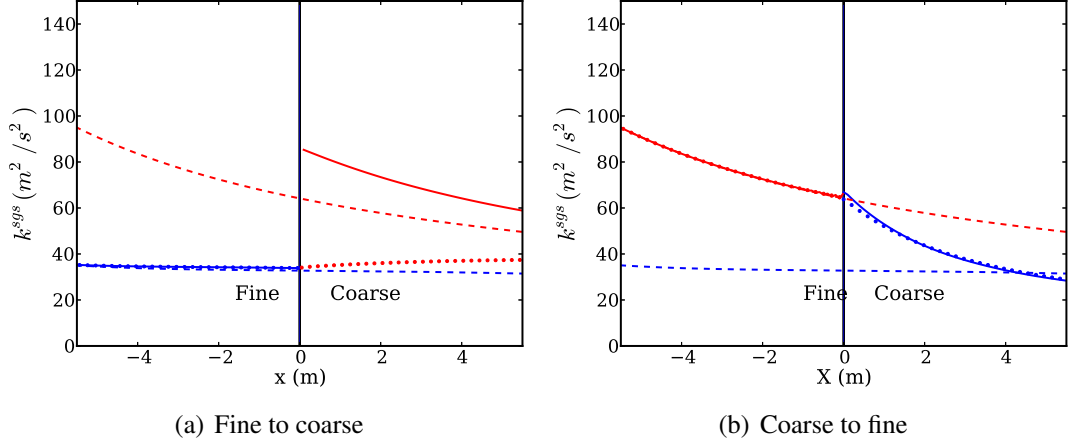


Figure 5.7: Averaged plot of resolved TKE,  $\tilde{u}_i \tilde{u}_i$  for (a) coarse to fine scenario and (b) fine to coarse scenario: — fine with correction; — coarse with correction; ..... fine without correction; ..... coarse without correction; --- uniform fine and --- uniform coarse.

a sudden change in the subgrid kinetic energy. The multi-level correction using Eq. (5.28) accounts for this change in the filter size, by explicitly adding the resolved part of the TKE on a finer grid which can not be resolved on an underlying coarser grid to the subgrid kinetic energy of the coarser grid. This ensures that the total resolved turbulent kinetic energy is conserved across different levels of refinement. The correction will not make any difference for an algebraic closure such as Dynamic Smagorinsky model. This is because, the flow solution on the coarser underlying patches are overwritten by the finer grid solution. The effect of correction is only relevant for a transport equation based sgs model where the 'memory' effect of subgrid turbulent kinetic energy upstream influences its value downstream. The effect of the correction can be clearly seen in Fig. 5.7(a). The jump in  $k^{sgs}$  is correctly accounted by the multi-level sgs model. Whereas, without the correction term, as is observed in Fig. 5.7(b), the jump in the subgrid kinetic energy is absent and is continuous across the grid interface. The  $k^{sgs}$  variation for a uniform coarse and fine grid is also shown for reference. Post the grid interface, the increase in  $k^{sgs}$  matches fairly with its value on a uniform coarse grid. The difference in the magnitude of the increase can be attributed to differences in prescription of the inflow conditions between a fine and a coarse grid. The numerical

diffusion of the scheme can also influence the state of the turbulence in the coarser grid. For the coarse to fine cases  $CF - WC$  and  $CF - NC$ , the correction does not result in any change in behavior at the grid interface. One observation that can be made from the results for  $CF - WC$  and  $CF - NC$  is that though the subgrid kinetic energy is continuous, there is a sudden change in its decay rate. The impact of the correction on resolved flow quantities will be next assessed.

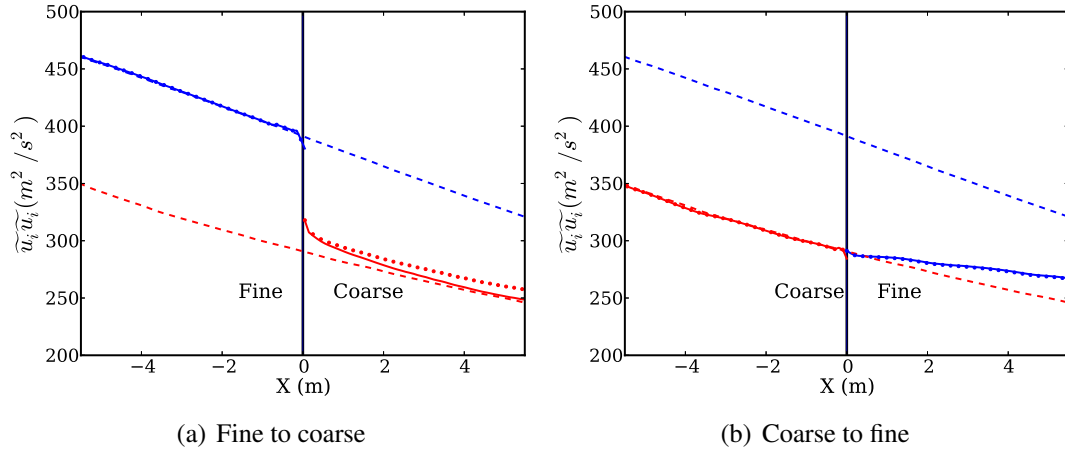


Figure 5.8: Averaged plot of resolved TKE,  $\tilde{u}_i \tilde{u}_i$  for (a) coarse to fine scenario and (b) fine to coarse scenario: — fine with correction; — coarse with correction; ..... fine without correction; ..... coarse without correction; --- uniform fine and --- uniform coarse.

The variation of the time and space averaged resolved TKE along the axial direction is shown in Figs. 5.8(a) and 5.8(b). In the case of fine to coarse transition, there is a sudden drop in the resolved level turbulent kinetic energy. This is expected as the sudden coarsening causes loss of small scale turbulent motion which results in a drop in the turbulent kinetic energy at the resolved level. For the case  $CF - NC$ , without the multi-level ksgs correction, this drop in the resolved level tke is lesser compared to case  $CF - WC$ . This is because, if the correction is not effected, the sudgrid stresses are under predicted resulting in lesser dissipation due to the subgrid scale motions. This is directly an effect of the insufficient raise in the subgrid kinetic energy in the post derefinement region. For the  $FC - WC$  and  $FC - NC$  cases, the correction does not make any difference as the  $k^{sgs}$  behavior does not change

with and without the multi-level correction. However, the coarse to fine cases however raises an important concern when dealing with a sudden refinement. The history effect of the subgrid energy helps in maintaining the total resolved turbulent kinetic energy. How other models such as Smagorinsky can handle a sudden refinement or coarsening is not clear and more investigation may be needed to study their suitability with AMR as there appears to be no mechanism for a non-transport equation based model to maintain the conservation of the total resolved TKE across the grid interface.

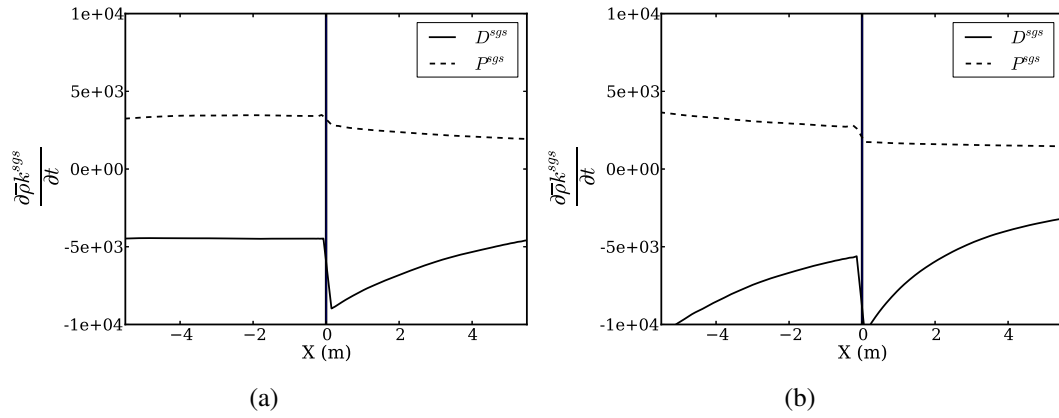


Figure 5.9: sgs budget for flow past an AMR grid discontinuity for (a) fine to coarse and (b) coarse to fine case.

More on the behavior of the different sgs terms in the transport of the subgrid kinetic energy when the flow encounters a grid interface can be understood from the plots in Fig. 5.9. The production term  $P^{sgs} = \tau_{ij}^{sgs} \tilde{S}_{ij}$ , is proportional to  $\nu_t \propto k^{sgs}$  and  $\tilde{S}_{ij} \tilde{S}_{ij}$  based on eddy-viscosity hypothesis. Across the fine/coarse interface, there are two competing effects: (1) jump in  $k^{sgs}$  and (2) Drop in  $|S| = \sqrt{S_{ij} S_{ij}}$  due to loss of small scale structures. Depending upon which of these effects are dominating, the production of  $k^{sgs}$  increases or decreases. Similarly the sgs dissipation,  $D^{sgs}$ , undergoes a sudden change across the interface. The sgs dissipation,  $D^{sgs} = C_\epsilon k^{sgs 3/2} / \bar{\Delta}$  depends on  $k^{sgs}$  and inversely on the filter size,  $\bar{\Delta}$ . Across an AMR interface, again there are competing effects. For a fine/coarse interface, the increase in the  $k^{sgs}$  can lead to increased dissipation while increase in the filter size will lead

to its decrease. For a coarse/fine interface, the dissipation will always increase with decrease in filter size. The  $k^{sgs}$ , as seen from the plots, remains continuous across an coarse/fine interface.

### 5.3.2 LES of $Re_d=3900$ flow past a cylinder

In this study, LES is employed to simulate the turbulent flow of  $Re_d = 3900$  over a cylinder of diameter,  $d$ . The simulations are performed in a large rectangular domain of size  $(30d \times 30d \times \pi d)$  with a base resolution of  $(150 \times 150 \times 20)$ . As shown in Fig.5.10, six AMR levels are employed such that the effective resolution at the cylinder surface is  $0.003125d$ , which falls in at around  $y^+ = 4$ , where  $+$  indicates non-dimensionalization by the viscous length scale. The first point of the wall is located at  $y^+ = 2$ . The grid resolution is comparable to a previous study of the same problem [145]. This problem has been extensively studied using both body conformal and immersed boundary approaches in the past and therefore is an ideal reference case for evaluating the current AMRLES closure with embedded boundaries. Characteristics based subsonic inflow is used in the left boundary while subsonic outflow condition is prescribed to the top, bottom and right boundary. Front and top surfaces are prescribed with periodic boundary condition.

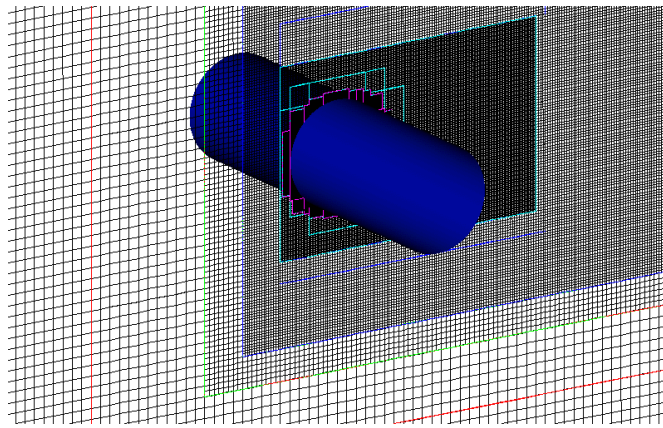


Figure 5.10: Snapshot of local mesh refinement near cylinder surface for  $Re_d = 3900$  flow past a cylinder.

The stringent wall resolution requirement is due to lack of use of any wall modeling for performing AMRLES which makes this a wall-resolved LES. The coefficients for the subgrid closure models are evaluated dynamically using the LDKM approach. The flow Mach number is set at  $M = 0.2$  which is low enough to avoid any compressibility effects. The time history of the drag and lift coefficient plots are shown in Fig. 5.11.

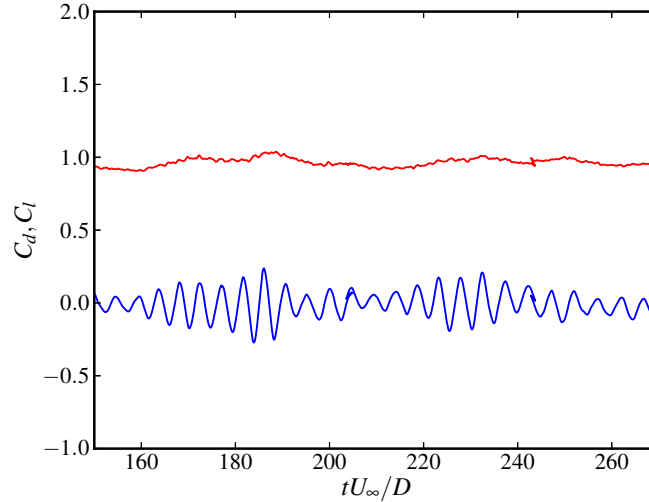


Figure 5.11: Time history of drag ( $C_d$ ) and lift ( $C_l$ ) coefficient of  $Re_d=3900$  flow past a cylinder.

The average drag coefficient of  $\overline{C_d} \approx 1$  matches with the data from past studies [146, 145]. The amplitude changes in the lift coefficient is due to vortex shedding events occurring downstream of the cylinder. The vortex structures in the wake of the cylinder are identified by the iso-surface of Q-criterion colored with streamwise velocity and are shown in Fig. 5.12. It can be observed that the boundary layer separates around the top and bottom of cylinder and forms shear layers which breaks up into coherent structures and eventually into small scale turbulence within a couple of diameters downstream of the cylinder.

The instantaneous snapshots of vorticity magnitude, subgrid kinetic energy and eddy viscosity ratio are shown in Fig. 5.13. An important observation from the subgrid kinetic energy plot is that the  $k^{sgs}$  is generated in shear layer following the coarsening of the finest AMR mesh covering the cylinder surface. As noted in the grid turbulence case study discussed in

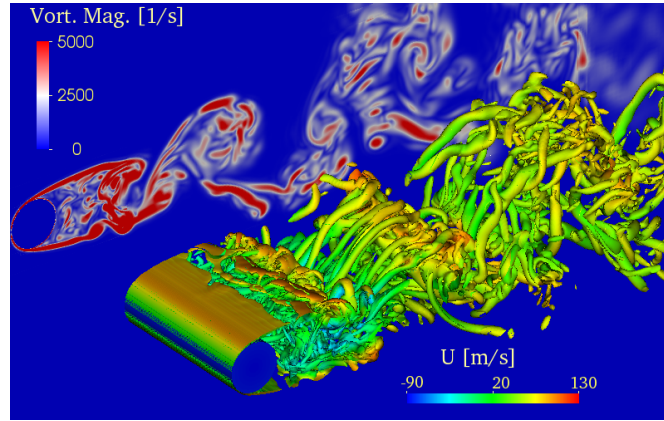


Figure 5.12: Vortex structures visualization by iso-surface of Q-criterion colored with streamwise velocity.

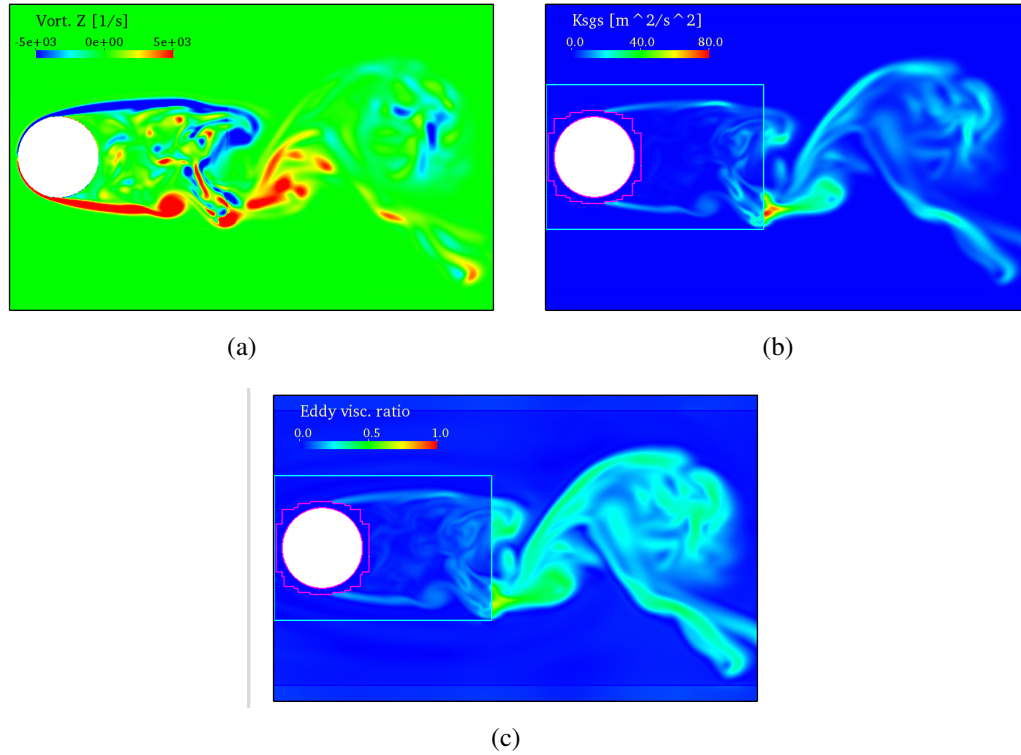


Figure 5.13: Instantaneous snapshot of (a) vorticity magnitude (b) subgrid kinetic energy and (c) eddy viscosity ratio in the center x-y plane



the previous section, the generation of  $k^{sgs}$  from a fine/coarse AMR interface occurs solely due to the multi-level subgrid closure. The inflow is laminar and therefore in the free-stream  $k^{sgs} = 0$ . Without the correction,  $k^{sgs}$  will remain zero in the wake resulting in insufficient dissipation at small scales.

Statistics are collected for 100 non-dimensionalized time units,  $t = d/u_\infty$ . In Fig. 5.14, the average pressure coefficient  $\overline{C_p}$  and the skin friction coefficient,  $\overline{C_f}$  are plotted over the surface of the cylinder. The data was averaged in space and also along the z-direction. Excellent agreement is obtained for the point of separation and pressure coefficient data. The skin friction coefficient is also matching well with the past data. Also, note the smoothness in the pressure and skin friction coefficient. To the best of the author's knowledge, such a smooth reconstruction, especially in the skin friction coefficient has never been shown in any of the past IB studies. Overall, the Cutcell-AMRLES approach captures the near wall solution very well. There are some oscillations in the skin friction coefficient plot around 50 degrees. These oscillations indicate the flux reconstruction in the cell present in these regions is not accurate. More investigation is needed to ascertain the source of these numerical artifacts, but the current hypothesis is that the cell clustering and thus the polynomial reconstruction is affected because of some degenerate small cells. Nevertheless, in other regions, the skin friction coefficient distribution is smooth.

To further assess the performance of the subgrid closure, the time averages plots of various flow and closure related quantities are presented in Fig. 5.15. The streamline plots along with the streamwise velocity contours clearly show two recirculation bubbles in the back of the cylinder which are close to symmetric with respect to the streamwise direction. The reattachment length from for bubble is around two diameters which matches with observations from past experimental studies. From the figure, the generation of  $k^{sgs}$  in the free shear layer formed from the boundary layer separation is clearly seen in the mean sense. The closure model parameters  $C_\nu$ ,  $C_\epsilon$  that are computed dynamically show a wide variation, especially in the wake region. As expected there is a significant increase the value of parameter  $\overline{C_\nu}$  in the

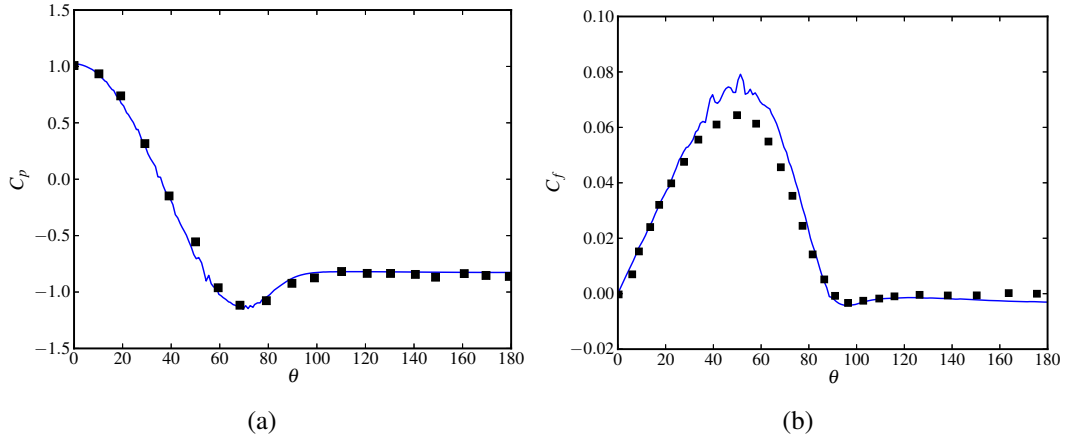


Figure 5.14: Time and spatially averaged (in homogeneous direction) data of (a) pressure coefficient  $\overline{C_p}$  and (b) skin friction coefficient for  $Re_d = 3900$  flow past cylinder. Block dots in (a) represent data from a past experimental study [147] and (b) represent data from a body fitted LES [145].

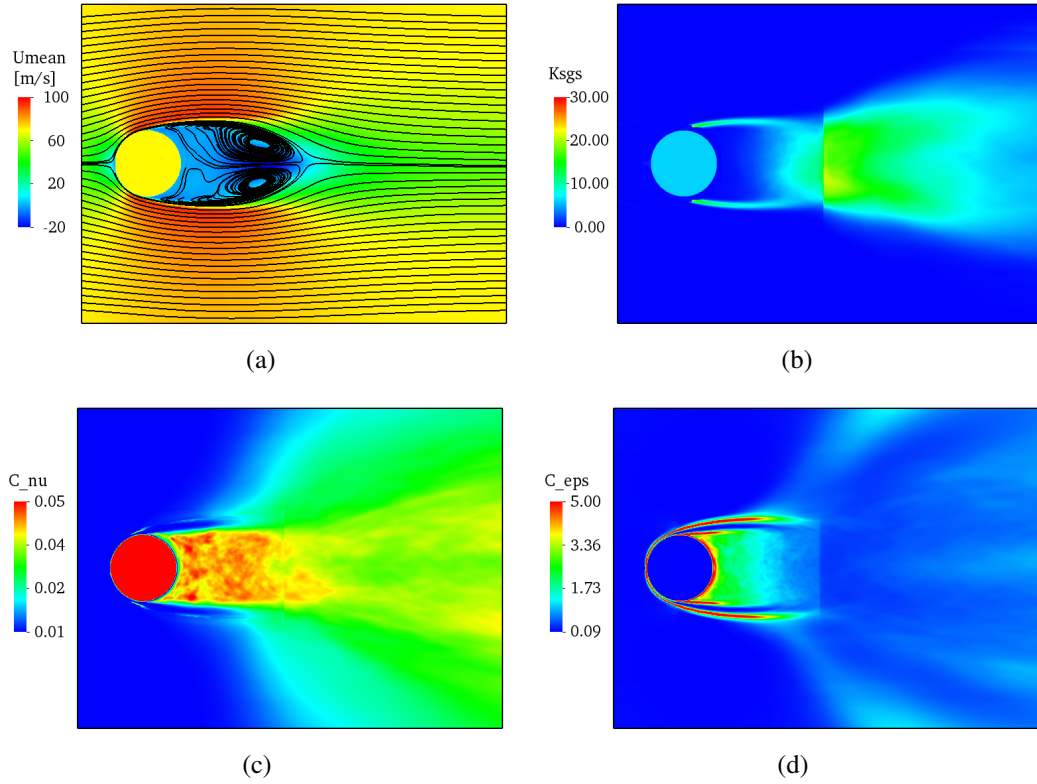


Figure 5.15: Time average plots of (a) Streamwise velocity (b) Subgrid kinetic energy (c) LDKM parameter  $C_\nu$  and (d) LDKM parameter  $C_\epsilon$  in center x-y plane.

wake region where the large scale vortex structures breakdown and flow become turbulent. The increase in  $C_\nu$  in turn increases the contribution of the subgrid stress to the momentum equation through Eq. (2.42). The plot of the time averaged  $C_\epsilon$  shows high values near the boundary and the shear layer. Downstream of the cylinder in the turbulent wake, the value of the  $C_\epsilon$  drops. Since this parameter is a scaling coefficient for the model of dissipation of subgrid turbulent kinetic energy, a high value of  $C_\epsilon$  implies increased subgrid dissipation in the near wall region and shear layer.

The quality of the wake predictions by the Cutcell-AMRLES approach is assessed by comparing the mean streamwise velocity along the centerline of the cylinder with previous data in Fig. 5.16. Overall the velocity deficit and recovery post reattachment is captured well in the current simulation. But it appears that the length of the recirculation bubble is over predicted which is causing a delayed reattachment. Since the near wall predictions are in excellent agreement with past data, the reason for this discrepancy is suspected to be mainly because of lack of convergence of the temporal statistics. A previous study [145] performed time averaging after 700 non-dimensionalized time units for an interval of 250 time units. Whereas in the current study, time statistics were collected after 150 time units for only an additional 100 time units. The wake predictions are expected to improve with collection of more time averaged data.

### 5.3.3 LES of $Re_d=3700$ flow past a sphere

Simulations of flow past spheres can be quite challenging with traditional body conformal structured grid methods mainly because of the complexity involved in generating a good quality mesh especially near the wake region. Here, the Cutcell-AMRLES approach is employed to simulate the turbulent flow of  $Re_d = 3700$  over a sphere of diameter,  $d$ . The simulations are performed in a rectangular domain of size  $30d \times 30d \times 30d$  with a base resolution of  $(150 \times 150 \times 150)$ . The AMR levels and grid resolution is kept same as the previous  $Re_d = 3900$  study as the Reynolds numbers are comparable. The plot of the AMR refine-

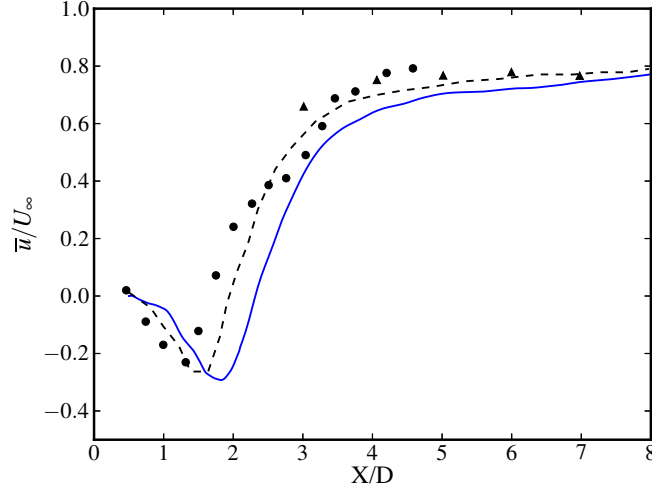


Figure 5.16: Time averaged streamwise velocity along the cylinder centerline. Blue solid line - Cutcell-AMRLES, Black dotted line - Body-fitted LES [145], Black filled dots - Experimental [148], Black filled triangles - Experimental [149].

ment for the sphere is shown in Fig. 5.17 Characteristics based subsonic inflow is used in the left boundary while subsonic outflow condition is prescribed to all the other boundaries. DNS simulation of the same Reynolds number has been performed in the past [150] using an body-conformal unstructured approach.

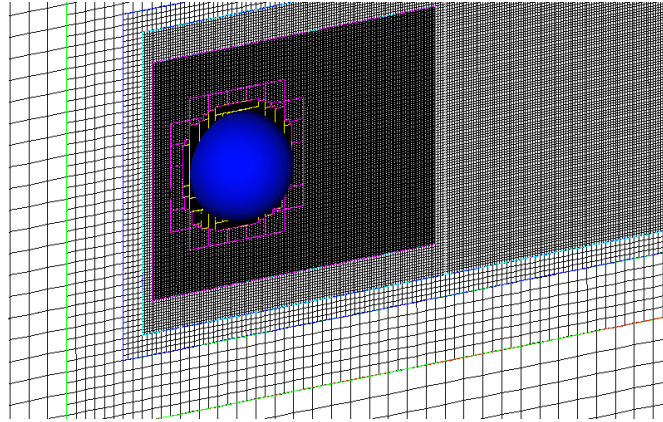


Figure 5.17: Snapshot of local mesh refinement near surface for  $Re_d = 3700$  flow past a sphere.

The time history of the drag and lift coefficient plots are shown in Fig. 5.18. The average value of the drag coefficient is found to be  $\overline{C_d} = 0.38$ . This is close to the value of  $\overline{C_{d,DNS}}$

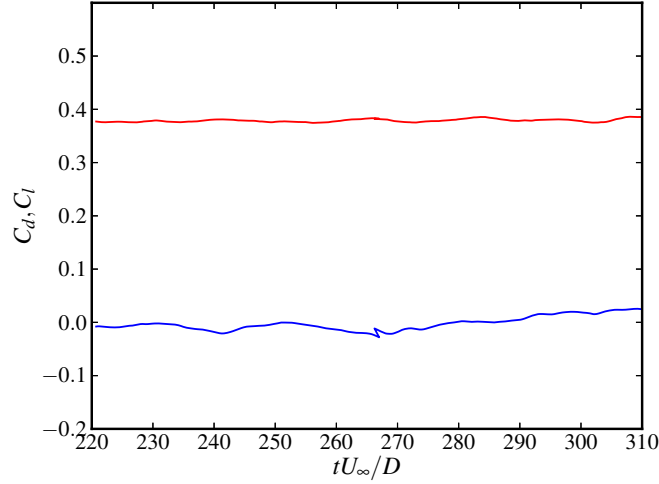


Figure 5.18: Time history of drag ( $C_d$ ) and lift ( $C_l$ ) coefficient of  $Re_d=3700$  flow past a sphere.

0.39 predicted by the DNS study. To visualize the vortex structures in the wake of the sphere, the iso-surface of Q-criterion colored with streamwise velocity is shown in Fig. 5.19. Similar to the cylinder case, the boundary separates from the sphere surface and forms shear layer envelope which breaks down rapidly into small scale turbulence within a couple of diameters downstream. Due to the three dimensional nature of the free shear layer, the break down to small scale turbulence is much faster compared to flow past a cylinder.

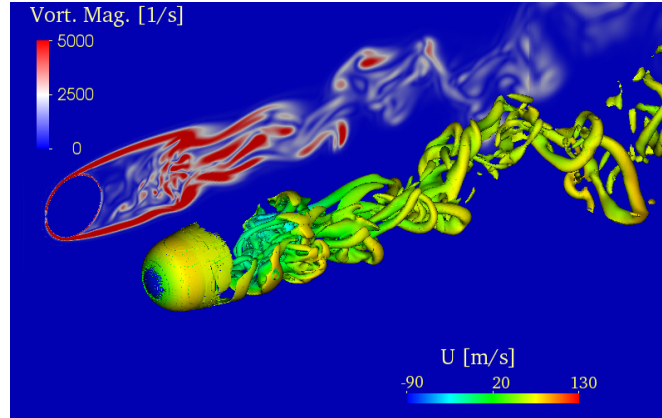


Figure 5.19: Vortex structures visualization by iso-surface of Q-criterion colored with streamwise velocity.

The instantaneous snapshots of subgrid kinetic energy and eddy viscosity ratio are shown

in Fig. 5.20. It can be seen from the figure that the behavior of the various flow field quantities

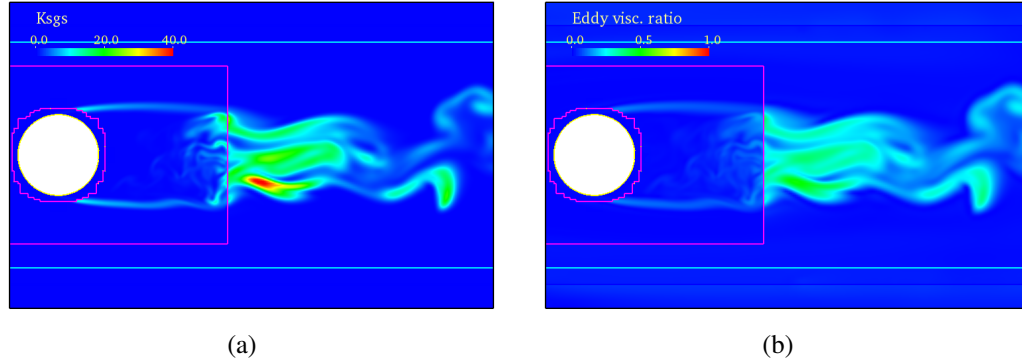


Figure 5.20: Instantaneous snapshot of (a) subgrid kinetic energy and (b) eddy viscosity ratio in the center x-y plane

is similar to the previous case of flow past cylinder. The multi-level closure injects  $k^{sgs}$  when near wall refinement ends into the shear layer. A jump in the subgrid kinetic energy and the eddy viscosity is observed after a fine/coarse AMR interface.

The data is time averaged over 100 non-dimensionalized time units. The plots of the average pressure coefficient  $\overline{C_p}$  and the skin friction coefficient,  $\overline{C_f}$  extracted along the mid-plane of the sphere, are presented in Fig. 5.21. The current results show excellent agreement with the data from DNS and an experimental study for the  $C_p$ ,  $C_f$ , the back pressure and the point of separation. Again it has to be reiterated that to the best of the author's knowledge, such a good match has never been reported in addition to smooth reconstruction of pressure and especially skin friction coefficient, in any of the past studies employing an embedded boundary technique. The contour plot of the pressure distribution on the sphere surface is shown in Fig. 5.22.

The wake predictions are assessed by comparing the mean streamwise velocity and the RMS of streamwise velocity along the centerline with previous DNS results in Fig. 5.23. The velocity deficit and recovery post reattachment is captured well in the current simulation. The magnitude of the rms of streamwise velocity is slightly over predicted but the peak locations match well with the DNS data. As for the cylinder study, the wake predictions are expected

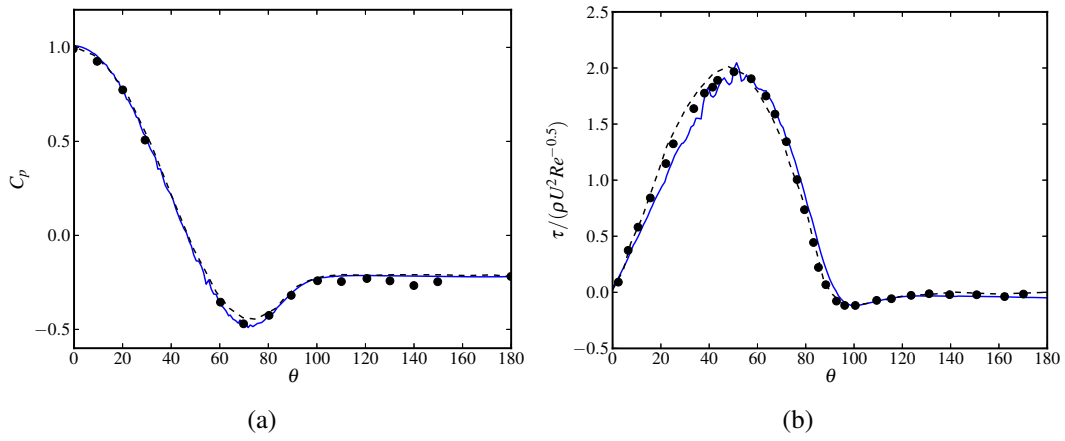


Figure 5.21: Time averaged data of (a) pressure coefficient  $\overline{C_p}$  and (b) skin friction coefficient for  $Re_d = 3700$  flow past cylinder. Solid blue line- Cutcell-AMRLES Block dots in (a) represent data from a past experimental study [147] and (b) represent data from a body fitted LES [145].

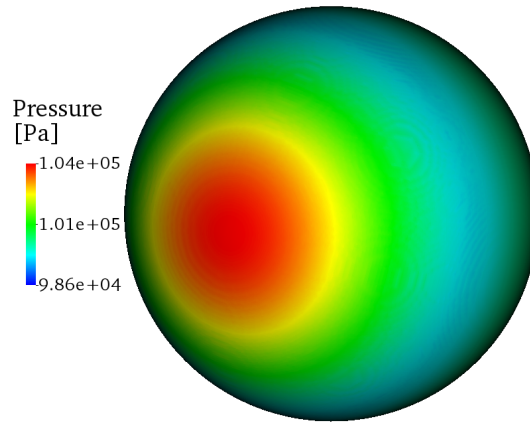


Figure 5.22: Smooth distribution of pressure on the sphere surface for  $Re_d = 3700$  flow past a sphere.

to improve with collection of more time averaged data.

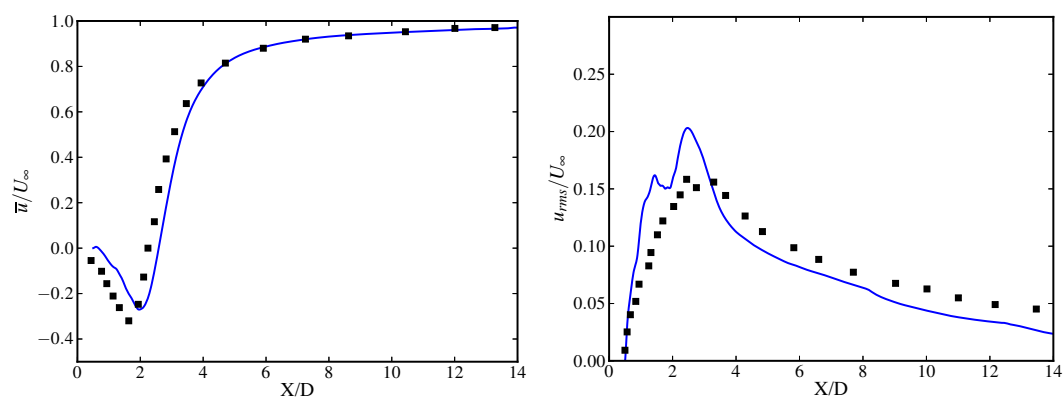


Figure 5.23: Time averaged streamwise velocity along the cylinder centerline. Blue - Cutcell-AMRLES, Black dots - Body-fitted unstructured DNS [150]



## CHAPTER 6

### MULTI-LEVEL REACTION RATE CLOSURE FOR CHEMISTRY

For LES of reacting flows, the filtered reaction rate requires a closure. A Linear Eddy Model (LEM) based reaction rate closure adapted for multi-level AMR grids (multi-level RRLES) is described in this chapter. The RRLES along with AMRLES is applied to study interaction of a freely propagating methane flame with a decaying isotropic turbulence. The RRLES implementation and the flame-turbulence interaction results presented in this thesis are taken from a past work [151] co-authored by the thesis author and are presented here with appropriate permissions.

#### 6.1 Formulation and implementation of a multi-level closure for filtered reaction rate

The subgrid closure for chemistry is a natural extension of the AMRLES closure. The closure model is developed and implemented as a part of this thesis and the complete description of the closure can be found in [151]. First, some of the single level closure problems related to scalars are discussed. The multi-level formulation is then later described.

##### *LEM Subgrid Model*

The original LEM model [108] was a stand-alone model to account for concurrent interactions between turbulence, molecular diffusion and reaction kinetics. The model as originally envisioned by Kerstein was one-dimensional (and hence, computationally very efficient), and contained three fundamental physics of scalar mixing and reaction kinetics: (a) molecular diffusion, (b) reaction kinetics and (c) stirring by turbulent eddies. These processes are implemented by solving the reaction-diffusion model for species and Temperature fields along

a notional 1D domain:

$$\rho^{LEM} \frac{\partial Y_k^{LEM}}{\partial t} + F_k^{stir} + \rho^{LEM} \frac{\partial}{\partial x} \left( -D_k \frac{\partial Y_k^{LEM}}{\partial x} \right) = \dot{\omega}_k, \quad (6.1)$$

$$\rho^{LEM} C_p \frac{\partial T^{LEM}}{\partial t} + F_T^{stir} + \sum_{k=1}^{N_s} C_{p,k} \frac{\partial}{\partial x} \left( D_k \frac{\partial Y_k^{LEM}}{\partial x} \frac{\partial T^{LEM}}{\partial x} \right) - \frac{\partial}{\partial x} \left( \kappa \frac{\partial T^{LEM}}{\partial x} \right) = \sum_{k=1}^{N_s} \dot{\omega}_k h_k. \quad (6.2)$$

The scalar fields  $Y_k^{LEM}$  and  $T^{LEM}$  are represented in notional 1D lines embedded inside each 3D cells. The scalar fields are concurrently modified by the stirring events  $F_k^{stir}$  and  $F_T^{stir}$  that punctuate the deterministic evolution in the reaction-diffusion process. This turbulent stirring is implemented as stochastic events (based on the so-called triplet maps that attempts to capture the effect of turbulent stirring (based on Kolmogorov scaling) on the scalar field and mimics the effect of vortices on the scalar field. Successive folding and compressive motions are modeled such as an initially monotonic profile of, say, mixture fraction can develop multiple extrema with stoichiometric points in between each corresponding to a flame location. At high turbulence intensity, the time scale of folding, compression, and diffusive mixing might become short enough relative to chemical time scales so that broad reaction zones, stirred internally by small eddies can be formed. This ability of LEM is unique in mixing model but it is also apparent that this feature of LEM limits its applicability to turbulent flows where inertial range scaling is applicable.

In 1D LEM the instantaneous maps represent the outcome of an individual eddy motion, although such a literal connection between maps and eddies is not required. An LEM simulation time advances the 1D unsteady diffusion-reaction equations, including associated dilatations along the 1D domain and this advancement is punctuated by instantaneous rearrangements of property profiles by mapping operations of a specified form. In effect, the outcome of each map constitutes a new initial condition for further time advancement.

The details of the 1D LEM as a stand alone model [152, 153] have been reported in details elsewhere and therefore, not repeated here. It has also been implemented as a sub-grid model for LES (called LEMLES) [153]. There are advantages and disadvantages to this implementation. Since the model is in 1D, the resolution can be fine enough to resolve the smallest scales and therefore, reaction kinetics and molecular diffusion can be simulated without any closure. Turbulent stirring in high  $Re$  flows recover turbulent diffusivity [154, 155], and the model has shown ability to capture both high and low Schmidt Number dependencies [156] without requiring any model adjustments. On the other hand, reduction to a 1D notional dimension (typically considered aligned normal to the scalar gradient) limits its ability in cases where the flame has to propagate in 3D as opposed to fluctuate around a statistically mean location. Fortunately, many combustion problems of practical interest as in swirl combustors, premixed burner etc., involve relatively stationary flames and therefore, this closure has shown ability in many applications in the past.

A variant of the LEMLES closure model that can be adapted to AMR is now described.

### *Multi-level RRLES*

The main idea of the multi-level RRLES approach is to employ the 1D LEM subgrid model on the coarsest level,  $l = 1$  to close the filtered reaction rate term  $\bar{\omega}_k^1$ . Accordingly, the subgrid reaction-diffusion equations ( Eqs. (6.1) and (6.2)) are solved on a 1D domain. This 1D LEM domain in the conventional LEMLES approach lies embedded within each LES grid cell. For a multi-level grid, there is now an option of locating these LEM 1D domains in any or all of the AMR grid levels. In this thesis, the approach proposed is to allocate these LEM 1D domains in the coarsest AMR level. Accordingly, the 1D LEM equations given by Eqs. (6.1) and (6.2) are solved at the subgrid level on only the first AMR grid level.

To enforce conservation of mass and ensure consistency of the species mass fraction, i.e.,  $\tilde{Y}_k^1$ , the 1D subgrid species mass fraction and temperature fields need to be reconstructed every time step based on the corresponding resolved quantities. This reconstruction approach

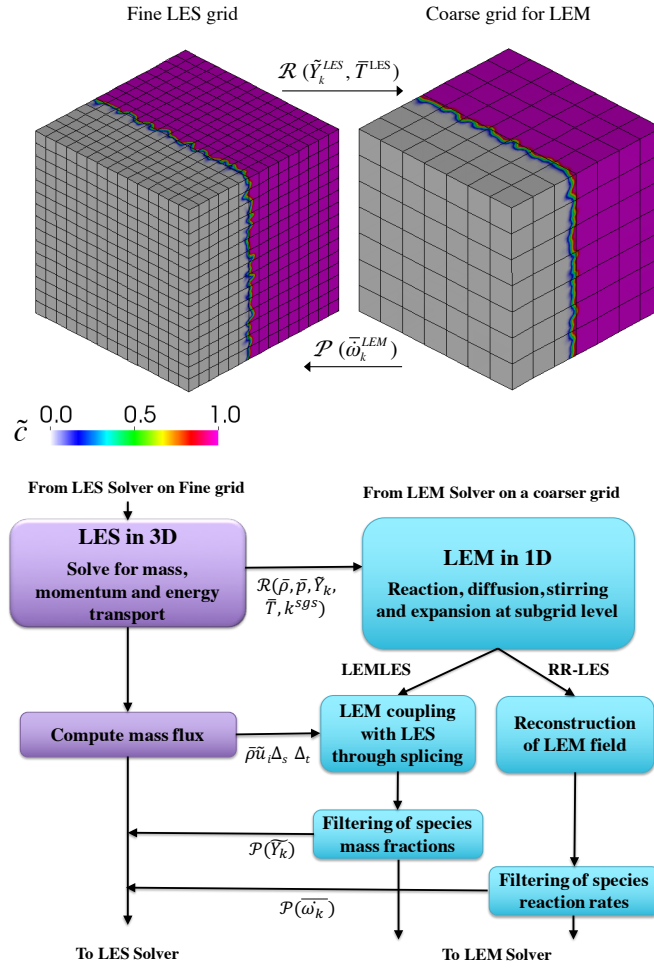


Figure 6.1: Schematic of the multi-level approach (a) and workflow (b) in the LEMLES and RRLES strategy. Subfigure (a) shows contours of progress variable on both the grids for a planar premixed flame configuration.

needs to be specified as the resolved level does not explicitly contains the subgrid information. A gradient based reconstruction model that relies on the notional idea that the 1D LEM domains are aligned along the direction of the maximum scalar gradient is proposed. Also, a multi-resolution approach for the numerical implementation of RRLES is employed wherein, the LEM subgrid scalar fields are hosted on a grid with relatively coarser resolution while the LES governing equations are solved on all AMR grid levels. An estimate of the subgrid field variation at the coarse grid can be made by employing a multi-resolution strategy. Therefore, the scalar gradient computed at the finest grid level is used at the coarse grid level to perform the subgrid reconstruction. Figure 6.1 shows a sketch of the multi-resolution LEMLES approach, demonstrating the multi-resolution strategy. Note that the multi-resolution based RRLES strategy is an alternate formulation in comparison to the traditional single resolution based LEMLES strategy, which is also shown in Figure 6.1. There are notable differences in the traditional LEMLES and the current RRLES formulations, which are also highlighted.

For the gradient based reconstruction, both the scalar fields and their gradients are filtered from the finest AMR grid level to the coarsest level and is given by the following equation:

$$(Y_k^{\text{LEM}}, T^{\text{LEM}})^1 = \mathcal{R}_N^1(Y_k, \nabla Y_k, T, \nabla T), \quad (6.3)$$

where  $\mathcal{R}$  is the restriction operator (see Figure 6.1) that does a conservative filtering from the finest grid to the coarsest grid to initialize the LEM fields. The scalar fields are then constructed using the following equations:

$$Y_{k,iLEM} = \tilde{\tilde{Y}}_k^1 - \frac{\widetilde{\widetilde{\nabla Y_k}}^1 \Delta x^1}{2} + (iLEM - 1) \frac{\widetilde{\widetilde{\nabla Y_k}}^1 \Delta x^1}{N_{LEM}}, \quad (6.4)$$

$$T_{iLEM} = \tilde{\tilde{T}}^1 - \frac{\widetilde{\widetilde{\nabla T}}^1 \Delta x^1}{2} + (iLEM - 1) \frac{\widetilde{\widetilde{\nabla T}}^1 \Delta x^1}{N_{LEM}}, \quad (6.5)$$

where  $iLEM = 1, 2, \dots, N_{LEM}$ . The reconstruction process is performed every time step and the idea is shown in Fig. 6.2 where  $GR(\tilde{\tilde{Y}}_k^1, \widetilde{\widetilde{\nabla Y_k}}^1, \tilde{\tilde{T}}^1, \widetilde{\widetilde{\nabla T}}^1)$  denotes the gradient reconstruction.

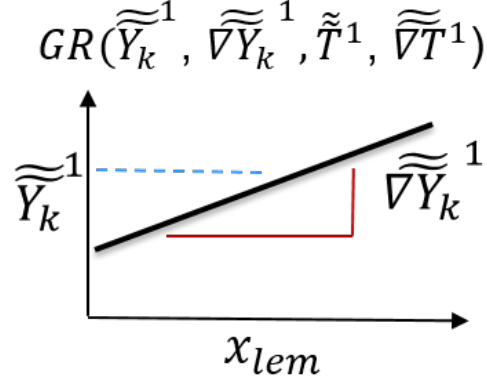


Figure 6.2: A schematic describing the gradient reconstruction of species scalar field at LEM level.

tion operation.

The filtered reaction rate within the 1D LEM are computed as:

$$\bar{\omega}_{k,\text{LEM}} = \frac{\sum_{m=1}^{N_{\text{LEM}}} \dot{\omega}_{k,m} \Delta V_m}{\sum_{m=1}^{N_{\text{LEM}}} \Delta V_m}, \quad (6.6)$$

where,  $\Delta V_m$  is the volume of the  $m^{\text{th}}$  LEM cell. Since the 1D LEM equations given by Eqs. (6.1) and (6.2) are solved at the subgrid level, the effects of the subgrid molecular diffusion and turbulent stirring (as in Step 1 of LEMLES) are implicitly included in Eq. (6.6). Hence the species governing equations in Eq. (5.14) are solved at the resolved grid level with the filtered reaction rate obtained from the subgrid level.

Afterward, Eq. (6.6) is projected to the finer grids (see Figure 6.1) using a prolongation operation, such that:

$$\bar{\omega}_{k,\text{LES}}^l = \mathcal{P}_1^l \left( \bar{\omega}_k^1 \right) \quad (6.7)$$

where  $\bar{\omega}_k^1 = \bar{\omega}_{k,\text{LEM}}$ . The entire multi-level RRLES closure procedure is summarized in Fig. 6.3.

There are advantages and disadvantages of this approach. For example, aforementioned limitation of the LEMLES approach in regions of low turbulence is avoided since there are more unresolved scales at the coarser grid where LEM is used. Also, since the “splicing”

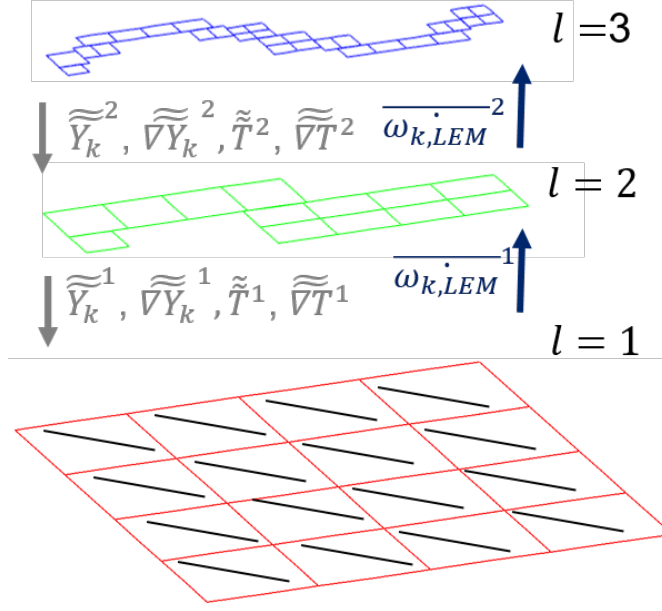


Figure 6.3: A schematic describing the multi-level RRLES closure for the filtered reaction rate.

algorithm of LEMLES (Step 2) is avoided all the limitations of this approach in the limiting case of DNS or in laminar regions are avoided since molecular diffusion at the LES level by the term  $\frac{\partial}{\partial x_i} \left[ \frac{\widetilde{\widetilde{\rho}}}{\widetilde{\widetilde{\rho}}} \widetilde{\widetilde{Y}}_k^l \widetilde{\widetilde{V}}_{k,i}^l \right]$  is explicitly included. On the other hand, counter-gradient transport is not feasible by this closure.

Another subtle issue observed is that in the asymptotic limit of low turbulence the filtered reaction rate term does not approach the quasi-laminar reaction rate limit [157]. In the quasi-laminar chemistry based closure in large-eddy simulation, which is sometimes also called as a no-model approach for the reaction-rate term, the filtered-reaction rate is simply expressed as:  $\overline{\omega}_{k,QL} = \dot{w}_k \left( \overline{P}, \widetilde{T}, \widetilde{Y}_1, \widetilde{Y}_2, \dots, \widetilde{Y}_{N_s} \right)$ . To achieve the asymptotic limit under both high and low turbulent conditions, a hybrid approach for the filtered reaction rate is used and Eq. (6.7) is replaced as:

$$\overline{\omega}_{k,LES}^l = f(\xi) \mathcal{P} \left( \overline{\omega}_k^1 \right) + [1 - f(\xi)] \overline{\omega}_{k,QL}^l, \quad (6.8)$$

where  $\xi = \nu_t^l / \nu^l$  is the ratio of the turbulent eddy viscosity and the kinematic viscosity at

level  $l$ , respectively and  $f$  is a blending function in the range  $[0, 1]$  and is given as:

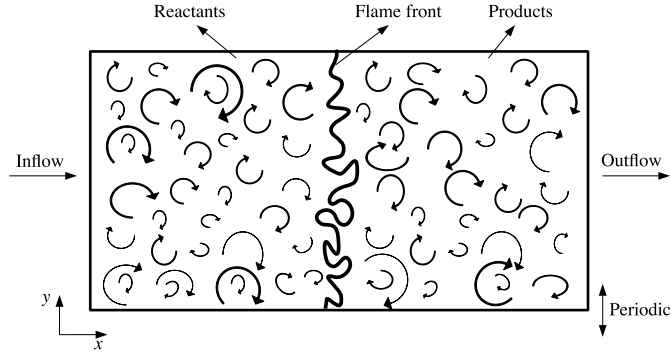
$$f(\zeta) = \frac{1}{2} + \frac{1}{2} \tanh \left[ a \left( \frac{\zeta}{\zeta + 1} - b \right) + c \right], \quad (6.9)$$

where  $a = 100$ ,  $c = -50$  and  $b = -0.475$  based on numerical experiments [151]. A preliminary assessment of the effect of the functional form of  $f(\xi)$  on the flame structure can be found in [151]. The requirement in Eq. (6.8) is that at low or negligible sgs turbulence level,  $f(\xi) \rightarrow 0$  whereas at higher turbulence level, which is characterized by  $\xi \gg 1$ ,  $f(\xi) \rightarrow 1$ . At moderate turbulence levels when the ratio  $\xi = \mathcal{O}(1)$ , the reaction rate computed from the LEM field and the fine grid LES are comparable and therefore both can contribute to the LES closure. The function  $f(\xi)$  is determined in a dynamic manner (since  $\nu_t^l$  is obtained using a localized dynamic approach, LDKM) and therefore, this approach adapts with the solution. Although a more comprehensive assessment of this hybrid approach will be reported in the future, the results reported in this thesis shows the potential of this approach as a multi-scale sgs closure for finite-rate kinetics modeling.

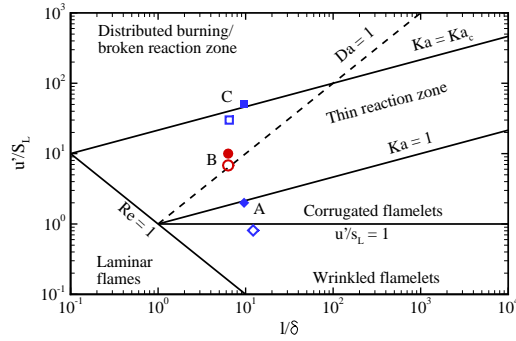
## **6.2 LES and DNS of a freely propagating premixed flame interacting with a decaying isotropic turbulence**

To assess the accuracy of the multi-level RRLES approach, interaction of a freely propagating methane flame with a decaying isotropic turbulence is studied at various levels of turbulence. Figure 6.4(a) shows a schematic of the premixed planar flame configuration. Three different turbulent premixed flames corresponding to the CF, TRZ and B/DRZ regimes (based on the initial turbulence and flame conditions) are considered in this study to analyze the resolved and sgs dynamics of flame-turbulence interaction. These cases are indicated on the premixed regime diagram [158] in Figure 6.4(b) at both the initial time and the time at which the flame statistics are analyzed. The initial flame front is obtained from a laminar premixed flame solution, and is specified near the center of the domain with reactants





(a)



(b)

Figure 6.4: A schematic of the turbulent premixed flame configuration (a) and the premixed flame regime diagram [158] (b) showing the cases considered in this study. Solid and open symbols indicate the initial state of the flame-turbulence interaction and the state at which analysis is performed, respectively.

and products on its left and right sides, respectively. The extent of the computational domain is  $L \times L \times L$  in the streamwise ( $x$ ), transverse ( $y$ ) and spanwise ( $z$ ) directions, where  $L = 0.0055$  m. The flow field is initialized using an isotropic turbulent flow field obtained using the Kraichnan spectrum [159]. It is further superimposed with the one-dimensional planar flame solution obtained at  $\phi = 0.8$ ,  $T_{\text{ref}} = 570$  K and  $P_{\text{ref}} = 1$  atm. Here,  $\phi$  denotes equivalence ratio of the methane-air mixture,  $T_{\text{ref}}$  is the temperature on the reactants side and  $P_{\text{ref}}$  is the reference pressure. The flame conditions, particularly the preheated conditions and the equivalence ratio chosen here are nominally based on past studies, which are typical of gas turbines, spark-ignition engines and combustors [160, 161]. A characteristic based inflow-outflow boundary condition is used in the streamwise ( $x$ ) direction and periodic boundary condition is used along the spanwise ( $z$ ) and the transverse ( $y$ ) directions.

Table 6.1 summarizes the simulation parameters of all the cases in terms of turbulence and flame parameters. The three premixed flames are estimated to be in the CF, TRZ and B/DRZ regimes based on initial turbulence intensity, and are respectively labeled as Case A, Case B and Case C. QLLES and LEMLES closures are used employed with the the same simulation parameters set for RRLES closure. In Table 6.1,  $l$  is the integral length scale,  $\delta = \nu/S_L$  is the Zeldovich flame thickness,  $u'$  is the turbulence intensity,  $S_L$  is the laminar flame speed, and  $Re$ ,  $Ka$  and  $Da$  are respectively, the integral Reynolds number, the Karlovitz number and the Damköhler number defined as  $Re = \frac{u'l}{\nu}$ ,  $Ka = \sqrt{\frac{u'^3\delta}{S_L^3l}}$ , and  $Da = \frac{S_L l}{u'\delta}$ . These values are estimated based on the initial conditions of the simulation.

The grid resolution,  $N_x$ ,  $N_y$  and  $N_z$  along  $x$ -,  $y$ - and  $z$ -directions, respectively is chosen based on the past studies, and for the conditions reported here is sufficient to reach  $k_{\text{max}}\eta \geq 1$  for DNS, where  $k_{\text{max}}$  is the largest wave number and  $\eta$  is the Kolmogorov length scale. In particular,  $k_{\text{max}}\eta = 7.23$ , 2.6 and 2.1 for Case A<sub>1</sub>, Case B<sub>1</sub> and Case C<sub>1</sub>, respectively. Note that the grid resolution of a well resolved LES of the flame-turbulence interaction is dictated by two requirements. First, the turbulence on the LES grid should be resolved in a manner so that it satisfies the Pope criterion [162], which requires that the resolved

Case	Closure	$N_x \times N_y \times N_z$	$u'/S_L$	$l/\delta$	$Re$	$Ka$	$Da$
A <sub>1</sub>	DNS	$384 \times 384 \times 384$	2.0	9.6	19.2	0.9	4.8
A <sub>2</sub>	RRLES	$96 \times 96 \times 96/48 \times 48 \times 48$	2.0	9.6	19.2	0.9	4.8
A <sub>3</sub>	QLLES	$96 \times 96 \times 96$	2.0	9.6	19.2	0.9	4.8
A <sub>4</sub>	LEMLES	$96 \times 96 \times 96$	2.0	9.6	19.2	0.9	4.8
B <sub>1</sub>	DNS	$384 \times 384 \times 384$	10.0	6.2	62.8	12.6	0.63
B <sub>2</sub>	RRLES	$96 \times 96 \times 96/48 \times 48 \times 48$	10.0	6.2	62.8	12.6	0.63
B <sub>3</sub>	QLLES	$96 \times 96 \times 96$	10.0	6.2	62.8	12.6	0.63
B <sub>4</sub>	LEMLES	$96 \times 96 \times 96$	10.0	6.2	62.8	12.6	0.63
C <sub>1</sub>	DNS	$512 \times 512 \times 512$	50.0	9.6	478.7	113.9	0.19
C <sub>2</sub>	RRLES	$128 \times 128 \times 128/64 \times 64 \times 64$	50.0	9.6	478.7	113.9	0.19
C <sub>3</sub>	QLLES	$128 \times 128 \times 128$	50.0	9.6	478.7	113.9	0.19
C <sub>4</sub>	LEMLES	$128 \times 128 \times 128$	50.0	9.6	478.7	113.9	0.19

Table 6.1: Initial turbulent premixed flame parameters for cases considered in this study.

turbulent kinetic energy should be approximately 80% of the total kinetic energy. Secondly, the flame structure should be adequately resolved, which requires approximately 10 points across the thermal flame thickness, i.e.,  $\delta_L = (T_b - T_u) / |\nabla T|_{\max}$ , when no closure is used for turbulence-chemistry interaction [163]. Here, subscript ‘b’ and ‘u’ denote burnt and unburnt regions, respectively. The LES cases for Case A, Case B and Case C approximately resolves about 90%, 80% and 70% of the total turbulent kinetic energy at  $t/t_0 = 2, 2$  and 3, respectively. Here  $t_0 = u'/l$  is the initial eddy turnover time. In addition, with the grids employed in the present study, it is estimated that the thermal flame thickness is resolved by around by 20 points in DNS and 5 points in LES in Case A. Clearly, the LES grid does not resolve the thermal flame thickness and can be considered as a borderline, particularly for the QLLES cases. For RRLES, two AMR levels are used with the finest level matching the resolution of other single level closures. For this case, the second AMR level completely covers the first level and therefore the dynamic refinement option is not used.

Also, 12 LEM cells are used in each LES cell for both LEMLES and RRLES. Estimates suggest that in the sgs scales eddies of size of the order of  $\eta/2$  are resolved. Simulation using an increased resolution with 24 LEM cells does not show any significant effects on the flame statistics (not shown here), and, therefore, all the results reported here are based on simu-

lations employing 12 LEM cells. For RRLES, two level of completely over-lapping grids are used. The simulations are carried out long enough to allow flame-turbulence interaction to evolve and all the results are compared after two (three) initial eddy turnover times for Case A/B (C), i.e.,  $t/t_0 = 2$  (3). Even though turbulence decays in time in the present study, there is a period during which flame-turbulence interaction attains a quasi-stationary state, and therefore, the dynamics and statistics associated with the flame-turbulence interaction can be analyzed during such period.

Figure 6.5(a)-(l) compares the flame structure from all the simulated cases. The wrinkling and stretching of the flame is predicted by RRLES in a consistent manner, and the increase in the wrinkling along with enhanced transport of heat from the reaction zone from Case A to Case C is also qualitatively captured. All simulations show a continuous flame structure and no sign of local extinction for these conditions. The RRLES the formulation can capture the flame structure as it includes the laminar diffusion and additionally, due to the blending approach employed by the formulation through Eq. (6.8), it asymptotes towards the quasi-laminar value of the filtered reaction-rate term when turbulence is either low or resolved.

The statistics of flame-turbulence interactions are analyzed after such interactions reach a quasi-stationary state. Figure 6.6 shows the conditional variation of the filtered reaction rate for methane. The peak location is shifted toward higher value of  $\tilde{c}$  for all cases. The improved predictions by the RRLES formulation is noticeable in all the cases, where a good agreement with the DNS data can be observed. The asymptotic behavior of the RRLES closure is again evident here, as can be observed in the prediction of approaches DNS and QLLES in Case A when the level of turbulence is small. For case C with a high level of turbulence, only the RRLES approach is able to match with the DNS result. The other single level closures, LEMLES and QLLES both over predict the reaction the rate. These predictions by the various closures highlights their abilities and limitations. The unphysical results predicted by LEMLES in Case A demonstrates the limitations of the formulation when the local flow conditions tend to have a low subgrid-scale turbulence.

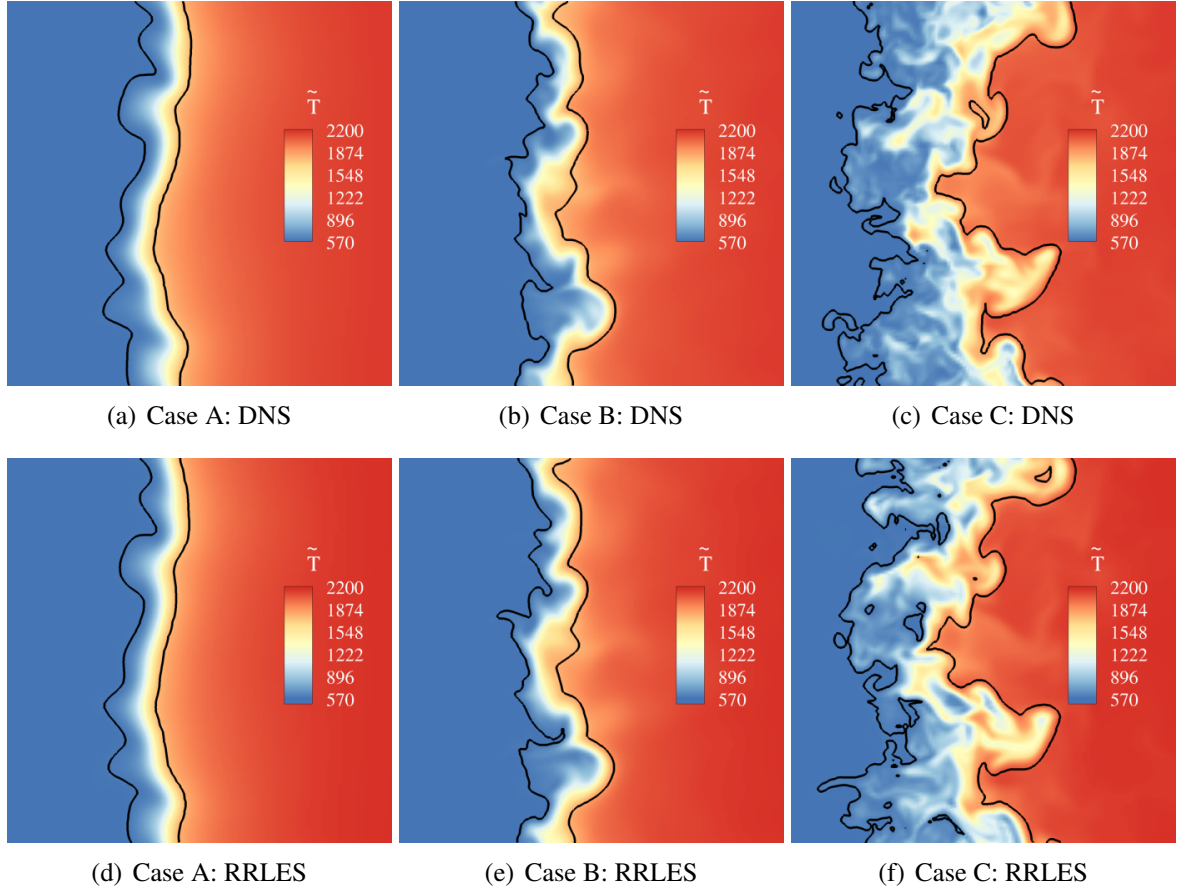


Figure 6.5: Contours of filtered temperature field overlaid with the flame brush extents in the central  $x - y$  plane identified using the filtered progress variable (iso-lines of  $\tilde{c} = 0.01$  and  $\tilde{c} = 0.99$ ) [151].

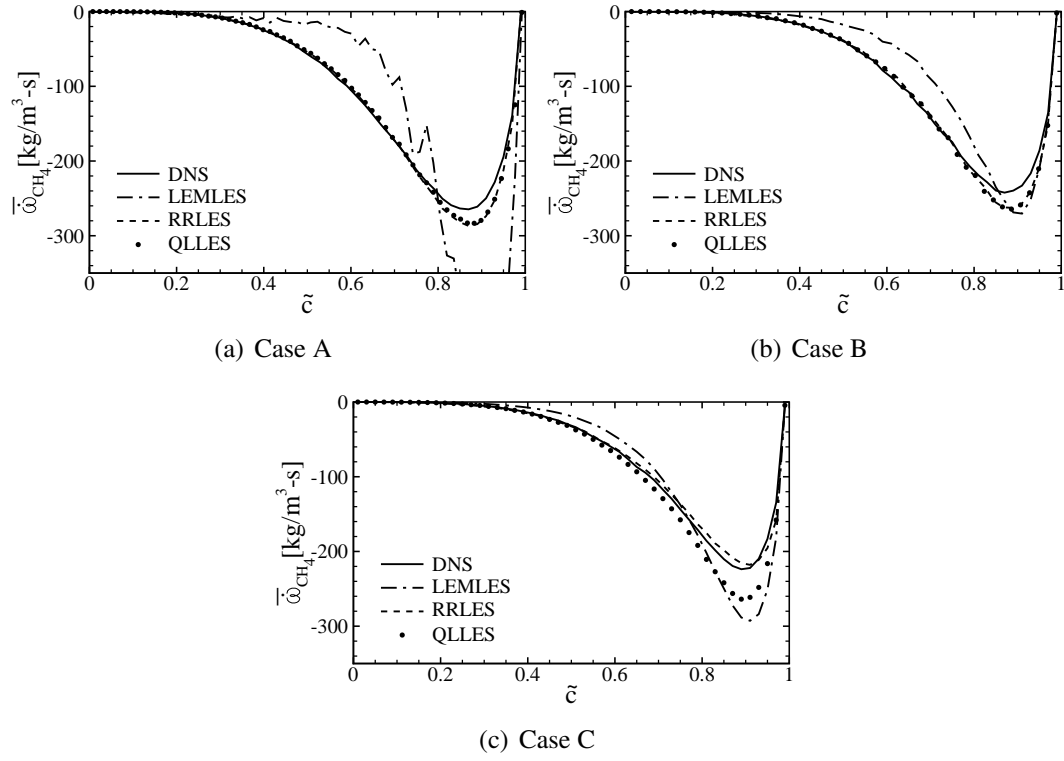


Figure 6.6: Conditional variation of the filtered reaction rate of  $\text{CH}_4$  with respect to the progress variable [151].

## **CHAPTER 7**

### **APPLICATION 1: LES OF SHOCK TURBULENCE INTERACTION**

Many of the engineering flows of interest are highly turbulent, for which Large Eddy Simulations (LES) is often used as a computational cost effective alternative to Direct Numerical Simulation (DNS) to resolve the entire range of scales of fluid motion involved. However, there are some applications, especially those involving shocks along with turbulence, for which it might be impossible (computationally) to accurately predict the wide range of scales involved using LES in a uniform grid. For such problems, an adaptive local refinement can help to adequately resolve and accurately predict the solution besides improving the computational efficiency significantly. While there are a number of studies [164] , [143] , [165], [144],[166] static and, adaptive mesh refinement (AMR) for LES of incompressible flows, there exists very limited studies on applying AMR to LES for compressible flows.

The developed framework of AMRLES can be applied to study a wide range of problems in the compressible flows involving turbulence along with phenomenon such as shocks, flames, etc. To demonstrate the applicability for such problems, two representative cases involving high turbulence and shocks are selected, one with a static shock and other with a moving shock.

#### **7.1 Introduction**

The resolution requirements for DNS and LES of shock-turbulence interaction have been well discussed in [167]. In many cases it is often not possible to resolve the shock. Therefore it is treated as a discontinuity in flow solution and the shock is captured over few grid points. In principle, the shock capturing scheme used will provide the required numerical dissipation in the vicinity of the shock to stabilize the solution. However, these schemes that are used are inherently dissipative throughout the solution regime and not just near the shock. To

avoid excessive numerical dissipation, a common practice is to employ a hybrid scheme [37] that switches to a shock capturing upwind scheme in the vicinity of the shock and to a low dissipation central scheme in the smooth regions of the flow. In order to reduce the dissipation, the regions in which the shock capturing scheme is active can be minimized [167] by using fine grid resolution. Additionally, the region immediately after the shock also requires a fine resolution as it has been observed that there is a significant reduction of turbulent length scales in the post shock region [168] in all directions. The adaptive mesh refinement can be used flexibly and easily to refine those required regions alone. There are different applications involving interaction various phenomena such as shocks, turbulence, flames and, detonation viz: blast turbulence interaction [169], flame-turbulence interaction [151], detonation-turbulence interaction [170] where AMR can be effectively employed to capture strong discontinuities with a background turbulent flow.

## 7.2 Results and discussion

### 7.2.1 Planar shock in isotropic turbulence

This is a canonical problem of a planar shock interacting with an isotropic turbulence, the schematic of which is shown in Fig.7.1. The case configurations that are chosen [168] are shown in Table 7.1. Two different  $Re$  numbers are chosen, one in the lower range with  $Re = 19.1$  and the other at a higher value with  $Re = 40$ . Both the cases are run with DNS, so that the accuracy of the LES solution obtained with the sub-grid closure models can be calibrated against DNS at two different  $Re$  number values. The LES of high  $Re$  is run with two grid resolutions, a relatively fine and a coarse resolution, to evaluate the dependence of the simulation results with the grid resolution. The grid resolution of the cases is based on the previous studies [168, 167, 171], which guides on the level of resolution nearby to the shock.

The inflow turbulence is precomputed, filtered and brought in using the Taylor's frozen turbulence hypothesis. For the case  $STI_{DNS1}$  corresponding to  $Re_\lambda = 19.1$  and  $M_t = 0.11$ ,



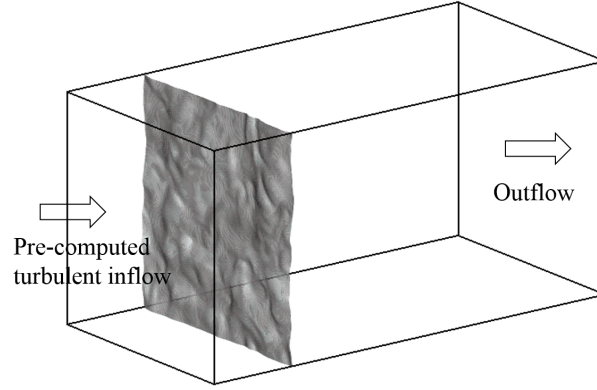


Figure 7.1: Schematic for the shock-turbulence interaction study.

Table 7.1: Summary of STI cases

Case	$Re_\lambda$	$Ma$	$M_t$	Type	AMR levels	Base grid resolution
$STI_{DNS1}$	19.1	1.29	0.11	DNS	4	$160 \times 80 \times 80$
$STI_{LES1}$	19.1	1.29	0.11	LES	4	$80 \times 40 \times 40$
$STI_{DNS2}$	40.0	1.5	0.22	DNS	2	$512 \times 256 \times 256$
$STI_{LES2F}$	40.0	1.5	0.22	LES	3	$256 \times 128 \times 128$
$STI_{LES2C}$	40.0	1.5	0.22	LES	4	$128 \times 64 \times 64$

the turbulence was evolved from an initial state of  $Re_\lambda = 40$  and  $M_t = 0.22$  in a  $2\pi^3$  triply periodic box with a grid resolution of  $80 \times 80 \times 80$  cells. The DNS data is filtered using a box filter onto a grid with  $40 \times 40 \times 40$  cells for the case  $STI_{LES1}$ . And for the higher  $Re$  case,  $STI_{DNS2}$ , an isotropic turbulence with  $Re_\lambda = 140$  and  $M_t = 0.33$  was evolved using DNS until it reached a state of  $Re_\lambda = 40.0$  and  $M_t = 0.22$ . The data is then filtered onto grids with two different grid resolutions of  $128^3$  cells and  $64^3$  cells respectively for cases  $STI_{LES2f}$  and  $STI_{LES2c}$ . Three independent realizations of the initial state are evolved and then stacked to form a  $(6\pi, 2\pi, 2\pi)$  box for providing the inflow turbulence data. Periodic boundary conditions are used in the transverse directions and a characteristic based subsonic outflow is used for the outflow boundary condition. The grid resolution is coarsened using the block-structured AMR technique adjacent to the outflow to damp the acoustic reflections from the outflow boundary condition.

The shock is initialized using the Rankine-Hugoniot jump conditions, which are calibrated to achieve a statistically stationary shock.. However, since the jump conditions are satisfied only instantaneously, the exact jump conditions resulted in a shock drift. This drift is corrected using the procedure detailed in [168]. The simulation is evolved for two flow-through times to get rid of the initial transience. The statistics are then collected by running the simulation for additional two flow-through times. Snapshots of the DNS data are stored at 60 time instants over a two flow through time period. The data is then filtered onto the LES grid and averaged over the 60 time instants and used for evaluating the LES results. The iso-surfaces of the Q-criterion colored by the pressure are shown in Fig. 7.2 for DNS clearly indicates the presence of fine scale vortical structures, which needs to be captured in the case of AMRLES as well.

### *Shock turbulence interaction for low Reynolds number case*

For the low  $Re$  case, the inflow turbulence and turbulent Mach number are not high enough to break it but can wrinkle the shock. The axial and transverse subgrid stresses are spatially

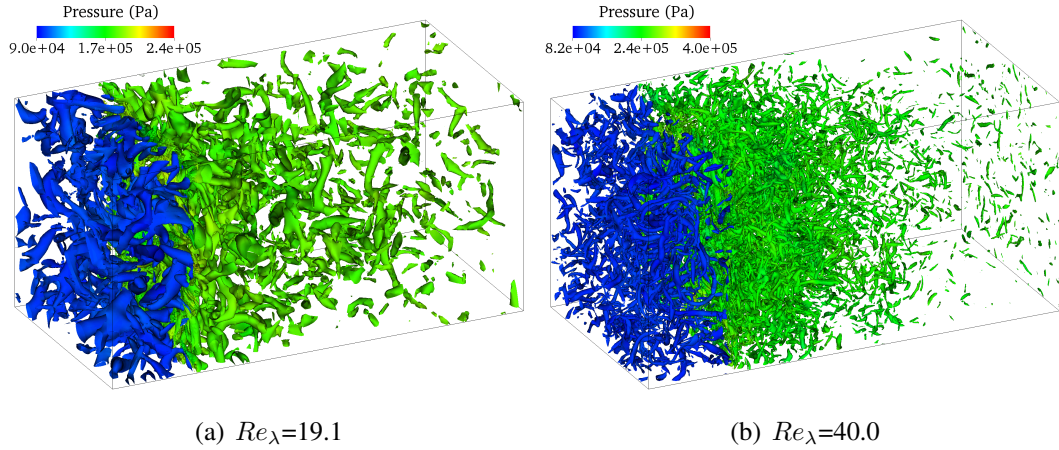


Figure 7.2: Iso-surfaces of Q-criterion colored with pressure for the cases  $STI_{DNS1}$  and  $STI_{DNS2}$ .

averaged in the two homogeneous directions and also averaged over two flow-through times. As is the practice in the past shock-turbulence studies, all the time averaged data are normalized using the values just upstream of the shock. In Fig. 7.3, the time averaged streamwise

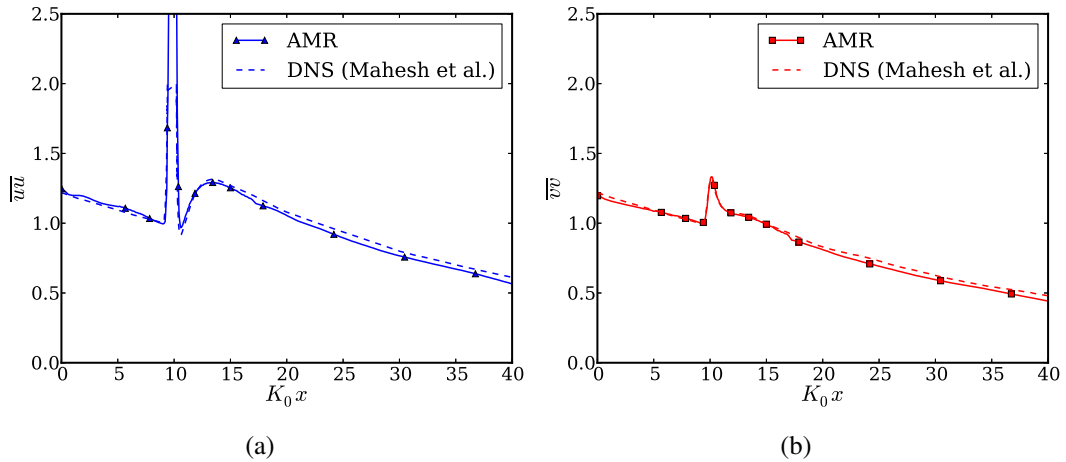


Figure 7.3: Comparison of (a) axial and (b) transverse Reynolds stresses for case  $STI_{DNS1}$  with DNS[171]

and transverse subgrid stresses for the low Reynolds number case are compared with a previous DNS simulation by Mahesh *et al.* [172] in which a stretched grid was employed. There is a very good agreement for both the axial and transverse Reynolds stresses. Although there

is a minor under prediction of the downstream intensity of the stresses, the decay rates agree quite well with the previous DNS result. The results from the LES simulations employing the multi-level sgs closure are next compared with the filtered data in Fig. 7.4. The time averaged subgrid stresses are obtained in the same procedure as described for the DNS data. The LES results agree well with the filtered data obtained from the DNS simulations. The post-shock decay is slightly under predicted for both the subgrid stress components resulting in slightly higher values downstream of the shock. The over-prediction is more pronounced for the transverse subgrid stress.

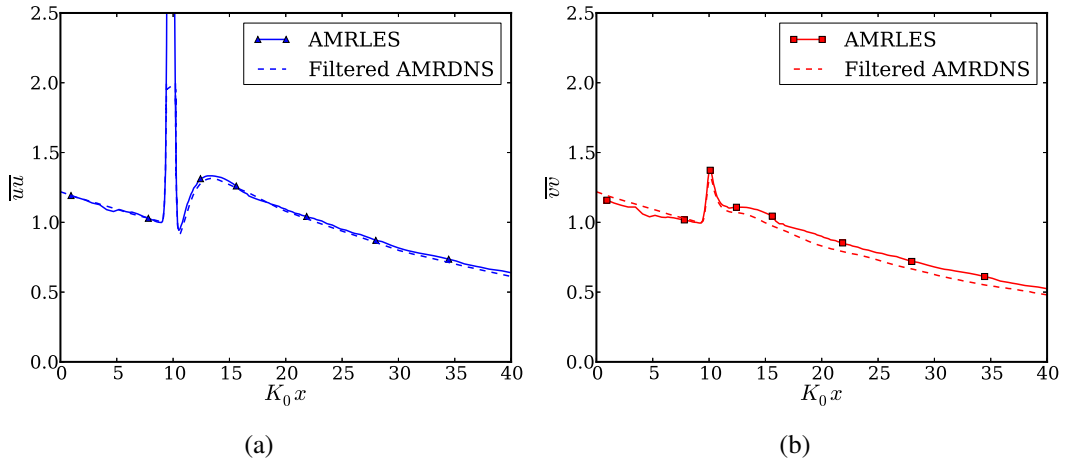


Figure 7.4: Comparison of (a) axial and (b) transverse Reynolds stresses for case STI<sub>LES1</sub> with filtered DNS data

### *Shock turbulence interaction for high Reynolds number case*

The quality of the DNS results for the high  $Re$  case are assessed by comparing the time averaged streamwise and transverse subgrid stresses obtained with the current DNS against those of the past DNS data [167], as shown in Fig. 7.5. The DNS data was digitized and shifted to match the shock location of the current simulations. The agreement is quite good considering the different methodologies used for generating the inflow turbulence and possibly some differences in the shock location. Regardless, the simulation results from DNS look quite reasonable and can serve as a reference for evaluating the LES results. The LES

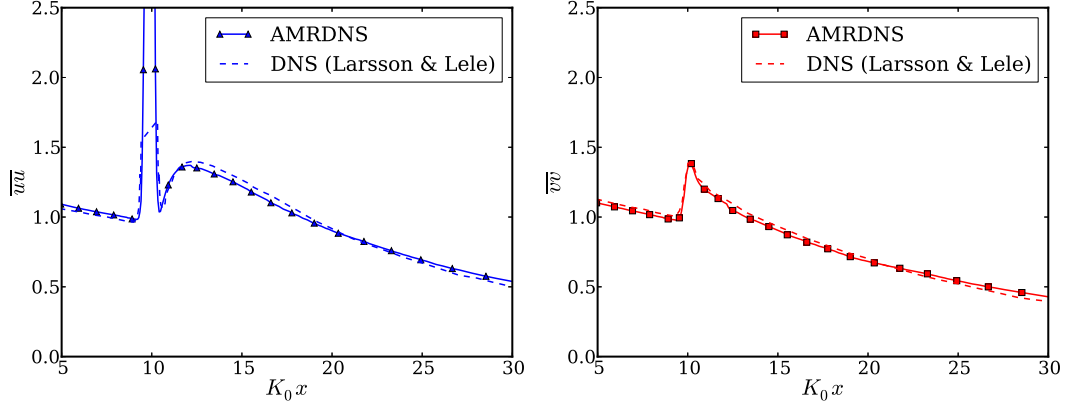


Figure 7.5: Comparison of axial and transverse Reynolds stresses for case  $STI_{DNS2}$  with a past DNS [167]

results for the time averaged subgrid stresses for both the fine and coarse grid resolutions (Table 7.1) are shown in Figs. 7.6 and 7.7 respectively. As can be seen from Fig.7.5 and Fig.7.6), the profiles of axial stress show a good match with the DNS in case of LES with fine grid resolution. However, the downstream decay rate of the transverse stress, on the other hand, seems to be slightly under predicted. With respect to the coarser grid resolution, ( $STI_{LES2C}$ ), as seen in Fig. 7.7 the underprediction in the decay rates are more pronounced for both the transverse Reynolds stress. Whereas, the axial stress matches well the DNS trend until the maximum value is reached, beyond which there is an underprediction in the downstream decay rate. Nevertheless, the current LES results have performed better in its comparison against DNS, than a previous study [171] One key observation from the results is that there emerges a consistent trend wherein the post-shock decay rates are not correctly predicted especially at coarser grid resolution. That could be due to the strict isotropic nature of modeled subgrid stresses, which therefore could not explain the anisotropy in the dissipation mechanisms causing the post-shock decay. This is actually a limitation of all the eddy-viscosity models, rather than of the AMRLES sub-grid closure as all of those eddy-viscosity models assume the eddy viscosity,  $\nu_t$  to be same in all the direction, which may not be always true.

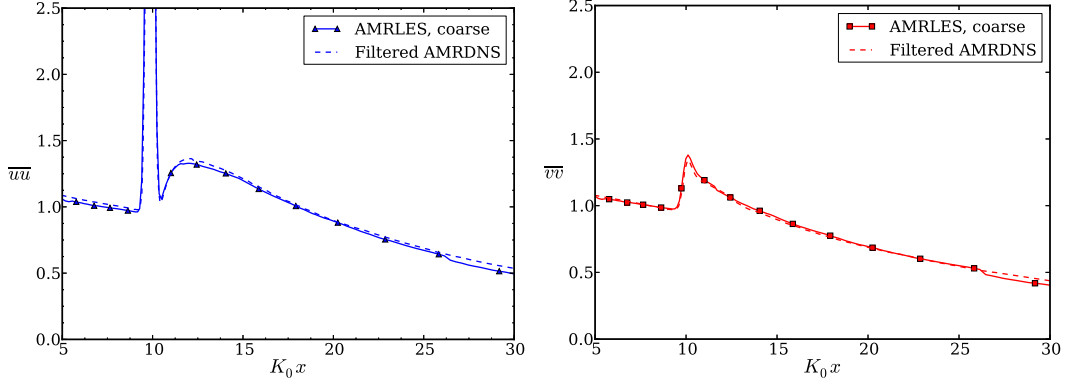


Figure 7.6:  $STI_{LES2f}$ : Comparison of axial and transverse Reynolds stresses for case LES of  $M=1.5$ ,  $Re_\lambda = 40.0$  with filtered DNS data

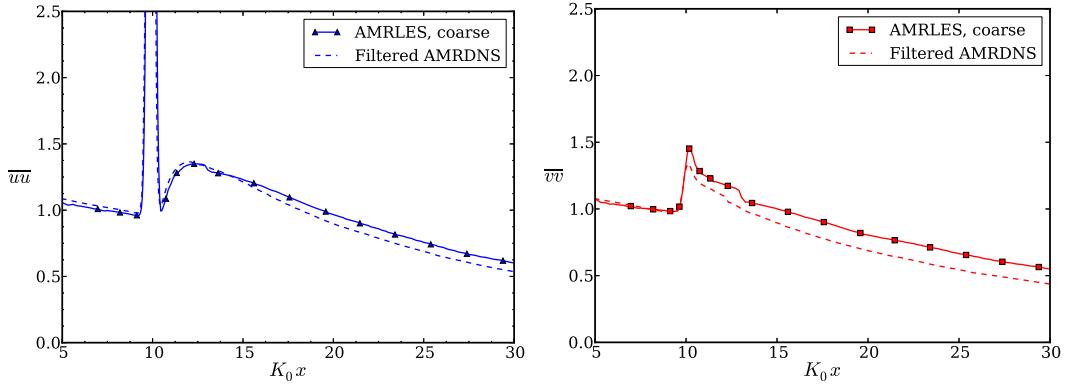
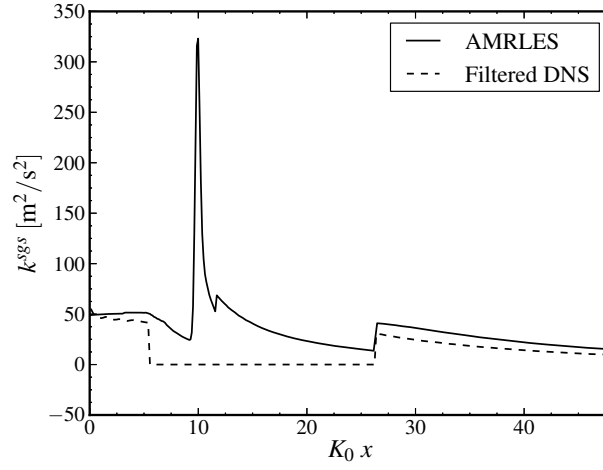


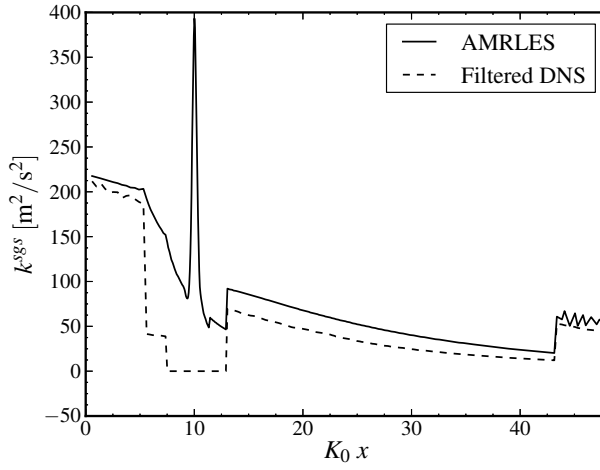
Figure 7.7:  $STI_{LES2c}$ : Comparison of axial and transverse Reynolds stresses for case LES of  $M=1.5$ ,  $Re_\lambda = 40.0$  with filtered DNS data

In order to assess the performance of the multi-level sgs closure, the filtered subgrid kinetic energy is compared with the model predicted value in Fig. 7.8 for the two cases  $STI_{LES2f}$  and  $STI_{LES2c}$ . The figure provides considerable insight into the behavior of the subgrid closure in a refinement region. Ideally, when there is a sudden reduction in the grid size, to conserve the total resolved turbulent kinetic energy, there must be an immediate transfer of the subgrid kinetic energy to the grid resolved turbulent kinetic energy,  $\tilde{u}_i \tilde{u}_i$ . Such a transfer mandates immediate population of small scales of the flow in regions of fine resolution with the subgrid kinetic energy dropping commensurately. The filtered  $k^{sgs}$  shows this behavior where the sgs kinetic energy drops to zero in well-resolved regions. However, such a transfer rarely happens with a subgrid closure as there is no explicit mechanism to enforce the transfer. Instead, as seen in the case of flow past discontinuity problem, there is a transition region over which the small scales develop resulting in a drop of the subgrid kinetic energy. This behavior is observed in Fig. 7.8 for both the cases. When the grid is refined in the vicinity of the shock,  $k^{sgs}$  is convected from the coarse grid solution and starts decaying rapidly by virtue of increased dissipation at smaller scales of motion. A spike in  $k^{sgs}$  is observed at the shock after which the decay continues. An increase in  $k^{sgs}$  then occurs when a refinement region ends and the mesh becomes coarser. There is a good agreement with filtered DNS data downstream of the shock for both the fine and coarse LES mesh cases. In the intermediate region, the remnant subgrid kinetic energy, through the closure model for the sgs stresses, provides required dissipation due to the subgrid scales for the resolved level turbulence.

An evaluation of the sgs budget can help to identify the contribution of various terms to the  $k^{sgs}$ . The different sgs terms (convection, production, transport, dissipation and pressure dilatation) that are summarized in Table 7.2 are evaluated from the instantaneous snapshots and time averaged over two flow-through times. The tke budget for case  $STI_{LES1}$  and  $STI_{LES2c}$  are shown in Fig.7.9. Prior to the shock, there is a sudden increase in sgs dissipation after every grid refinement interface and this increase is balanced by the convective



(a)  $STI_{LES2F}$



(b)  $STI_{LES2C}$

Figure 7.8: Comparison of the filtered  $k^{sgs}$  with simulation predictions for the fine and coarse LES of  $M=1.5$ ,  $Re_\lambda = 40.0$ .

Table 7.2: Closure models for various terms in transport equation of  $k^{sgs}$

Term	Closure
$T^{sgs}$	$\frac{\partial}{\partial x_i} \left[ (\bar{\rho}\nu_t + \mu) \frac{\partial \bar{k}^{sgs,n}}{\partial x_i} + \frac{\bar{\rho}\nu_t \tilde{R}}{Pr_t} \frac{\partial \tilde{T}}{\partial x_i} \right]$
$pd_{k^{sgs}}$	$\alpha_{pd} M_t^{sgs2} \left( \frac{\bar{\rho} \tilde{S} \bar{k}^{sgs,n}}{D^{sgs}} \right)^2 (P^{sgs} - D^{sgs})$
$P^{sgs}$	$\tau_{ij}^{sgs} \tilde{S}_{ij}$
$D^{sgs}$	$\bar{\rho} C_\epsilon \left( \bar{k}^{sgs,n} \right)^{3/2} / \bar{\Delta}$



term. Whereas, at the shock, all the terms go up in magnitude. The pressure dilatation term is seen to be active only at the shock. The production term acts as a source for the sgs, and as sink term for the resolved turbulent kinetic energy transport equation [173]. The increase in the sgs production implies increased transfer of energy from the resolved level turbulent kinetic energy to the subgrid kinetic energy. The subgrid diffusion is not found to play any major role in the transport of the sgs kinetic energy and is only active near the shock due to intermittency.

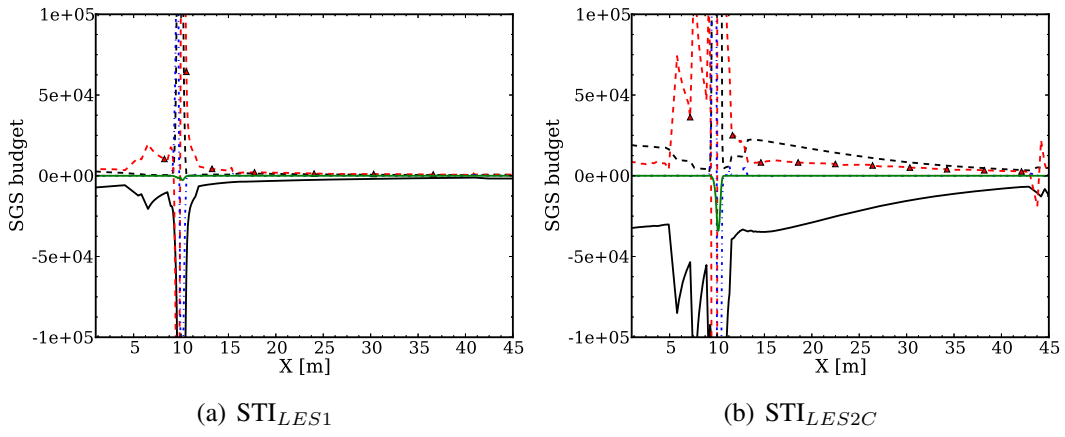


Figure 7.9:  $k^{sgs}$  budget for the low and high Re cases. —  $\langle D^{sgs} \rangle$ ; ---  $\langle P^{sgs} \rangle$ ; - - -  $\langle \frac{\partial \tilde{\rho} \tilde{u}_i k^{sgs}}{\partial x_i} \rangle$ ; - · -  $\langle T^{sgs} \rangle$ ; —  $\langle pd^{sgs} \rangle$ .

### 7.2.2 Blast turbulence interaction

The objective of this case study is to apply the multi-level sgs closure to a moving shock problem. The particular interest is in the sgs dynamics across a propagating shock. An isotropic turbulence of  $Re_\lambda = 40$  and  $M_t = 0.22$  is initialized in a periodic  $2\pi^3$  box. The initial turbulent state is the same as used for providing the precomputed inflow turbulence for the higher Reynolds number case,  $STI_{LES2f}$  of the planar shock-turbulence interaction problem. First, the Taylor blast problem is studied without the ambient turbulence. The initial profile is setup using a similarity solution which was presented in a seminal paper by Taylor [174]. An approximation of the solution to the similarity laws is also provided in the

journal and is used in the current study. The analytical solution for the location of the blast as a function of time is given by the following equation:

$$R_s(t) = S(\gamma)\rho_0^{-1/5}E^{1/5}t^{2/5}, \quad (7.1)$$

where,  $R_s$  is the radius of the blast front at any time  $t$ ,  $S(\gamma)$  is a function dependent on  $\gamma$ ,  $\rho_0$  is the density of the ambient fluid and  $E$  is the initial energy deposited. The scaling exponent for the time from Eq. (7.1) is 0.4. The case without turbulence is run with 3 levels of AMR refinement with the base grid resolution as 128 x 128 x 128. The finest resolution was chosen based on an grid independence study (not shown here). Radial averaging is done, for all the radial plots shown, in the following manner:

$$f(r) = \frac{1}{N(r)} \sum_{i=1}^{N(r)} \phi_i, \quad (7.2)$$

$$N(r) = \left\lceil \frac{r - r_{min}}{r_{max} - r_{min}} \right\rceil N_{bins}, \quad (7.3)$$

where  $\phi$  is any cell centered quantity,  $N(r)$  is the  $N^{th}$  bin with a radius range  $r + dr/2$  and  $r - dr/2$ . Here  $dr = (r_{max} - r_{min})/N_{bins}$  is the size of a single bin with  $r_{max}$ ,  $r_{min}$  being the maximum and minimum allowed radius and  $N_{bins}$  is the total number of bins. The refinement criteria is based on scaled gradients of pressure and density. The evolution of the AMR mesh with time for the case without turbulence is shown in Fig. 7.10a). As can be clearly seen, the AMR refinement is able to correctly track the moving blast front as it expands with time. In Fig. 7.11(b), the radial plots of pressure at different time instants are shown. Note that the profiles are self-similar in nature as is expected for a Taylor blast solution. The evolution of the blast radius characterized by the location of the peak pressure is shown in Fig. 7.11(a). The reference slope based on the exact analytical solution is also shown for comparison, which shows a very good agreement with the predicted solution from the simulation.

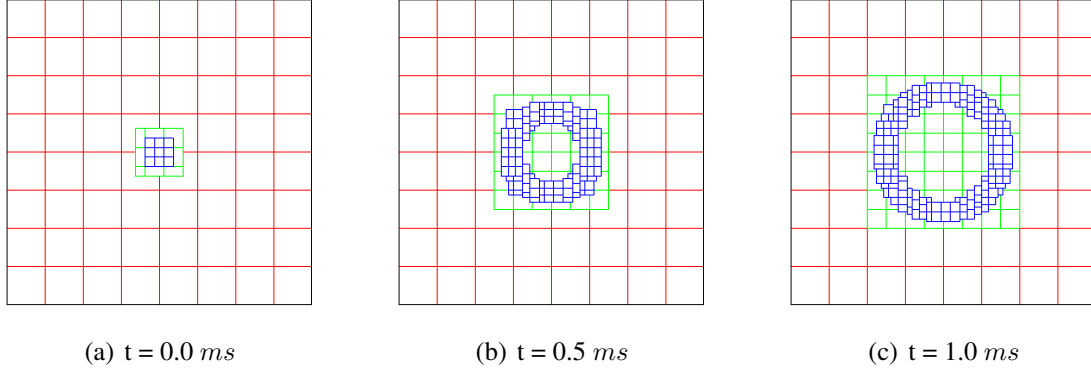


Figure 7.10: Time series of snapshot of AMR patches field at central XY plane for a Taylor blast. Red - 1<sup>st</sup> level refinement, green - 2<sup>nd</sup> level of refinement and blue - finest level of refinement.

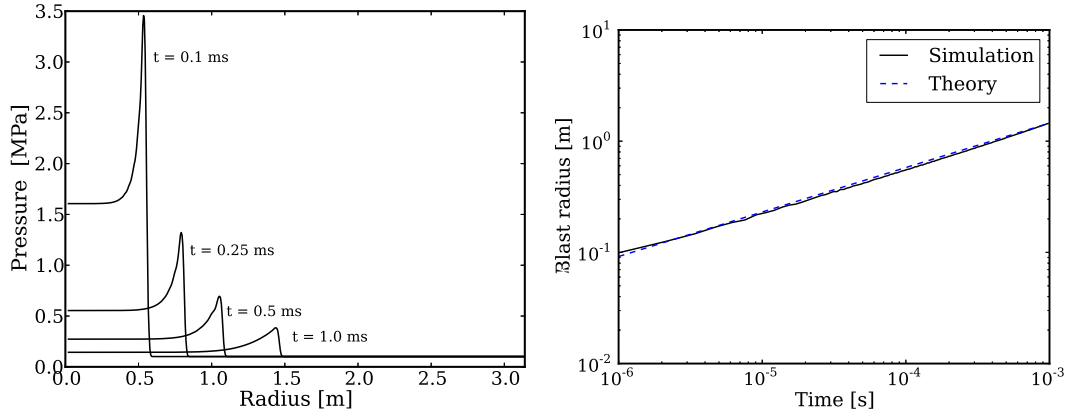


Figure 7.11: Line plots for interaction of a blast with an isotropic turbulence  $Re_\lambda = 40.0$ .

Having validated the Taylor blast setup, it is then seeded with a background turbulence. The evolution of the blast is then tracked over time. Comparison of the radially averaged plots of pressure at different time instants are shown in Fig. 7.12. For the given turbulent conditions, there is not much effect of the turbulence on the blast pressure profile but the peak value of the pressure spike is marginally lesser when the turbulence is present. The

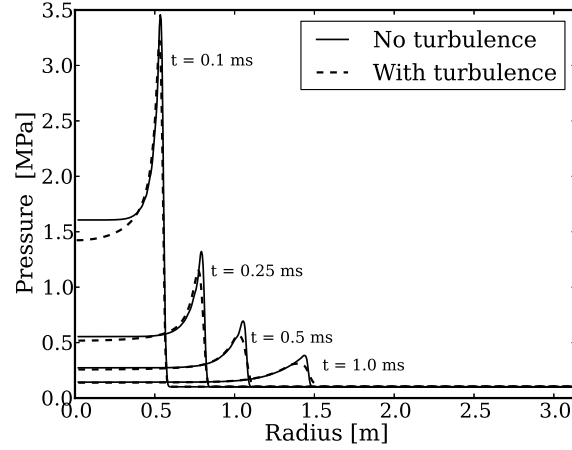
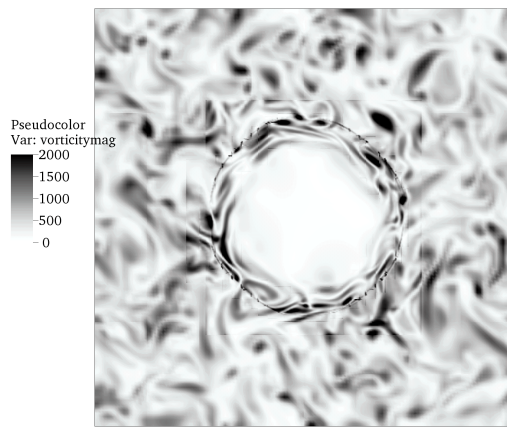


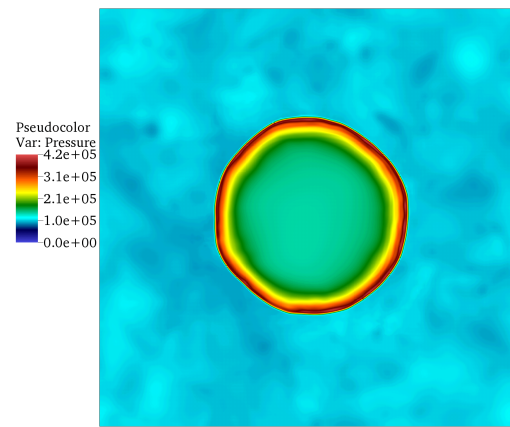
Figure 7.12: Comparison of radially averaged pressure profile at time = 1 ms with and without turbulence.

instantaneous plots of vorticity magnitude, pressure and the subgrid scale kinetic energy at time = 1 ms are shown in Fig. 7.13. Due to the interaction, perturbations from the spherical nature of the blast are seen in the pressure contours. The vorticity magnitude contours indicate that the vortical structures dissipate in the core of the blast. This is due to the high non-physical temperature in the core of the blast as a result of the artificial initialization. It is shown in many previous studies that the Taylor blast solution is valid only at later times of a blast. The early period dynamics can be better captured with a more physical initialization as used in [175]. There is an occurrence of turbulent structures immediately after the blast front, however they dissipate quickly as they moved towards the core of the blast. The sgs kinetic energy also increases sharply at the blast front.

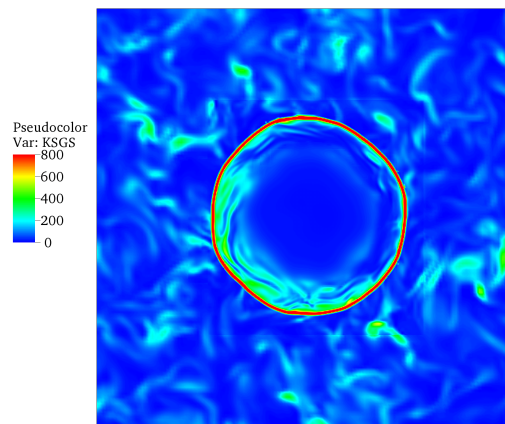
Finally, the role of different sgs terms in the evolution of the subgrid kinetic energy is assessed for this case as was done for the shock-turbulence interaction problem. The radi-



(a) Vorticity



(b) Pressure



(c) Subgrid kinetic energy

Figure 7.13: Plots of various quantities at  $t = 1$  ms for the case of blast interacting with an isotropic turbulence.

ally averaged sgs budget is presented in Fig. 7.14. Across the blast, the sgs production and sgs dissipation both sharply raise. The contribution of the other terms to the sgs kinetic energy evolution is found to be negligible. The dynamics of the sgs production and dissipation completely dominates the other effects such as the diffusion of  $k^{sgs}$  and the pressure dilatation. Overall, the behavior of the closure model across a strong propagating blast appears to be consistent with what is expected. More parametric studies with different blast strengths and turbulence levels can be performed to characterize the behavior of the turbulence, the blast and their interaction. This study only serves to evaluate the multi-level subgrid closure behavior across a propagating strong blasts.

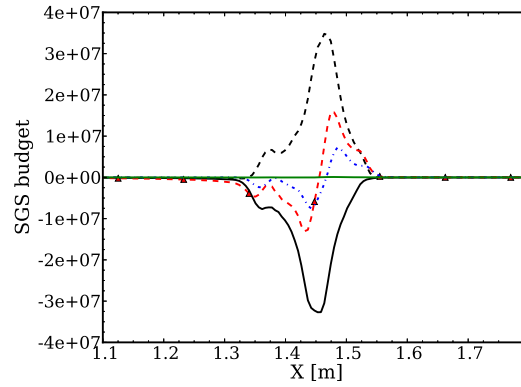


Figure 7.14: Radially averaged sgs budget for the blast-turbulence interaction problem at  $t = 1.0$  ms. —  $\langle D^{sgs} \rangle$ ; ---  $\langle P^{sgs} \rangle$ ; - - -  $\langle \frac{\partial \rho \tilde{u}_i k^{sgs}}{\partial x_i} \rangle$ ; - · -  $\langle T^{sgs} \rangle$ ; —  $\langle pd^{sgs} \rangle$ .

### 7.3 Conclusions

The main highlight of the study is the application of AMR for turbulent flow both in DNS and LES methodologies. The good match between the DNS results with past data and especially smooth transition of resolved turbulence across a grid interface should alleviate any concerns in the employment of AMR for turbulent flows. The multi-level sgs closure (AMRLES) is then applied to study problems involving a planar shock and, a moving shock interacting with turbulence. Although there exist some discrepancies in some of the comparisons with the DNS results, overall, it is found that there is a good agreement between the results predicted

by AMRLES. The sgs budget analysis for LES of shock and blast turbulence indicates the consistent behavior of the multi-level closure model across AMR boundaries. This study has therefore looked into and addressed some of the problems related to applying LES with AMR.

## **CHAPTER 8**

### **APPLICATION 2: LES OF NON-REACTING/REACTING JET IN CROSS FLOW**

In this chapter LES of non-reacting and reacting transverse jet in cross-flow is performed using the cutcell-AMRLES approach. The presence of wide range of scales for flow and flame in JICF configurations is well known. A fixed grid without any local refinement, when used for simulation of JICF, will require high grid resolution making the computations very expensive. AMR can be efficiently employed to resolve some of the fine scale flame and flow structures present in this configuration. Many studies in the past have shown the importance of resolving the jet inflow pipe geometry as it particularly affects the jet penetration into the cross-flow. An embedded boundary representation of the inflow pipe on a Cartesian AMR grid is therefore required to simulate the JICF configuration accurately. Thus, the challenges of doing LES (and subgrid modeling) using a Cutcell-AMRLES strategy is addressed in this chapter.

#### **8.1 Introduction**

A gaseous jet exiting into a cross flow is a configuration that is seen in many reacting/non-reacting flow systems such as in gas turbine combustors for dilution [176] and in turbine blades for film cooling [177], etc. In such systems, the interaction of the transverse jet with the cross flow results in myriad of flow structures such as the jet shear layer vortices, Counter-Rotating Vortex Pairs (CVPs), horse shoe vortices and wake vortices [178]. The presence of these structures significantly increases the mixing between the jet and the cross-flow and thus JICF is a canonical configuration of great interest.

Numerous experimental and numerical studies of the non-reacting JICF have been done in the past and a good understanding of the flow characteristics has been developed [179, 180, 181, 178, 182, 183, 184, 185, 186]. For a reacting JICF, however, the understanding



of the mechanisms involved in flame anchoring, and its stabilization is far from complete and only few studies have been reported on this subject matter. Canonical experimental data for this configuration is also limited and is available for only very specific setups, e.g., sonic jet in supersonic crossflow. Numerically, Grout *et al* [187], [188] performed Direct Numerical Simulations (DNS) of a nitrogen diluted hydrogen transverse square jet in a heated cross-flow. However, performing a DNS for reacting JICF problems is very computationally expensive due to the high spatial resolution required to resolve the turbulent flow structures and the employment of detailed chemistry.

A more practical alternative is to use Large Eddy Simulation (LES) in which the large scale processes are directly simulated and only the smaller subgrid scale processes need to be modeled. This can result in a significant reduction of computational expense without the need to resolve all the flow and time scales as required for a DNS. But there has been no reported study of a LES of reacting subsonic JICF to the best of authors' knowledge. Establishing an affordable strategy to perform LES can help in a long way in understanding the different aspects of the reacting jet in cross-flow problem. There are many challenges for an affordable and an accurate LES of JICF, since there is a wide range of fluid and chemical time scales involved and their resolution is critical in predicting the lifted flame stabilization mechanism.

## 8.2 Problem description

The case configuration is based on the experiments done at DLR [189] and is shown Fig. 8.1. As the jet penetration depth is dependent on the velocity ratio, and is a key factor in understanding the flame anchoring mechanism, three different jets of varying velocity ratio are investigated. Three jets of different velocity ratios numbers are investigated for both the reacting and the non-reacting JICF, and the case conditions of which are summarized in Table 8.1. The velocity ratio for all the cases is given by  $R_m = \sqrt{\frac{\rho_j u_j^2}{\rho_{cf} u_{cf}^2}}$  with  $\rho_j$  and  $u_j$  being the jet fluid density and velocity while  $\rho_{cf}$  and  $u_{cf}$  being the cross-flow density and velocity,

Case	Jet vel(m/sec)	$Re_{jet}$	$r_m$
1	200	6000	2.9
2	150	4500	2.2
3	100	3000	1.4

Table 8.1: Jet conditions different JICF cases

respectively. Note that the velocity ratio is defined as  $r_m = \sqrt{J}$ , where  $J$  is often called the momentum ratio and the jet Reynolds number is defined as  $Re_{jet} = \rho_{jet} u_{jet} d / \mu$ . The configuration considered consists of a turbulent heated cross flow of air at  $T = 750K$  and a jet that exits from a nozzle placed at  $5d$  from the inflow boundary, where  $d$  represents the diameter of the jet. The numerical domain is of size  $20d \times 15d \times 10d$  and is based on past DNS studies [187]. The jet fluid comprises of 70%  $H_2$  and 30%  $N_2$  by volume and enters the domain at  $423K$ . A detailed chemistry mechanism [190] for hydrogen combustion in air with 19-steps and 9-species is employed for the gas phase combustion. This mechanism was widely used in many of the past DNS studies of similar JICF configurations [187, 188].

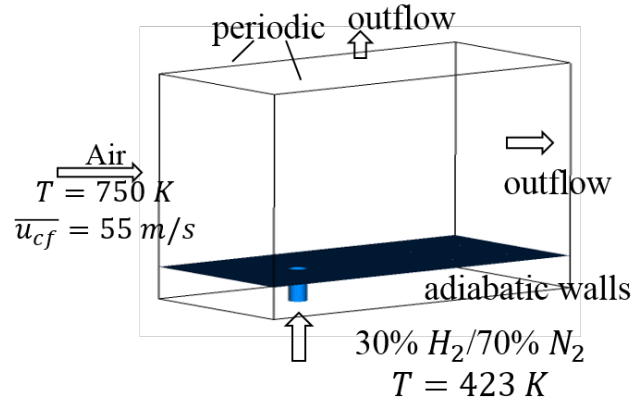


Figure 8.1: Schematic of the JICF configuration.

### 8.3 Results and discussion

The mean profile for the turbulent inflow in all cases are specified based on the data from experiments [189] performed for the same configuration. Synthetic Kraichnan turbulence

[159] is superimposed such that the intensity of the fluctuations matches with the experimental data. The boundary conditions are: partially reflecting inflow at  $x = 0$ , partially reflecting outflow at  $x = L_x, y = L_y$ , adiabatic no slip wall at  $y = 0$  and periodic boundary conditions in the span wise direction ( $z = 0, L_z$ ).

The inlet pipe boundary surface is resolved by using cut-cell and three AMR levels are employed for all the cases with the effective resolution in terms of wall coordinates being  $\Delta x^+ = \Delta y^+ = \Delta z^+ = 2$  ( $=62.5\mu m$ ). Here,  $^+$  indicates the non-dimensionalization by the viscous length scale. The first point of the wall is located at  $y^+ = 1$ . A snapshot of the AMR grid for the JICF configuration is shown in Fig. 8.2. The above resolution for LES is almost three times as coarse as the DNS resolution used by Grout et al [187]. The dynamic refinement is performed based on the criteria of density and temperature ( $\epsilon_T$  and  $\epsilon_\rho$  in Eq. (3.13)) and is turned off once the flow is fully established and steady in case of non-reacting case. Whereas, in case of reacting case, the dynamic refinement is turned off once the flame attained a quasi stationary state. The statistics are collected for all the cases with the frozen static refinement.

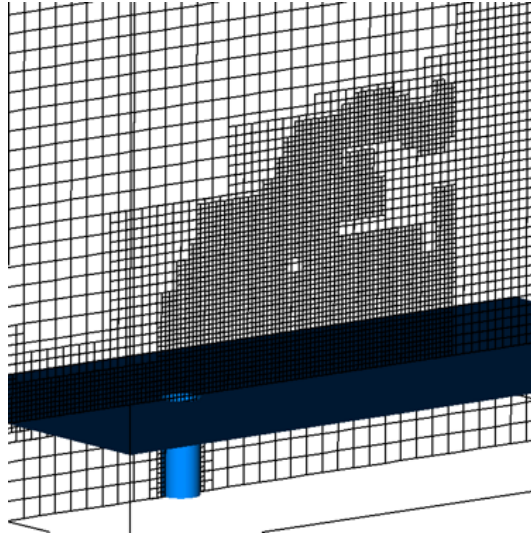


Figure 8.2: Snapshot of the AMR mesh for JICF configuration (only every 4 mesh points shown).

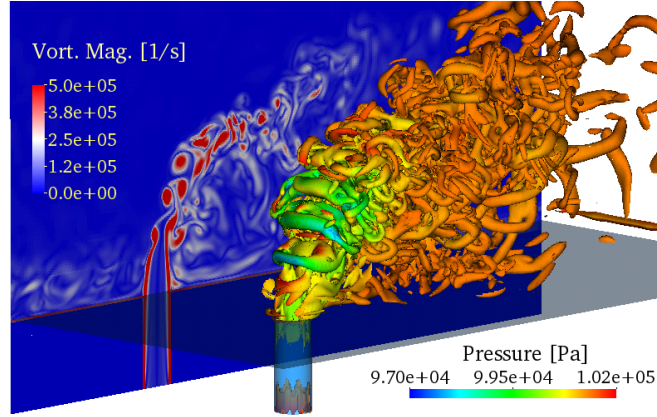
### 8.3.1 Non-reacting JICF

Cutcell-AMRLES results of a non-reacting JICF with a round jet is presented in this section. Conditions for the different non reacting case studies are summarized in Table. 8.1. Simulations are run for approximately seven flow through times while the time averaging of the flow field data are done over last four flow through times. Here, the flow through time is defined as  $t_f = L_x/u_{cf}$ , where  $L_x$  being the domain length in  $x$  direction and  $u_{cf}$  is the cross flow velocity.

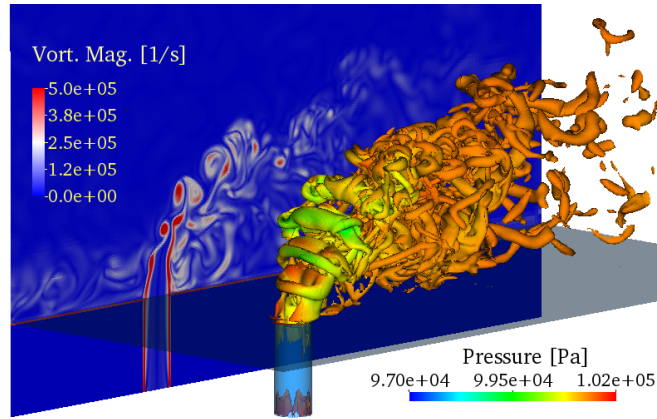
#### *Instantaneous flow field results*

As the flow is highly unsteady and complex in a JICF configuration, instantaneous flow field snapshots can aid in identifying some important flow phenomena. Fig. 8.3 shows the vortical structures visualized based on the  $Q$ -criterion. Also shown is a shadow plot of the vorticity magnitude in the jet center XY plane. Some widely noted flow features stand out in Fig. 8.3. The jet shear layer vortices in the windward side of the jet as well as the wake and upright vortices in the leeward side of the jet can be clearly seen.

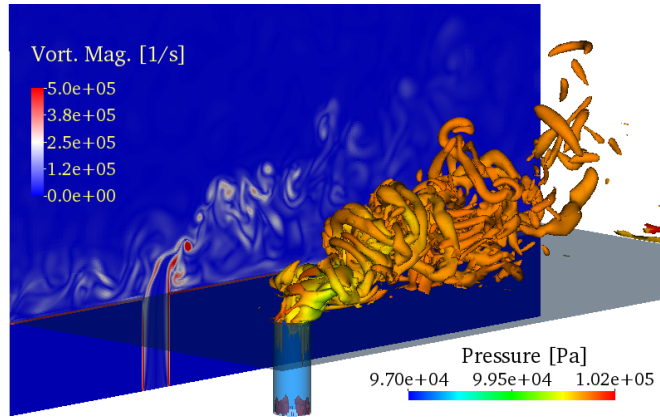
The eddy viscosity ratio is used to estimate the level of unresolved turbulence in a region of flow. High eddy viscosity ratios denote the presence of significant unresolved subgrid turbulence while a low ratio might be indicative of either a laminar flow region or a region where all scales of turbulent motion are completely resolved. For the case of JICF, the wake of the jet is characterized by highly unsteady vortical motions and their subsequent breakdown enables mixing between the injected fluid and the cross-stream. The eddy viscosity ratio shown in Figure 8.4 on jet center  $x - y$  plane and also on  $x - z$  plane at  $y = 6d$  from jet exit suggests that a high viscosity ratio is observed in the jet shear layer regions and the ratio is also significant in the wake of the jet where the large scale coherent structures of the jet breaks up into smaller vortical structures. Value of this ratio as high as 3 is seen in some regions suggesting that these regions are not well resolved in the grid and LES model has to provide the necessary dissipation for the subgrid kinetic energy.



(a)  $r_m = 2.9$



(b)  $r_m = 2.2$



(c)  $r_m = 1.4$

Figure 8.3: Instantaneous snapshot of vortical structures identified by Q-criterion and colored with vorticity magnitude for jet velocities

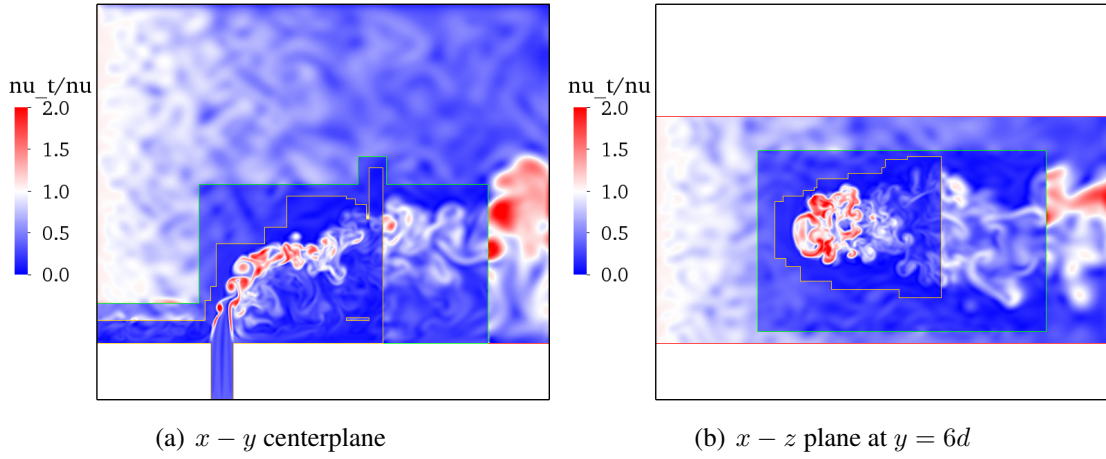


Figure 8.4: Eddy viscosity ratio for the  $Re_j = 6000$  case

Another measure of the quality of a LES is to determine the energy spectrum, which for a well resolved LES should show a  $-5/3$  slope in the inertial range. Velocity data is collected in a region where the jet breaks down and a significant level of turbulence is observed. The typical spectra for the time sampled data is shown in Figure 8.5. Satisfactory match with the  $-5/3$  slope is observed in the inertial range and this shows the resolution to be adequate for a LES with present AMR grid.

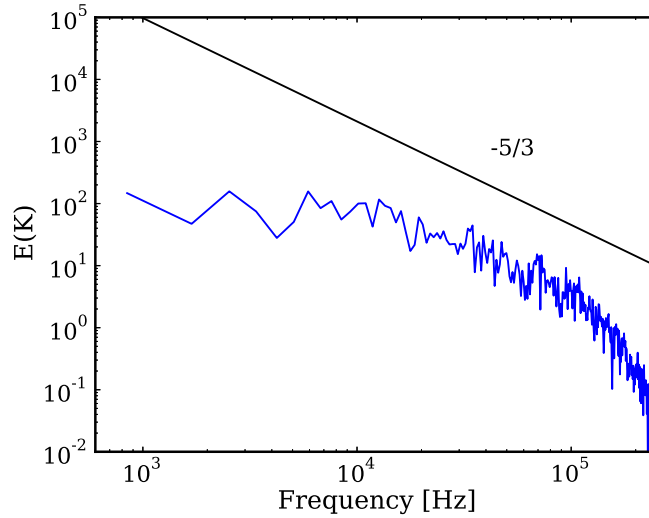


Figure 8.5: Turbulent kinetic energy spectra

### *Time averaged flow field results*

Figure 8.6 shows the averaged velocity magnitude fields in the jet centerplane for the three cases. The streamlines corresponding to the time averaged flow field velocities are also superimposed over the velocity magnitude contours. The jet trajectory, as expected, bends more sharply for the low jet Reynolds number case. All the three cases indicate the presence of nodes in the near field of jet on the leeward side. The presence of a small downward component of velocity can be seen just before the jet for both the cases. This is due to the high pressure region formed ahead of the jet column forcing the cross flow downwards. The above observations are consistent with previous studies and an extensive discussion on this can be found in Mahesh and Muppidi [184].

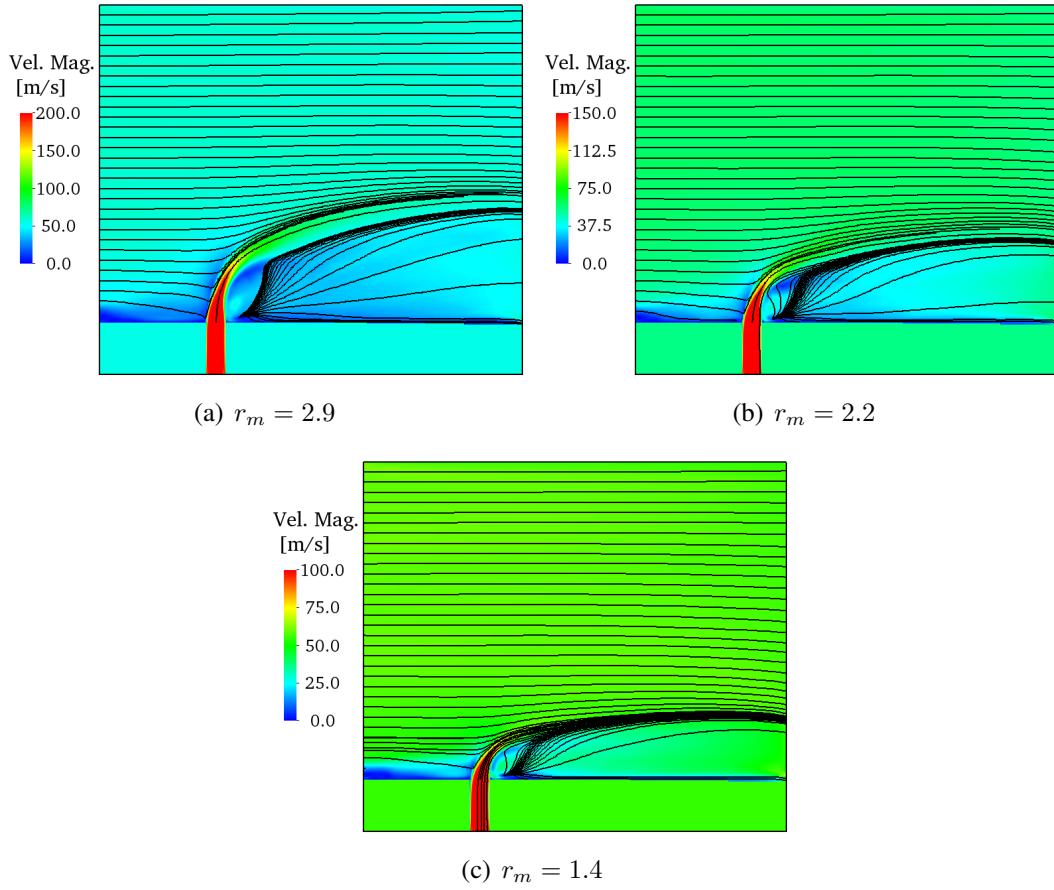


Figure 8.6: Time averaged flow field contours for the Jet center  $x - y$  plane

Mean jet trajectories along the center streamline for the different cases are compared against the experimental observations in Figure 8.7. As seen in the figure, the jet trajectories for the cases collapse when scaled with velocity ratios and diameter. The trajectories predicted by the Cutcell-AMRLES simulations show a reasonable agreement with those predicted by Su and Mungal [182] and New *et al.* [191] .

These results suggest that the current approach appears to capture the nature of JICF in agreement with past observations. Also, it is seen that with the current number of levels of refinement employed, there is still a significant amount of unresolved subgrid turbulence and therefore a subgrid closure is required.

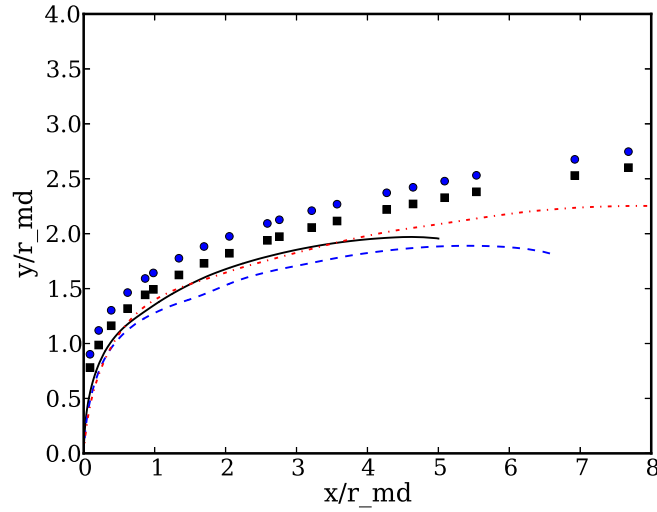


Figure 8.7: Jet centerline trajectory comparisons scaled with only  $r_m d$ . Solid black -  $r_m = 2.9$ , dashed blue -  $r_m = 2.2$ , dash-dot red -  $r_m = 1.4$ , blue dots - Su Mungal [182], black squares - New *et al.* [191].

To understand the significance of resolving the flow inside the pipe geometry, mean velocity magnitude contour plots along with streamlines are studied at the jet inflow x-z plane and also on the x-y central plane. These plots are shown in Fig. 8.8. As noted in the figures, there is a significant downward component very close to the jet inflow. A strong recirculation pattern is also seen immediately in the wake of the jet. Without resolving the jet inflow accurately, these feature may not be captured correctly.



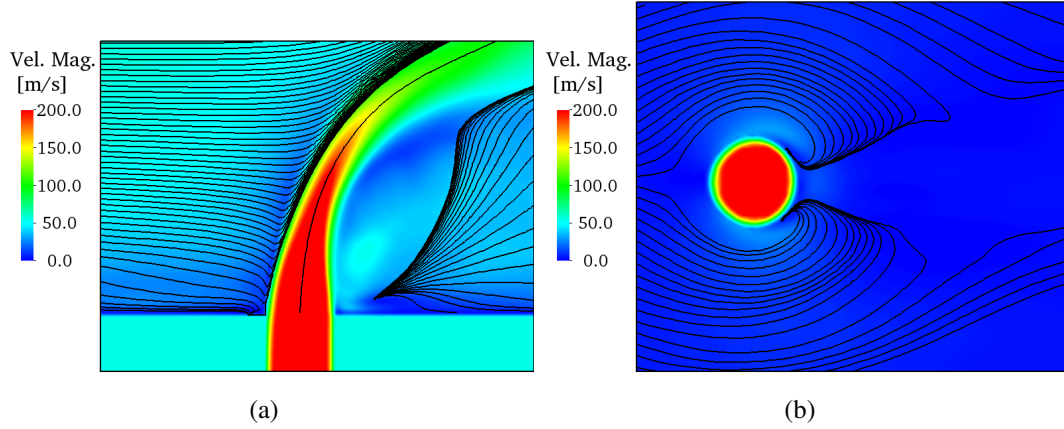


Figure 8.8: Flow pattern in the near field of the jet inflow in the (a) x-y central plane and (b) x-z plane at  $y = 0$ .

### 8.3.2 Reacting JICF

Results for the LES of reacting jet in crossflow are presented here. A similar JICF configuration with lower Reynolds number was investigated previously using DNS with detailed chemistry [187] and on a grid of 1.6 billion points with a minimum resolution of  $10 \mu m$ . The current simulations are of size 20 million with a minimum resolution of  $62.5 \mu m$ . There is a 80 X reduction in the grid size through use of AMR and LES together.

As seen in the non-reacting case studies, the wake of the jet is highly turbulent with unsteady vortical motions with a cascade of length scales. A strong interaction between these flow structures and the flame is expected especially near the flame anchoring point [187, 188]. Additionally, detailed chemical kinetics are found to play a significant role in flame ignition/extinction and stabilization characteristics.

To ignite the mixture, a small cylindrical volume of size 0.2 mm and height 2 mm present in the recirculation zone just behind the jet column is patched with adiabatic flame temperature and burnt products in the non-reacting flow solution. Roughly one flow through time was allowed for the initial transients to exit the domain and flame to get stabilized. The data was time averaged over  $1.2 ms$  corresponding to approximately 1.5 flow through time.

Simulations were run on 1024 processors on a Cray XE6 with AMD Opteron and Inter-

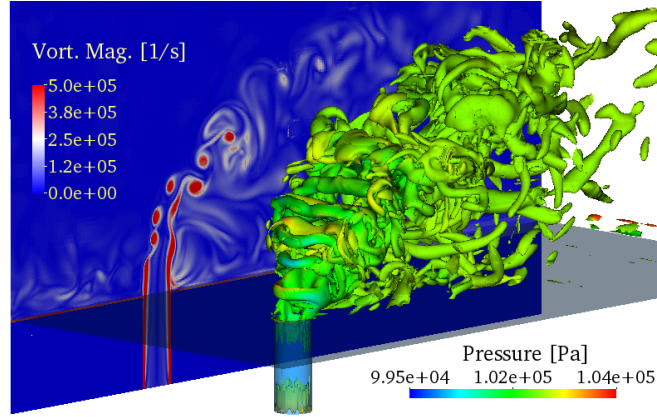
lagos processors for around 100K CPU hours. In comparison, the DNS for the same case was run on 48000 cores of a Cray XT5 and used approximately 4M cpu hours [187]. It is also noted that the refined grid in the AMR third level would correspond to around 115 M cells if the same grid resolution is used in the entire domain. With AMR, the grid size on an average (as the number of grid points change frequently due to dynamic refinement) is around 20 Million. The initial grid in which the flow solution evolved is even coarser with only around 5 Million cells.

### *Instantaneous flow field results*

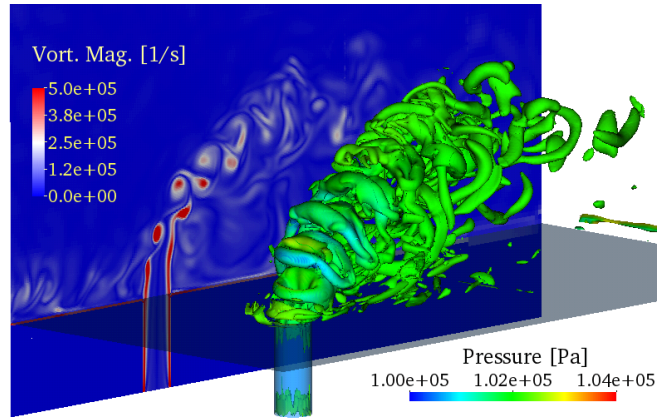
Figure 8.9 shows the instantaneous snapshot of the iso-surface of Q-criterion colored with axial velocity. The shadow plot on the jet center  $x - y$  plane presents the contours of the instantaneous vorticity magnitude. In comparison to the non-reacting cases, there is clearly loss of small scale structures in flow because of heat release effects. The heat release due to combustion increases the temperature of the mixtures and thus its viscosity. Due to the increase in viscosity, the small scale flow structures are dissipated.

The instantaneous structure of the flame for the three jet Reynolds numbers are presented in Fig. 8.10. It does appear that instantaneously the flame is lifted for all the three cases. The flame is anchored in the leeward side of the jet where the velocity magnitude is low. The strong recirculation zone formed in the wake of the jet facilitates mixing of burnt hot products with ignitable mixture, thus sustaining the flame. There appears to be no flame in the windward side of the jet as seen in some reacting jets in cross-flow configurations.

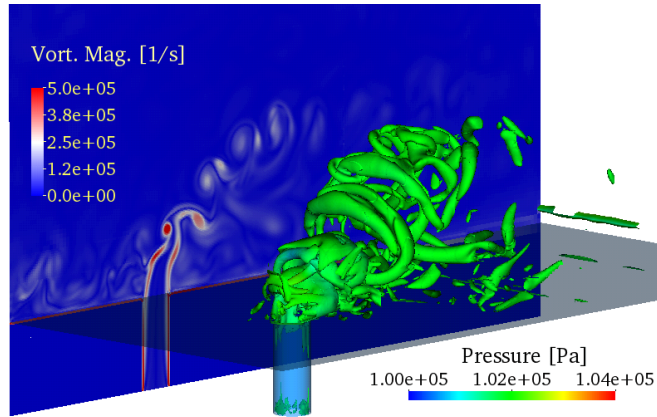
The flame stabilization mechanisms and mixture preparation are investigated for the highest jet Reynolds number/velocity ratio case and the plots of the heat release rate ( $HRR$ ) and flame index ( $FI$ ) are presented in Figures 8.11 (a)-(b). Flame index, defined as  $FI = \frac{\nabla H_2 \cdot \nabla O_2}{|\nabla H_2| |\nabla O_2|} \times \dot{\omega}_{H_2}$ , is shown on the jet centerplane in Figure 8.11. The value of flame index indicates the level of alignment of the gradients between fuel and oxidizer. A high positive indicates complete alignment and is generally observed for premixed flames, whereas



(a)  $r_m=2.9$



(b)  $r_m=2.2$



(c)  $r_m=1.4$

Figure 8.9: Instantaneous snapshot of vortical structures identified by Q-criterion and colored with vorticity magnitude for different jet Reynolds numbers.

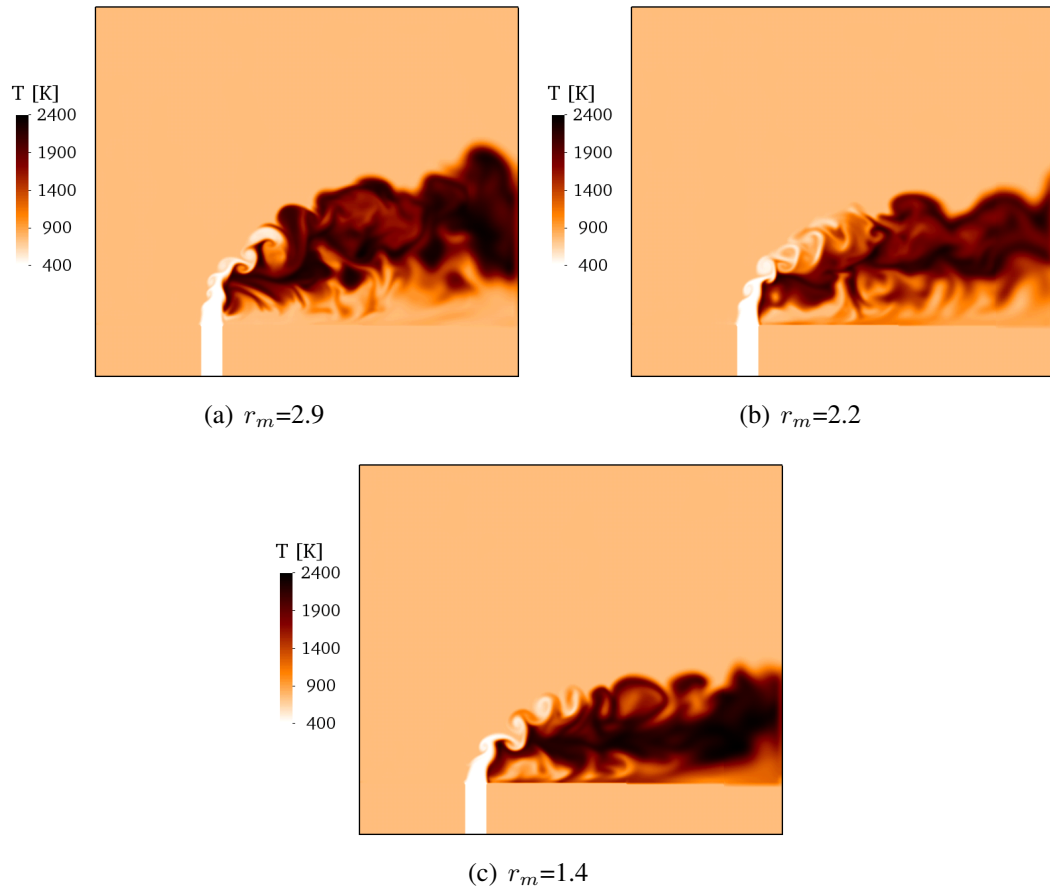


Figure 8.10: Instantaneous temperature contours in the jet central x-y plane.

a negative value indicates a complete misalignment and is generally seen in non premixed flames. A strong correlation can be noted in Figure 8.11 between the regions of high heat release rates and positive flame index suggesting that the flame is partially premixed near the anchoring zone. Also, the flame index is used to as a coloring label in the scatter plot of  $Da$  vs heat release rate shown in Fig. 8.12. A high positive value of flame index can be clearly observed in the regions of low  $Da$  and high heat release. Put together, the above observations of a high flame index, low  $Da$  indicating well mixed condition and high heat release rates strongly suggests that the flame is stabilized via partial premixing. Also from the instantaneous heat release plots, there appears to be two flame anchoring regions, one in the wake of the jet and another which is slightly lifted and further downstream of the jet.

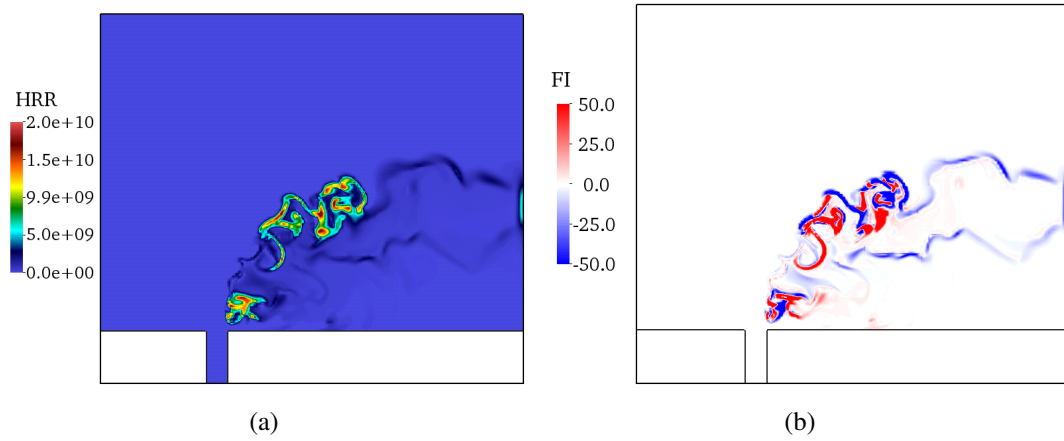


Figure 8.11: Instantaneous snapshot of (a) Heat Release Rate (HRR) and (b) scaled flame index for  $Re_j=6000$ .

In Figure 8.12,  $Da$  is computed as the ratio of flow time  $\tau_{flow}$  based on local mixing time scale and chemical time  $\tau_{chem}$  based on  $H_2O$  reaction rate (Equation 8.1). Lu *et al.* [192] studied a non-premixed flame and used a similar approach for computing  $Da$  based on  $H_2O$ .

$$Da = \frac{\tau_{flow}}{\tau_{chem}}; \text{ where } \tau_{flow} = \frac{\Delta}{u_{\Delta}}; \tau_{chem} = \frac{\rho Y_{H_2O}}{\omega_{H_2O}} \quad (8.1)$$

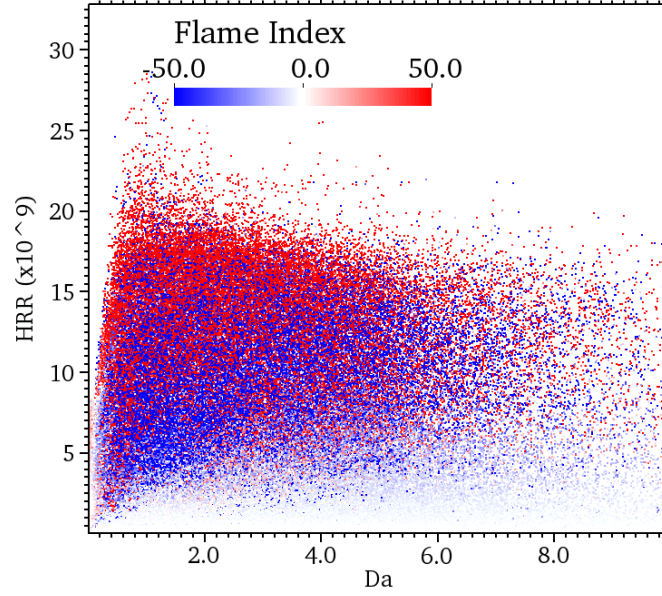


Figure 8.12: Scatter plot of  $Da$  number and HRR colored with flame index.

where,  $\Delta$  refers to filter size,  $u_\Delta = \sqrt{2K_{sgs}}$ ,  $Y_{H_2O}$  and  $\omega_{\dot{H}_2O}$  are the species mass fraction and reaction rate of  $H_2O$ , respectively. A high value of  $Da$  indicates that the flow time scales dominate and the flame is thin, whereas, a low value could indicate that the flame is distributed with chemical time scales dominating for flow time scales. In the limit  $Da \gg 1$ , the turbulence chemistry interaction is intense and ignoring the subgrid species fluctuations in computing the filtered reaction rate  $\overline{\dot{\omega}_k(Y; T)}$  might lead to significant errors. For the limit  $Da < 1$  however the subgrid species fluctuations can be ignored by assuming the state of the fuel and oxidizer to be well mixed locally. As seen in Figure 8.11, regions of high heat release are characterized by  $Da \sim 1$ . Grout *et al* in their DNS, report that the average  $Da < 10$  with  $\tau_{chem}$  based on chemical explosive mode analysis (CEMA), correspond to a distributed reaction in a well-stirred reaction zone which is subjected to intense turbulence. The range of Damkohler numbers seen for a non-premixed jet flame [192] was between  $\sim 1 - 20$  but with a much larger variance ( $0 - 110$ ). Compared to the wide ranges reported for Damkohler numbers, the current extent of  $0 - 2$  is suggestive of a distributed flame regime. It can be clearly seen from the scatter plot in Fig. 8.12 that in the regions of high heat release rates,

$Da \sim 1$ .

Finally, one of the interesting research questions is the effect of heat release on vorticity dynamics of the flow. The study of vorticity dynamics for a reacting JICF is particularly important due to the role of the vortex structures in anchoring the flame. From many previous studies, the mixing of hot products and fresh reactants by the vortex structures in the leeward side of the jet are understood to be the primary mechanism by which flame is stabilized. One of the main contributors of vorticity generation for reacting flows is the baroclinic torque  $\mathbf{BT} = \frac{|\nabla p \nabla \rho|}{\rho^2}$ , which is resulted when the pressure and density gradients are not aligned. Due to heat release in reacting flow, the density gradients are enhanced which can lead to increase in the magnitude of the baroclinic torque. A comparison plot of the magnitude of baroclinic torque for a reacting and a non-reacting case for the highest jet Reynolds number case is presented in Fig. 8.13. In both, the case, the magnitude of the baroclinic torque is high near the jet shear layers. For the reacting case, there is a noticeable increase in  $|BT|$  downstream of the jet. The dilatation,  $\nabla u$  acts as a sink of the vorticity and is also compared. The heat release causes expansion which results in increase dilatation killing vorticity. In the region where the dilatation effects are strong, the vorticity magnitude is damped with loss small-scale flow structures.

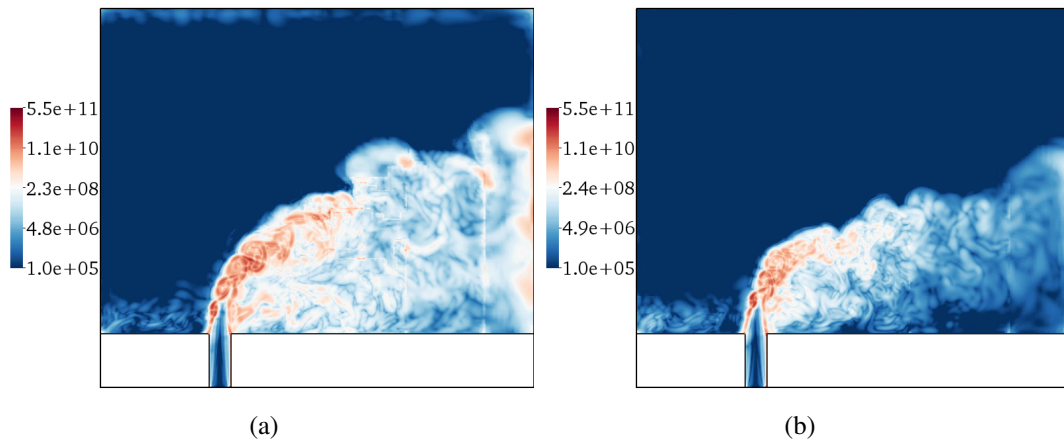


Figure 8.13: Comparison of the magnitude of the baroclinic torque between reacting and non-reacting cases for  $Re_j = 200$ .

### *Time averaged flow field results*

In Fig. 8.14, the mean temperature contours for the three different jet Reynolds numbers are shown. As noted from the instantaneous results, the flame is lifted for all the three cases anchoring in the leeward side of the jet. As noted in experiments [189], there are two flame branches: a 'lee' stabilized flame branch and a lifted flame branch. These two branches seem to be merged for the low jet velocity case and appears more distinct as the jet velocity increases.

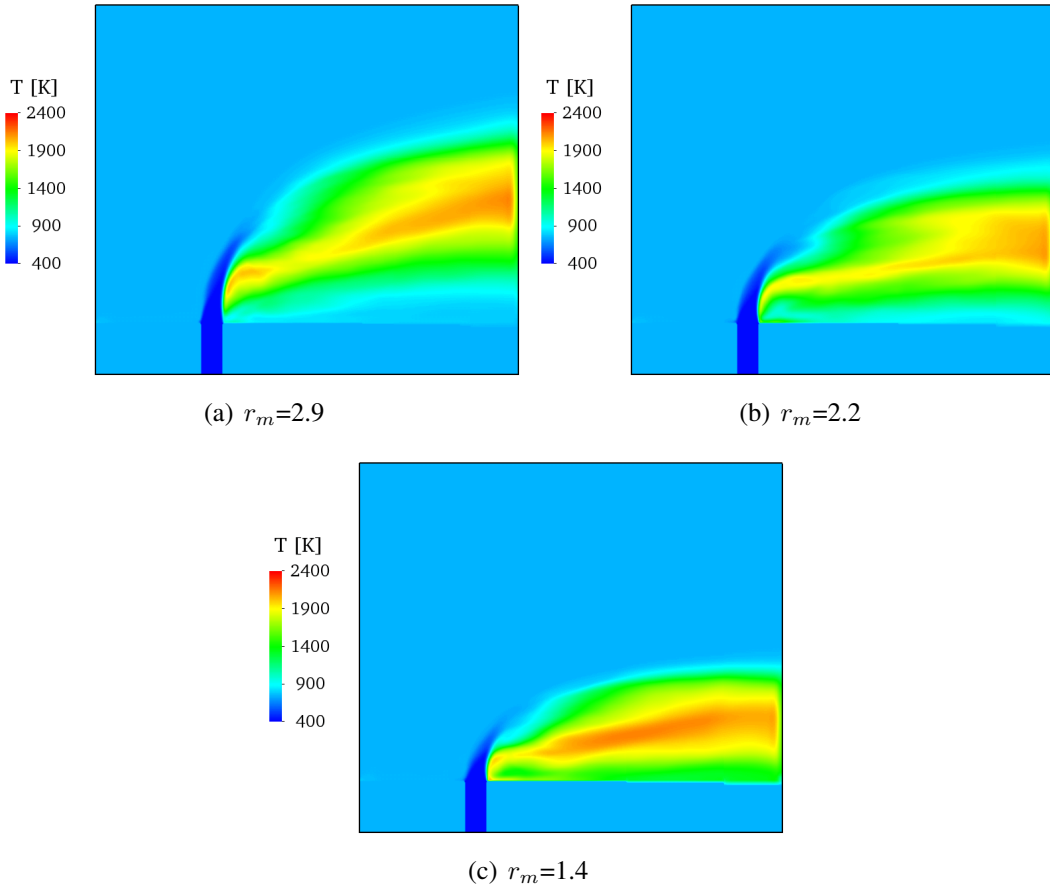


Figure 8.14: Mean temperature contours at jet center x-y plane for different cases.

A comparison of the time averaged streamwise velocity for  $r_m = 2.9$  case with experimental data is presented in Fig. 8.15. The jet trajectory tracked through the center streamline is also plotted for both the simulation and the experiment. As seen, the results from cur-



rent simulation is in reasonable agreement with the experimental data. There is a very good agreement in the jet centerline trajectory between the simulation and the experiments. The recirculation region is stronger and bigger in the simulations compared to its size from the experimental plot. This can be seen as a direct effect of the jet bending later in the simulations in comparison to the experiments. As the jet column height is higher in the simulations, the wake behind the jet in the leeward side is bigger and stronger.

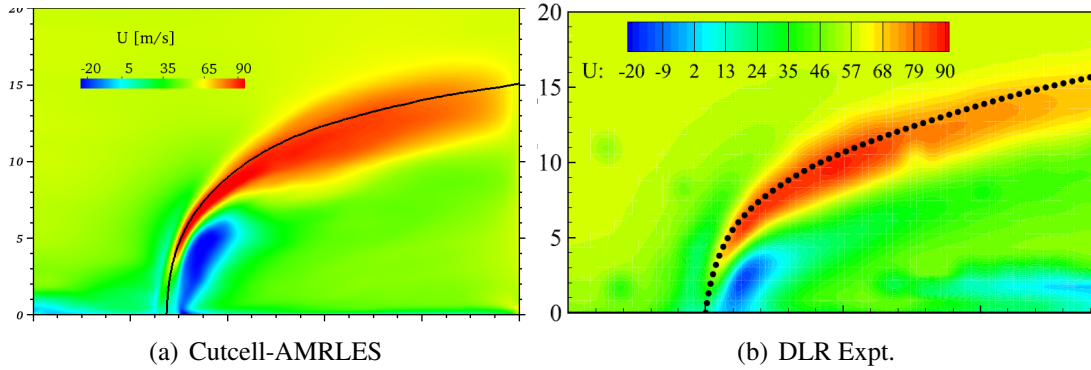


Figure 8.15: Comparison of the mean jet behavior between the current simulations and DLR experimental data [189]. Experimental image taken from [193].

Line plot comparisons of mean streamwise velocity, rms of streamwise velocity and average temperature along various axial locations at central jet plane are shown in Fig. 8.16. For the streamwise velocity plots, there is a noticeable difference in the simulation results and experiments closer to jet, but the agreement improves significantly further downstream. The RMS values of the streamwise fluctuation  $u_{rms}$  are in much better agreement except for close to jet inflow. Note that in the current simulations, the jet inflow had no turbulence. Whereas, the experiments show significant levels of RMS of the streamwise velocity at the jet inflow. Adding inflow turbulence to the current cases can improve the predictions for  $u_{rms}$ . The time averaged temperature profile comparisons reveal that overall the flame location is captured reasonably well. Near the jet inflow region, the simulation over predicts the temperature values as compared to experiments. A possible cause for this might be because of the presence of a stronger recirculation zone due to which the flame anchoring location is shifted

downwards. This might be resulting in higher near wall temperatures causing differences with experimental data.

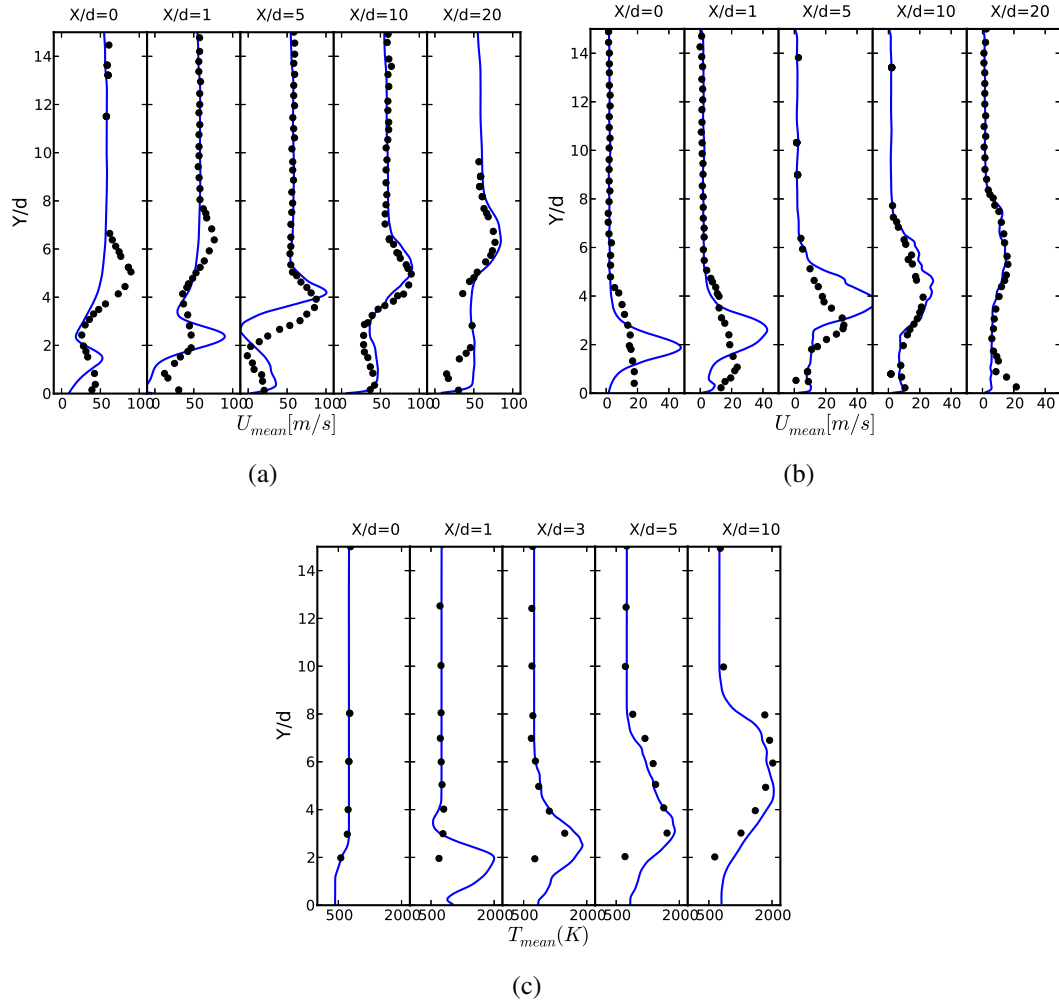


Figure 8.16: Line plots of (a) mean streamwise velocity (b) rms of streamwise velocity and (c) mean temperature at various axial locations on x-y jet centerplane. Solid blue line - Cutcell-AMRLES, black dots - DLR experiments [189].

To further understand the flame anchoring zone, the iso-volume of time-averaged heat release rate clipped between 10- 90 % of the total heat release is shown in Fig. 8.17 for the three velocity ratios. An interesting observation is that the heat release zone appears to be continuous with a ring-like structure. This is in contrast to the observations made with only the 2D slices which indicated the anchoring zones to be disconnected and separate.

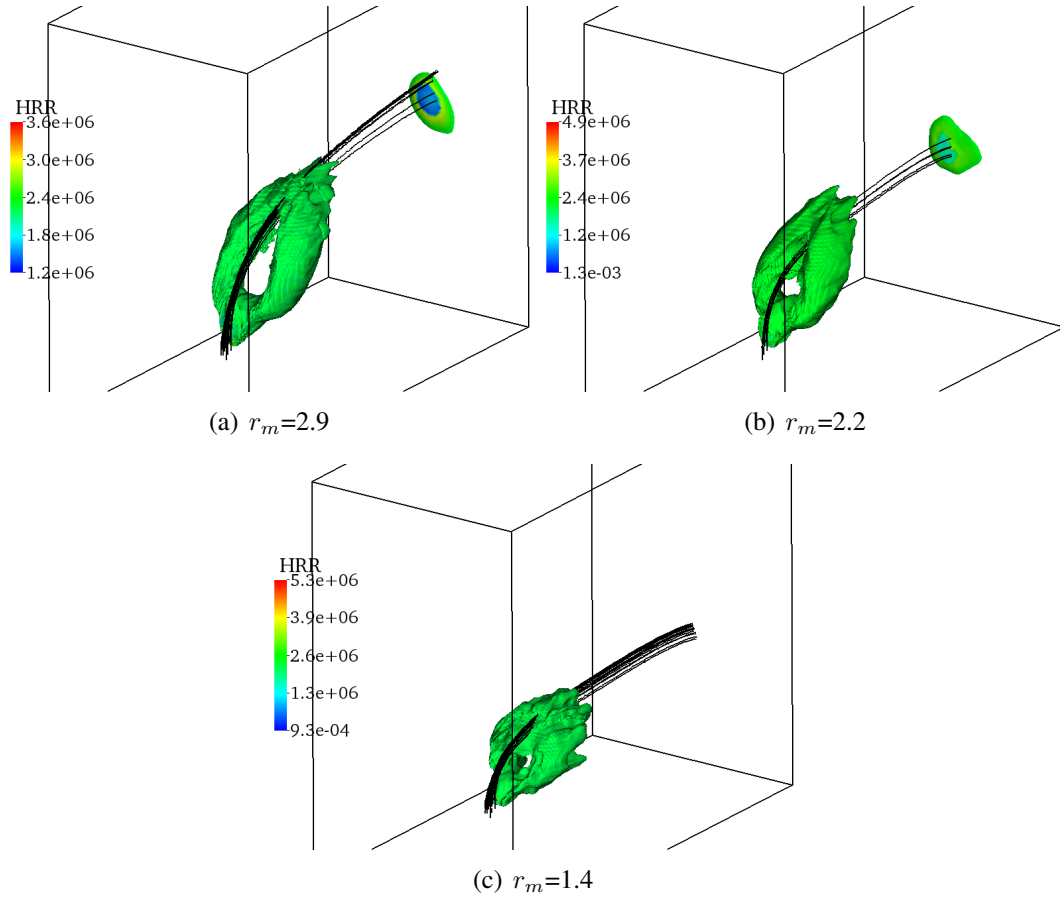


Figure 8.17: Iso-volume of heat release rate clipped between 10 and 90 percent of the total heat release for the three cases.

## 8.4 Conclusions

The Cutcell-AMRLES along with multi-level RRLES closure is employed to investigate the flame anchoring mechanism and vorticity dynamics of a transverse reacting jet in cross flow configuration at different jet Reynolds numbers. For all the three Reynolds numbers, a lifted flame is observed as in experiments of the same JICF configuration. This investigative study attempted to first understand the behavior of a non-reacting jet in cross flow and also study the behavior of the subgrid closure model for this complex flow system. The dynamics of the subgrid kinetic energy and eddy viscosity ratio are consistent with model behavior expected for a multi-level AMR mesh. Mean jet trajectories for different jet Reynolds number compare well with that predicted by an empirical scaling law. Further analysis of the reacting JICF suggests that the flame is anchored in a low-velocity region on the leeward side of the jet and the flame stabilization is achieved through partial premixing for all the three jet Reynolds numbers. The quality of the current predictions for the high Reynolds number case is assessed by comparing with the experimental data and it is concluded that the Cutcell-AMRLES approach captures all the trends seen in experiments with sufficient accuracy. The results look promising regarding the ability to predict the flow and flame characteristics and can be potentially used to perform design studies and better understand the reacting JICF configurations.

## **CHAPTER 9**

### **APPLICATION 3: DETONATION INITIATION AND STABILIZATION BY MOVING PROJECTILES IN A REACTIVE MIXTURE**

In this chapter, the cut-cell method for moving boundaries is used to investigate detonation initiation and stabilization by high speed projectiles moving in a reactive mixture. Both prescribed projectile motion with constant velocity and coupled motion due to hydrodynamics forces acting on the projectile surface are investigated. The results of the simulation are compared with past experimental data or analytical solution if available.

#### **9.1 Introduction**

High speed projectile behavior in detonable gases have significant implications on the initiation of combustion processes in ram accelerators and other hypersonic propulsion systems. Such systems based on detonation have gained an increasing interest in the past few years, owing to their higher efficiency resulting from fast heat release and thereby generated high peak pressures[1]. Understanding the processes that govern the detonation initiation by hypervelocity projectiles is thus critical to explore possible applications of propulsion systems such as Oblique Wave Engines (ODWs) and Pulse Detonation Engines (PDEs). To that end, the moving cut-cell method along with the developed AMR framework are used to solve some application problems, representative of the actual engineering systems of interest. The problems that are chosen are systems where detonation is initiated by i) a hypersonic moving piston, ii) a hypersonic cylinder, and iii) a hypersonic sphere. The results from each of the different studies are described in the following sections.

## 9.2 Results and discussion

All the simulations, unless mentioned, use a time step based on a CFL number of 0.5. For the one dimensional piston and the three dimensional spherical projectile reactive studies, a 27 steps detailed hydrogen oxygen mechanism used in the Shock Detonation Toolbox (SDT) library developed at Caltech [194] is employed. A quadratic reconstruction  $k = 2$  is employed for all the cases. This provides a third order accuracy in the computation of inviscid fluxes and second order accuracy for viscous fluxes evaluation in regions of smooth solution. The hybrid cut-cell scheme using the high-order CENO reconstruction in smooth regions of flow and a second order limited MUSCL reconstruction in regions of flow discontinuities is used for the all the simulations.

### 9.2.1 Piston initiated detonation.

The ignition of a detonation wave by a piston moving at a constant velocity or equivalently by the reflection of a shock from the end wall of a shock tube is studied here. The first scenario is a moving boundary problem, which when cast in the reference frame of the moving piston, becomes a fixed boundary problem as described as an equivalent scenario. Both the fixed boundary and its equivalent moving boundary case are considered to study the ignition problem and demonstrate the applicability of the current moving boundary cut-cell method for reacting flows. This problem has been extensively studied analytically [195], numerically [196, 197] as well as experimentally [198]. In the first case, a piston moving with a velocity of 800 m/s in a tube filled with a hydrogen-oxygen-argon mixture with a molar ratio of 2:1:7 is considered. The piston velocity is chosen so as to produce a shock of just enough strength to raise the temperature of the mixture above its auto-ignition temperature. A domain of length  $3.0 \times 0.1$  m is used with a piston initially located at  $x = 0$ . Supersonic outflow conditions are prescribed at the right most boundary and symmetry condition is imposed on the top and the bottom boundaries. Two effective grid resolutions of  $40\mu m$  and  $80\mu m$  are

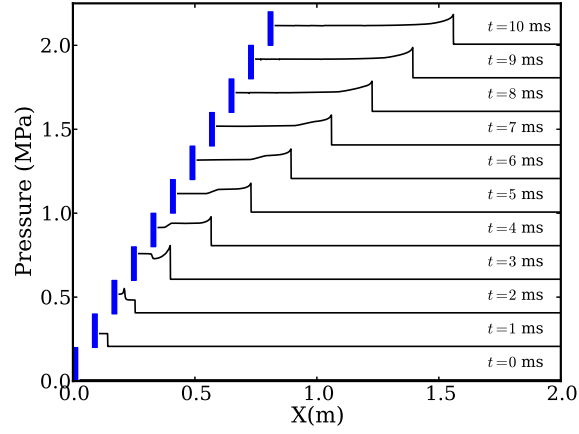
Table 9.1: Flow conditions of the mixture.

	moving	static
$\rho$ ( $kg/m^3$ )	0.08497	0.08497
$p$ (kPa)	6.67	6.67
$u$ ( $m/s$ )	0.0	-800.0
$T$ (K)	298	298

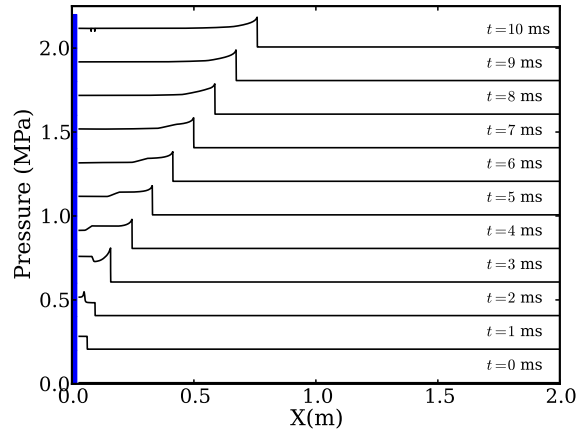
employed using 5 and 4 levels of refinement respectively. The flow conditions of the mixture that are used, are reported in Table 9.1.

At  $t=0$ , the piston is suddenly accelerated to  $v_p = 800$  m/s. The same problem is also considered in the reference frame of the piston, wherein the piston at the left end is kept stationary and the flow is initiated with a velocity  $u = -800$  m/s. As both the scenarios are equivalent with just a change of reference frame, they must result in the same solution. The time history of the pressure profile for the static and the moving cases are shown in Figs. 9.1(a) and 9.1(b). The pressure value at various times shown are shifted by 200 Kpa for clarity.

As seen from Fig.9.1(a), the motion of the piston creates a shock ahead of the piston which raises the temperature of the mixture above its auto-ignition limit. After an induction time  $t_{ind}$ , reactions occur in the region adjacent to the piston faces and raises the pressure locally. The high-pressure reaction zone moves rightwards towards the propagating shock wave. And when the reaction zone couples with the leading shock wave, it leads to detonation reaction. Similarly, in the case of static piston case (in Fig.9.1(b)), a reflected shock forms at the closed left end, which propagates towards the right. As observed in the case of the moving piston, a high pressure reaction zone forms nearer to the closed end, the subsequent movement of which coupled with the leading shock can be seen in Fig. 9.1(b). To verify if the obtained solutions are the same between the two equivalent cases, the pressure profiles are overlaid from the two cases and compared in Fig. 9.2. As the frame of reference is different in the two cases, the static wall cases are shifted in x-axis such that the closed end now corresponds to the location of the piston at a particular time instant and are overlaid



(a) Moving piston



(b) Static wall

Figure 9.1: 1D profiles at various time instants (0 - 1.0 ms) for (a) the moving piston and (b) the static wall problem. Pressure values are shifted by 200 kPa every for each time instant for clarity.



on one another. As observed, there is nearly an exact match in the pressure profiles between the static and the moving piston cases, which verifies the validity of the moving cut-cell scheme along with the reaction closure.

In addition, this case also serves as a stringent test for the conservative property of the scheme in case of reacting flow problems with moving boundaries. With the reaction occurring instantaneously with the piston movement, resulting in a huge mass and energy content, any loss of conservation in mass, energy or momentum will result in a delay in the shock wave propagation and further in its coupling with the reaction zone. The near precise match of the profiles of pressure, density and temperature for the moving and the static cases validates the current cut-cell scheme for reacting problems with moving boundaries, more particularly its conservative nature in these cases.

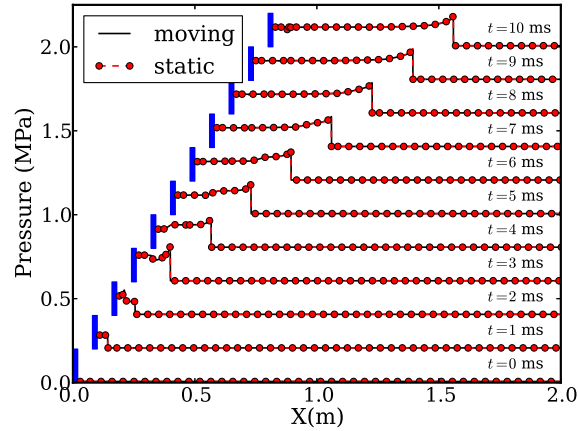


Figure 9.2: Comparison of the pressure profile history between the moving and stationary reacting piston problem.

The grid resolution studies are performed for the moving boundary problem using resolutions of  $40 \mu m$  and  $80 \mu m$  and the pressure profiles obtained from both the cases are compared in Fig. 9.3(a) with a zoomed in view of which at  $t = 1$  ms is shown in Fig. 9.3(b). The detonation characteristics obtained for both the resolutions are compared along with previous studies in Table 9.2 and are found to be in good agreement.

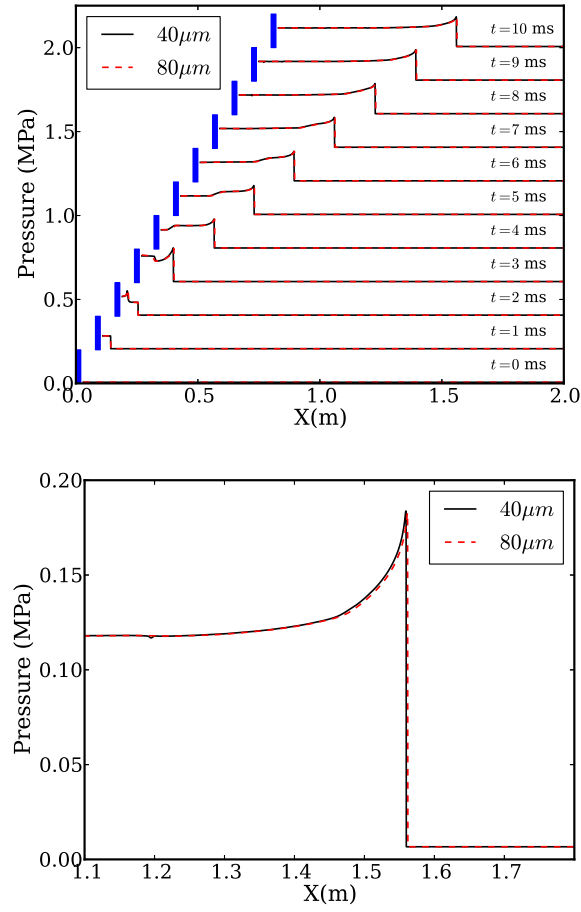


Figure 9.3: Comparison 1D profiles at (a) various time instants (0 - 1.0 ms) (b) zoomed in view at  $t = 1.0$  ms for the two grid resolutions  $\Delta x = 40 \mu m$  and  $80 \mu m$

Table 9.2: C-J characteristics of the mixture for various grid resolution for the moving piston problem.

	Deiterding [199]	$40 \mu m$	$80 \mu m$
$P_{vn}$ (kPa)	177.3	180.0	176.4
$T_{vn}$ (K)	1921.7	1980.0	1972.0
$U_{vn}$ (m/s)	1231.4	1258.0	1250.0
$D_{CJ}$ (m/s)	1629.9	1651.0	1650.3

### 9.2.2 Detonation initiation due to an impulsive cylinder motion

As the former case of detonation initiation by a hypersonic piston is a more simplified case, a better representation of the more generic class of problems involving detonation initiation due to accelerating/decelerating hypersonic projectile can be obtained by using a hypersonic rigid cylinder as the projectile. This problem was previously investigated by using an overlapping grid methodology by Henshaw *et al.*[43]. Similar case conditions as those used by Henshaw *et al.*[43] are adopted for the current study, wherein the reactive flow is modeled by a single step chemistry with Arrhenius kinetics and the linear depletion rate,  $\dot{\omega}$  as:

$$\dot{\omega} = \sigma(1 - Y) \exp \frac{1}{\epsilon} \left( 1 - \frac{1}{T} \right). \quad (9.1)$$

Here  $\sigma$  is the pre-exponential scale factor,  $\epsilon$  is the dimensionless reciprocal of activation energy and  $T = p/\rho$  is temperature of the mixture such that gas constant is unity. For small values of  $\epsilon$ , the reaction rate is very highly sensitive to temperature variations. And, when the values of  $T$  is very small ( $T < 1$ ), the reaction rate is also exponentially small, however increases rapidly as  $T$  approaches 1. In this problem, the values of  $T$  are chosen to be sufficiently closer to 1.0 and therefore any abrupt motion in the system can create a compression wave that can heat up the mixture and initiate the chemical reaction, which can later turn into a detonation.

The initial state of the flow is set as  $\rho_0 = 1$ ,  $u = v = 0$ ,  $T_0 = 0.93$ . The computations are performed on a two-dimensional channel with domain boundaries  $-0.5 < x < 1.5$  and  $|y| < 0.75$  using an effective resolution of  $\Delta x = 3.125 \times 10^{-4}$  via 4 levels of adaptive mesh refinement. The cylinder is initially centered at  $x = y = 0$  with a radius 0.15 and mass of 1.0. At  $t = 0$ , the cylinder is given an impulse corresponding to  $u = 1$  and its subsequent motion is then tracked using Eq. (4.34) and Eq. (4.35). The heat release from the reaction is assumed to be  $Q = -4$  and the reaction rate is determined based on assuming  $\epsilon = 0.06$  and  $\sigma = \epsilon/(\gamma - 1)|Q|$  from Eq.9.1. The values of the kinetic parameters are based on an earlier

study [200], in which mechanisms for detonation formation due to temperature gradient was investigated.

Shown in Fig. 9.4 are snapshots of the Schlieren image of density contours in the detonation front at various stages of the detonation formation, which clearly indicates the formation of cellular structures at front. A more clearer representation of the cellular structures can be seen from the numerical soot foil image shown in Fig. 9.5(a), which is generated by record-

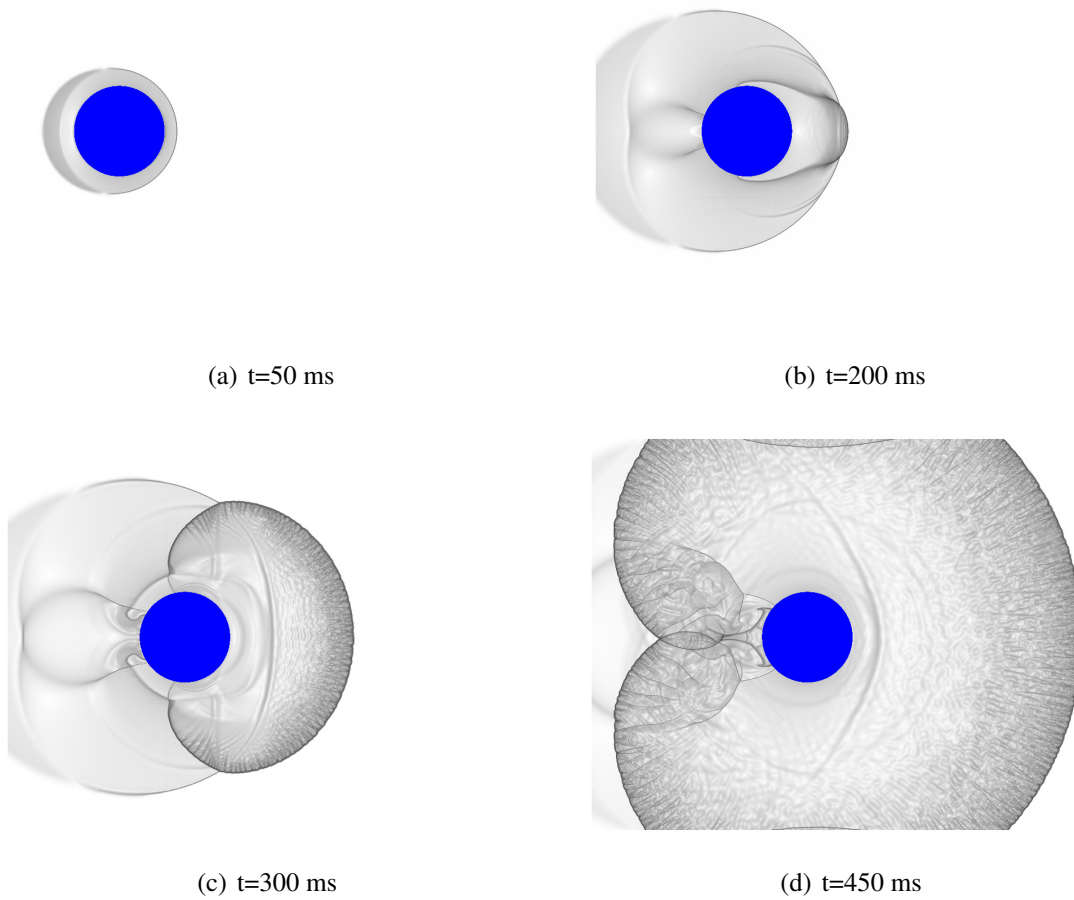


Figure 9.4: Time series of Schlieren image of the detonation front for the case of impulsive cylinder motion in a reacting mixture.

ing the movement of triple points over time. The spiral cellular structures observed in the numerical solution was also noted earlier in the experiments of similar system (Fig. 9.5(b)).

The figure in Fig. 9.5(b) is an open-shuttle photograph of a cylindrically diverging detonation. As seen from the two soot foil images, the adaptive cut-cell solution is clearly able to predict the qualitative behavior of the front very well. Further analysis on the detonation front propagation can be performed by determining terms such as average detonation velocity,  $D_{CJ}$ , the theoretical value of which can be computed as follows [200]:

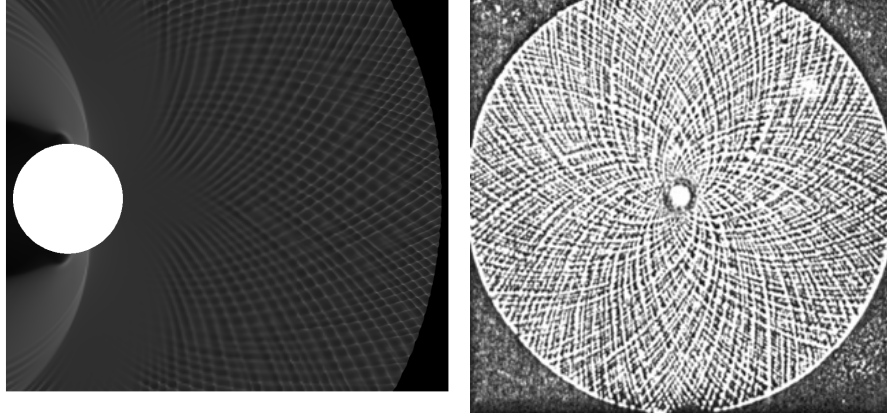


Figure 9.5: Visualization of cellular structures Left: Numerical soot foil from AMR simulations. Right: Open-shuttle photograph of a diverging cylindrical detonation[201]

$$\left(\frac{D_{CJ}}{a_0}\right)^2 = v + \sqrt{v^2 - 1}; v = 1 + (\gamma^2 - 1) \frac{-Q}{a_0^2}, \quad (9.2)$$

where  $a_0 = \sqrt{\gamma p_0 / \rho_0}$  is the mixture speed of sound. The instantaneous velocity of the front from the numerical simulation is determined based on the rate of change of the peak pressure and is presented in Fig. 9.6. As observed in the figure, though the front propagation velocity varies between 0.6 to 1.25 of the C-J value, the average velocity is very close to the C-J value  $D_{CJ} = 3.18$  for this mixture computed from Eq.(9.2).

### 9.2.3 Detonation initiation and stabilization over spherical projectiles

In this final case study, a more challenging problem of initiation and stabilization of an Oblique Detonation Wave (ODW) over spherical projectiles shot into a hydrogen-oxygen-argon mixture with a molar ratio of 2:1:3 at super detonative velocities is investigated. The

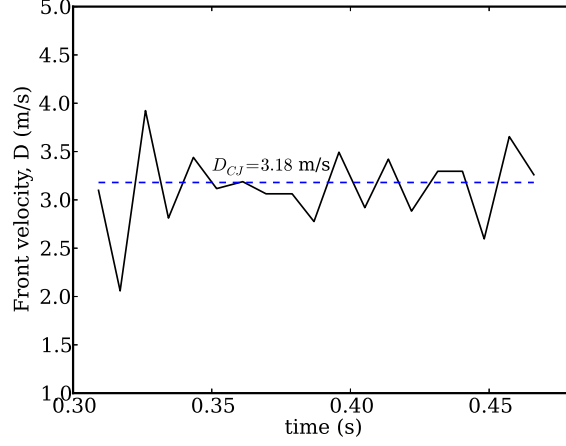


Figure 9.6: Time history of the velocity of propagation of the diverging detonation front.

case configuration is based on a recent experimental study by Maeda *et al.* [202], in which the effect of filling pressure and projectile size on the detonation stabilization was investigated for acetylene and hydrogen-oxygen-argon mixture. The case conditions are summarized in Table 9.3 and are chosen to cover the different combustion regimes that were observed in experiments. It is to be noted that the conditions are clustered around the critical limit for pressure ( $p_{crit}$ ), which is required for a stabilized ODW.

For computational cost considerations, only a quadrant of the sphere is considered by imposing symmetry conditions in Y and Z directions. A domain size of  $80D \times 5D \times 5D$  is used with the sphere initially located at  $(1.5D, 0, 0)$ , where  $D$  is the diameter of the sphere. The assumptions around choosing a quadrant sphere and the domain size can be justified considering that the wake behind the sphere is not expected to exhibit any large scale coherent structures for supersonic flows. Therefore, all the key characteristics of the flow relevant for the detonation stabilization mechanism such as the bow shock ahead of the projectile, oblique shock that stabilizes near the wake and the flow separation points can be captured accurately even with the symmetry assumption. Four levels of AMR are employed resulting in an effective mesh resolution of the  $80\mu m$ . The induction length for the mixture under the given conditions is around  $l_{ig} \approx 300\mu m$ , which is sufficiently resolved by the grid.

Table 9.3: Case conditions for the detonation initiation study by supersonic spherical projectiles.

Mixture composition	$2H_2 + O_2 + 3Ar$
Projectile diameter (mm)	3.18
$u_{projectile}$ (m/s)	2170.0
Filling pressure, $p$ (kPa)	90, 95, 96, 97.5, 100
Temperature, $T$ (K)	298

Also, based on the one dimensional reacting piston studies (Fig.9.3), a resolution of  $80\mu m$  was found sufficient to predict correct detonation characteristics of the mixture. It must be noted that the near wall resolution for this case is not sufficient to capture the boundary layer effects accurately. However, since the objective of the study is to investigate the detonation stabilization mechanism, which is affected only by the bow shock ahead of the projectile, the current results are deemed to be sufficiently accurate. Besides, the principal objective of this case is to demonstrate a practical and challenging application of the moving cut-cell method for reacting flows. A snapshot of the AMR mesh for this problem is shown in Fig. 9.7.

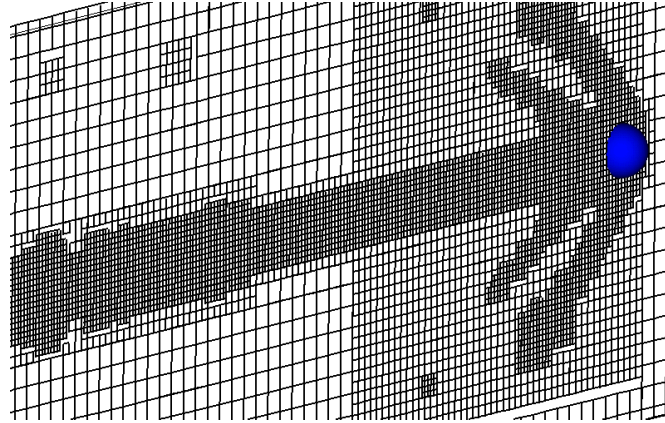


Figure 9.7: Snapshot of the AMR mesh for the problem detonation initiation by a hypersonic projectile (only every four grid points shown).

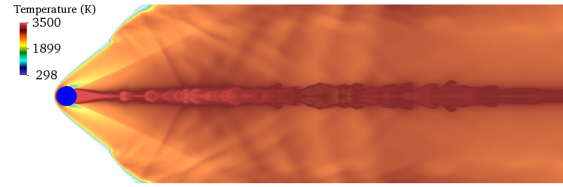
Some interesting observations can be made on the coupling of the reaction and the leading shock from the contour plots in Fig. 9.8. The decoupling of the reaction zone and the leading shock is clearly visible for the pressure conditions corresponding to  $p = 90$  kPa and  $p = 95$  kPa. It is clear that for  $p = 95$  kPa, the initial detonation which resulted from coupling

of the combustion zone with the leading the shock front is getting attenuated. At  $p = 96$  kPa, a highly unsteady leading shock front is observed. Local explosions are visible downstream of the projectile, which appear to stabilize the ODW. A series continued explosions are in fact observed for this pressure condition during the projectile's flight. Similar observations were made in experiments [202] and it was postulated that these local explosions then facilitate the formation of an steady ODW. At pressures above the critical pressure, for example at  $p = 97.5$  kPa, the coupling between the reaction zone and the shock wave is fairly immediate resulting in an ODW. Figure 9.9 summarizes the different combustion regimes observed across the various filling pressures. It can be seen from the plots that the critical pressure that is required for stabilization of the ODW for the given projectile velocity is around  $p_{crit} \approx 100 \text{ kPa}$ . The C-J velocities required for computing the non-dimensional projectile velocity ( $V_p/D_{CJ}$ ) for various filling pressure are computed using Shock Detonation Tool box (SDT) developed at EDL, Caltech [194].

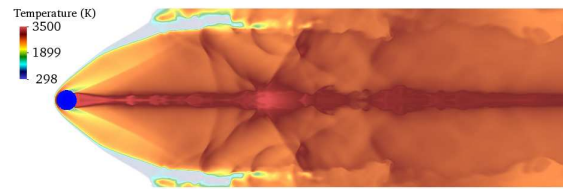
Figure 9.9 summarizes the different combustion regimes observed across various filling pressures. The different stages of the combustion regimes observed in the current study were also noted in experiments and the Schlieren snapshots of the different regimes from the experiments are shown in Fig. 9.10. As discussed in the previous study [202], the bow shock ahead of the projectile raises the temperature of the mixture in the post shock region. After an induction time that is dependent on the initial pressure, the mixture starts reacting. If the induction time is relatively short, then the reaction zone couples with the shock front resulting in a successfully initiation and stabilization of ODW. Whereas, if the initial pressure is low, the reaction zone decouples from the shock front resulting in a failure of ODW. The mechanism responsible for this initial pressure dependent behaviour was investigated in experimental studies [202] and it was found that the curvature effect of the three dimensional ODW plays a significant role in detonation stability. Further, it was also observed that the curvature effect is responsible for the stabilizing the criticality of detonation waves.

To further understand the nature of the stabilization mechanism, the three dimensional

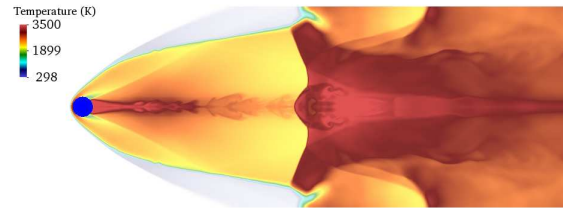




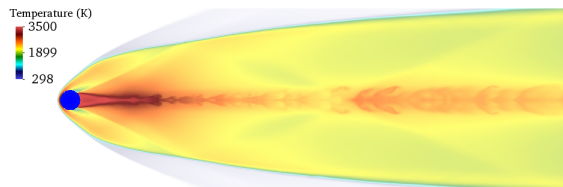
(a) Stabilized ODW



(b) Straw hat type ODW



(c) Unsteady attenuated ODW



(d) SIC

Figure 9.8: Pseudocolor plots of temperature in Y-plane at the same time instants for various filling pressures ( $p_{filling} = 97.5, 96, 95$  and  $90$  kPa) for the case of supersonic projectile shot into a stoichiometric  $H_2/O_2$  mixture.

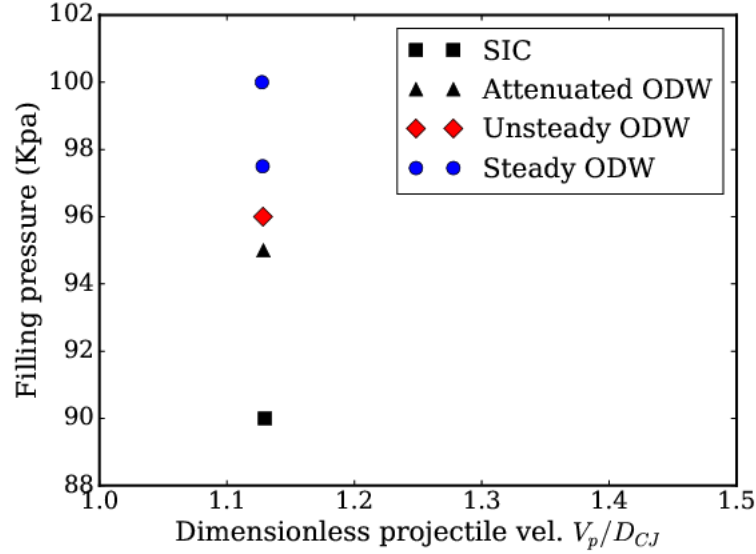


Figure 9.9: Different combustion regimes observed for various filling pressures (SIC - Shock induced combustion, ODW - Oblique Detonation Wave).

iso-surface plots of temperature are shown in Fig. 9.11. The temperature iso surface for a steady ODW is largely axi-symmetric and smooth. But for an unsteady ODW, the temperature iso-surface is characterized by a highly three dimensional structure resulting from a series of local explosions. Although the large scale structures appear axi-symmetric for the higher pressure conditions, the leading shock structure is distorted and three dimensional in nature as seen in Fig. 9.11. The experimental visualization of the ODW stabilization is available only in the center plane as it is very difficult to capture the full three dimensional structure. Whereas, in the current numerical simulations, complete data is available using which any relevant three dimensional effects can be explored.

It can be seen from the plots that the critical pressure that is required for stabilization of the ODW for the given projectile velocity,  $u_{projectile}$  is around  $p_{crit} \approx 100 kPa$ . The C-J velocities required for computing the non-dimensional projectile velocity ( $V_p/D_{CJ}$ ) for various filling pressure are determined using the Shock Detonation Tool box (SDT) developed at EDL, Caltech [194]. The critical pressure from the current simulations is found to be around  $p_{crit} = 96 kPa$ . However, the experiments noted that the criticality was observed near,

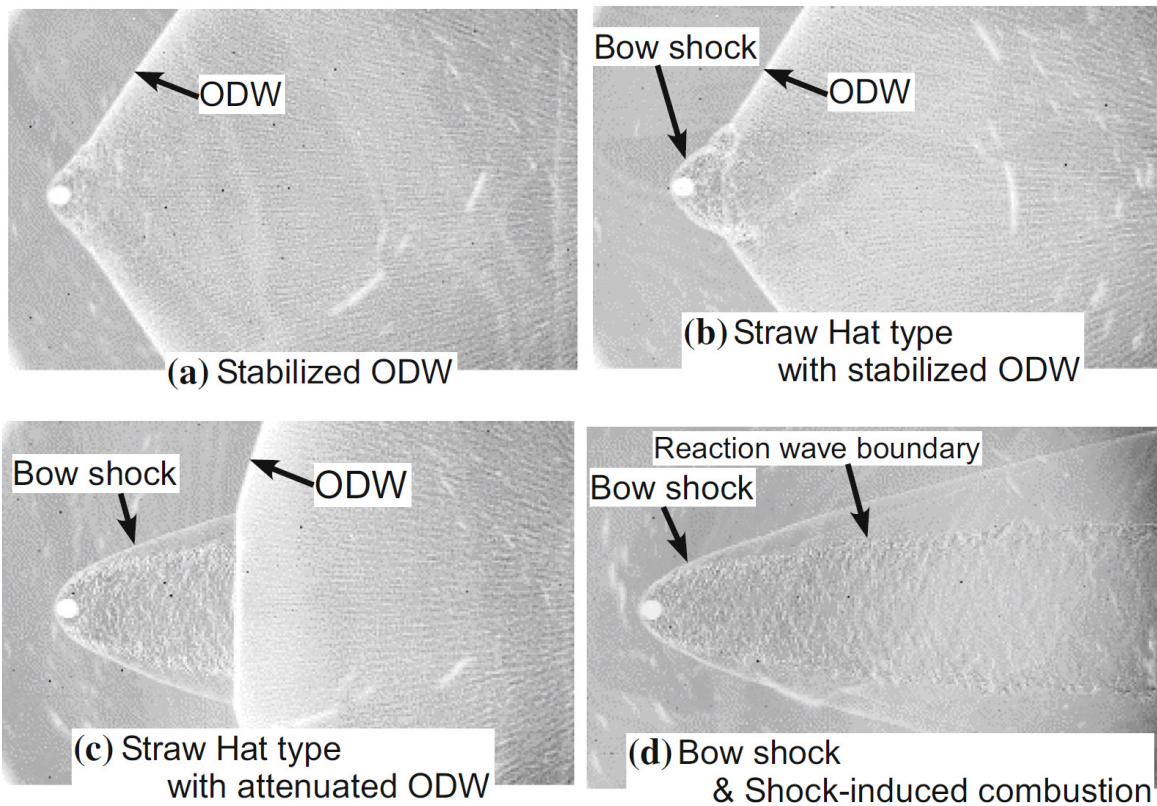


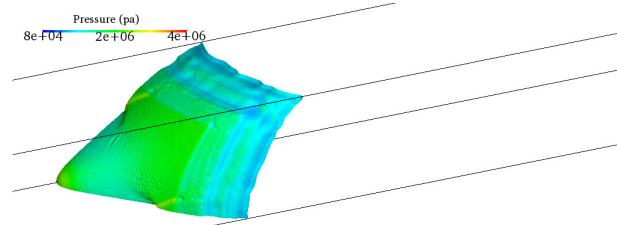
Figure 9.10: Schlieren snapshots from experiments [202] of the different combustion regimes observed for the case of supersonic projectile shot into a stoichiometric  $H_2/O_2$  mixture (figure taken from [202] with permissions).

$p_{crit} = 140$  kPa. The differences in the critical pressure between the current simulations and the experiments may be attributed to the differences in the projectile velocity. Moreover, since the induction time of the mixture plays a major role in the stabilization, the critical pressure prediction can also heavily be influenced by the chemical mechanism used for the simulations.

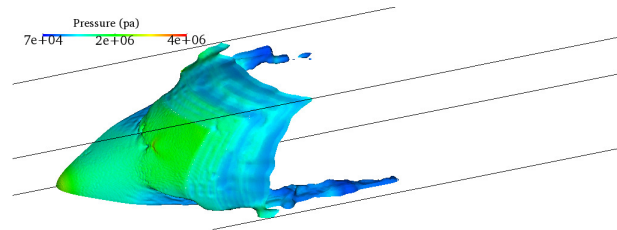
In summary, as seen from the results, the 3D curvature effect of ODW and the overall trend of transitioning from a successful detonation to a shock-induced combustion is captured correctly by the current simulations. More rigorous studies with different projectile velocities and different mechanisms are required to identify the parameter set that predicts the critical pressure closer to the experimental value. Nevertheless, all the key physics seen in experiments are captured qualitatively by the current simulations. The application studies that can be investigated using the developed numerical framework of (cutcell-AMR-RRLES) are demonstrated using some representative problems in this and the previous two chapters. The next chapter presents a summary of this thesis contributions and provides some suggestions on future research in this direction.

### 9.3 Conclusions

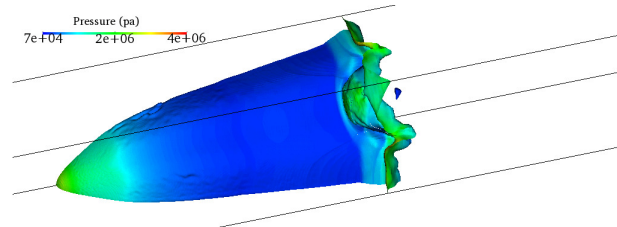
For the complex and challenging problem of detonation initiation and stabilization by supersonic projectiles, the numerical simulations accurately predict the detonation characteristics when a cylinder is impulsively moved in a reacting mixture. For the case of spherical projectiles shot into a  $H_2 - O_2 - Ar$  mixture, the simulation captures all the four combustion regimes and the trend matches well with the experimental observations. With a drop in pressure, a successful ODW first recedes to form a straw hat type ODW and eventually attenuates to a shock-induced combustion. The differences in the critical pressure prediction between the numerical simulation and experimental data for the same configuration is attributed to the chemical mechanism used. Nevertheless, the current results are very encouraging and strongly support some of the hypothesis made in experiments on stabilization of the ODW.



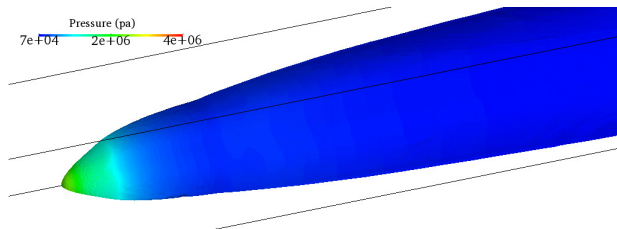
(a) Stabilized ODW



(b) Straw hat type ODW



(c) Unsteady attenuated ODW



(d) SIC

Figure 9.11: Instantaneous iso-surface of temperature colored with pressure for various filling pressures ( $p_{filling} = 90, 95, 96$  and  $97.5$  Kpa) for the case of supersonic projectile shot into a stoichiometric  $H_2/O_2$  mixture.

## CHAPTER 10

### CONCLUSIONS, CONTRIBUTIONS AND FUTURE RESEARCH DIRECTIONS

#### 10.1 Conclusions

The main goal of this thesis is to develop a comprehensive, high-order accurate and robust numerical framework to perform LES of challenging engineering problems of practical interests involving complex geometries with moving boundaries in a compressible reacting flow environment. A holistic approach is taken to identify and address several objectives required to achieve this goal. The specific contributions along with the key components of the numerical framework that is developed are listed below:

- **Ability to perform AMR:** One of the primary requirement for cost effective simulation of many practical flow problems of interest is the ability to perform dynamic local mesh refinement. Among the several approaches existing in the literature, the block structured Adaptive Mesh Refinement (AMR) methodology is chosen as most suited due to its ability to adapt to existing multi-block structured CFD codes. BoxLib which is an open source library is interfaced with in-house multi-block structured solver LESLIE to perform local mesh refinement. Although an existing AMR library is used to implement AMR within the in-house compressible solver, coupling the solver with the library and ensuring a consistent and synchronized communication between the two is highly challenging and involved a significant intellectual input. The AMR is the major contribution of this thesis over which the other numerical and modeling components are built. In fact, once interfaced, the existing capabilities of BoxLib library provided new opportunities for model development which is leveraged successfully in this thesis. The AMR framework is the bedrock over which the embedded boundary scheme and multi-level subgrid closure models are built. One of the major contribu-

tions of this thesis is the development of comprehensive understanding the nuts and bolts of performing patch based refinement.

- **A high order method for treatment of embedded boundaries:** A principal contribution of this thesis is the development and implementation of a high-order strictly conservative cut-cell method for treating embedded boundaries in viscous reacting flow. The method is shown to achieve upto fourth order accuracy for inviscid flows and third order accuracy for viscous flows in case of stationary boundaries. For moving boundaries, the method is formally second order accurate. A novel ‘small cell’ algorithm termed as cell clustering is developed to ensure the stability while still retaining the high-order accuracy of the scheme. It is shown that this new small cell treatment procedure ensures smooth reconstruction of wall shear stress on immersed boundaries and thus is able to capture physically accurate flow physics for complex configurations. The  $k$ -exact reconstruction used in the cut-cell method which is shown to be fourth-order accurate, can be extended to arbitrary orders of accuracy. The robustness and accuracy of the model were established by a series of test cases that are carefully chosen to best challenge the model’s ability. There are many other sharp interface methods used in the past but to the best of author’s knowledge none that can ensure exact conservation and also provide a smooth reconstruction of flow solution. Preserving high-order nature is especially important for LES as the numerical errors at the boundary can propagate into the flow solution and contaminate the quality of the results.

- **Development of closure models suited to AMR and embedded boundaries:** Closure model development was necessary to apply the developed numerical techniques to perform LES. A multi-level subgrid closure is developed which is an extension of the previously developed Local Dynamic  $k$ -equation model (LDKM) based sgs closure to a block-structured AMR framework with embedded boundaries termed as Cutcell-

AMRLES. The proposed correction through test cases is shown to have a consistent representation of the total turbulent kinetic energy across the different levels of AMR refinement. This consistency is shown to be required when a turbulent flow passes through a coarse/fine or fine/coarse AMR interface. For reacting flows, a multi-level reaction rate based closure (RRLES) is developed by extending the Linear Eddy Model to an AMR framework. The extension not only ensured LEM was able to work with AMR, but also in some cases shown to be more accurate than the baseline LEM model. The RRLES formulation alleviates some of the limitations associated with the original LEMLES formulation. In particular, the RRLES formulation includes large-scale molecular diffusion, which is ignored in the LEMLES formulation, and therefore, the model can be used in cases where the turbulence is either resolved at the LES level as in a DNS or if the turbulence is negligible. Additionally, due to the utilization of a multi-level strategy in the RRLES formulation, there are more unresolved scales available at the subgrid LEM level, thus leading to improved predictions.

The numerical techniques and closure modeling are validated using numerous test cases. Only the highlights of these cases along with important conclusions are discussed here. Multiple test cases demonstrated the accuracy of the AMR framework for reacting and non-reacting flow problems. The cost effectiveness of the AMR methodology was particularly realized for the 3D blast problem which required only a very small fraction of the computation resource if this problem is run with a uniform non-AMR grid. For the 3D blast simulations, since the origin is exactly resolved in comparison to a sector grid, the secondary shock propagation characteristics were more accurately captured.

The test cases for the cut-cell method were picked to best demonstrate its capabilities. In particular, a third order local and global accuracy in reconstruction is demonstrated for an immersed circular 2D domain. The effect of small cell treatment and the improvement in reconstruction of derivatives with the proposed cell clustering approach is shown using a Laplace's problem with immersed domains. Further validation and assessment of new



approach are carried out for flow past cylinder and results indicate that the current solver is able to achieve overall third-order accuracy and smooth solution even at a relatively low grid resolution. The flow patterns and phase transitions in vortex shedding are accurately predicted for the cases involving flow over staggered cylinders. The new approach is also extended to full 3D flows and used to investigate flow over single and multiple spheres, both of which are challenging problems for a body-fitted method. Also, the ability of the adaptive high-order cut-cell scheme in handling narrow gaps and sharp edges is clearly evident from the results of the problem of flow past two cylinders separated by a narrow gap and low Reynolds number flow over a corrugated airfoil. To the best of author's knowledge, the case of two cylinders in very close proximity to each other was never studied in the past due to the problem of resolving the narrow gap with a numerical grid. Such narrow gaps, as demonstrated, can be easily handled using the proposed scheme while still maintaining high orders of accuracy. The lift and drag predictions for the case of flow past a corrugated airfoil with sharp edges and abrupt changes in geometry, match well with the experimental data. This again showcases the accuracy of the scheme even in the presence of abrupt geometrical changes.

For moving boundary problems, the small cell clustering algorithm is extended to enable the transfer of mass, momentum and energy to/from newly emerging/vanishing cell events caused by boundary motion. It is shown that the proposed method achieves smooth reconstruction of near-wall shear stress and pressure even for moving boundaries. Numerical oscillations in the integrated drag coefficient, though present, is shown to diminish significantly with mesh refinement. The accuracy and robustness of the scheme are demonstrated through several non-reacting and reacting flow examples. A strong asset of the method is in ensuring strict conservation even for reacting flows with moving boundaries. The extended cell clustering method for treating the cell vanishing/emerging events is observed to reduce the formal order of accuracy of the method to second order. But using a high-order reconstruction, the magnitude of the error is shown to reduce even though the formal order of

accuracy is limited to second order. The ejection/injection of mass, momentum and energy for vanishing /emerging cell is currently done to and from neighboring cells are selected based on the cell finding algorithm developed for stationary boundaries. This may result in some numerical artifacts locally in cases when the boundary motion direction is not aligned with the local surface normal.

The multi-level AMRLES method is examined by studying decaying isotropic turbulence past a discontinuity. For this case, the method is shown to prevent the piling up of small scale turbulent kinetic energy near a fine to coarse transition. For the case of a flow past a coarse to fine transition, there is a smooth recovery of the small scale structures. The Cutcell-AMRLES method has some interesting properties that tackled some issues related to applying the existing closure models to transitional turbulent flows. The method accurately predicted the near surface and wake solution for LES of flow past a sphere and cylinder close to critical Reynolds numbers. In both the cases, the inflow is laminar and transition to turbulence occurs in the shear layers resulting from boundary layer separation. Existing one-equation based  $k^{sgs}$  can not be used without some approximation since the model is based on fully developed turbulent flows. The multi-level AMRLES approach, on the other hand, is able to correctly provide the boundary conditions for the subgrid kinetic energy from a wall resolved DNS and is therefore theoretically capable of handling transitional flows.

Three application studies, each focusing on one or more of the components in the numerical framework are studied. The important problem of flame anchoring in non-premixed transverse JICF configurations is studied using the framework developed. Several key modes and mechanisms responsible for anchoring the flame are identified from the study. It can be argued that the current framework is the most accurate and cost effective method of studying this problem. Another important problem of detonation initiation by moving supersonic projectiles is investigated using the moving cut-cell method. Particular focus is on the conditions that can stabilize a detonation over the projectile. The effect of ambient pressure on the stabilization is investigated and the different modes of combustion are analyzed. The validity

and behavior of the multi-level closure model are analyzed for the canonical problem shock and blast interacting with turbulence.

## 10.2 Thesis contributions

Many of approaches developed in this thesis have been well established with several contributions in the past. However, a number of key advances in the methods employed in this thesis. These are both algorithmic and conceptual. The highlights of this thesis are summarized below:

1. Conceptual understanding of performing block structured refinement with a multi-block structured code. The methodology developed in this thesis for interfacing BoxLib open source library and LESLIE is applicable to any general multi-block structure code. The whole approach is portable with easily substituting BoxLib with any other library or LESLIE with any other multi-block structured code.
2. Development of a high order cut-cell method by extending the  $k$ -exact CENO reconstruction approach. This approach has the potential of achieving arbitrary order of accuracy in embedded boundary methods [26].
3. A robust and accurate cell clustering scheme for handling the ‘small cell’ problem.
4. Development of a robust neighbor finding algorithm for cell clustering that works equally well in 2D/3D and for arbitrary geometries
5. A new approach to achieving conservation for mass, momentum and energy for moving boundaries by extending the cell clustering algorithm
6. A multi-level  $k^{sgs}$  closure for performing LES with AMR and cut-cell for embedded boundaries.
7. A multi-level reaction rate based closure [151] for performing LES of reacting flow problems with AMR and cutcell. approach.

### 10.3 Future recommendations

This thesis work is an inception of a new paradigm for dealing some of the most challenging aspects of simulation practical engineering problems. There are a number of future directions that can be taken to extend or improve the capabilities developed in this thesis.

#### Wall modeling for LES

Currently, wall resolved LES can be performed as there are no wall models employed. Exploring use of wall models suited for embedded boundaries can significantly reduce the cost requirements for high Reynolds number flows. In fact without wall modelling the computational cost of simulating high Reynolds number flow is prohibitively high with the current framework. There are already several efforts on this front and wall models additions can be done without any major effort.

#### Lagrangian particle tracking with AMR

Local adaptive mesh refinement can be effectively used along with Lagrangian particle tracking for simulation of multiphase dispersed flows. The framework for AMR and its coupling with a multi-block structured communication layout is already well developed and understood. Only moderate effort is needed to interface Lagrangian particle communication into the AMR framework.

#### Multiphase interface tracking

Multiphase tracking of continuous miscible fluids is relevant in many spray systems. The primary and secondary breakup of spray jets can be effectively analyzed using levelset techniques. In fact all the necessary tools and equations are already present in the developed framework and with minimal effort, multiphase interface tracking with levelset with AMR can be easily added .

### Fluid structure interaction (FSI)

All the solid boundary motion are prescribed or due to rigid body dynamics. Surface deformation due to hydrodynamic forces can modeled with addition of structural solvers to the framework to provide FSI capability. This effort is expected to be substantial as development structural solver and coupling with flow solver is a non-trivial task.

### Heat and mass transfer due to surface burning

In devices such solid rocket motors and ammunition systems, burning and regressing surfaces release mass and energy into the surrounding fluid. Burning/regressing surfaces and the associated heat and mass transfer can be effectively modeled using the current framework. The coupling of the mass and energy transfer from surface to the flow can be easily added with minimal effort.

### Cut-cell for complex geometries

The cut-cell method was shown to effectively handle complex geometrical features such as narrow gaps and sharp boundaries. For applying the method for practical combustor geometries, a translator is required which can extract signed distance levelset function, which is the input required for the cut-cell scheme, from the CAD.

### Performance improvements

Load balancing properties of the current framework can be improved to provide better performance and scaling on modern high performance clusters. Since by design the embedded boundary calculations are independent of the solver interior calculations, these embedded boundary routines can be 'offloaded' to performance accelerators such as GPU or intel phi processors.

### Quadrature integration for three dimensional cut-cell scheme

In this thesis, the Gaussian quadrature points for flux integration are implemented only for the two-dimensional cut-cell scheme. Quadrature rules need to be extended for the three-dimensional cut-cell scheme to achieve formal higher order accuracy. With the current framework, high order reconstruction can be still done for three-dimensional flows, but because of use of only one quadrature point per face, the formal order of accuracy is limited to second order.

### Faster access and extensible data structure for cut-cell stencils

In the developed framework, the cut-cells are built as array of objects. Every time a boundary undergoes a displacement, the entire cut-cell data structure is rebuilt. This can be avoided if a list based structure is adopted such that only cut-cells near displace boundaries are rebuilt. This could provide significant performance gains for moving cut-cell method.

# **Appendices**

## APPENDIX A

### CONSERVATION ANALYSIS FOR MOVING BOUNDARIES IN A UNIFORM CROSS FLOW

To understand the corrections described for moving cut-cell method, a boundary moving in an uniform constant flow with the same velocity,  $\mathbf{v}_s$ , as of the flow is considered. To facilitate the analysis we consider the arbitrary Lagrangian-Eulerian formulation of Eq. (2.1). The simplified form of the transport equation for conservative quantities,  $\mathbf{U}$ , over a cell for this case without any source terms then becomes:

$$\frac{\partial}{\partial t} \int_v \mathbf{U} dV + \int_s \mathbf{U}(\mathbf{u} - \mathbf{v}_s) \cdot \mathbf{n} ds = 0, \quad (\text{A.1})$$

where  $\mathbf{u}$  is the fluid velocity vector and  $\mathbf{n}$  is the surface normal vector. The corresponding semi-discrete form is given by:

$$(V\mathbf{U})_k^{n+1} = (V\mathbf{U})_k^n - \Delta t \left( \sum_{m=1}^M \mathbf{U}^n (u_i - v_{s,i}) n_{i,m} A_m^n \right)_k, \quad i = 1, 2, \text{ and } 3. \quad (\text{A.2})$$

Since the flow velocity is same as the velocity of the boundary,  $\Gamma$ ,  $u_i = v_{s,i}$  everywhere except at the boundary surface where  $u_i n_{i,\Gamma} = u_{n,\Gamma} = 0$ , Eq. (A.2) reduces to:

$$(V\mathbf{U})_k^{n+1} = (V\mathbf{U})_k^n + \Delta t (\mathbf{U}^n v_{s,i} n_{i,\Gamma} A_\Gamma^n)_k. \quad (\text{A.3})$$

If the corrections are consistent, then flow state  $\mathbf{U}_k$  in any cell  $k$  must be left unaltered. For a fluid cell,  $k$  that is not intercepted by a boundary either at  $t_n$  or  $t_{n+1}$ , the time update given by Eq. (A.3) would result in:

$$(V\mathbf{U})_k^{n+1} = (V\mathbf{U})_k^n, \quad (\text{A.4})$$



as there are no solid faces in the cell  $k$ . Since for this cell  $V_k^{n+1} = V_k^n$ , and flow state before and after the time update remains the same.

When the boundary moves such that, a cell  $k$  transitions from fluid to solid cell ( $V_k^n > 0$  and  $V_k^{n+1} = 0$ ), its adjacent cell neighbor  $l$  receives the vanishing cell's mass, momentum and energy. This scenario is shown in Fig.4.7(a). The time updates for the both the cells,  $k$  and  $l$  would be:

$$V_k^n (\mathbf{U})_k^{n+1,*} = (V\mathbf{U})_k^n - \Delta t (\mathbf{U}^n v_{s,\Gamma} A_\Gamma^n)_k, \quad (\text{A.5})$$

$$V_l^{n+1} (\mathbf{U})_l^{n+1,*} = (V\mathbf{U})_l^n, \quad (\text{A.6})$$

as the cell  $l$  is a full cell before the boundary motion and the net flux over its faces is therefore zero for an uniform flow. Here again, the conservative vectors  $\mathbf{U}_k^{n+1,*}$ , and  $\mathbf{U}_l^{n+1,*}$  represents the flow state of cells  $k$  and  $l$ , respectively before performing the cell clustering operation. For cell  $k$ , at the boundary face  $v_{s,i} n_i = -v_{s,\Gamma}$ . Considering cell  $l$ , since  $V_l^{n+1} < V_l^n$ , the flow state after the time update is altered. The following cell clustering correction between cells  $l$  and  $k$  according to Eq. (4.32) results in:

$$(V\mathbf{U})_l^{n+1} = V_l^{n+1} (\mathbf{U})_l^{n+1,*} + V_k^n (\mathbf{U})_k^{n+1,*}, \quad (\text{A.7})$$

$$= (V\mathbf{U})_l^n + (V\mathbf{U})_k^n - \Delta t (v_{s,\Gamma} \mathbf{U}^n A_\Gamma^n)_k, \quad (\text{A.8})$$

$$= \mathbf{U}_l^n \underbrace{(V_l^n + V_k^n - \Delta t (v_{s,\Gamma} A_\Gamma^n)_k)}_{GCL}. \quad (\text{A.9})$$

Noticing that  $(\mathbf{U})_k^n = (\mathbf{U})_l^n$  as both the cells  $l$  and  $k$  are part of the same cluster and  $V_l^n + V_k^n - \Delta t (v_{s,\Gamma} A_\Gamma^n)_k = V_l^{n+1}$  is the Geometric Conservation Law (GCL) for the volume change of the cluster comprising the cells,  $l$  and  $k$ , Eq. (A.9) gives  $\mathbf{U}_l^{n+1} = \mathbf{U}_l^n$ .

For the case when the boundary motion exposes a new cell  $k$ , such that  $V_k^n = 0$ ,  $V_k^{n+1} >$

0 and,  $v_{s,i}n_i = v_{s,\Gamma}$ , the time updates for the cell  $k$  and its neighbor  $l$  are given by:

$$V_l^{n+1}(\mathbf{U})_l^{n+1,*} = (V\mathbf{U})_l^n + \Delta t (v_{s,\Gamma} \mathbf{U}^n A_\Gamma^n)_l, \quad (\text{A.10})$$

$$V_k^{n+1}(\mathbf{U})_k^{n+1,*} = 0. \quad (\text{A.11})$$

This scenario is depicted in Fig. 4.7(b). The cell clustering correction according to Eq. (4.33) for both the cells can be shown to result in the following flow states:

$$\mathbf{U}_l^{n+1} = \mathbf{U}_k^{n+1} = V_k^{n+1}(\mathbf{U})_k^{n+1,*} / (V_k^{n+1} + V_l^{n+1}), \quad (\text{A.12})$$

$$= \mathbf{U}_l^n \underbrace{(V_l^n + \Delta t (v_{s,\Gamma} A_\Gamma^n)_l)}_{\text{GCL}} / (V_k^{n+1} + V_l^{n+1}). \quad (\text{A.13})$$

Since  $V_l^n + \Delta t (v_{s,\Gamma} A_\Gamma^n)_l = V_k^{n+1} + V_l^{n+1}$ , the right hand side of Eq. (A.13) reduces to  $\mathbf{U}_l^n$ . This analysis provides a basic understanding of the correction procedure to ensure exact conservation. It is important to note that without the time update given by Eq. (4.31), conservation is not ensured. The same correction steps given above are valid to any given stage of a multi-step Runge-Kutta scheme. The above analysis is described for the case of a cluster comprising only two cells,  $l$  and  $k$  for clarity. But the main strength of the extended cell clustering approach in handling cell emerging and vanishing events is that the procedure is applicable even in cases where the cluster comprises of more than two cells.

## APPENDIX B

### COMPUTATIONAL PERFORMANCE

The computational performance of  $k = 2$  and 3 reconstruction is analyzed for the problem of flow over a sphere. The three main steps that take up 99% of the computational time required per solver step are found to be:

1. Computing the solution,  $\mathbf{x}$ , to the least-square problem for determining reconstruction polynomial. This involves matrix multiplication of the pre-computed pseudo inverse matrix,  $A^\dagger$  with the neighbor flow solution matrix,  $\mathbf{b}$  ( $\mathbf{x} = A^\dagger \mathbf{b}$ ). This must be done every time step to update the coefficients of the reconstruction polynomial.
2. Computing the inviscid flux,  $\mathbf{F}^{\text{inv}}(\mathbf{U})$ , Eq. (2.55).
3. Computing the viscous flux,  $\mathbf{F}^{\text{vis}}(\mathbf{U})$ , Eq. (2.56).

The fraction of time spent by each of the above step is reported in Table B.1. As seen from the table, the main increase in computational time required for  $k = 3$ , is due to the overhead in computing the linear least square solution. This is due to the increase in stencil size requiring 124 neighbors for solving Eq. (4.9). The size of the matrices,  $A^\dagger$  and  $\mathbf{b}$  increased from  $9 \times 27$  and  $27 \times 1$  for  $k = 2$  to  $19 \times 125$  and  $125 \times 1$  for  $k = 3$ , respectively. The significant increase in the size of matrix systems contribute to the bulk of the cost increase. For any higher order reconstruction, i.e. for  $k > 3$ , the cost increase can be expected to be mainly due to the increase in stencil size and number of terms in the reconstruction polynomial. The cost increase for  $k = 4$  from  $k = 3$ , is expected not to be as significant as for  $k = 3$  from  $k = 2$  because the stencil width for both  $k = 4$  and 3 is the same. Only the number of terms in the reconstruction polynomial would go up from 19 to 34 as determined from Eq. (4.11).

Table B.1: Fraction of time spent by various routines for a time integration step.

Order	$t_{\mathbf{x}=A^\dagger \mathbf{b}}$	$t_{\mathbf{F}^{\text{inv}}(\mathbf{U})}$	$t_{\mathbf{F}^{\text{vis}}(\mathbf{U})}$
$k=2$	0.39	0.17	0.44
$k=3$	0.64	0.09	0.27

## REFERENCES

- [1] K. Kailasanath. “Review of propulsion applications of detonation waves”. In: *AIAA J.* 38.9 (2000), pp. 1698–1708.
- [2] J. Choi, M. Cakmak, and S. Menon. “Simulation of composite solid propellant combustion using adaptive mesh refinement”. In: *49th AIAA Aerospace Sciences Conference, Orlando, FL* AIAA-2011-0417 (2011).
- [3] K. Vanden et al. *Hypersonic and Unsteady Flow Science Issues for Explosively Formed Penetrator Warheads*. Tech. rep. DTIC Document, 2006.
- [4] K.J. Vanden and D.V. Nance. “Aerothermodynamic study of a generic EFP configuration”. In: *6th AIAA Biennial National Forum on Weapon System Effectiveness* AFRL-RW-EG-TP-2010-7404 (2009).
- [5] J-Y. Jang and M-C. Wu. “Numerical and experimental studies of three dimensional plate-fin and tube heat exchangers”. In: *Int. J. Heat Mass Transfer* 39.14 (1996), pp. 3057–3066.
- [6] I. Kim, S. Elghobashi, and W. Sirignano. “Three-dimensional flow over two spheres placed side by side”. In: *J. Fluid Mech* 246 (1993), pp. 465–488.
- [7] Z. Ali et al. “Block topology generation for structured multi-block meshing with hierarchical geometry handling”. In: *Procedia Engineering* 163 (2016), pp. 212–224.
- [8] D.F. Hawken, J. J. Gottlieb, and J. S. Hansen. “Review of some adaptive node-movement techniques in finite-element and finite-difference solutions of partial differential equations”. In: *J. Comput. Phys.* 95.2 (1991), pp. 254–302.
- [9] F. Alauzet. “A changing-topology moving mesh technique for large displacements”. In: *Engineering with Computers* 30.2 (2014), pp. 175–200.
- [10] A. Jameson, T.J. Baker, and N.P. Weatherill. “Calculation of inviscid transonic flow over a complete aircraft”. In: *24th AIAA Conference, Reno, NV* 0103 (1986), pp. 86–103.
- [11] J. Peraire et al. “Adaptive remeshing for compressible flow computations”. In: *J. Comput. Phys.* 72 (1987), pp. 449–466.

- [12] T.E. Tezduyar. “Finite Element Methods for Flow Problems with Moving Boundaries”. In: *Arch. Comput. Methods. Eng.* 8 (2001), pp. 83–130.
- [13] P. Cocks, M. C. Soteriou, and V. Sankaran. “Impact of numerics on the predictive capabilities of reacting flow LES”. In: *Combustion and Flame* 162.9 (2015), pp. 3394–3411.
- [14] G. Yang, D.M. Causon, and D.M. Ingram. “Calculation of compressible flows about complex moving geometries using a three-dimensional Cartesian cut cell method”. In: *Int. J. Num. Meth. Fluids* 33 (2000), pp. 1121–1151.
- [15] R. Mittal, H.S. Udaykumar, and W. Shyy. “An accurate Cartesian grid method for viscous incompressible flows with complex immersed boundaries”. In: *J. Comput. Phys.* 156 (1999), pp. 209–240.
- [16] E.A. Fadlun et al. “Combined immersed-boundary finite-difference methods for three-dimensional complex flow simulations”. In: *J. Comput. Phys.* 161 (2000), pp. 35–60.
- [17] TH. Tseng and J. Freziger. “A ghost-cell immersed boundary method for flow in complex geometry”. In: *J. Comput. Phys.* 192 (2003), pp. 593–623.
- [18] A. Pogorelov, Meinke M., and W. Schröder. “Cut-cell method based large-eddy simulation of tip-leakage flow”. In: *Phys. Fluids* 27.075106 (2015), pp. 1–21.
- [19] M.J. Berger and P. Colella. “Local adaptive mesh refinement for shock hydrodynamics”. In: *J. Comput. Phys.* 82 (1989), pp. 64–84.
- [20] R. Mittal and G. Iaccarino. “Immersed boundary methods”. In: *Annual Rev. Fluid Mech.* 37 (2005), pp. 239–261.
- [21] Z. J. Wang et al. “High-order CFD methods: current status and perspective”. In: *Int. J. Num. Methods. Fluids* 72.8 (2013), pp. 811–845.
- [22] A. G. Kravchenko and P. Moin. “On the effect of numerical errors in large eddy simulations of turbulent flows”. In: *J. Comput. Phys.* 131.2 (1997), pp. 310–322.
- [23] T. Plewa, T. Linde, and V. G. Weirs. “Adaptive mesh refinement-theory and applications”. In: *Proceedings of the Chicago workshop on adaptive mesh refinement methods*. Vol. 41. Springer. 2003.
- [24] M. Vanella, A. Posa, and E. Balaras. “Adaptive mesh refinement for immersed boundary methods”. In: *J. Fluids Engg.* 136.4 (2014), p. 040909.

- [25] D. Hartmann, M. Meinke, and W. Schröder. “A strictly conservative Cartesian cut-cell method for compressible viscous flows on adaptive grids”. In: *Comput. Methods Appl. Mech. Engrg.* 200 (2011), pp. 1038–1052.
- [26] B. Muralidharan and S. Menon. “A high-order adaptive Cartesian cut-cell method for simulation of compressible viscous flow over immersed bodies”. In: *J. Comput. Phys.* 321 (2016), pp. 342–368.
- [27] M. J. Aftosmis, M. J. Berger, and G. Adomavicius. “A parallel Cartesian approach for external aerodynamics of vehicles with complex geometry”. In: *Proceedings of the Thermal and Fluids Analysis Workshop, NASA Marshall Spaceflight Center, Huntsville, AL*, (1999).
- [28] R. Deiterding. “A parallel adaptive method for simulating shock-induced combustion with detailed chemical kinetics in complex domains”. In: *Comput. Struct.* 87.11 (2009), pp. 769–783.
- [29] K. G. Powell, P. L. Roe, and J. J. Quirk. *Adaptive mesh algorithms for computational fluid dynamics*. Ed. by M. Y. Hussaini, A. Kumar, and M. D. Salas. Springer, 1992.
- [30] C. Dapogny, C. Dobrzynski, and P. Frey. “Three-dimensional adaptive domain remeshing, implicit domain meshing, and applications to free and moving boundary problems”. In: *J. Comput. Phys.* 262 (2014), pp. 358–378.
- [31] CCSE. *Boxlib user guide*. Tech. rep. <https://ccse.lbl.gov>: Center for Computational Sciences and Engineering, 2012.
- [32] P. Colella et al. *Chombo software package for amr applications-design document*. 2000.
- [33] P. MacNeice et al. “PARAMESH: A parallel adaptive mesh refinement community toolkit”. In: *Computer physics communications* 126.3 (2000), pp. 330–354.
- [34] A. M. Wissink et al. “Large scale parallel structured AMR calculations using the SAMRAI framework”. In: *Supercomputing, ACM/IEEE 2001 Conference*. IEEE. 2001, pp. 22–22.
- [35] M. J. Berger and LeVeque R. J. *AMRCLAW software*.
- [36] R. Deiterding. *AMROC-blockstructured adaptive mesh refinement in object-oriented C++*. 2003.
- [37] F. Génin and S. Menon. “Dynamics of sonic jet injection into supersonic crossflow”. In: *J. Turbulence* 11 (2010), pp. 1–30.

- [38] F. Genin and S. Menon. “Dynamics of sonic jet into supersonic crossflow”. In: *J. Turbul.* 11.4 (2010), pp. 1–30.
- [39] F. Génin and S. Menon. “Studies of shock/turbulent shear layer interaction using Large-Eddy Simulation”. In: *Computers and Fluids* 39 (2010), pp. 800–819.
- [40] J. Donea, S. Giuliani, and J. P. Halleux. “An arbitrary Lagrangian-Eulerian finite element method for transient dynamic fluid-structure interactions”. In: *Comput. Methods Appl. Mech. Engrg.* 33.1-3 (1982), pp. 689–723.
- [41] T. J. Hughes, W. K. Liu, and T. K. Zimmerman. “Lagrangian-Eulerian finite element formulation for incompressible viscous flows”. In: *Comput. Methods Appl. Mech. Engrg.* 3 (1981), pp. 329–349.
- [42] J.L. Steger, F.C. Dougherty, and J.A. Benek. “A chimera grid scheme”. In: *Advances in Grid Generation, ASME FED-5, Ghia KN* (1983), pp. 59–69.
- [43] W.D. Henshaw and D.W. Schwendeman. “Moving overlapping grids with adaptive mesh refinement for high-speed reactive and non-reactive flow”. In: *J. Comput. Phys.* 216 (2006), pp. 744–779.
- [44] D. Kershaw et al. “3D unstructured mesh ALE hydrodynamics with the upwind discontinuous finite element method”. In: *Comput. Meth. Appl. Mech. Engrg* 158 (1998), pp. 81–116.
- [45] A. Soria and F. Casadei. “Arbitrary Lagrangian-Eulerian multicomponent compressible flow with fluid-structure interaction”. In: *Int. J. Numer. Meth. Fluids* 25 (1997), pp. 1263–1284.
- [46] R. Löhner et al. “Fluid-structure interaction simulations using parallel computers”. In: *Lecture notes in Computer Science* 2565 (2003), pp. 3–23.
- [47] A. Gilmanov and F. Sotiropoulos. “A hybrid Cartesian/immersed boundary method for simulating flows with 3D, geometrically complex, moving bodies”. In: *J. Comput. Phys.* 207 (2005), pp. 457–492.
- [48] X.Y. Hu et al. “A conservative interface method for compressible flows”. In: *J. Comput. Phys.* 219 (2006), pp. 553–578.
- [49] F. Örley et al. “Cut-element based immersed boundary method for moving geometries in compressible liquid flows with cavitation”. In: *J. Comput. Phys.* 283 (2015), pp. 1–22.
- [50] L. Schneiders et al. “An Accurate moving boundary formulation in cut-cell methods”. In: *J. Comput. Phys.* 235 (2012), pp. 786–809.



- [51] C.S. Peskin. “The fluid dynamics of heart valves: experimental, theoretical and computational methods”. In: *Annual Rev. Fluid Mech.* 14 (1981), pp. 235–259.
- [52] D. Clarke, M. Salas, and H. Hassan. “Euler calculations for multi-element airfoils using Cartesian grids”. In: *AIAA J.* 24 (Jan. 1986), pp. 1128–1135.
- [53] C. S. Peskin. “Numerical analysis of blood flow in the heart”. In: *J. Comput. Phys.* 25 (1977), pp. 220–252.
- [54] B. Griffith and C.S. Peskin. “On the order of accuracy of immersed boundary method: higher order convergence rates for sufficiently smooth problems”. In: *J. Comput. Phys.* 208 (2005), pp. 75–105.
- [55] C-S. Kim. “An immersed-boundary finite volume method for simulations of flow in complex geometries”. In: *J. Comput. Phys.* 171 (2001), pp. 132–150.
- [56] M. Lai and C.S. Peskin. “An immersed-boundary method with formal second-order accuracy and reduced numerical viscosity”. In: *J. Comput. Phys.* 160 (2000), pp. 705–719.
- [57] A. Roma, C.S. Peskin, and M. Berger. “An adaptive version of the immersed boundary method”. In: *J. Comput. Phys.* 153 (1999), pp. 509–534.
- [58] J.M. Stockie and B.R. Wetton. “Analysis of stiffness in the immersed boundary method and implications for time-stepping schemes”. In: *J. Comput. Phys.* 154 (1998), pp. 41–64.
- [59] J. Mohd-Yosuf. “Combined immersed boundary/B-spline methods for simulation of flow in complex geometries”. In: *Annual Res. Briefs, Cent. Turb. Res* (1997), pp. 317–328.
- [60] R. Verzicco et al. “LES in complex geometries using boundary body forces”. In: *AIAA J.* 38 (2000), pp. 427–433.
- [61] E. Balaras. “Modeling complex boundaries using an external force field on fixed Cartesian grids in large eddy simulations”. In: *Comput. Fluids* 33 (2004), pp. 375–404.
- [62] X. Zeng and C. Farhat. “A systematic approach for constructing high-order immersed boundary and ghost fluid methods for fluid-structure interaction problems”. In: *J. Comput. Phys.* 231 (2012), pp. 2892–2923.
- [63] S. Sambasivan, A. Kapahi, and H.S. Udaykumar. “Simulation of high speed impact, penetration and fragmentation problems on locally refined Cartesian grids”. In: *J. Comput. Phys.* In Press (2012).

- [64] M. Arienti et al. “A level set approach To Eulerian-Lagrangian coupling”. In: *J. Comput. Phys.* 185 (2003), pp. 213–251.
- [65] H.S. Udaykumar et al. “A sharp interface Cartesian grid method for simulating flows with complex moving boundaries”. In: *J. Comput. Phys.* 174 (2001), pp. 345–380.
- [66] R. LeVeque and Z. Li. “The Immersed Interface Method for Elliptic Equations with Discontinuous Coefficients and Singular Sources”. In: *SIAM J. Numer. Anal.* 31.4 (1993), pp. 1019–1044.
- [67] R. P. Fedkiw et al. “A non-oscillatory Eulerian approach to interfaces in multima-  
terial flows (the ghost fluid method)”. In: *J. Comput. Phys.* 152.2 (1999), pp. 457–  
492.
- [68] R. Mittal et al. “A versatile sharp interface immersed boundary method for incom-  
pressible flows with complex boundaries”. In: *J. Comput. Phys.* 10 (2008), pp. 4825–  
4852.
- [69] S. Kang, G. Iaccarino, and P. Moin. “Accurate immersed boundary reconstructions  
for viscous flow simulations”. In: *AIAA J.* 47 (2009), pp. 1750–1760.
- [70] A. Mark and B.G.M. van Wachem. “Derivation and validation of a novel implicit  
second-order accurate immersed boundary method”. In: *J. Comput. Phys.* 227 (2008),  
pp. 6660–6680.
- [71] N. Peller et al. “High-order stable interpolations for immersed boundary methods”.  
In: *Int. J. Numer. Methods Fluids* 52 (2006), pp. 1175–1193.
- [72] D.D. Marshall and S.M. Ruffin. “An embedded boundary Cartesian grid scheme for  
viscous flows using a new viscous wall boundary condition treatment”. In: *42nd  
AIAA Conference, Reno, NV* 0581 (2004).
- [73] S. Majumdar, G. Iaccarino, and P.A. Durbin. “RANS solver with adaptive structured  
boundary non-conforming grids”. In: *Annual Res. Briefs, Cent. Turb. Res* (2001),  
pp. 353–364.
- [74] J. Lee et al. “Sources of spurious force oscillations from an immersed boundary  
method for moving-body problems”. In: *J. Comput. Phys.* 230.7 (2011), pp. 2677  
–2695.
- [75] R. Ghias, R. Mittal, and T. Lund. “A non-body conformal grid method for simu-  
lation of compressible flows with complex immersed boundaries”. In: *42nd AIAA  
Aerospace Sciences Meeting and Exhibit*. 2004, p. 80.

- [76] H. Udin, R.M.J. Kramer, and C. Pantano. “A Cartesian-based embedded geometry technique with adaptive high-order finite differences for compressible flow around complex geometries”. In: *J. Comput. Phys.* 262 (2014), pp. 379–407.
- [77] J.D. Lee and S.M. Ruffin. “Development of a turbulent wall-function based viscous Cartesian-grid methodology”. In: *45th AIAA Conference, Reno, NV* 1326 (2007).
- [78] S. M. Ruffin, M. Zaki, and S. Sekhar. “A normal ray refinement technique for Cartesian-grid based Navier–Stokes solvers”. In: *Int. J. Comput. Fluid Dynamics* 26.4 (2012), pp. 231–246.
- [79] M. Vanella, P. Rabenold, and E. Balaras. “A direct-forcing embedded-boundary method with adaptive mesh refinement for fluid-structure interaction problems”. In: *J. Comput. Phys.* 229 (2010), pp. 6427–6449.
- [80] K. Wang et al. “Algorithms for interface treatment and load computation in embedded boundary methods for fluid and fluid-structure interaction problems”. In: *Int. J. Num. Meth. Fluids* 67 (2011), pp. 1175–1206.
- [81] H. Forrer and M. Berger. “Flow simulations on Cartesian grids involving complex moving geometries flows”. In: *Int. Ser. Num. Math* 129 (1998), pp. 315–324.
- [82] J. Lee and D. You. “An implicit ghost-cell immersed boundary method for simulations of moving body problems with control of spurious force oscillations”. In: *J. Comput. Phys.* 233 (2013), pp. 295–314.
- [83] M. Bergmann, J. Hovnanian, and A. Iollo. “An Accurate Cartesian Method for Incompressible Flows with Moving Boundaries”. In: *Commun. Comput. Phys.* 15.5 (2014), pp. 1266–1290.
- [84] H.S. Udaykumar, W. Shyy, and M.M. Rao. “A mixed Eulerian-Lagrangian method for fluid flows with complex and moving boundaries”. In: *Int. J. Numer. Methods* 22 (1996), pp. 691–705.
- [85] D. Cecere and E. Giacomazzi. “An immersed volume method for large eddy simulation of compressible flows using a staggered-grid approach”. In: *Comput. Methods Appl. Mech. Engrg.* 280 (2014), pp. 1–27.
- [86] C. Merlin, P. Domingo, and L. Vervisch. “Immersed boundaries in large eddy simulation of compressible flows”. In: *Flow Turbul. Combust.* 90.1 (2012), pp. 29–68.
- [87] W.J. Coirier and K.G. Powell. “Solution-adaptive Cartesian cell approach for viscous and inviscid flows”. In: *AIAA J.* 34.5 (1996), pp. 938–945.

- [88] M. Meyer, S. Hickel, and N.A. Adams. “Assessment of implicit large-eddy simulation with a conservative immersed interface method for turbulent cylinder flow”. In: *Int. J. Heat Fluid Flow* 31.3 (2010), pp. 368–377.
- [89] J.H. Seo and R. Mittal. “A sharp interface immersed boundary method with improved mass conservation and reduced spurious pressure oscillations”. In: *J. Comput. Phys.* 230 (2011), pp. 7347–7363.
- [90] T. Ye et al. “An accurate Cartesian grid method for viscous incompressible flows with complex immersed boundaries”. In: *J. Comput. Phys.* 156 (1999), pp. 209–240.
- [91] M.H. Chung. “Cartesian cut cell approach for simulating incompressible flows with rigid bodies of arbitrary shape”. In: *Comput. Fluids* 35 (2006), pp. 606–623.
- [92] M. Kirkpatrick, S. Armfield, and J. Kent. “A representation of curved boundaries for the solution of the Navier-Stokes equations on a staggered three dimensional Cartesian grid”. In: *J. Comput. Phys.* 184 (2003), pp. 1–36.
- [93] W. Noh. “CEL: A time dependent, two-space dimensional, coupled Eulerian-Lagrangian code”. In: *Fundamental methods of Hydrodynamics, Methods of Computational Physics* 3 (1964), pp. 117–179.
- [94] D. Hartmann, M. Meinke, and W. Schröder. “An adaptive multilevel multigrid formulation for Cartesian hierarchical grid methods”. In: *Comput. Fluids* 37 (2008), pp. 1103–1125.
- [95] M. Berger and M.J. Aftosmis. “Progress towards a Cartesian cut-cell method for viscous compressible flow”. In: *50th AIAA Conference, Nashville, TN AIAA-2012-1301* (Jan. 2012).
- [96] H.S. Udaykumar, R. Mittal, and P. Rampunggoon. “Interface tracking finite volume method for complex solid-fluid interactions on fixed meshes”. In: *J. Comput. Phys.* 18 (2002), pp. 89–97.
- [97] D. Hartmann, M. Meinke, and W. Schröder. “A general formulation of boundary conditions on Cartesian cut-cells for compressible viscous flow”. In: *19th AIAA CFD Conference, San Antonio, Texas* 3878 (June 2009).
- [98] F. Gao et al. “The development of a Cartesian cut cell method for incompressible viscous flows”. In: *Int. J. Numer. Meth. Fluids* 54 (2007), pp. 1033–1053.
- [99] O. Botella and Y. Cheny. “On the treatment of complex geometries in a Cartesian grid flow solver with the level set method”. In: *European Conference On Computational Fluid Dynamics, Netherlands* 181 (2006).

- [100] M. Meyer et al. “A conservative immersed interface method for large eddy simulation for incompressible flows”. In: *J. Comput. Phys.* 229 (2010), pp. 6300–6317.
- [101] G. Yang et al. “A Cartesian cut cell method For compressible flows Part A: static body problems”. In: *The Aeronautical J.* 101 (1997), pp. 47–56.
- [102] G. Yang et al. “A Cartesian cut cell method for compressible flows Part B: moving body problems”. In: *The Aeronautical J.* 101 (1997), pp. 57–65.
- [103] X.Y. Hu and B.C. Khoo. “An interface interaction method for compressible multi-fluids”. In: *J. Comput. Phys.* 198 (2004), pp. 35–64.
- [104] L. Schneiders et al. “An Accurate moving boundary formulation in cut-cell methods”. In: *J. Comput. Phys.* 311 (2016), pp. 62–86.
- [105] R. Pember et al. “An adaptive Cartesian grid method for unsteady compressible flow in irregular regions”. In: *J. Comput. Phys.* 120 (1995), pp. 278–304.
- [106] L. Chen, Y. Yu, and G. Hou. “Sharp-interface immersed boundary lattice Boltzmann method with reduced spurious-pressure oscillations for moving boundaries”. In: *Phys.Rev.* 87.053306 (2013), pp. 1–11.
- [107] H. Ji, F-S. Lien, and E. Yee. “Numerical simulation of detonation using an adaptive Cartesian cut-cell method combined with a cell-merging technique”. In: *Comput. & Fluids* 39.6 (2010), pp. 1041–1057.
- [108] A. R. Kerstein. “Linear-eddy modeling of turbulent transport. II: Application to shear layer mixing”. In: *Combust. Flame* 75 (1989), pp. 397–413.
- [109] S. B. Pope. *Turbulent flows*. 2001.
- [110] Christer Fureby and S-I Möller. “Large eddy simulation of reacting flows applied to bluff body stabilized flames”. In: *AIAA J.* 33.12 (1995), pp. 2339–2347.
- [111] W. W. Kim and S. Menon. “An unsteady incompressible Navier-Stokes solver for large eddy simulation of turbulent flows”. In: *I. J. for Numer. Meth. Fluids.* 31 (1999), pp. 983–1017.
- [112] R. MacCormack. “The effect of viscosity in hypervelocity impact cratering”. In: *J. spacecraft and rockets* 40.5 (2003), pp. 757–763.
- [113] E.F. Toro. “Riemann solvers and numerical methods for fluid mechanics”. In: *Springer, 3rd ed.* (2009).

- [114] L. Ivan and C.P.T. Groth. “High-order solution-adaptive Central Essentially Non-Oscillatory (CENO) method for viscous flows”. In: *J. Comput. Phys.* 257.A (2014), pp. 830–862.
- [115] J. Loeliger and M. McCullough. *Version Control with Git: Powerful tools and techniques for collaborative software development.* ” O’Reilly Media, Inc.”, 2012.
- [116] K. Martin and B. Hoffman. *Mastering CMake: a cross-platform build system.* Kitware, 2010.
- [117] L. I. Sedov. *Similarity and dimensional methods in mechanics.* CRC press, 1993.
- [118] K. C. Gottiparthi and S. Menon. “A study of interaction of clouds of inert particles with detonation in gases”. In: *Combustion Science and Technology* 184.3 (2012), pp. 406–433.
- [119] S. R. Turns et al. *An introduction to combustion.* Vol. 287. McGraw-hill New York, 1996.
- [120] K. Balakrishnan et al. “Numerical study of blast characteristics from detonation of homogeneous explosives”. In: *Shock Waves* 20.2 (2010), pp. 147–162.
- [121] S. Osher and J.A. Sethian. “Fronts propagating with curvature-dependent speed: algorithms based on Hamilton-Jacobi formulations”. In: *J. Comput. Phys.* 79 (1988), pp. 12–49.
- [122] S. Osher and R.P. Fedkiw. *Level set methods and dynamic implicit surfaces.* Applied mathematical science. New York, N.Y.: Springer, 2003. ISBN: 0-387-95482-1.
- [123] C.O. Gooch and M. Alten. “A high order accurate unstructured mesh finite volume scheme for the advection diffusion equation”. In: *J. Comput. Phys.* 181 (2002), pp. 729–752.
- [124] C. Lawson and R. Hanson. *Solving least squares problems.* Prentice Hall Inc., 1974.
- [125] R. Penrose. “A generalized inverse for matrices”. In: *Proc. Camb. Philos. Soc.* 51 (1955), pp. 406–413.
- [126] D.M. Ingram, D.M. Causon, and C.G. Mingham. “Developments in Cartesian cut cell methods”. In: *Math. Comput. Sim.* 61 (2003), pp. 561–572.
- [127] C. Liang, S. Premasuthan, and A. Jameson. “Higher order accurate simulation of low Mach laminar flow past two side by side cylinders using spectral difference method”. In: *Comput. Struct.* 87 (2009), pp. 812–827.

- [128] D. Tritton. “Experiments on flow past a circular cylinder at low Reynolds numbers”. In: *J. Fluid Mech.* 6 (1959), pp. 547–567.
- [129] C. Williamson. “Oblique and parallel modes of vortex shedding in the wake of circular cylinder at low Reynolds numbers”. In: *J. Fluid Mech.* 206 (1989), pp. 579–627.
- [130] S. Kang. “Characteristics of flow over two circular cylinders in a side-by-side arrangement at low Reynolds numbers”. In: *Phys. Fluids* 15.9 (2003), pp. 2486–2498.
- [131] D. Sumner, S.J. Price, and P. Paidoussis. “Flow-pattern identification for two staggered circular cylinders in cross-flow”. In: *J. Fluid Mech.* 411 (2000), pp. 263–303.
- [132] B. Kesel A. “Aerodynamic characteristics of dragonfly wing sections compared with technical aerofoils”. In: *J. Exp. Biol.* 203 (2000), pp. 3125–3135.
- [133] A. Vargas, R. Mittal, and H. Dong. “A computational study of the aerodynamic performance of a dragonfly wing section in gliding flight”. In: *Bioinsp. Biomim.* 3.026004 (2008), pp. 1–13.
- [134] H. Hu and M. Tamai. “Bioinspired corrugated airfoil at low Reynolds Numbers”. In: *J. Aircraft* 45.6 (2008), pp. 2068–2077.
- [135] T. Johnson and V. Patel. “Flow past a sphere upto a Reynolds number of 300”. In: *J. Fluid Mech.* 378 (1999), pp. 19–70.
- [136] S. Marella et al. “Sharp interface Cartesian grid method I: an easily implemented technique for 3D moving boundary computations”. In: *J. Comput. Phys.* 210 (2005), pp. 1–31.
- [137] Y. Dubief and F. Delcayre. “On coherent-vortex identification in turbulence”. In: *J. turbulence* 1.1 (2000), pp. 011–011.
- [138] H. W. Liepmann and A. Roshko. *Elements of gas dynamics*. John wiley and sons, 1957.
- [139] S. M. Murman, M. J. Aftosmis, and M. J. Berger. “Implicit approaches for moving boundaries in a 3D Cartesian method”. In: *41st AIAA Conference, Reno, NV AIAA-2003-1119* (2003).
- [140] J.F. McCarthy Jr and T. Kubota. “A study of wakes behind a circular cylinder at  $M=5.7$ ”. In: *AIAA J.* 2 (1964), pp. 620–636.
- [141] F. S. Billig. “Shock-wave shapes around spherical and cylindrical-nosed bodies”. In: *J. Spacecraft* 4.6 (1967), pp. 822–823.

- [142] M. Terracol, P. Sagaut, and C. Basdevant. “A multilevel algorithm for large-eddy simulation of turbulent compressible flows”. In: *J. Comput. Phys.* 167.2 (2001), pp. 439–474.
- [143] M. Vanella, U. Piomelli, and E. Balaras. “Effect of grid discontinuities on large eddy simulation statistics and flow fields”. In: *J. Turbul.* 9 (2008), pp. 1–23.
- [144] L. Goodfriend et al. “Large-eddy simulation of decaying isotropic turbulence across a grid refinement interface using explicit filtering and reconstruction”. In: *J. Turbul.* 14.12 (2013), pp. 58–76.
- [145] R. Ranjan and S. Menon. “On the application of the two-level large-eddy simulation method to turbulent free-shear and wake flows”. In: *J. Turbul.* 16.2 (2015), pp. 136–166.
- [146] J. S. Son and T. J. Hanratty. “Velocity gradients at the wall for flow around a cylinder at Reynolds numbers from  $5 \times 10^3$  to  $10^5$ ”. In: *J. Fluid Mech.* 35.02 (1969), pp. 353–368.
- [147] C. Norberg. “Effects of Reynolds number and a low-intensity freestream turbulence on the flow around a circular cylinder”. In: *Chalmers University, Goteborg, Sweden, Technological Publications* 87.2 (1987).
- [148] W. C. L. Shih et al. “Experiments on flow past rough circular cylinders at large Reynolds numbers”. In: *Journal of Wind Engineering and Industrial Aerodynamics* 49.1-3 (1993), pp. 351–368.
- [149] L. Ong and J. Wallace. “The velocity field of the turbulent very near wake of a circular cylinder”. In: *Experiments in fluids* 20.6 (1996), pp. 441–453.
- [150] I. Rodriguez et al. “Direct numerical simulation of the flow over a sphere at  $Re=3700$ ”. In: *Journal of Fluid Mechanics* 679 (2011), pp. 263–287.
- [151] R. Ranjan et al. “Subgrid-Scale Modeling of Reaction-Diffusion and Scalar Transport in Turbulent Premixed Flames”. In: *Combust. Sci. Technol.* 188.9 (2016), pp. 1496–1537.
- [152] S. Menon, P.A. McMurtry, and A. R. Kerstein. “A Linear Eddy Mixing Model for Large Eddy Simulation of Turbulent Combustion”. In: *LES of Complex Engineering and Geophysical Flows*. Ed. by B. Galperin and S. Orszag. Cambridge University Press, 1993, pp. 287–314.
- [153] Suresh Menon and Alan R Kerstein. “The Linear-Eddy Model”. In: *Turbulent Combustion Modeling*. Springer, 2011, pp. 221–247.



- [154] T. M. Smith and S. Menon. “One-Dimensional Simulations of Freely Propagating Turbulent Premixed Flames”. In: *Combust. Sci. Technol.* 128 (1997), pp. 99–130.
- [155] Vaidyanathan Sankaran and Subesh Menon. “Structure of premixed turbulent flames in the thin-reaction-zones regime”. In: *Proc. Combust. Inst.* 28.1 (2000), pp. 203–209.
- [156] V. Chakravarthy and S. Menon. “Large Eddy Simulation of Turbulent Premixed Flames in the Flamelet Regime”. In: *Combust. Sci. Technol.* 162 (2001), pp. 175–222.
- [157] FF Grinstein and K Kailasanath. “Three-dimensional numerical simulations of unsteady reactive square jets”. In: *Combust. Flame* 101 (1995), p. 192.
- [158] N. Peters. *Turbulent Combustion*. Cambridge University Press, 2000.
- [159] R. H. Kraichnan. “Diffusion by a random velocity field”. In: *Phys. Fluids* 13 (1970), pp. 22–31.
- [160] V. Sankaran and S. Menon. “Subgrid combustion modeling of 3-D premixed flames in the thin-reaction-zone regime”. In: *Proc. Combust. Inst.* 30 (2005), pp. 575–582.
- [161] Ramanan Sankaran et al. “Structure of a spatially developing turbulent lean methane–air Bunsen flame”. In: *Proc. Combust. Inst.* 31 (2007), pp. 1291–1298.
- [162] Stephen B Pope. “Ten questions concerning the large-eddy simulation of turbulent flows”. In: *New journal of Physics* 6.1 (2004), p. 35.
- [163] O. Colin et al. “A thickened flame model for large eddy simulations of turbulent premixed combustion”. In: *Physics of Fluids* 12 (2000), pp. 1843–1863.
- [164] A.J. Kravachenko, P. Moin, and R. Moser. “Zonal embedded grids for numerical simulations of wall-bounded turbulent flows”. In: *J. Comput. Phys.* 127.2 (1996), pp. 412–423.
- [165] P. Sullivan, C-H. Moeng, and J.C. McWilliams. “A grid nesting method for large eddy simulation of planetary boundary-layer flows”. In: *Boundary-Layer Meteorology* 80 (1996), pp. 167–202.
- [166] P. Quemere, P. Sagaut, and V. Couailler. “A new multi-domain/multi-resolution method for large-eddy simulation”. In: *International Journal for Numerical Methods and Fluids* 36 (2001), pp. 391–416.
- [167] J. Larsson. “Effect of Shock-Capturing Errors on Turbulence Statistics”. In: *AIAA J.* 48.7 (2010), pp. 1554–1557.

- [168] J. Larsson and S. K. Lele. “Direct numerical simulation of canonical shock/turbulence interaction”. In: *Phys. Fluids* 21.126101 (2009).
- [169] A. Bhagatwala and S. Lele. “Interaction of a Taylor blast wave with isotropic turbulence”. In: *Phys. Fluids* 23.035103 (2011).
- [170] T. L. Jackson, M. Y. Hussaini, and H. S. Ribner. “Interaction of turbulence with a detonation wave”. In: *Phys. Fluids A: Fluid Dynamics* 5.745 (1993).
- [171] X. Chai and K. Mahesh. “Dynamic K-equation model for large eddy simulation of compressible flows”. In: *J. Fluid Mech.* 699 (2012), pp. 385–413.
- [172] K. Mahesh, S. K. Lele, and P. Moin. “The influence of entropy fluctuations on the interaction of turbulence with a shock wave”. In: *J. Fluid Mech.* 334 (1997), pp. 353–379.
- [173] U. Piomelli et al. “Subgrid-scale backscatter in turbulent and transitional flows”. In: *Phys. Fluids A* 3 (1991), pp. 1766–1771.
- [174] G. I. Taylor. “The formation of a blast wave by a very intense explosion”. In: *Proc. R. Soc. London, Ser. A* 201.159 (1950).
- [175] B. Kaushik et al. “Numerical study of blast characteristics from detonation of homogeneous explosives”. In: *Shock Waves* 20.147-162 (2010).
- [176] K. Doebbeling, J. Hellat, and H. Koch. “25 Years of BBC/ABB/Alstom lean pre-mix combustion technologies”. In: *ASME J. Engng for Gas Turbines and Power* 19 (2007), pp. 2–12.
- [177] W. Jessen, W. Schroeder, and M. Klass. “Evolution of jets effusing from inclined holes into crossflow”. In: *Int. J. Heat Fluid Flow* 28 (2007), pp. 1312–26.
- [178] T.F. Fric and A. Roshko. “Vortical structure in the wake of a transverse jet”. In: *J. Fluid Mech.* 279 (1994), pp. 1–47.
- [179] J. Andreopoulos and W. Rodi. “Experimental investigation of jets in a cross flow”. In: *J. Fluid Mech* 138 (1984), pp. 93–127.
- [180] J. Andreopoulos. “On the structure of jets in a cross flow”. In: *J. Fluid Mech* 157 (1985), pp. 163–197.
- [181] S.L.V. Coelho and J.C.R. Hunt. “The dynamics of the near field of strong jets in cross flows”. In: *J. Fluid Mech* 200 (1989), pp. 95–120.

- [182] L.K. Su and M.G. Mungal. “Simultaneous measurements of scalar and velocity field evolution in turbulent cross-flowing jets”. In: *J. Fluid Mech* 513 (2004), pp. 1–45.
- [183] S.H. Smith and M.G. Mungal. “Mixing, structure and scaling of jet in cross flow”. In: *J. Fluid Mech* 357 (1998), pp. 83–152.
- [184] S. Muppidi and K. Mahesh. “Study of trajectories of jets in cross flow using direct numerical simulations”. In: *J. Fluid Mech* 530 (2004), pp. 81–100.
- [185] A.R. Karagozian. “Transverse jets and their control”. In: *Prog. Energy. Combust. Sci.* 36 (2010), pp. 531–53.
- [186] K. Mahesh. “The interaction of jets with cross flow”. In: *Annu. Rev. Fluid Mech.* 45 (2013), pp. 379–407.
- [187] R.W. Grout et al. “Direct numerical simulation of flame stabilization downstream of a transverse fuel jet in cross-flow”. In: *Proc. Combust. Inst.* 33 (2011), pp. 1629–37.
- [188] R.W. Grout et al. “A direct numerical simulation study of turbulence and flame structure in transverse jets analysed in jet- trajectory based coordinates”. In: *J. Fluid Mech* 706 (2012), pp. 351–383.
- [189] A. M. Steinberg et al. “Structure and stabilization of hydrogen jet flames in cross-flows”. In: *Proceedings of the Combustion Institute* 34.1 (2013), pp. 1499–1507.
- [190] J. Li and A. Karazov. “An updated comprehensive kinetic model of hydrogen combustion”. In: *Int. J. Chem. Kinetics* 36 (2004), pp. 566–575.
- [191] T. H. New, T. T. Lim, and S. C. Luo. “Effects of jet velocity profiles on a round jet in cross-flow”. In: *Experiments in Fluids* 40.6 (2006), pp. 859–875.
- [192] T.F. Lu et al. “Three-dimensional direct numerical simulation of a turbulent lifted hydrogen jet flame in a heated coflow: a chemical explosive mode analysis”. In: *J. Fluid Mech* 652 (2010), pp. 45–64.
- [193] W. L. Chan and M. Ihme. “Large-Eddy Simulation of a Turbulent Reacting Jet in Crossflow”. In: *8th US National Combustion Meeting* 070LT-0108 (2013).
- [194] S. Browne, J. Ziegler, and J. E. Shepherd. “Numerical solution methods for shock and detonation jump conditions”. In: *GALCIT Report FM2006.006* (2006).
- [195] J.B. Bdzil and A.K. Kapila. “Shock-to-detonation transition: A model problem”. In: *Phys. Fluids* 4 (1992), pp. 409–418.

- [196] J.W. Dold and A.K. Kapila. “Comparison between shock initiations of detonation using thermally-sensitive and chain-branching chemical models”. In: *Combustion and Flame* 85 (1991), pp. 185–194.
- [197] G.J. Sharpe. “Numerical simulations of pulsating detonations: II piston initiated detonations”. In: *Combustion Theory and Modeling* 5 (2001), pp. 623–638.
- [198] G.O. Brown C.J. and Thomas. “Experimental studies of shock-induced ignition and transition to detonation in ethylene and propylene mixtures”. In: *Combustion and Flame* 117 (1999), pp. 861–870.
- [199] R. Deiterding. *Parallel adaptive simulation of multi-dimensional detonation structures*. Citeseer, 2003.
- [200] A. K. Kapila and D. W. Schwendeman. “Detonation initiation modeling computation and mechanisms”. In: *ICHMT, Int. Symp. Adv. in Comp. Heat Transfer, Norway* CHT-04-C2 (2004).
- [201] Z. Jiang et al. “Self-organized generation of transverse waves in diverging cylindrical detonations”. In: *Combustion and Flame* 156 (2009), pp. 1653–1661.
- [202] S. Maeda et al. “Scale effect of spherical projectiles for stabilization of oblique detonation waves”. In: *Shock waves* 25 (2015), pp. 141–150.

## VITA

Balaji Muralidharan joined Computational Combustion Lab (CCL), Georgia Institute of Technology in Spring 2010 and pursued doctoral studies under the guidance of Professor Suresh Menon. His area of research was in the development of high order embedded boundary methods for simulation of turbulent reacting flow problems. Before joining CCL, he worked as an application engineer at ANSYS for two years from 2007 - 2009. Balaji completed his masters in mechanical engineering jointly from Indian Institute of Technology, Madras and Technical University of Munich, Germany from 2005 - 2007. He did his bachelors in mechanical engineering from Anna University, India from 2001 - 2005.

**SPRINGER LICENSE  
TERMS AND CONDITIONS**

May 02, 2017

This Agreement between Balaji Muralidharan ("You") and Springer ("Springer") consists of your license details and the terms and conditions provided by Springer and Copyright Clearance Center.

License Number	4101090080661
License date	May 02, 2017
Licensed Content Publisher	Springer
Licensed Content Publication	Shock Waves
Licensed Content Title	Scale effect of spherical projectiles for stabilization of oblique detonation waves
Licensed Content Author	S. Maeda
Licensed Content Date	Jan 1, 2015
Licensed Content Volume	25
Licensed Content Issue	2
Type of Use	Thesis/Dissertation
Portion	Figures/tables/illustrations
Number of figures/tables/illustrations	1
Author of this Springer article	No
Order reference number	
Original figure numbers	2
Title of your thesis / dissertation	Simulation of reacting flow problems in complex geometries with moving and static boundaries
Expected completion date	May 2017
Estimated size(pages)	248
Requestor Location	Balaji Muralidharan 251 10th Street, C409  ATLANTA, GA 30318 United States Attn: Balaji Muralidharan
Billing Type	Invoice
Billing Address	Balaji Muralidharan 251 10th Street, C409  ATLANTA, GA 30318 United States Attn: Balaji Muralidharan
Total	0.00 USD
Terms and Conditions	

**Introduction**

The publisher for this copyrighted material is Springer. By clicking "accept" in connection

with completing this licensing transaction, you agree that the following terms and conditions apply to this transaction (along with the Billing and Payment terms and conditions established by Copyright Clearance Center, Inc. ("CCC"), at the time that you opened your Rightslink account and that are available at any time at <http://myaccount.copyright.com>).

#### Limited License

With reference to your request to reuse material on which Springer controls the copyright, permission is granted for the use indicated in your enquiry under the following conditions:

- Licenses are for one-time use only with a maximum distribution equal to the number stated in your request.

- Springer material represents original material which does not carry references to other sources. If the material in question appears with a credit to another source, this permission is not valid and authorization has to be obtained from the original copyright holder.

- This permission

- is non-exclusive

- is only valid if no personal rights, trademarks, or competitive products are infringed.

- explicitly excludes the right for derivatives.

- Springer does not supply original artwork or content.

- According to the format which you have selected, the following conditions apply accordingly:

- **Print and Electronic:** This License include use in electronic form provided it is password protected, on intranet, or CD-Rom/DVD or E-book/E-journal. It may not be republished in electronic open access.

- **Print:** This License excludes use in electronic form.

- **Electronic:** This License only pertains to use in electronic form provided it is password protected, on intranet, or CD-Rom/DVD or E-book/E-journal. It may not be republished in electronic open access.

For any electronic use not mentioned, please contact Springer at [permissions.springer@spi-global.com](mailto:permissions.springer@spi-global.com).

- Although Springer controls the copyright to the material and is entitled to negotiate on rights, this license is only valid subject to courtesy information to the author (address is given in the article/chapter).

- If you are an STM Signatory or your work will be published by an STM Signatory and you are requesting to reuse figures/tables/illustrations or single text extracts, permission is granted according to STM Permissions Guidelines: <http://www.stm-assoc.org/permissions-guidelines/>

For any electronic use not mentioned in the Guidelines, please contact Springer at [permissions.springer@spi-global.com](mailto:permissions.springer@spi-global.com). If you request to reuse more content than stipulated in the STM Permissions Guidelines, you will be charged a permission fee for the excess content.

Permission is valid upon payment of the fee as indicated in the licensing process. If permission is granted free of charge on this occasion, that does not prejudice any rights we might have to charge for reproduction of our copyrighted material in the future.

- If your request is for reuse in a Thesis, permission is granted free of charge under the following conditions:

This license is valid for one-time use only for the purpose of defending your thesis and with a maximum of 100 extra copies in paper. If the thesis is going to be published, permission needs to be reobtained.

- includes use in an electronic form, provided it is an author-created version of the thesis on his/her own website and his/her university's repository, including UMI (according to the definition on the Sherpa website: <http://www.sherpa.ac.uk/romeo/>);

- is subject to courtesy information to the co-author or corresponding author.

#### Geographic Rights: Scope

Licenses may be exercised anywhere in the world.

**Altering/Modifying Material: Not Permitted**

Figures, tables, and illustrations may be altered minimally to serve your work. You may not alter or modify text in any manner. Abbreviations, additions, deletions and/or any other alterations shall be made only with prior written authorization of the author(s).

**Reservation of Rights**

Springer reserves all rights not specifically granted in the combination of (i) the license details provided by you and accepted in the course of this licensing transaction and (ii) these terms and conditions and (iii) CCC's Billing and Payment terms and conditions.

**License Contingent on Payment**

While you may exercise the rights licensed immediately upon issuance of the license at the end of the licensing process for the transaction, provided that you have disclosed complete and accurate details of your proposed use, no license is finally effective unless and until full payment is received from you (either by Springer or by CCC) as provided in CCC's Billing and Payment terms and conditions. If full payment is not received by the date due, then any license preliminarily granted shall be deemed automatically revoked and shall be void as if never granted. Further, in the event that you breach any of these terms and conditions or any of CCC's Billing and Payment terms and conditions, the license is automatically revoked and shall be void as if never granted. Use of materials as described in a revoked license, as well as any use of the materials beyond the scope of an unrevoked license, may constitute copyright infringement and Springer reserves the right to take any and all action to protect its copyright in the materials.

**Copyright Notice: Disclaimer**

You must include the following copyright and permission notice in connection with any reproduction of the licensed material:

"Springer book/journal title, chapter/article title, volume, year of publication, page, name(s) of author(s), (original copyright notice as given in the publication in which the material was originally published) "With permission of Springer"

In case of use of a graph or illustration, the caption of the graph or illustration must be included, as it is indicated in the original publication.

**Warranties: None**

Springer makes no representations or warranties with respect to the licensed material and adopts on its own behalf the limitations and disclaimers established by CCC on its behalf in its Billing and Payment terms and conditions for this licensing transaction.

**Indemnity**

You hereby indemnify and agree to hold harmless Springer and CCC, and their respective officers, directors, employees and agents, from and against any and all claims arising out of your use of the licensed material other than as specifically authorized pursuant to this license.

**No Transfer of License**

This license is personal to you and may not be sublicensed, assigned, or transferred by you without Springer's written permission.

**No Amendment Except in Writing**

This license may not be amended except in a writing signed by both parties (or, in the case of Springer, by CCC on Springer's behalf).

**Objection to Contrary Terms**

Springer hereby objects to any terms contained in any purchase order, acknowledgment, check endorsement or other writing prepared by you, which terms are inconsistent with these terms and conditions or CCC's Billing and Payment terms and conditions. These terms and conditions, together with CCC's Billing and Payment terms and conditions (which are incorporated herein), comprise the entire agreement between you and Springer (and CCC) concerning this licensing transaction. In the event of any conflict between your obligations established by these terms and conditions and those established by CCC's Billing and Payment terms and conditions, these terms and conditions shall control.



**Jurisdiction**

All disputes that may arise in connection with this present License, or the breach thereof, shall be settled exclusively by arbitration, to be held in the Federal Republic of Germany, in accordance with German law.

**Other conditions:**

V 12AUG2015

Questions? [customercare@copyright.com](mailto:customercare@copyright.com) or +1-855-239-3415 (toll free in the US) or +1-978-646-2777.

---

---

# ELSEVIER LICENSE TERMS AND CONDITIONS

May 15, 2017

This Agreement between Balaji Muralidharan ("You") and Elsevier ("Elsevier") consists of your license details and the terms and conditions provided by Elsevier and Copyright Clearance Center.

License Number	4104480767510
License date	
Licensed Content Publisher	Elsevier
Licensed Content Publication	Journal of Computational Physics
Licensed Content Title	A high-order adaptive Cartesian cut-cell method for simulation of compressible viscous flow over immersed bodies
Licensed Content Author	Balaji Muralidharan,Suresh Menon
Licensed Content Date	15 September 2016
Licensed Content Volume	321
Licensed Content Issue	n/a
Licensed Content Pages	27
Start Page	342
End Page	368
Type of Use	reuse in a thesis/dissertation
Intended publisher of new work	other
Portion	full article
Format	electronic
Are you the author of this Elsevier article?	Yes
Will you be translating?	No
Order reference number	
Title of your thesis/dissertation	Simulation of reacting flow problems in complex geometries with moving and static boundaries
Expected completion date	May 2017
Estimated size (number of pages)	248
Elsevier VAT number	GB 494 6272 12
Requestor Location	Balaji Muralidharan 251 10th Street, C409  ATLANTA, GA 30318 United States Attn: Balaji Muralidharan
Publisher Tax ID	98-0397604
Billing Type	Invoice
Billing Address	Balaji Muralidharan 251 10th Street, C409

ATLANTA, GA 30318  
United States  
Attn: Balaji Muralidharan

Total

0.00 USD

[Terms and Conditions](#)

## INTRODUCTION

1. The publisher for this copyrighted material is Elsevier. By clicking "accept" in connection with completing this licensing transaction, you agree that the following terms and conditions apply to this transaction (along with the Billing and Payment terms and conditions established by Copyright Clearance Center, Inc. ("CCC"), at the time that you opened your Rightslink account and that are available at any time at <http://myaccount.copyright.com>).

## GENERAL TERMS

2. Elsevier hereby grants you permission to reproduce the aforementioned material subject to the terms and conditions indicated.

3. Acknowledgement: If any part of the material to be used (for example, figures) has appeared in our publication with credit or acknowledgement to another source, permission must also be sought from that source. If such permission is not obtained then that material may not be included in your publication/copies. Suitable acknowledgement to the source must be made, either as a footnote or in a reference list at the end of your publication, as follows:

"Reprinted from Publication title, Vol /edition number, Author(s), Title of article / title of chapter, Pages No., Copyright (Year), with permission from Elsevier [OR APPLICABLE SOCIETY COPYRIGHT OWNER]." Also Lancet special credit - "Reprinted from The Lancet, Vol. number, Author(s), Title of article, Pages No., Copyright (Year), with permission from Elsevier."

4. Reproduction of this material is confined to the purpose and/or media for which permission is hereby given.

5. Altering/Modifying Material: Not Permitted. However figures and illustrations may be altered/adapted minimally to serve your work. Any other abbreviations, additions, deletions and/or any other alterations shall be made only with prior written authorization of Elsevier Ltd. (Please contact Elsevier at [permissions@elsevier.com](mailto:permissions@elsevier.com)). No modifications can be made to any Lancet figures/tables and they must be reproduced in full.

6. If the permission fee for the requested use of our material is waived in this instance, please be advised that your future requests for Elsevier materials may attract a fee.

7. Reservation of Rights: Publisher reserves all rights not specifically granted in the combination of (i) the license details provided by you and accepted in the course of this licensing transaction, (ii) these terms and conditions and (iii) CCC's Billing and Payment terms and conditions.

8. License Contingent Upon Payment: While you may exercise the rights licensed immediately upon issuance of the license at the end of the licensing process for the transaction, provided that you have disclosed complete and accurate details of your proposed use, no license is finally effective unless and until full payment is received from you (either by publisher or by CCC) as provided in CCC's Billing and Payment terms and conditions. If full payment is not received on a timely basis, then any license preliminarily granted shall be deemed automatically revoked and shall be void as if never granted. Further, in the event that you breach any of these terms and conditions or any of CCC's Billing and Payment terms and conditions, the license is automatically revoked and shall be void as if never granted. Use of materials as described in a revoked license, as well as any use of the materials beyond the scope of an unrevoked license, may constitute copyright infringement and publisher reserves the right to take any and all action to protect its copyright in the materials.

9. Warranties: Publisher makes no representations or warranties with respect to the licensed material.

10. **Indemnity:** You hereby indemnify and agree to hold harmless publisher and CCC, and their respective officers, directors, employees and agents, from and against any and all claims arising out of your use of the licensed material other than as specifically authorized pursuant to this license.

11. **No Transfer of License:** This license is personal to you and may not be sublicensed, assigned, or transferred by you to any other person without publisher's written permission.

12. **No Amendment Except in Writing:** This license may not be amended except in a writing signed by both parties (or, in the case of publisher, by CCC on publisher's behalf).

13. **Objection to Contrary Terms:** Publisher hereby objects to any terms contained in any purchase order, acknowledgment, check endorsement or other writing prepared by you, which terms are inconsistent with these terms and conditions or CCC's Billing and Payment terms and conditions. These terms and conditions, together with CCC's Billing and Payment terms and conditions (which are incorporated herein), comprise the entire agreement between you and publisher (and CCC) concerning this licensing transaction. In the event of any conflict between your obligations established by these terms and conditions and those established by CCC's Billing and Payment terms and conditions, these terms and conditions shall control.

14. **Revocation:** Elsevier or Copyright Clearance Center may deny the permissions described in this License at their sole discretion, for any reason or no reason, with a full refund payable to you. Notice of such denial will be made using the contact information provided by you. Failure to receive such notice will not alter or invalidate the denial. In no event will Elsevier or Copyright Clearance Center be responsible or liable for any costs, expenses or damage incurred by you as a result of a denial of your permission request, other than a refund of the amount(s) paid by you to Elsevier and/or Copyright Clearance Center for denied permissions.

### LIMITED LICENSE

The following terms and conditions apply only to specific license types:

15. **Translation:** This permission is granted for non-exclusive world **English** rights only unless your license was granted for translation rights. If you licensed translation rights you may only translate this content into the languages you requested. A professional translator must perform all translations and reproduce the content word for word preserving the integrity of the article.

16. **Posting licensed content on any Website:** The following terms and conditions apply as follows: Licensing material from an Elsevier journal: All content posted to the web site must maintain the copyright information line on the bottom of each image; A hyper-text must be included to the Homepage of the journal from which you are licensing at <http://www.sciencedirect.com/science/journal/xxxxx> or the Elsevier homepage for books at <http://www.elsevier.com>; Central Storage: This license does not include permission for a scanned version of the material to be stored in a central repository such as that provided by Heron/XanEdu.

Licensing material from an Elsevier book: A hyper-text link must be included to the Elsevier homepage at <http://www.elsevier.com>. All content posted to the web site must maintain the copyright information line on the bottom of each image.

**Posting licensed content on Electronic reserve:** In addition to the above the following clauses are applicable: The web site must be password-protected and made available only to bona fide students registered on a relevant course. This permission is granted for 1 year only. You may obtain a new license for future website posting.

17. **For journal authors:** the following clauses are applicable in addition to the above:

#### Preprints:

A preprint is an author's own write-up of research results and analysis, it has not been peer-reviewed, nor has it had any other value added to it by a publisher (such as formatting, copyright, technical enhancement etc.).

Authors can share their preprints anywhere at any time. Preprints should not be added to or enhanced in any way in order to appear more like, or to substitute for, the final versions of articles however authors can update their preprints on arXiv or RePEc with their Accepted Author Manuscript (see below).

If accepted for publication, we encourage authors to link from the preprint to their formal publication via its DOI. Millions of researchers have access to the formal publications on ScienceDirect, and so links will help users to find, access, cite and use the best available version. Please note that Cell Press, The Lancet and some society-owned have different preprint policies. Information on these policies is available on the journal homepage.

**Accepted Author Manuscripts:** An accepted author manuscript is the manuscript of an article that has been accepted for publication and which typically includes author-incorporated changes suggested during submission, peer review and editor-author communications.

Authors can share their accepted author manuscript:

- immediately
  - via their non-commercial person homepage or blog
  - by updating a preprint in arXiv or RePEc with the accepted manuscript
  - via their research institute or institutional repository for internal institutional uses or as part of an invitation-only research collaboration work-group
  - directly by providing copies to their students or to research collaborators for their personal use
  - for private scholarly sharing as part of an invitation-only work group on commercial sites with which Elsevier has an agreement
- After the embargo period
  - via non-commercial hosting platforms such as their institutional repository
  - via commercial sites with which Elsevier has an agreement

In all cases accepted manuscripts should:

- link to the formal publication via its DOI
- bear a CC-BY-NC-ND license - this is easy to do
- if aggregated with other manuscripts, for example in a repository or other site, be shared in alignment with our hosting policy not be added to or enhanced in any way to appear more like, or to substitute for, the published journal article.

**Published journal article (JPA):** A published journal article (PJA) is the definitive final record of published research that appears or will appear in the journal and embodies all value-adding publishing activities including peer review co-ordination, copy-editing, formatting, (if relevant) pagination and online enrichment.

Policies for sharing publishing journal articles differ for subscription and gold open access articles:

**Subscription Articles:** If you are an author, please share a link to your article rather than the full-text. Millions of researchers have access to the formal publications on ScienceDirect, and so links will help your users to find, access, cite, and use the best available version.

Theses and dissertations which contain embedded PJAs as part of the formal submission can be posted publicly by the awarding institution with DOI links back to the formal publications on ScienceDirect.

If you are affiliated with a library that subscribes to ScienceDirect you have additional private sharing rights for others' research accessed under that agreement. This includes use for classroom teaching and internal training at the institution (including use in course packs and courseware programs), and inclusion of the article for grant funding purposes.

**Gold Open Access Articles:** May be shared according to the author-selected end-user license and should contain a [CrossMark logo](#), the end user license, and a DOI link to the

formal publication on ScienceDirect.

Please refer to Elsevier's [posting policy](#) for further information.

**18. For book authors** the following clauses are applicable in addition to the above:

Authors are permitted to place a brief summary of their work online only. You are not allowed to download and post the published electronic version of your chapter, nor may you scan the printed edition to create an electronic version. **Posting to a repository:** Authors are permitted to post a summary of their chapter only in their institution's repository.

**19. Thesis/Dissertation:** If your license is for use in a thesis/dissertation your thesis may be submitted to your institution in either print or electronic form. Should your thesis be published commercially, please reapply for permission. These requirements include permission for the Library and Archives of Canada to supply single copies, on demand, of the complete thesis and include permission for Proquest/UMI to supply single copies, on demand, of the complete thesis. Should your thesis be published commercially, please reapply for permission. Theses and dissertations which contain embedded PJAs as part of the formal submission can be posted publicly by the awarding institution with DOI links back to the formal publications on ScienceDirect.

### **Elsevier Open Access Terms and Conditions**

You can publish open access with Elsevier in hundreds of open access journals or in nearly 2000 established subscription journals that support open access publishing. Permitted third party re-use of these open access articles is defined by the author's choice of Creative Commons user license. See our [open access license policy](#) for more information.

#### **Terms & Conditions applicable to all Open Access articles published with Elsevier:**

Any reuse of the article must not represent the author as endorsing the adaptation of the article nor should the article be modified in such a way as to damage the author's honour or reputation. If any changes have been made, such changes must be clearly indicated.

The author(s) must be appropriately credited and we ask that you include the end user license and a DOI link to the formal publication on ScienceDirect.

If any part of the material to be used (for example, figures) has appeared in our publication with credit or acknowledgement to another source it is the responsibility of the user to ensure their reuse complies with the terms and conditions determined by the rights holder.

#### **Additional Terms & Conditions applicable to each Creative Commons user license:**

**CC BY:** The CC-BY license allows users to copy, to create extracts, abstracts and new works from the Article, to alter and revise the Article and to make commercial use of the Article (including reuse and/or resale of the Article by commercial entities), provided the user gives appropriate credit (with a link to the formal publication through the relevant DOI), provides a link to the license, indicates if changes were made and the licensor is not represented as endorsing the use made of the work. The full details of the license are available at <http://creativecommons.org/licenses/by/4.0>.

**CC BY NC SA:** The CC BY-NC-SA license allows users to copy, to create extracts, abstracts and new works from the Article, to alter and revise the Article, provided this is not done for commercial purposes, and that the user gives appropriate credit (with a link to the formal publication through the relevant DOI), provides a link to the license, indicates if changes were made and the licensor is not represented as endorsing the use made of the work. Further, any new works must be made available on the same conditions. The full details of the license are available at <http://creativecommons.org/licenses/by-nc-sa/4.0>.

**CC BY NC ND:** The CC BY-NC-ND license allows users to copy and distribute the Article, provided this is not done for commercial purposes and further does not permit distribution of the Article if it is changed or edited in any way, and provided the user gives appropriate credit (with a link to the formal publication through the relevant DOI), provides a link to the license, and that the licensor is not represented as endorsing the use made of the work. The full details of the license are available at <http://creativecommons.org/licenses/by-nc-nd/4.0>. Any commercial reuse of Open Access articles published with a CC BY NC SA or CC BY NC ND license requires permission from Elsevier and will be subject to a fee.

Commercial reuse includes:

- Associating advertising with the full text of the Article
- Charging fees for document delivery or access
- Article aggregation
- Systematic distribution via e-mail lists or share buttons

Posting or linking by commercial companies for use by customers of those companies.

## 20. Other Conditions:

v1.9

Questions? [customercare@copyright.com](mailto:customercare@copyright.com) or +1-855-239-3415 (toll free in the US) or +1-978-646-2777.

---